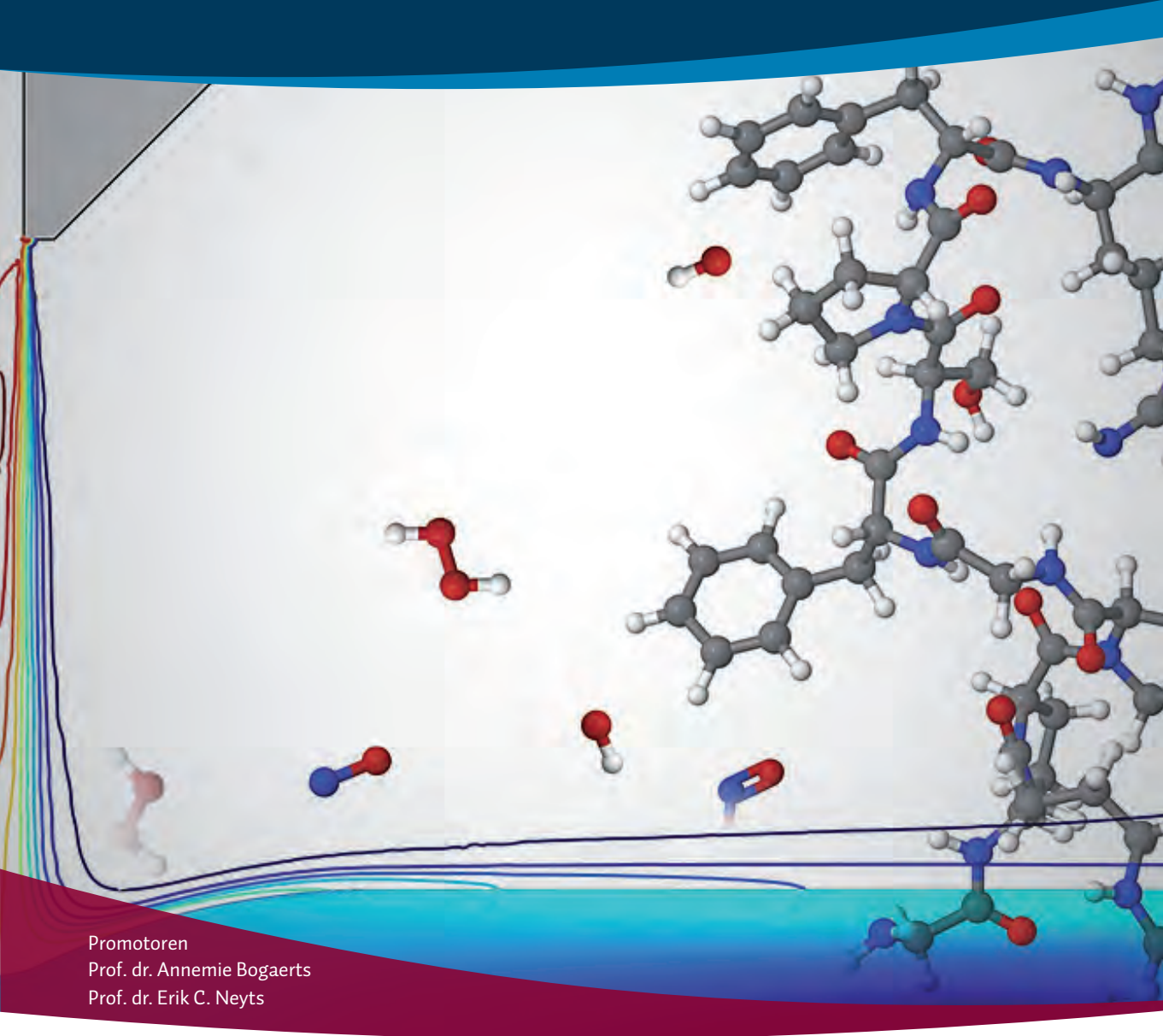


# The behavior of plasma-generated reactive species in plasma medicine

Proefschrift voorgelegd tot het behalen van de graad van doctor in  
de wetenschappen aan de Universiteit Antwerpen te verdedigen door

**Christof Verlackt**



Promotoren  
Prof. dr. Annemie Bogaerts  
Prof. dr. Erik C. Neyts



**Faculteit Wetenschappen**

Departement Chemie

The behavior of plasma-generated reactive species in  
plasma medicine

De rol van reactieve deeltjes, gegenereerd door plasma's, in  
plasma geneeskunde

Proefschrift voorgelegd tot het behalen van de graad van doctor in de  
Wetenschappen aan de Universiteit Antwerpen te verdedigen door  
**Christof Verlackt**

Promotoren:           Prof. Dr. Annemie BOGAERTS  
                              Prof. Dr. Erik C. NEYTS

Antwerpen, 2018



# Table of Contents

<b>Dankwoord</b> .....	IX
<b>Summary</b> .....	XI
<b>Samenvatting</b> .....	XV
<b>List of abbreviations</b> .....	XIX
 <b>1 Introduction to Plasma Medicine</b> .....	 1
<b>1-1 Plasma</b> .....	3
1-1.1 What is a plasma.....	3
1-1.2 Non-thermal plasma .....	5
<b>1-2 Plasma medicine</b> .....	9
1-2.1 Background.....	9
1-2.2 Plasma sources used in the medical field .....	12
1-2.2a Overview .....	12
1-2.2b Dielectric Barrier Discharges (DBD) .....	15
1-2.2c Atmospheric Pressure Plasma Jets (APPJ) .....	17
1-2.2d Plasma Treated Liquids .....	18
1-2.3 Applications in plasma medicine .....	21
1-2.3a Introduction .....	21
1-2.3b Chronic wound healing .....	22
Introduction to wound healing .....	22
Chronic wound healing and plasma treatment.....	23
1-2.3c Cancer .....	25
Introduction to the biology of cancer <sup>133–135</sup> .....	25
Treatment of cancer .....	29
Plasmas for cancer treatment .....	32
1-2.3d Plasma-cell interactions .....	33
Transport of RONS across the cell membrane.....	34
Impact of RONS to cellular activity .....	36
Biological responses over longer distances .....	47

1-2.4	Summary – Aim of this PhD work .....	48
1-3	<b>Appendix-1</b> .....	51
1-4	<b>References</b> .....	55
2	<b>Methodology Molecular Dynamics</b> .....	73
2-1	<b>Computational research – An introduction</b> .....	75
2-2	<b>Molecular dynamics</b> .....	79
2-2.1	Introduction .....	79
2-2.2	Classical MD – ReaxFF .....	79
2-2.2a	Introduction .....	79
2-2.2b	Integration methods .....	80
2-2.2c	MD molecular system .....	82
2-2.2d	Thermostat .....	84
2-2.2e	Boundary conditions .....	85
2-2.2f	Interatomic potentials .....	86
2-2.2g	Reactive force fields .....	87
2-2.2h	ReaxFF potential .....	89
2-2.3	Quantum mechanical MD - DFTB .....	90
2-2.3a	Introduction .....	90
2-2.3b	Density-functional based Tight-binding .....	91
2-3	<b>References</b> .....	95
3	<b>Molecular Dynamics Simulations: D-Glucose</b> .....	101
3-1	<b>Introduction</b> .....	103
3-1.1	Saccharides .....	103
3-1.2	Impact of plasma treatment .....	105
3-2	<b>Computational setup</b> .....	107
3-3	<b>Results and discussion</b> .....	111
3-3.1	Experimental results .....	111

3-3.2	Computational results .....	114
3-3.2a	Vacuum .....	114
	OH radical .....	114
	O radical .....	121
3-3.2b	D-glucose in aqueous solution .....	124
3-3.2c	D-glucose in amorphous surface .....	126
<b>3-4</b>	<b>Concluding remarks .....</b>	<b>131</b>
<b>3-5</b>	<b>Appendix-3 .....</b>	<b>135</b>
<b>3-6</b>	<b>References .....</b>	<b>137</b>
<b>4</b>	<b>Molecular Dynamics Simulations: DNA.....</b>	<b>139</b>
<b>4-1</b>	<b>Introduction.....</b>	<b>141</b>
<b>4-2</b>	<b>Computational setup .....</b>	<b>145</b>
<b>4-3</b>	<b>Results .....</b>	<b>151</b>
4-3.1	H <sub>2</sub> O <sub>2</sub> and HO <sub>2</sub> .....	151
4-3.1a	H <sub>2</sub> O <sub>2</sub> .....	151
4-3.1b	HO <sub>2</sub> .....	151
4-3.2	OH radicals.....	152
4-3.2a	Dodecamer DNA simulations: 0 – 500 ps .....	152
4-3.2b	Dodecamer DNA simulations: 500 – 1000 ps .....	158
<b>4-4</b>	<b>Conclusion.....</b>	<b>163</b>
<b>4-5</b>	<b>References .....</b>	<b>165</b>
<b>5</b>	<b>Molecular Dynamics Simulations: Peptides .....</b>	<b>169</b>
<b>5-1</b>	<b>Small peptides angiotensin and bradykinin .....</b>	<b>171</b>
5-1.1	Introduction.....	171
5-1.2	Computational setup.....	172

5-1.3	Experimental details .....	176
5-1.4	Results and Discussion .....	178
5-1.4a	Peptide impact simulations .....	178
5-1.4b	Amino acid impact simulations .....	183
5-1.4c	Non-reactive MD simulations.....	187
<b>5-2</b>	<b>Cysteine as a reference for plasma-induced modifications .....</b>	<b>197</b>
5-2.1	Introduction .....	197
5-2.2	Computational setup .....	198
5-2.3	Simulations of cysteine reacting with RONS .....	199
5-2.4	Experimental part .....	204
5-2.4a	Experimental setup .....	204
5-2.4b	Results and discussion .....	205
<b>5-3</b>	<b>Glutathione .....</b>	<b>209</b>
5-3.1	Introduction .....	209
5-3.2	Computational setup .....	210
5-3.3	Simulation of GSH reacting with RONS .....	211
5-3.4	Experimental part .....	214
5-3.4a	Experimental setup .....	214
5-3.4b	Results and discussion .....	215
<b>5-4</b>	<b>Conclusion .....</b>	<b>219</b>
5-4.1	Two small peptides .....	219
5-4.2	Cysteine and glutathione .....	221
5-4.3	Concluding remarks .....	222
<b>5-5</b>	<b>References .....</b>	<b>223</b>
<b>6</b>	<b>Molecular Dynamics Simulations: Water .....</b>	<b>227</b>
<b>6-1</b>	<b>Introduction .....</b>	<b>229</b>
<b>6-2</b>	<b>Results and discussion .....</b>	<b>231</b>
6-2.1	OH radicals in water .....	232
6-2.2	O atoms in water .....	234

<b>6-3</b>	<b>Conclusion</b> .....	237
<b>6-4</b>	<b>References</b> .....	239
<b>7</b>	<b>Fluid Dynamics Simulations: Plasma-Liquid Interactions</b> .....	241
<b>7-1</b>	<b>Introduction</b> .....	243
<b>7-2</b>	<b>Methodology</b> .....	247
7-2.1	General processes described in the model .....	247
7-2.2	Simulated system .....	249
7-2.3	Mesh.....	251
7-2.4	Fluid flow .....	251
7-2.5	Transport of heat.....	252
7-2.6	Chemistry and transport of species .....	252
7-2.7	Boundary conditions at the interface .....	256
<b>7-3</b>	<b>Results and discussion</b> .....	257
7-3.1	Flow behavior of gas and liquid phase.....	257
7-3.2	Temperature profile in gas and liquid phase .....	260
7-3.3	Species concentrations in the gas phase.....	262
7-3.4	Transport of species in the liquid phase .....	265
7-3.5	Species concentrations in the liquid phase .....	266
7-3.6	Overview of the liquid chemistry .....	270
<b>7-4</b>	<b>Conclusion</b> .....	277
<b>7-5</b>	<b>Appendix-7</b> .....	279
<b>7-6</b>	<b>References</b> .....	283
	<b>Conclusion and outlook</b> .....	289
	<b>Academic curriculum vitae</b> .....	297
	List of publications related to this thesis .....	299
	List of publications not included in this thesis .....	301
	Conference contributions.....	303





## Dankwoord

Over het dankwoord heb ik de voorbije 5 jaar al veel nagedacht. Er is veel gebeurd en veranderd in deze periode, en het was niet altijd even gemakkelijk om door te zetten. Ik ben dan ook veel mensen dankbaar voor hun bijdrage en steun tijdens deze 5 jaar van mijn doctoraat.

Eerst en vooral, de personen die ervoor gezorgd hebben dat ik deze kans gekregen heb. Dat zijn mijn beide promotoren: Prof. Dr. Annemie Bogaerts en Prof. Dr. Erik Neyts. Beiden hebben mij de kans gegeven om mij te bewijzen en ontplooiën als wetenschapper in chemie. Zij hebben mij hun vertrouwen geschonken door mij aan te nemen als doctoraatstudent in de groep PLASMANT. Beiden stonden ook altijd klaar om mij raad te geven bij zowel wetenschappelijke als ook sociale problemen. Ik zal hen hier altijd dankbaar om zijn. Hier aansluitend wil ik ook Prof. Dr. Wim Wenseleers en Prof. Dr. Sofie Cambré van de onderzoeksgroep *Experimental Condensed Matter Physics* (ECM) bedanken voor het eerste jaar van mijn doctoraat. Ik ben me ervan bewust dat ik een trage leerling ben, maar ik heb uit dit jaar erg veel bijgeleerd dat mij heeft geholpen bij het uitvoeren van mijn werk binnen PLASMANT.

Evenveel dank gaat ook uit naar mijn vader, Erik Verlackt, en zijn partner, Tanja Van Oprooy, en mijn moeder, Sandra Geeraers. Zonder hun steun en vertrouwen had ik mijn academische carrière niet kunnen starten en voltooien. Ik ben me bewust dat we harde tijden gezien hebben maar we zijn er telkens beter uitgekomen. Jullie hebben in mij blijven geloven en dat heeft mij de kracht gegeven om te blijven doorzetten.

Speciale dank gaat uit naar Toon Peeters, alsook Steven Vanuytsel en Stijn Huygh. Naast de durende vriendschap en de geweldige tijden, hebben zij een grote en onmisbare bijdrage geleverd met het bekomen van de nodige kennis op vlak van biochemie, medicinale en computationele chemie. Daarnaast hebben zij mij ook enorm bijgestaan tijdens de moeilijke tijden van de voorbije 5 jaar. Vervolgens wil ik ook Toon Peeters en Lynn Michiels bedanken voor hun steun en hulp bij het schrijven van dit doctoraat.

Thanks to all the colleagues of PLASMANT for the interesting and funny times/discussions during work and at the office, with in particular the people from

the plasmamed group: Maksud, Jonas, Wilma, Jamol, Narjes, Balu, Naresh, Pankaj, Yury, Abraham, Angela, Patrick and Stefan. Special regards go to Luc Van 't Dack for his invaluable technical support.

Of course, this doctoral work also involved many international trips and I would like to thank my international colleagues, with in particular the colleagues from the Ruhr-Universität Bochum for the fun times, beers and interesting conversations!

Tot slot, wil ik nog een bijzondere dank geven aan Ann Medaer, zij was er de voorbije jaren altijd om mij te steunen en helpen als ik dit vroeg. Het spijt me dat dit soms harde tijden waren.

Maar, de lijst zou niet compleet zijn zonder mijn kat Lumi te bedanken om mij elke dag op te wachten na het werk en erbij te zijn bij elke stap tijdens mijn doctoraat!

Christof Verlackt – Januari 2018

## Summary

To date, the treatment of cancer is one of the most difficult challenges in the medical world. A lot of research is performed looking for new therapies and approaches for the selective killing of these malignant cells. The main problem lies in the ever-mutating nature of cancerous cells as they can become immune to the applied anti-cancer therapy and differentiation with the healthy surrounding tissue appears to be problematic. For this reason, more selective and efficient therapies are required, which specifically act on the nature of these malignant cells. Atmospheric pressure plasmas can play a key role in the development of these efficient anti-cancer therapies, as they are able to produce biologically relevant reactive species to impose stress on the treated substrates, which will harm cancerous cells while stimulating their healthy counter-parts. However, the exact mechanisms with which the plasma-induced stress triggers the desired cellular responses is still largely unknown.

In this thesis, the role of the biologically relevant reactive species (*i.e.*, reactive oxygen and nitrogen species, RONS) at the frontline of the plasma-assisted treatment has been investigated, in order to elucidate their initial interactions with the biological substrate. This was performed using computational methods to obtain detailed information on the expected mechanisms, which are often very difficult, if not impossible, to obtain experimentally. The work described in this thesis can be divided in two parts: (i) investigation of the chemical modifications induced by these reactive species on various cellular components using molecular dynamics (MD) simulations; (ii) study of the transport of plasma-generated reactive species in a liquid by means of MD and a 2D fluid dynamics model (fluid), which was developed in this work. In the first part, three biological systems were considered: sugars (more specifically, D-glucose), DNA and proteins. In all three cases, oxidation of the biomolecules was observed, which was found to be case-specific and which was in agreement with multiple independent experimental observations.

The oxidation of D-glucose was limited and yielded an overall increase in C=O double bonds and a slight decrease in ether bonds. This correlated well with the experimental results obtained by the Ruhr-Universität Bochum. In contrast, DNA and proteins were found to be more susceptible to chemical modifications by the introduced RONS.

In the case of DNA, precursors to various well-known oxidation products were observed during the simulations. The chemical modifications were focused on the C-8 position of purines (adenosine and guanosine) and the phosphodiester bond found in the backbone of the two DNA strands. This resulted in the formation of 8-hydroxy-purines (which form the precursors for oxidation products known to induce DNA mutations) and DNA strand breaks. These oxidation products are correlated to severe DNA damage, which can eventually activate cell death.

The impact of the biologically relevant reactive species with proteins was investigated in more detail, for four biological systems: two small peptides (studied with classical MD), the amino acid cysteine and the cysteine-holding antioxidant glutathione (GSH), both studied with density-functional based tight-binding (DFTB) MD. This was combined with experimental work, performed at the University of Antwerp (for the two small peptides), the Ruhr-Universität of Bochum (for cysteine and GSH) and the Leibniz Institute for Plasma Science and Technology (for cysteine). Taken together, the results indicated that sulfur-holding and aromatic amino acids are the main targets for oxidation by RONS. Moreover, it became clear that environmental factors play an important role in the expected chemical modifications on the investigated biomolecules. Indeed, some amino acids showed different oxidation rates than expected from literature, attributed to the contact surface and chemical environment of the targeted amino acids. In addition, the results presented in this thesis indicate that overoxidation can have devastating effects on the activity of the affected biological molecules such as GSH. Although GSH serves as an antioxidant, by detoxifying reactive species through the oxidation of cysteine, overoxidation resulted in an irreversible deactivation of GSH and therefore the consumption of this important cellular antioxidant.

In the second part of this thesis, the formation and accumulation of plasma-generated reactive species in liquid water was investigated. For this part, both MD and fluid simulations were used. Employing DFTB, the interaction between highly reactive ROS (*i.e.*, hydroxyl radicals and atomic oxygen) and liquid water was evaluated. On one hand, these results have indicated that hydroxyl radicals can interact with each other in two ways: either through a head-to-tail reaction, leading to the formation of water and atomic oxygen, or a side-to-side interaction, leading to

a stable cluster in solution. On the other hand, the stability of atomic oxygen in liquid water was dependent on the electronic state of the atom. When found in the singlet state, a cluster with water was observed, which is expected to form hydrogen peroxide, while triplet oxygen was found to be stable in the solution throughout the simulated timescale (10 ps).

To evaluate the generation and accumulation of biologically relevant RONS in water, a fluid model was developed in the final part of this work. This model was based on the treatment of liquid water with the well-characterized plasma jet, kINPen. The obtained results indicated that convection plays an important role in determining the plasma chemistry in the liquid. It was observed that short-lived species remain at the liquid interface and are consumed towards the formation of long-lived species, which were found to migrate to the bulk liquid. The reactive species that accumulated in the bulk liquid finally yield the formation of hydrogen peroxide, nitrous and nitric acid over longer timescales. This indicates that, for the conditions investigated in this thesis, mainly these long-lived species will be able to come in contact with liquid covered tissues and are responsible for initiating the impact of plasma during treatment.

Taken together, this thesis provides detailed information on the initial interactions between the plasma species and the affected (liquid covered) biological substrates. Many different plasma devices and biological substrates exist, and the initial interactions are highly dependent on the used working conditions, which define which RONS are primarily formed. Because of this, efforts should be made to elucidate the impact of the used working conditions on the generation and accumulation of biologically relevant reactive species, in order to better understand and control the initial interactions with the biological substrate. Only then are we able to better control and anticipate the biological response to the plasma treatment.



## Samenvatting

De behandeling van kanker vormt één van de grootste uitdagingen voor de medische wereld, waar de zoektocht naar nieuwe therapieën voor het selectief doden van kankercellen blijft doorgaan. Het probleem ligt voornamelijk bij de muterende eigenschappen die de kankercellen bezitten. Deze eigenschappen geven hen de mogelijkheid om zich continu aan te passen, waardoor de differentiatie met gezonde cellen moeilijk wordt en waarbij de kankercellen immuun kunnen worden voor de antikankerbehandelingen. Om deze reden zijn er steeds selectievere en efficiëntere methodes nodig, die beroep doen op het karakter van deze kwaadaardige cellen. Het is in deze context dat koude atmosferische plasma's een belangrijke rol kunnen spelen in de ontwikkeling van efficiënte antikankerbehandelingen. Dit komt omdat koude plasma's in staat zijn om biologisch belangrijke reactieve deeltjes te produceren (reactieve zuurstof en stikstof deeltjes, ENG: *RONs*), die ook door de cellen zelf aangemaakt en gebruikt worden, en dit bij atmosferische condities (kamertemperatuur en -druk). Deze reactieve deeltjes kunnen dan gebruikt worden om stress te induceren op het te behandelen biologisch materiaal, welke schadelijk zijn voor kankercellen en tegelijkertijd de gezonde cellen stimuleren. Echter, hoewel deze biologische reacties op de plasmabehandeling reeds duidelijk zijn aangetoond, zijn de onderliggende mechanismes nog voor een groot deel onbekend.

In deze thesis werd de rol van biologisch relevante reactieve deeltjes bestudeerd wanneer ze in contact komen met het biologisch materiaal. Dit werd uitgevoerd door gebruik te maken van computersimulaties om zo gedetailleerde informatie te kunnen verschaffen over de verwachte mechanismes, welke erg moeilijk te verkrijgen zijn via experimentele studies. Deze thesis kan opgedeeld worden in twee delen: (i) het bestuderen van de chemische modificaties van biologische componenten, veroorzaakt door *RONs*, met behulp van moleculaire dynamica (MD) simulaties; (ii) het onderzoeken van het transport en gedrag van plasma-gegenereerde reactieve deeltjes in vloeibaar water, door gebruik te maken van zowel MD als 2D fluid dynamische (kortweg, fluid) simulaties. Voor het eerste deel werden drie biologische systemen beschouwd: suikers (meer specifiek, D-glucose), DNA en eiwitten. In alle drie de gevallen werden chemische modificaties aangetroffen, die gedomineerd werden door oxidatieprocessen welke systeem-



specifiek waren en consistent met experimentele observaties.

De oxidatie van D-glucose bleef vrij beperkt: hydroxyl-groepen werden omgezet naar carbonyl-groepen (stijging in het aantal C=O bindingen) en in enkele gevallen brak de glucose etherverbinding als een gevolg van de stijging in carbonyl-groepen. Dit komt overeen met de experimentele resultaten verkregen aan de Ruhr-Universität in Bochum. Echter, de resultaten in deze thesis hebben aangetoond dat DNA en eiwitten gevoeliger waren aan reacties met de geïntroduceerde RONS.

De interacties tussen DNA en RONS leidde tot de vorming van de voorlopers van verschillende biologisch relevante oxidatieproducten. Deze chemische modificaties werden voornamelijk aangetroffen op de C-8 positie van adenine en guanine, en aan de fosfodiëster verbindingen die zich situeren aan de ruggengraat van de twee DNA-strengen. Dit zorgt voor de vorming van 8-hydroxy-purines (dit zijn de voorlopers van oxidatieproducten bekend om DNA-mutaties te veroorzaken) en breuken in de DNA-streng. Deze oxidatieproducten zijn gecorreleerd aan ernstige DNA-schade welke kunnen leiden tot de activatie van celdood.

De impact van biologisch relevante reactieve deeltjes met eiwitten werd in meer detail bestudeerd. Hiervoor werden vier systemen beschouwd: twee kleine peptiden (met klassieke MD), het aminozuur cysteïne en de cysteïne-houdende antioxidant glutathion (GSH), met “*density-functional based tight-binding*” (DFTB) MD. Dit onderzoek werd uitgevoerd in combinatie met experimentele studies uitgevoerd aan de Universiteit Antwerpen (voor de kleine peptiden), de Ruhr-Universität in Bochum (voor cysteïne en GSH) en het Leibniz Institute for Plasma Science and Technology (voor cysteïne). Samengevat wijzen de resultaten erop dat zwavelhoudende aminozuren, samen met de aromatische aminozuren, de voornamelijke doelen zijn van oxidatie door RONS. Daarenboven blijkt dat de onmiddellijke omgeving een grote impact kan hebben op de uiteindelijke oxidatieproducten, vermits in specifieke gevallen de bekomen resultaten niet overeenkwamen met observaties uit de literatuur. Dit werd verklaard door het verschil in contactoppervlakken en de chemische omgeving waarin de desbetreffende aminozuren zich bevonden. Vervolgens toonden de bekomen resultaten ook aan dat een te hoge oxidatiegraad nefast kan zijn voor de activiteit van de betrokken biomoleculen, zoals GSH. Hoewel GSH een antioxidant is, welke oxiderende deeltjes

effectief kan neutraliseren via de oxidatie van cysteïne, kan overoxidatie zorgen voor irreversibele schade aan GSH, met een permanente deactivatie van het antioxidant karakter tot gevolg.

In het tweede deel van deze thesis werd de productie van plasma-gegenereerde deeltjes in vloeibaar water bestudeerd. Hiervoor werden zowel MD als fluid simulaties uitgevoerd. Door gebruik te maken van DFTB werden de interacties tussen zeer reactieve ROS (hydroxyl radicalen en zuurstofatomen) en vloeibaar water in detail bestudeerd. In dit onderzoek werd aangetoond dat hydroxyl radicalen in staat zijn om met elkaar te interageren op twee wijzen: via een hoofd-aan-staart interactie, welke leidt tot de vorming van water en een zuurstofatoom, of via een zij-aan-zij interactie, welke stabiel blijft doorheen de simulaties. De stabiliteit van zuurstofatomen in water blijkt afhankelijk van zijn elektronische toestand, in die zin dat zuurstofatomen in de singlet status een cluster vormen met water, welke bekend staat om waterstofperoxide te vormen, terwijl zuurstofatomen in de triplet status stabiel bleven in oplossing gedurende de simulatietijd (10 ps).

Het gedrag en de productie van biologisch relevante deeltjes in oplossing tijdens plasmabehandeling werd bestudeerd aan de hand van een fluid model dat in het laatste hoofdstuk van deze thesis werd ontwikkelend. Dit model is gebaseerd op de behandeling van vloeibaar water met een goed bestudeerde plasmajet, de kINPen. De bekomen resultaten hebben aangetoond dat convectie een belangrijke rol speelt in de bekomen chemie in oplossing: de kortlevende reactieve deeltjes blijven aan het vloeistofoppervlak, en geven aanleiding tot de vorming van meer stabiele reactieve deeltjes. Deze laatste waren in staat om de bulk van de vloeistof te bereiken, waarna ze de productie van waterstofperoxide, salpeterigzuur en salpeterzuur bevorderden. Deze bevindingen leiden tot de vaststelling dat het deze langlevende reactieve deeltjes zijn die uiteindelijk in aanraking komen met het te behandelen (door vloeistof bedekte) biologisch materiaal, om zo de initiële interacties te veroorzaken tijdens de plasmabehandeling, voor de condities zoals ze waren tijdens de simulaties.

Samengevat kan gesteld worden dat het werk, gepresenteerd in deze thesis, gedetailleerde informatie verschaft over de initiële interacties tussen de plasma-gegenereerde deeltjes en het behandelde biologisch materiaal. Echter, door de hoge flexibiliteit van de gebruikte plasma's, alsook de brede waaier aan biologisch

materiaal, zijn de initiële interacties sterk afhankelijk van de gebruikte condities. Hierdoor is het belangrijk om de invloed van verschillende parameters op de productie van biologisch relevante RONS te bestuderen om zo beter inzicht en controle te verkrijgen op de initiële interacties met het behandelde materiaal. Enkel op deze manier kunnen de biologische reacties beter begrepen en gecontroleerd worden tijdens het gebruik van koude plasma's in medische toepassingen zoals wonden kankerbehandeling.

## List of abbreviations

Abbreviation	Explanation	Page first reference
(V)UV	(Vacuum) ultraviolet	11
$\mu$ -APPJ	Microscale atmospheric pressure plasma jet	167
$\mu$ VT	Grand-canonical ensemble	83
A-His	Angiotensin with oxidized His	187
AIF	Apoptotic induction factors	46
AKT	Protein kinase B	36
AMD	Age-related macular degeneration	10
A-Nat	Native angiotensin	187
A-ox2	Angiotensin with two oxidized AA	187
A-ox3	Angiotensin with three oxidized AA	187
APPJ	Atmospheric pressure plasma jet	6
A-Pro	Angiotensin with oxidized Pro	187
AQP	Aquaporin	34
ARE	Antioxidant response element	44
Arg	Arginine	179
ASK1	Apoptosis signal-regulating kinase 1	41
Asp	Aspartic acid	179
ATP	Adenosine triphosphate	23
A-Tyr	Angiotensin with oxidized Tyr	187
B-Arg	Bradykinin with oxidized Arg	187
Bax	Bcl2-associated X protein	46
Bcl2	B-cell lymphoma 2	46
B-Nat	Native bradykinin	187
BO	Bond order	147
B-ox2	Bradykinin with two oxidized AA	187
B-ox3	Bradykinin with three oxidized AA	187

B-Phe	Bradykinin with oxidized Phe	187
B-Pro	Bradykinin with oxidized Pro	187
CAP	Cold atmospheric pressure plasma	6
caspase	Cysteine-aspartic protease	40
CD44	Cluster of differentiation 44 protein	36
cMD	Classical MD	79
Cys-SNO	S-nitroso cysteine	199
Cys-SO <sub>2</sub> H	Cysteine-based sulfinic acid	206
Cys-SO <sub>3</sub> H	Cysteine-based sulfonic acid	206
dAMP	Deoxyadenosine monophosphate	141
DBD	Dielectric barrier discharge	6
dCMP	Deoxycytidine monophosphate	141
DFT	Density functional theory	75
DFTB	Density-functional based tight-binding	91
DFTB3	3 <sup>rd</sup> order DFTB	93
dGMP	Deoxyguanosine monophosphate	141
DOPA	3,4-dihydroxyphenylalanine	185
DSB	Double strand break	156
dTMP	Deoxythymidine monophosphate	141
ERK1/2	Extracellular regulated kinase	36
ESI	Electrospray ionization	177
FapydA	2,6-diamino-4-hydroxy-5-formamido- pyrimidine	155
FapydG	2,6-diamino-4-hydroxy-5-formamido- pyrimidine	155
FBC	Free boundary conditions	85
FTIR	Fourier-transform infrared	111
GapDH	Glyceraldehyde 3-phosphate dehydrogenase	171
Gly	Glycine	181

GSH	Glutathione	39
GSNO	S-nitroso glutathione	211
GSO <sub>2</sub> H	Glutathione sulfinic acid	209
GSO <sub>3</sub> H	Glutathione sulfonic acid	209
GSSG	Glutathione disulphide	209
HD	Hydrodynamics	75
His	Histidine	179
HMOX1	Heme oxygenase 1	43
Ile	Isoleucine	179
IM	Ion mobility	177
JNK	c-Jun N-terminal kinase	36
KEAP1	Kelch-like ECH-associated protein 1	43
LDA	Local-density approximation	92
MAPK	Mitogen-activated protein kinases	41
MMP	Matrix metalloproteinase	23
MS	Mass spectrometry	6
mtDNA	Mitochondrial DNA	144
mTOR	Mammalian target of rapamycin	40
NAC	N-acetyl-L-cysteine	41
NADH	Nicotinamide adenine dinucleotide	105
nDNA	Nuclear DNA	144
NMR	Nuclear magnetic resonance spectroscopy	193
NPT	Isothermal–isobaric ensemble	83
NQO1	NAD(P)H dehydrogenase 1	43
NRF2	Nuclear factor erythroid 2	43
NVE	Microcanonical ensemble	83
NVT	Canonical ensemble	83
PAL	Plasma activated liquids	15
PAM	Plasma activated media	20

PARP1	Poly (ADP-ribose) polymerase 1	36
PBC	Periodic boundary conditions	85
PBS	Phosphate buffered saline	20
PCA	Principle component analysis	175
Phe	Phenylalanine	179
PI3K	Phosphatidylinositol-4,5-bisphosphate 3-kinase	40
PME	Particle mesh Ewald method	175
Pro	Proline	179
PTEN	Phosphatase and tensin homolog	40
PTL	Plasma treated liquids	15
PTM	Plasma treated media	20
PTW	Plasma treated water	20
QM	Quantum mechanical	75
qMD	Quantum mechanical MD	79
RBC	Reflective boundary conditions	85
RNA	Ribonucleic acid	105
RNS	Reactive nitrogen species	19
RONs	Reactive oxygen and nitrogen species	11
ROS	Reactive oxygen species	19
SCC-DFTB	Self-consistent DFTB	92
Ser	Serine	178
SOD	Superoxide dismutase	39
SSB	Single strand break	156
TNF	Tumor necrosis factor	41
TRPM2	Transient receptor potential cation channel, subfamily M, member 2	46
Tyr	Tyrosine	178
Val	Valine	178

$\gamma$ H2AX	H2A histone, member X, phosphorylated on serine 139	36
---------------	---	----





# **1 Introduction to Plasma Medicine**



## 1-1 Plasma

### 1-1.1 What is a plasma

In physics and chemistry, a plasma is known as an ionized gas. The word ‘*plasma*’ originates from the Greek word πλάσμα meaning ‘something formed’ or ‘creation’ and was first described by Sir William Crookes in 1879 as *Radiant Matter* due to its visual properties—a gas able to emit a constant stream of photons<sup>1</sup>. During his experimental studies, he used the so-called Crookes tubes, which were closed glass tubes containing a partial vacuum. The Crookes tubes were used to generate cathode rays (stream of electrons), able to partially ionize the gas present in the glass tube. The term *Plasma* itself was first introduced by Irving Langmuir in 1928, nearly 5 decades after the discovery of the cathode rays<sup>2</sup>:

*“Except near the electrodes, where there are sheaths containing very few electrons, the ionized gas contains ions and electrons in about equal numbers so that the resultant space charge is very small. We shall use the name plasma to describe this region containing balanced charges of ions and electrons.” Langmuir-1928*

Plasmas are, however, more than only a balance between positively and negatively charged particles (ions and electrons) for a quasi-neutral state. A plasma is composed of a mixture of neutral atoms and molecules, electrically charged and excited species, radicals, photons and electromagnetic fields. Basically, a plasma is created from the gas phase by introducing energy, such as temperature, as illustrated

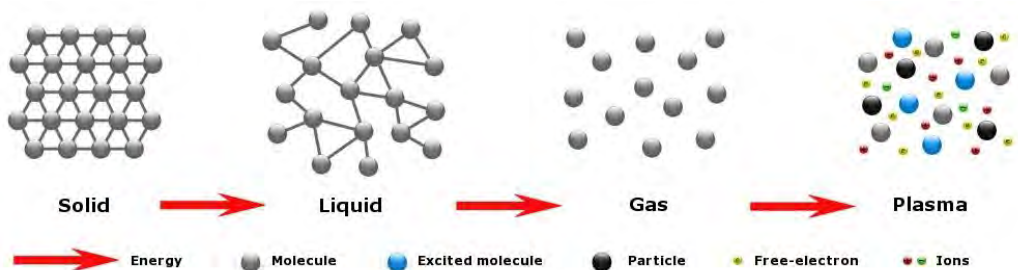


**Figure 1-1. Schematic representation of the atomic structure of the four phases of matter with increasing energy.** Figure reprinted from [www.acxys.com/plasma-technology.html](http://www.acxys.com/plasma-technology.html).



**Figure 1-2. Images of naturally occurring plasmas:** Left) lightning, picture taken from [omweer-online.be](http://omweer-online.be); Right) aurora, picture reprinted from [www.northandaway.be](http://www.northandaway.be)

in Figure 1-1. When the temperature of a gas is increased, the total energy of the particles will rise accordingly. As a result, the particles will start moving with higher velocities and collisions will occur with higher impact. During the transition from a gas to a plasma, the collisions will have such an impact that the particles start to break apart, resulting in the formation of free electrons, ions, atoms, excited species, radicals and molecules. Furthermore, the excited species will generate photons. The mixture of different generated particles and electromagnetic fields (generated upon applying electric power to the plasma device) is known as a plasma.

In the above example, temperature is used to create the first plasma species, but other sources of energy can also be used, such as microwaves and magnetic fields<sup>3</sup>. Sir W. Crookes used electrodes to create free electrons with a high enough energy to induce the collisions needed to create a plasma.

In general, two types of plasmas can be distinguished: naturally occurring plasmas and artificial plasmas, on one hand. Despite the fact that naturally occurring plasmas are hardly seen on the surface of the earth, most of the visible universe (more than 99%) is found in the plasma state<sup>3,4</sup>. Most well-known examples are the Sun, as well as lightning and *Aurora Borealis/australis* (cf. Figure 1-2). The emission of photons is clearly visible in every single example, confirming the observation of Sir W. Crookes.

Artificial plasmas, on the other hand, are generated on industrial or laboratory scale and are, again, divided in two groups<sup>3,4</sup>: (i) high-temperature or fusion plasmas, used in nuclear fusion (with temperatures in the order of a few million degrees Centigrade), (ii) and low-temperature plasmas or gas discharges, used in a wide

range of applications (with temperatures in the order of 1000 °C down to room temperature, hence significantly lower than fusion plasmas).

Gas discharges, in turn, are known to exist in either thermal equilibrium (*thermal plasma*, not to be confused with high-temperature plasmas) or in non-thermal equilibrium (*non-thermal plasma*)<sup>3-7</sup>. This classification is based on the distribution of the temperature/energy of the species in the ionized gas. In a thermal plasma, all species contain similar energies (similar temperatures), while a plasma is called non-thermal if this is not the case. Indeed, for non-thermal plasmas, the temperature of the gas molecules is usually found in the order of (or somewhat above) room temperature, while the much lighter electrons are characterized with a temperature reaching a multitude of 10,000 °C. This results in a plasma at room temperature (up to tens or hundreds of degrees Centigrade) while still being able to sustain itself. It is clear that the electrons are of utmost importance as they are primary responsible for the generation of the plasma species and new electrons, to sustain the plasma. The combination of ‘cold’ plasma gas species and energetic electrons results in a plasma with a low net temperature, able to be used in sensitive applications without causing thermal damage, *e.g.*, surface modifications and medical applications. The latter gave rise to a successful new research field called **Plasma Medicine**<sup>8-10</sup> which forms the main subject of this thesis.

*As this thesis is situated in plasma medicine, we will only consider non-thermal plasmas from this point on.*

## 1-1.2 Non-thermal plasma

As explained in 1-1.1, non-thermal plasmas are a group of low-temperature plasmas where the electrons typically contain a much higher temperature than the heavy particles (*i.e.*, atoms and molecules), which can be found close to room temperature. They are receiving increasing interest in the scientific world over the last decades. This is due to the characteristic features of this group of plasmas: their environmentally friendly and energy saving nature, flexibility and the ability to create new products at low temperature<sup>11</sup>. This combination opens the door to a wide range of applications<sup>5-7</sup>. For example, in the field of material technology plasmas can play an important role in surface applications for, *e.g.*, the deposition of a protective

coating against corrosion, to increase the hardness or to enhance specific properties. The characteristic of emitting photons at low temperature has resulted in the use of plasmas in the light-industry, to produce, *e.g.*, TL-tubes, xenon car lights and plasma television screens. In addition to material technology and the lighting industry, plasmas can also be used for chemical analysis due to their ionizing and chemically exciting nature. This way, the chemical composition of a solid material, liquid or gaseous compound can be investigated in combination with spectroscopic techniques like optical emission spectroscopy or mass spectrometry (MS). Furthermore, non-thermal plasmas can also be used as “chemical reactors”, for instance for the decomposition of toxic molecules to CO<sub>2</sub> and water, the production of ozone, or the conversion of CO<sub>2</sub> to value-added compounds. Finally, and as mentioned previously, non-thermal plasmas can be used in medicine for the treatment of thermally-sensitive surfaces or living tissues. The use of so-called ‘cold plasmas’ in medicine has proven to be successful for the decontamination of medical equipment (plastics, rubber, living tissue, *etc.*), dental treatment, blood coagulation, wound and ulcer healing, and even for the treatment of cancers<sup>8,10</sup>.

*The use of non-thermal plasmas for medical applications is the application of interest in this thesis and will be elaborated in the following sections.*

A variety of plasma sources for cold atmospheric pressure plasmas (CAPs) are available<sup>5,7,9</sup>: dielectric barrier discharge (DBD), corona discharges, atmospheric pressure plasma jets (APPJs), magnetron discharges, *etc.* The simplest form of non-thermal plasmas can be generated between two parallel electrodes with a gas pressure ranging between 10<sup>-3</sup> and 1 atm. When applying a potential difference between the electrodes, the electrons, originating from the gas or from the negatively charged electrode (*i.e.*, cathode), will be accelerated towards the positively charged electrode (*i.e.*, anode) because of the electric field. The accelerated electrons will collide with gas species, resulting in excitation, ionization and dissociation processes. The generated reactive species, in turn, will be able to react further in the gas which leads to a wide variety of other reactive species, photons (as a result of relaxation processes of excited species) and new electrons. The creation of new electrons, due to ionization collisions, plays a key role in sustaining the plasma, as already mentioned

in **section 1-1.1**, as these electrons will again be accelerated, resulting in the generation of more reactive species. These reactive species are generally reactive oxygen and nitrogen species such as hydrogen peroxide ( $\text{H}_2\text{O}_2$ ), ozone ( $\text{O}_3$ ), nitric oxide ( $\text{NO}$ ), nitrous acid ( $\text{HNO}_2$ ) and nitric acid ( $\text{HNO}_3$ ).

A more detailed explanation on the plasma-generated components and the plasma sources used in plasma medicine will be given in **sections 1-2.1** and **1-2.2**, respectively.





## 1-2 Plasma medicine

### 1-2.1 Background

The use of CAPs for biomedical applications –plasma medicine– is an emerging field combining plasma physics and chemistry, biochemistry and medicine<sup>8–10</sup>. In the past 10-15 years, a large amount of research has been performed to study:

- (i) the interactions of CAPs with biological and biochemical materials<sup>12–25</sup>. This can be split up in three parts: studying the plasma plume itself, investigating the plasma-liquid interactions and elucidating the interactions between plasma species (potentially in liquid phase) and biochemical structures (see Figure 1-3).
- (ii) the operation of various cold plasma sources and treatments<sup>26–32</sup>.
- (iii) plasma-biochemical applications and the macroscopic plasma-induced effects<sup>33–43</sup>.

Although plasma medicine, as such, is a relatively young and rapidly growing field of research, the use of plasmas in medicine and biotechnology is not a new idea. In the 1850s, dielectric barrier discharges (DBD) were used by Siemens to generate ozone in water to biologically decontaminate the liquid<sup>44,45</sup>. In the field of medicine, plasmas were used as a source of high temperature (far exceeding room temperature)

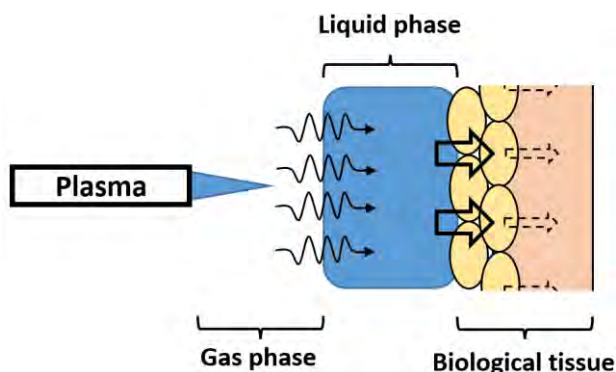


**Figure 1-3. Schematic representation of the different boundaries and phases which plasma-generated components need to cross in order to induce changes inside the affected cells and tissues.**

with decontamination, blood coagulation and tissue removal as the earliest applications. Interestingly, non-thermal plasmas were used as a home-held solution, called the High-Frequency Apparatus, for multiple medical complications like head-aches, infections, diabetes or common viral infections (*cf.* Figure 1-4). Although these applications were used on a large scale, the underlying mechanisms were hardly understood.

The use of CAPs in medicine rapidly emerged when the focus shifted from the thermal to the non-thermal properties. It was only then that the term *plasma medicine* was introduced<sup>9</sup>. Focusing on the non-thermal effects of plasmas, CAPs have been applied successfully and directly to living cells and tissue, in the field of selective

decontamination (for the removal of endotoxins and micro-organisms like bacteria, spores, fungi and viruses), wound healing, dental treatment, inflammation, blood coagulation, treatment of various diseases like Alzheimer, Huntington and age-related macular degeneration (AMD), and even cancer treatment<sup>16,34,46–55</sup>. Studies towards these applications have demonstrated that CAPs are capable of inflicting stresses on the treated area which can damage micro-organisms and endotoxins, promote cell proliferation, enhance genetic transfection, stimulate immune responses, promote regeneration of tissues towards wound healing and even induce senescence (*i.e.*, state in which cells are unable to reproduce) and apoptosis (*i.e.*, controlled cell death) in malignant cells such as cancer.

The success of plasmas in medicine is, first of all, based on the capability of tuning the sub-lethal plasma effects for selective treatment of tissues without damaging the surrounding living matter. Furthermore, the production of non-thermal plasmas is possible using very simple and flexible devices. However, the underlying mechanisms, both physically and biochemically, are still not completely understood, and more research is required to understand both the plasma-liquid,



**Figure 1-4. Example of the use of the High-Frequency Apparatus for treating children.** Image from the manual of a Dutch High-Frequency Apparatus sold in the 1930's.

plasma-cell and cell-to-cell interactions, and to be able to predict, for instance, selective activity in order to optimize the working conditions of the plasma for the application at hand.

In this context, the use of CAPs usually means the utilization of the synergy between the different plasma-generated components. Among these components are reactive oxygen and nitrogen species (RONS), electromagnetic fields and (V)UV<sup>9,10,30,56</sup>.

- *Reactive oxygen and nitrogen species* form a crucial, if not the most important, part of the plasma activity for biomedical applications. RONS is a collective term for reactive species like atoms, radicals and small molecules, which are based on oxygen and nitrogen<sup>21,57–61</sup>. The RONS generated by plasma have been identified using mass spectrometry, Fourier Transform Infrared spectroscopy and optical emission spectroscopy<sup>62–64</sup>. These RONS include, among others, hydroxyl radicals (OH,  $E^0 = +2.8$  V), ozone (O<sub>3</sub>,  $E^0 = +2.1$  V), hydrogen peroxide (H<sub>2</sub>O<sub>2</sub>,  $E^0 = +1.77$  V), hydroperoxyl radicals (HO<sub>2</sub>,  $E^0 = +1.7$  V), atomic oxygen (O,  $E^0 = +2.42$  V), peroxyxynitrous acid (ONOOH,  $E^0 = +1.37$  V) and nitrogen dioxide radicals (NO<sub>2</sub>,  $E^0 = +1.4$  V).  $E^0$  is the standard reduction potential of the respective RONS, indicating the tendency of these species to be reduced. More interestingly, more and more evidence reveals that RONS are inherent to a wide range of biochemical and cellular activities<sup>65–70</sup>. Typical examples are the generation of RONS for antibacterial and antiviral defense by the mammalian immune system<sup>71,72</sup>, to assist wound healing<sup>73</sup>, invoke cell differentiation, migration, for controlled cell death, and they play important roles in the regulation of other cellular functions<sup>10,70,74,75</sup>. This will be covered in more detail in **section 1-2.3**. Furthermore, an extensive overview of the effects of plasma-generated RONS can be found in<sup>10,69</sup>.
- *Electromagnetic fields* are important in the case of direct plasma treatment (*e.g.*, using a dielectric barrier discharge, see **section 1-2.2**). Electroporation is expected when the electric field is sufficiently high<sup>76–78</sup>. During electroporation, temporal microscopic pores are created in the cell membrane which facilitates the exchange of small (bio)molecules between the cytosol (*i.e.*, interior of the cell) and the external bio-plasma (*i.e.*, biochemical liquid surrounding

mammalian cells, not to be confused with non-thermal plasmas) including certain drugs or other therapeutic molecules.

- *Ultraviolet radiation*, in particular UV-C, produced by CAPs, has been used extensively for decontamination due to its antibacterial and antiviral activity<sup>8,79</sup>. Moreover, intense radiation is known to induce DNA and protein damage as well as lipid peroxidation<sup>80</sup>. However, UV intensity generated by CAPs suited for biomedical applications is usually very low and the role of UV radiation during plasma treatment in this field can often be excluded<sup>47</sup>.

*In the following parts, an overview of plasma sources typically used in plasma medicine and examples of applications will be presented.*

## 1-2.2 Plasma sources used in the medical field

### 1-2.2a Overview

A multitude of CAP sources, specifically to be used in biomedical applications, have been developed in the past decades by various research groups worldwide<sup>28,29,32,45,81</sup>. Among these sources are DBDs and floating-electrode DBDs, APPJs, microscale APPJs and the plasma needle. As they all operate at atmospheric conditions (near ambient temperature and pressure), they are ideally suited for the treatment of both (viable) biological tissues as well as medical and thermally-sensitive equipment. Various laboratories worldwide have developed a number of plasma sources including the X-Jet from RUB (Ruhr-Universität, Bochum – Germany)<sup>82</sup>, the kINPen from INP (Leibniz-Institut für Plasmaforschung und Technologie, Greifswald – Germany)<sup>83,84</sup>, the plasma pencil from the Old Dominion University (Norfolk – USA)<sup>85</sup>, the MicroPlaster from the collaboration of the Max Planck Institute (Garching – Germany) and Adtec Plasma Technology (Hiroshima – Japan)<sup>86</sup>, to name only a few. As a result, a wide variety of setups, parameters and conditions are available for biomedical applications. These varieties range from direct to indirect plasma sources (*i.e.*, does the plasma come in contact with the treated area), uniform to cell specific applications, and so on<sup>3,30,47,87</sup>. In 2010, Weltmann published a review<sup>30</sup> where he divided the available sources in three main groups: DBDs, plasma jets and corona discharges. However, recent developments and research activities in plasma medicine are mainly focused on DBD and APPJs,

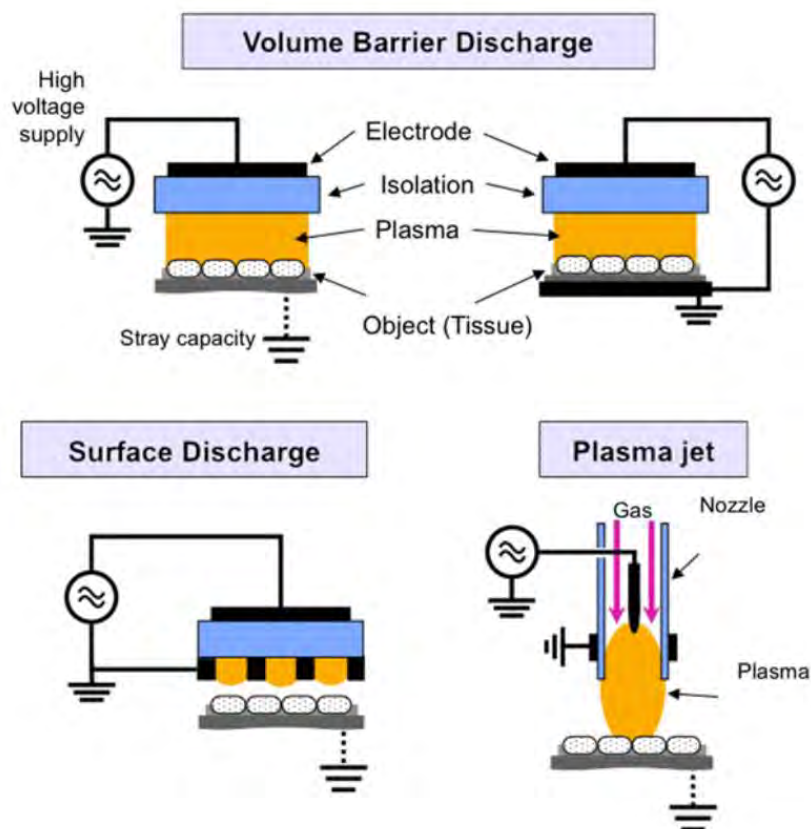


**Figure 1-5. Overview of different plasma sources typically used in plasma medicine.** Adopted from<sup>9</sup>.

which are schematically illustrated in Figure 1-5. Both plasma sources will be introduced in more detail in the following **sections 1-2.2b** and **1-2.2c**.

The wide range of different sources has significantly increased the complexity of the plasma medicine field, making it very difficult to compare the different experiments performed worldwide, and thus preventing fast development in the field. This issue was first tackled in 2012 by the members of the European COST Action MP1011 on ‘Biomedical Applications of Atmospheric Pressure Plasma Technology’<sup>88</sup>. Here, the idea was launched to develop a plasma device that could act as a reference source for all research done in the field of plasma medicine. The result of this was published in 2016 as the COST Reference Microplasma Jet<sup>29</sup> –which will be referred to as the COST reference jet or simply the COST jet–. The COST jet was developed in such a way that it is simple, robust, inexpensive and available to all who are

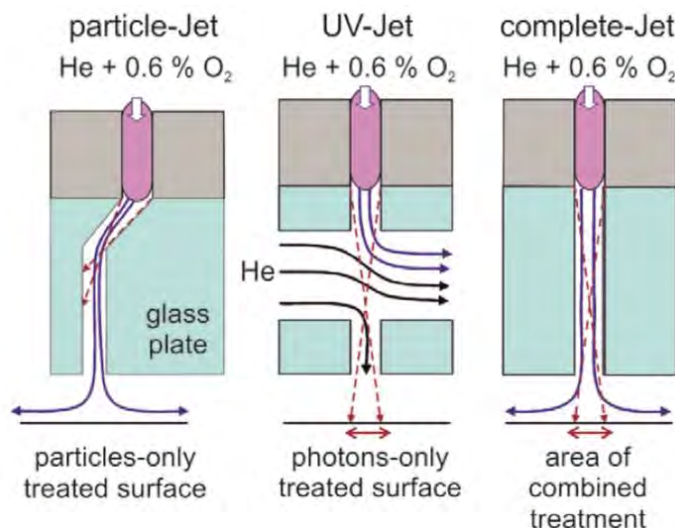


**Figure 1-6. Schematic representation of the three different plasma jets used for the treatment of D-glucose.** Three individual jets are used for comparison of the treatment performed by reactive species ( $O$ ,  $O_3$ ,  $O_2a(^1\Delta g)$ ), photons or combined treatment. Left) Particles-jet, shielding the treated surface from the VUV/UV radiation; Middle) UV-jet, shielding the treated surface from plasma-generated reactive particles; Right) Combined jet, allowing both the reactive species (blue arrows) as well as the photons (red arrows) to come in contact with the treated surface. Adopted from<sup>63</sup>.

interested. It contains internal probes, to monitor the operation conditions, is airtight and usable in different laboratories. To date, both the generation of reactive species as well as the operating conditions are well characterized for the COST jet<sup>29,63,62,89,90</sup>. The existence of the COST reference jet prompted the idea to compare the treatment of simple biomolecules between the COST jet and the kINPen, developed by INP Greifswald<sup>84</sup>, which was developed for clinical applications. The obtained results were supported by numerical simulations that are part of this thesis and will be presented in **chapter 5**.

Furthermore, the development of the COST jet is tightly connected to the creation of the so-called X-jet, which was presented in 2011 by Schneider *et al.*<sup>82</sup>. The X-jet was designed to be able to separate the generated species and photons from the plasma during treatment as presented in Figure 1-6. Depending on the used channel of the plasma-jet a particle-jet, UV-jet or combined-jet can be obtained<sup>63</sup>. As such, the impact of both plasma components (species and photons) on the treated substrate can be investigated. With this setup, the impact of the different plasma components, and

their synergy, was investigated both on model molecules, such as D-glucose in solution (results will be discussed in **chapter 3**), and prokaryotic cells in vitro<sup>63,91</sup>.

As already stated, among the different types of non-thermal plasma sources, APPJ and DBDs are most frequently used in plasma medicine. However, in the field of plasma medicine a new method of applying RONS in medical applications has been introduced and investigated in the last few years: the use of RONS containing liquids as a result of prior plasma treatment. These liquids are commonly known as *Plasma Treated Liquids* (PTL) or *Plasma Activated Liquids* (PAL)<sup>92–94</sup>. In the following sections, we will look at both physical plasma sources (DBD and APPJ) and PTLs in more detail.

### 1-2.2b Dielectric Barrier Discharges (DBD)

DBDs are plasmas far from equilibrium and are generated between two layers (usually with a gap in the range of 1 mm – 1 cm), where at least one layer is isolated with a dielectric barrier. Typical dielectric materials are quartz, glass and ceramics, but other insulating materials can be used as well<sup>27</sup>. The dielectric barrier is required to limit the current of the discharge and prevent the formation of an arc-discharge (*i.e.*, going from a non-thermal to a thermal plasma; *cf.* **section 1-1.1**). Typical electrode geometries are given in Figure 1-7, taken from Ehlbeck *et al.*<sup>81</sup>. From this figure, one of the main advantages of DBDs becomes clear: the ability to treat extensive surfaces.

Depending on the geometry, two different types of DBDs are classified. The first and simplest one is the volume or planar DBD. Here, direct treatment of the tissue, or surface, is possible as the treated object forms the second electrode and therefore an active part of the plasma discharge (*cf.* Figure 1-5 and Figure 1-7). Being part of the plasma, the substrate will come in contact with all plasma-generated components, like reactive species, but also electrons, photons, electric fields, *etc.* This is an important difference compared to indirect treatment where only longer-lived species (usually, radicals and neutral atoms or molecules) come in direct contact with the treated surface. The second type of DBD is created using more special electrode geometries, generating surface and coplanar discharges. When both electrodes are placed on the isolating layer, the plasma will be created on the isolator and does not come in contact with the treated surface (*cf.* Figure 1-5 and Figure 1-7).



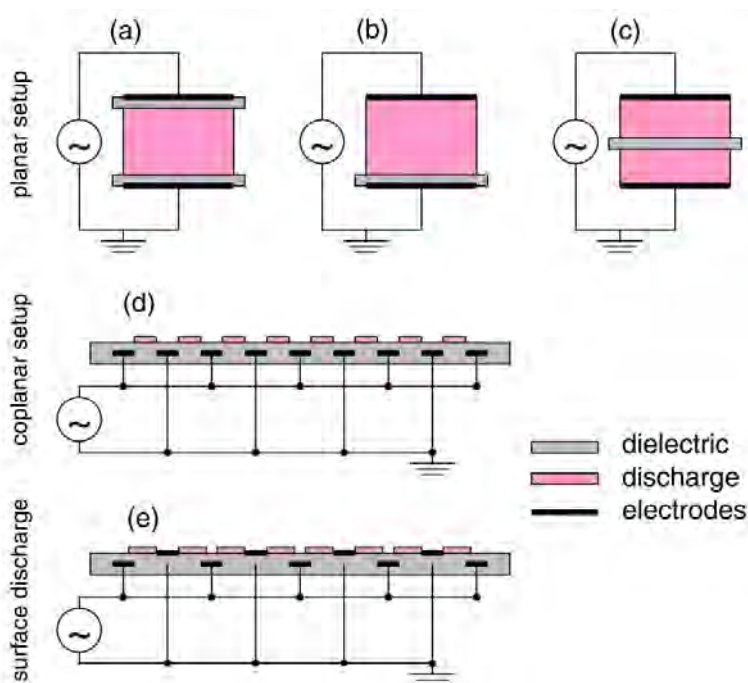


**Figure 1-7. Schematic representation of various dielectric barrier discharges.** (a) Planar DBD with a dielectric barrier at both electrodes, (b) Planar with only one electrode covered with a dielectric barrier, (c) Planar with a dielectric barrier in the discharge gap, (d) Coplanar setup where both electrodes are embedded inside the dielectric barrier, (e) Setup for surface discharge generation with one of both electrodes embedded in the dielectric barrier. Adopted from<sup>81</sup>.

This setup can also be miniaturized to build microplasma arrays<sup>44,95</sup>.

A few advantages have already been mentioned: the ability to treat extensive surfaces and the wide range of possible electrode geometries. Moreover, the stability of DBDs also ensures a straightforward ignition and a wide range of operating conditions. As such, nearly every mixture of gases can be used to generate a DBD plasma, including noble gases, ambient air, water vapor and special admixtures of oxygen and nitrogen. Moreover, very low flow rates (up to 100 standard cubic centimeters (sccm) or 0.1 L/min) can be used, making them ideally suited for industrial use. However, in order to ignite the plasma, relatively high ignition voltages are required, in the range of kV and more, depending on the electrode gap. Finally, when DBD's are ignited using the surrounding air, the resulting plasma (and generated reactive species) are highly dependent on the ambient air conditions, such as temperature and humidity. An overview on some applications and DBD

setups can be found in the work of Ehlbeck *et al.*<sup>81</sup>.

### 1-2.2c Atmospheric Pressure Plasma Jets (APPJ)

APPJs are created in a device with one or two electrodes (Figure 1-8)<sup>28,30,32,81</sup>. Using a radio frequency of typically 13.56 to 27.12 MHz, the plasma can be ignited inside the device, which is then transported by the feeding gas to the treated object forming a jet- or torch-like plasma. Numerous plasma jets have been developed, mainly differing in the electrode geometry and operating properties, *i.e.*, type of gas and frequency. Indeed, multiple electrode geometries are possible including ring-shaped electrodes (*cf.* Figure 1-8). In addition, also single electrode jets can be established where the treated substrate forms the counter electrode. In this way, the substrate forms an active part of the plasma discharge. The distance between the electrodes is usually in the millimeter range, while the treatment distance towards the object can be centimeters. It should be noted that most often, the device itself is a DBD, so a dielectric layer is still required to generate this non-thermal plasma.

In contrast to DBDs, the working gases for plasma jets are usually noble gases, like helium and argon, using high flow rates (*i.e.*, up to several liters per minute), although plasma jets operating in air exists as well. The use of noble gases enables

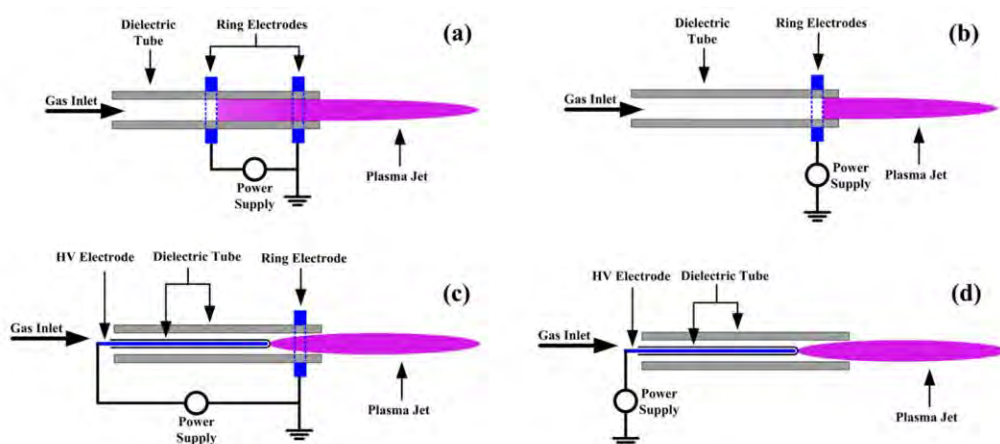


**Figure 1-8. Schematic representation of various plasma jets used for biomedical applications.** (a) The jet consists of a dielectric tube with two metal ring electrodes on the outer side of the tube, (b) jet created with only one ring electrode, (c) the second ring electrode of (a) is replaced by a pin electrode, (d) jet created with only the pin electrode. Adopted from<sup>28</sup>.

the generation of UV radiation which can be used during the plasma treatment. As APPJs use pre-assembled working gases, the working conditions can be more controlled and are more stable throughout the treatment. This also allows to vary the gas composition to control the reactive species generated<sup>96</sup>. Furthermore, the light-weight plasma jet makes it possible to treat narrow gaps due to its small dimensions. This way, the plasma plume is able to penetrate structured cavities and capillaries for an easy treatment of more complex surfaces. Moreover, the use of APPJs allows for fast 3D movements and accurate treatment, making them ideally suited for biomedical applications. However, the small size also acts as a disadvantage for the homogenous and/or simultaneous treatment of larger areas. This can be solved when multiple APPJs are connected forming an array of plasma jets<sup>97,98</sup>. However, more research is needed to better understand the fine-tuning of the operating conditions of plasma jet arrays<sup>56</sup>. Finally, high etch rates are observed after the treatment with APPJs, making them the method of choice for microbial inactivation. Again, an overview on various applications and setups is presented in<sup>81</sup>.

The plasma jets used in the experimental parts of this thesis are the kINPen, the X-Jet and COST-jet. The kINPen consists of a powered pin electrode surrounded by a dielectric tube which serves as the outer electrode (*cf.* Figure 1-8d). The X-Jet and COST-jet consist of two electrodes (one RF driven and one ground electrode), where the discharge gap is confined by two quartz glass plates (details are provided in **section 5-1.3**). In this way, the plasma discharge is maintained inside the device, which greatly reduces the density of fast-reacting species (*e.g.*, radicals and excited species) in comparison with the kINPen, where some discharge can also be found outside the device, yielding a visible afterglow.

### *1-2.2d Plasma Treated Liquids*

Recently, a novel approach for biomedical plasma treatment has been introduced and became the subject of increasing investigation (*cf.* Table 1-A in the **Appendix-1** at the end of this chapter): the use of PTL (*Plasma Treated Liquids*), often called PAL (*Plasma Activated Liquids*) in literature. Using PTL, biological substrates are treated with a liquid that has been in contact with plasma prior to the biomedical application, as presented schematically in Figure 1-9. This way, the plasma-generated species are ‘stored’ in the liquid which, in turn, carries these

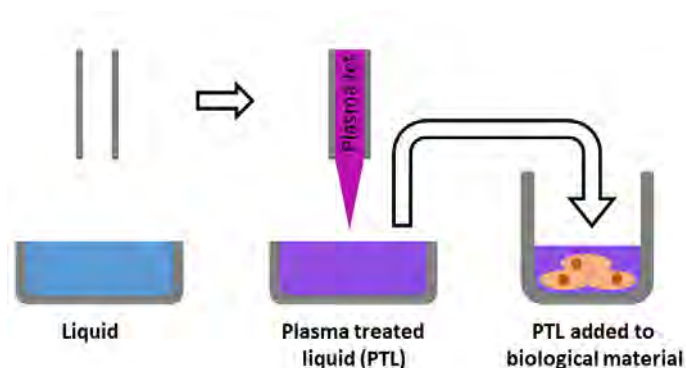


**Figure 1-9. Schematic representation of the use of PTL for biomedical applications.** A liquid is treated with a CAP source (left to middle figure). The resulting RONS-holding liquid is then used during medical applications (middle to right figure).

plasma components to the biological substrate of interest. Furthermore, the concentration of various reactive species can be controlled and fine-tuned when adjusting the plasma or treatment working conditions. In this way, Uchida *et al.* demonstrated that treatment distance can be used to adjust the ROS-to-RNS ratio<sup>99</sup> (*i.e.*, reactive oxygen species and reactive nitrogen species, respectively). Additionally, a recent study, performed by Ito *et al.*, evaluated the effect of a shielding gas for the production of reactive species inside the liquid<sup>100</sup>.

The use of PTL during medical applications, first of all, ensures a more homogenous treatment of the liquid covered tissue and the ability to store the plasma activity<sup>37,101</sup>. This way, plasma treatment can be applied even at moments or at places where no (suitable) plasma source is present or available. Furthermore, the substrate only comes in contact with liquid soluble and long-lived reactive species such as  $\text{H}_2\text{O}_2$ ,  $\text{HNO}_2$  and  $\text{HNO}_3$ . These liquids can be injected inside the tissue whereas direct CAP treatment transports RONS only to the first few layers (typically 3 to 5 cell layers)<sup>102</sup> due to the often high reactivity (high reaction rates) and short half-life of most species<sup>103</sup>. Using PTL, one is able to identify the concentration of the generated species before treatment and therefore also to partly control the therapy. Indeed, while direct treatment results in an inhomogeneous and often concentrated therapy, at least at the first layers of the treated object, PTL offers a way to apply a more uniform and controlled treatment of the tissue.

In literature, a range of different liquids have been used to generate PTLs,

ranging from pure water –*Plasma Treated Water* (PTW)– and buffered solutions to complex biomedical media –*Plasma Treated Media* (PTM)–. The choice of liquid greatly influences the resulting PTL in terms of concentrations of reactive species, ROS-to-RNS ratio, acidity, *etc.*<sup>100,104,105</sup>. In a recent study, performed in collaboration with the Ruhr-Universität Bochum, we noticed that the treatment of non-buffered water resulted in a noticeable decrease in pH, due to the generation of acids like  $\text{HNO}_2$ ,  $\text{HNO}_3$  and  $\text{HO}_2$  (up to  $\text{pH} \approx 1$  after 5 minutes of plasma treatment)<sup>106</sup>. This can be avoided by using buffered solutions like PBS (Phosphate Buffered Saline)<sup>106</sup>. Additionally, aqueous liquids often contain ions like  $\text{Cl}^-$  which forms hypochlorous acid ( $\text{HOCl}$ ), a strong antibacterial agent, in an oxidative environment<sup>107</sup>. Being a reactive species,  $\text{HOCl}$  is known to interact and react not only with biomolecules, such as DNA and proteins, but also with other reactive species in solution like  $\text{H}_2\text{O}_2$  and  $\text{O}_2^-$ , influencing the plasma chemistry in the liquid<sup>65,108,109</sup>. Finally, it is expected that the presence of ions can have an impact on the reactive species in solution. Indeed, transition metals are expected to interact with the plasma-generated reactive species, forming certain complexes and, as a result, partly stabilize the radicals in solution.

A wide range of media, containing a mixture of biomolecules mimicking cellular conditions (*e.g.*, amino acids, sugars, ions, *etc.*) can also be used, leading to the creation of PTM, often called PAM (*Plasma Activated Media*) in literature. Note that this differs significantly from (buffered) PTW as a new combination of long-lived reactive species can be generated such as amino acid peroxides. This offers a new dimension for biomedical applications as these biochemical reactive species (often having a larger life-time compared to most RONS) can be used to transport the oxidative activity to and in cells which are found far away from the treated area<sup>25,46,110–112</sup>. However, this also limits the storage of RONS in PTM as they will be involved in various reactions with the biomolecules present in the medium<sup>37</sup>. Treatment with PTM has the great advantage that it introduces the reactive species to the cells by using their own environment. As such, most of the research performed in this field is focused on the use of PTM (*cf.* Table 1-A). Furthermore, the presence of certain amino acids (*i.e.*, phenylalanine, alanine, histidine, arginine, tyrosine, and lysine) has proven to enhance the anti-tumor activity of PTMs<sup>111</sup>. The opposite effect

has been observed in the presence of other amino acids, *i.e.*, cysteine, proline, aspartic acid, serine, glutamic acid, threonine, leucine, and glycine. This highlights the possibility to control the activity of PTLs for medical applications, in order to fine-tune the impact of reactive species on the biomedical target.

Although it is a fairly new approach for biomedical applications, mainly focused on decontamination (necessary for wound healing) and cancer treatment, and to some extent also on other applications like the treatment of AMD (Age-related Macular Degeneration)<sup>55,93,113–116</sup>, the confidence for the use of PTLs is increasing in the plasma medicine field, as well as in medicine more in general, where increasing amount of research has been performed. Table 1-A in the **Appendix-1** summarizes the work done using PTL for cancer treatment as an example.

## 1-2.3 Applications in plasma medicine

### *1-2.3a Introduction*

In plasma medicine, as already mentioned in **1-2.1**, CAPs and PTLs are used in the fields of wound and ulcer healing, dental treatment, decontamination, blood coagulation, implants, cancer treatment, dermatology and even eye-related diseases. In this context, CAPs serve as a controllable source for reactive species, in synergy with the electric fields and UV radiation. Indeed, while direct therapy focuses on the synergetic effect of all plasma-generated components, the treatment of cells found deeper inside the tissue, or the treatment with PTL, depends on the RONS concentrations and their impact on the biology of the treated area.

In biology, the dual nature of various reactive species is observed, which highlights the success of plasma treatment even further<sup>69</sup>. It has long been established that ROS, like hydrogen peroxide ( $\text{H}_2\text{O}_2$ ) and hydroxyl radicals (OH), are used by the immune system to fight against infections and malignant cells. Simultaneously, increasing evidence points towards the role of RONS at low concentrations, such as nitric oxide (NO) and  $\text{H}_2\text{O}_2$ , as cellular signaling messengers in, for example, blood coagulation and cell proliferation, and to their crucial role in the redox system of mammalian cells<sup>67,107,117</sup>. Although great efforts have been made to better understand the role of the (plasma-generated) reactive species inside cells

and during the different applications, knowledge of the relevant mechanisms and interactions is still lagging.

The use of CAPs for decontamination and the treatment of wounds and cancer are among the most investigated fields within plasma medicine<sup>8,10,35,47,118</sup>. While wound healing requires only the treatment of the outermost cell layers of the wound, the treatment of cancer involves significant depths and, in the case of metastasis (*i.e.*, migration of cancerous cells to other places), the full body. As such, the treatment of cancer is very challenging and diverse.

*The work presented in this thesis is dedicated to the above-mentioned two areas in plasma medicine. In this regard, an introduction to wound healing and cancer will be provided in the following sections 1-2.3b and 1-2.3c.*

### 1-2.3b Chronic wound healing

#### *Introduction to wound healing*

A very complex cascade of cellular activity is initiated in order to heal wounds. Indeed, a whole network of biochemical processes is activated in order to disinfect the area, keep the tissue at optimal conditions (temperature and humidity) and stimulate cell regeneration<sup>66</sup>. Under normal circumstances, the healing of a wound follows several phases: blood coagulation, inflammation, proliferation and differentiation. As indicated in the reviews presented by Childress<sup>66</sup> in 2002 and Sen<sup>67</sup> in 2008, most of these processes, if not all, are heavily dependent on the presence of O<sub>2</sub> and biologically reactive species such as NO and H<sub>2</sub>O<sub>2</sub>.

First of all, blood coagulation is controlled and initiated which is necessary to increase the blood flow around the injured tissue. This is essential for the transport of O<sub>2</sub>, white blood cells and other relevant products<sup>107</sup>. This process is called hemostasis and forms the first step towards wound healing by transforming liquid blood into a gel-like substance (to prevent the loss of essential products). Furthermore, infections are avoided using O<sub>2</sub>-dependent respiratory bursts, *i.e.*, the production of reactive oxygen species, which demands a high oxygen supply<sup>67</sup>. Note that this is directly linked to the antibacterial and antiviral properties of RONS. Finally, a cascade of cellular activities is initiated where RONS are known to play a crucial part in the signaling processes.

An example is the role of RONS, in particular  $\text{H}_2\text{O}_2$ , in the re-epithelialization of the wound (*i.e.*, closing the wound). Here, low concentrations of  $\text{H}_2\text{O}_2$  are able to activate cell motility via the activation of the so-called *pro-MMP-2* which, in turn, activates the matrix metalloproteinase (MMP) in order to break the extracellular matrix of tissue<sup>119</sup>. This is required in order to allow the reorganization of cells, increasing the motility. Furthermore, upregulation of ROS not only enhances cell motility but also morphological transformations which are necessary to reconstruct damaged tissues. Another example is the crucial contribution of NO to angiogenesis (*i.e.*, formation of new blood vessels)<sup>73,74,120,121</sup>. However, the exact role of this small molecule in these bioregulatory mechanisms still has to be elucidated.

In order to regenerate and reconstruct tissue after being damaged, a high supply on energy is required. This is provided by means of oxidative metabolism which, again, is  $\text{O}_2$ -dependent. This highlights the importance of angiogenesis and the stimulation of the blood flow. A detailed overview of the biochemical processes and the role of reactive species during wound healing is presented in various review papers<sup>66,67,122</sup>.

#### *Chronic wound healing and plasma treatment*

As mentioned before, these phases occur under normal circumstances. In this context, the wound will heal over time. However, when the healing fails, acute wounds can become chronic wounds. This can be caused by infections, hypoxia due to insufficient oxygen transport, or a dysfunctional repair. In this case, the wound is unable to heal and close, which increases the stresses and the chance of infections. This, in turn, will further disrupt the healing process. As a response to infections, inflammation is initiated by the body, which prevents the release of the growth factors that are required for the regeneration of tissue<sup>66</sup>. Although inflammation is required for wound healing, the exaggerated activation at this stage prevents the initiation of the necessary proliferation phases.

It is clear that (chronic) wound healing is heavily oxygen- and RONS-dependent. Although great efforts were made to enhance the healing processes, the treatment of chronic wounds and ulcers remains challenging. Techniques based on the delivery and stimulation of growth factors<sup>123</sup>, ATP (adenosine triphosphate; needed for cellular energy)<sup>124</sup>, and other important products are being developed.



Among these therapies are the delivery of reactive species and the stimulation of the oxidative metabolism. In this regard, the treatment with CAPs can provide an excellent and sterilizing alternative. Indeed, CAPs have been utilized for decades to sterilize heat-sensitive equipment and tissues<sup>86,125–127</sup>. Interestingly, serving as a source of RONS, multiple *in vivo* works have proven that plasma treatment is able to simultaneously sterilize the wound (by attacking and killing micro-organisms like bacteria and viruses), enhance blood coagulation (due to the generation of NO and H<sub>2</sub>O<sub>2</sub>), stimulate cell proliferation and increase the blood flow<sup>41,128–130</sup>. Although great efforts are being made to elucidate the interactions between RONS and the tissue, and the important mechanisms enhancing wound healing, the role of O<sub>2</sub> and the influence of plasma treatment on the circulation of O<sub>2</sub> remains largely unexplored, in spite of the utmost importance<sup>131</sup>.

Another important factor during the treatment of wounds is the temperature. This is important as values above 40 °C result in degeneration processes within the treated tissues. Here, a slight increase of the temperature of the tissue (typically to 38.5 °C) stimulates cell proliferation, which is required for wound healing, as already mentioned above<sup>66</sup>. Although CAPs are generated at atmospheric conditions, temperatures above room temperature are generally measured within the plasma discharge. In this context, the gas temperature of a plasma jet device, on one hand, is typically found in the range of 46 to 63 °C<sup>30</sup> which decreases with increasing distance from the nozzle. The temperature profile of the kINPen plasma jet has been determined using a 0D chemical kinetics model for a plug flow<sup>64</sup>. Here, a gas temperature of around 54 °C has been determined at the nozzle, which decreases in a quasi-linear fashion with increasing distance, reaching 41 °C after 1 cm. The gas temperature can further be controlled by operating in a burst mode, *i.e.*, a period of HF voltage supply (plasma on) is interrupted with a break period (plasma off). On the other hand, the gas temperature in a DBD can reach 102 °C in the case of direct treatment (when the skin serves as a counter-electrode)<sup>132</sup>. Despite the high gas temperature of the discharge, the temperature on the treated substrates is significantly lower, reaching room temperature. Due to the very short lifetimes of such discharges (typically in the range of nanoseconds), the actual temperature drops rapidly. Taken together, the used plasma sources are ideally suited for the treatment

of chronical wounds due to their low temperature and generation of biologically active species.

### *1-2.3c Cancer*

#### *Introduction to the biology of cancer*<sup>133–135</sup>

In a living multicellular organism, cells can be seen as individuals of a biological society which prioritize the survival of this society above all else. A vast range of different types of cells are present in this society, all having their own specialty, going from transport, security and defense to healing and maintenance. These members, more than  $10^{14}$  for an average human body, are able to reproduce via cell division (forming an identical copy of the parent-cell), collaborate as an organization –representing living tissue– and sacrifice themselves when needed/requested. In this way, cells act as instructed by certain control signals. These signals can be sent, received and interpreted by the cells to maintain the order and to ensure a constructive behavior for the sake of the whole organism. In this way, for example, red blood cells deliver  $O_2$ , a source of energy, to every cell in the organism. Another example are neurons which play an important role in the communication between tissues and the brain.

Members which act differently than instructed, as a result of a molecular disruption, can cause a disturbance in the organism. When these disruptions are a result of genetic or epigenetic modifications (see later), the cell might adapt a selective advantage, able to act against, or even without the need of external control signals. When this mutated cell is able to oppose the order of, *e.g.*, cell-death, or is able to divide and grow at a much higher rate compared to normal cells, the cell may become the start of a new mutated colony based on the same abilities. Further modifications within members of these colonies can incite even more ‘selfish’ behaviors which, in turn, can jeopardize certain constructions and organizations, and, when left alone, can be fatal for the organism as a whole. This principle is depicted in Figure 1-10.

However, a viable series of modifications is required for the production of such malignant cells and colonies. As explained above, modifications are either genetic or epigenetic. This means that either a change in the cell’s DNA sequence occurred –genetic– or a change in gene expression –epigenetic –. Both can have a huge effect

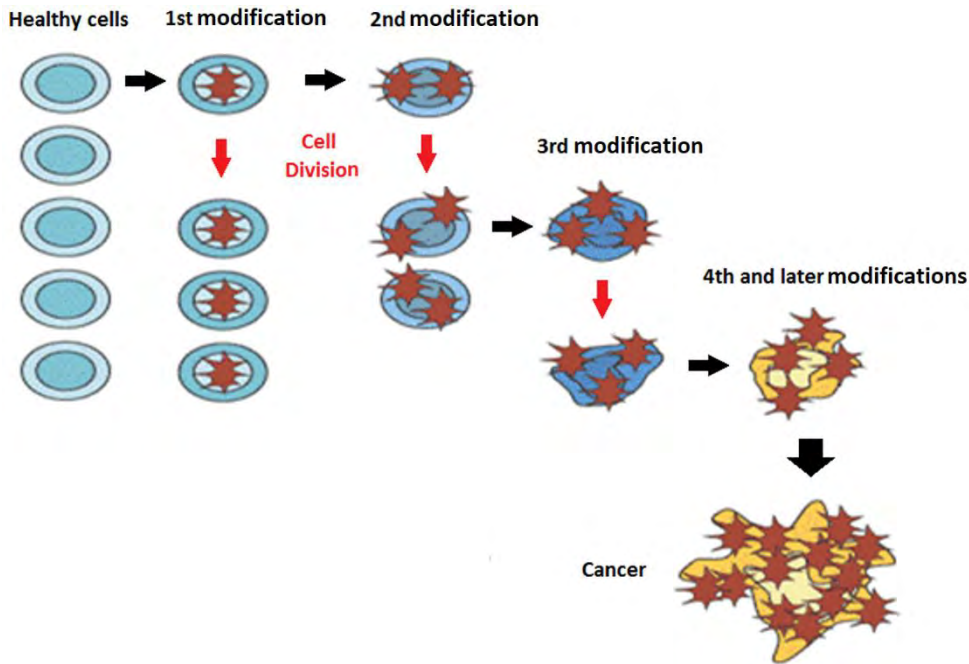


**Figure 1-10. Schematic representation of the development of cancerous cells.** Multiple viable modifications are required in order to obtain malignant cells (yellow). Mutated cells are able to divide (red arrows), creating new mutated cells which, in turn, are able to mutate themselves (black arrows).

on the biochemistry of the affected cells. Similar to the idea that mutated colonies can be fatal to the organism, cells are not always capable of surviving a series of modifications. In this case, the modifications are clearly not viable. This explains the need of a viable series of modifications for the production of malignant cells, which should be able to survive and prosper from these (epi)genetic changes.

*Cancer* is based on this principle (*cf.* Figure 1-10) and encircles a group of diseases where cells are mutated in such a way that they: (i) are able to ignore the normal constraints of cell division and growth, thus dividing at a much higher rate compared to their normal counterparts, and (ii) are able to invade other tissues – *metastasis*– to start a new colony of malignant cells, a *neoplasm* or *tumor*. It should be noted that metastasis does not imply an overall increase in cell mobility, which would result in the destabilization of a tumor mass. In this context, metastasis is the ability of a small piece of the tumor to migrate to other sites in the affected body.

Given the immense number of cells in the human body (order of  $10^{14}$ ), all

having the potency to mutate, the organism always contains a significant number of malignant cells. However, these cells are rarely able to divide and grow into a recognizable tumor mass. This is due to the constant struggle of cancerous cells to survive and the continuous effort of the body and immune system to eliminate defects and/or hazardous elements. Indeed, despite the presence of a viable and malignant biochemistry, cancerous cells need to remain hidden or defend themselves against the body's immune system. Moreover, cells need to satisfy multiple hallmarks in order to become cancer cells, where uncontrolled cell division and growth, avoiding immune responses and the capability of invading other tissues, are just three of them<sup>134</sup>. For a cell line (cells of the same group) to become cancerous, its biochemistry must be able to (*cf.* Figure 1-11):

- (i) evade growth suppressors (also known as cancer suppressors).
- (ii) avoid immune responses and destruction (*i.e.*, able to remain unseen to the immune system of the organism).
- (iii) enable replicative immortality (as healthy cells are only able to divide a limited amount of times).
- (iv) induce tumor-promoting inflammation (which speeds up the growth process).
- (v) activate invasion and metastasis (*i.e.*, be able to invade other tissue in the body).
- (vi) induce angiogenesis (*i.e.*, promote the creation of blood vessels for the delivery of important nutrition and energy).
- (vii) induce genome instability and modifications (which enables the cell to adapt to the environment for its own survival).
- (viii) resist cell death (*i.e.*, be able to ignore pro-apoptotic signals).
- (ix) change the cellular energetics (as the affected organism is unable to provide enough energy for fast growing tissue; this is related to angiogenesis).

- (x) sustain proliferative signaling (*i.e.*, suppress apoptosis even when a large amount of stress is present).

Going into detail on the different hallmarks of cancer would lead too far for this thesis. More information can be found in the review of Hanahan and Weinberg<sup>134</sup>.

In the past decades, increasing evidence has shown that tumors can contain cancer cells which possess characteristics of stem cells, and are known as cancer stem cells. This results in the ability to differentiate in various specialized cells, which can self-renew and are tumorigenic. Because of this, cancer stem cells are able to adapt themselves to their environment and can show a high resistance to anti-cancer therapies (see below), leading to the recurrence of the tumor after treatment.

As the human body contains a large number of different cells, an enormous range of different cancer cells have been encountered in clinical history. Since the development of the *US National Cancer Institute 60 human tumor cell line anticancer drug screen* (NCI60) in 1980, around 1300 unique cancer cells have been included in pharmacogenomic databases<sup>135</sup>. In this respect, also a variety of different malignant

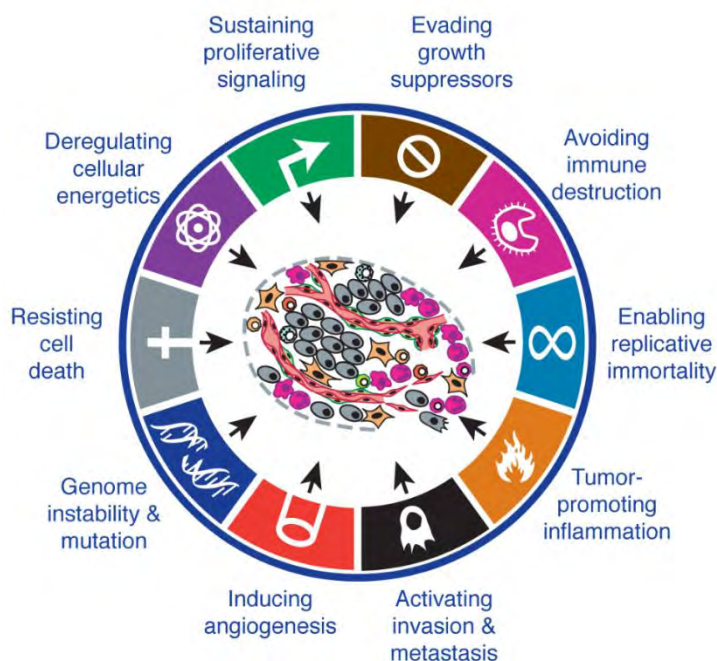


**Figure 1-11. Schematic representation of the hallmarks of cancer.** Adopted from<sup>134</sup>.

cells is typically encountered in a single neoplasm, as different sets of modifications are able to occur in a single colony of malignant cells. For this particular reason, it is extremely difficult to treat cancer as a whole, while leaving the surrounding, healthy cells unharmed. This is because all cancerous cells may act differently towards the used treatment and because their mutating and proliferative nature creates the potential to resist these anti-cancer therapies.

### *Treatment of cancer*

Being one of the major illnesses of the modern age, great efforts have been made, aiming to treat cancer. As such, techniques like surgery, radiation therapy, chemotherapy, ion beam treatments, photodynamic therapy, gene-targeted therapies and non-thermal plasma treatments were developed. While the former three techniques offer a broad treatment, in the sense that they are able to kill the majority of known and unknown cancerous tissue, they prove to be harmful for healthy cells as well, leading to various unwanted side effects.

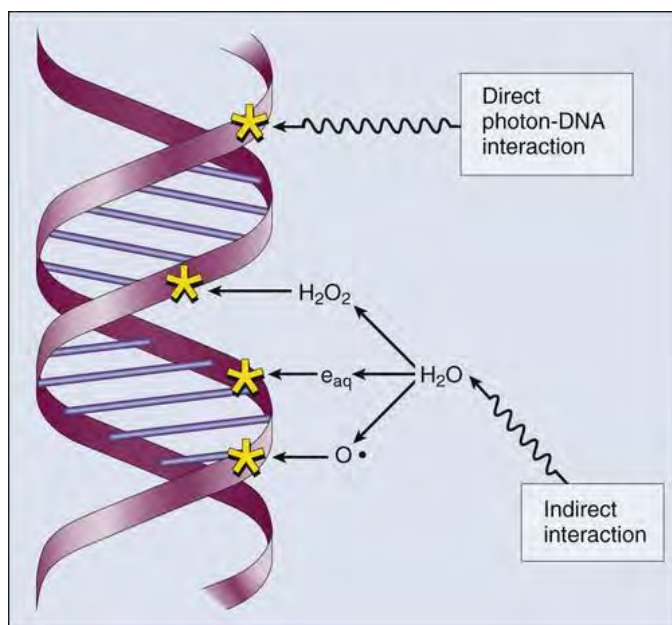


**Figure 1-12. Schematic representation of radiation therapy.** Due to ionization,  $H_2O$  inside the cell will break in ROS (*i.e.*,  $H_2O_2$ ,  $O$ ,  $OH$ ,  $e^-$ ) which will oxidize and damage DNA. In addition, chemical bonds in DNA can be broken through direct photon ionization. Figure adapted from<sup>136</sup>.

In the case of *radiation therapy*, ionizing radiation is used to control or kill fast dividing cells. As cancerous cells are characterized by fast and uncontrolled cell division, radiation therapy focusses on these malignant cells<sup>136</sup>. The aim of radiation therapy is to damage DNA of the malignant cells by directly ionizing the biomolecule or by the creation of ROS (like OH radicals) as a result of the ionization of the surrounding cytosol (*cf.* Figure 1-12). This is considered a broad technique because damage and ionization are inflicted locally inside the treated cells in an indiscriminate manner, meaning that this is independent of the cell type. In this way, also healthy cells can be damaged. However, as this DNA damage mainly manifests during the cell-cycle, fast-dividing cells will be affected the most, resulting in apoptosis, while the majority of healthy cells are slow-dividing and are able to react to the applied stresses by initiating repair mechanisms or by growing back. Indeed, fast-dividing healthy cells, like blood cells and hair-follicles, will suffer from the treatment as well, leading to known side effects like nausea, damage to the epithelial surface, swelling, inflammation, but also hair loss and even cancer<sup>137</sup>.

*Traditional chemotherapy* uses non-specific intracellular toxins, which typically inhibit mitosis (*i.e.*, cell division). Additionally, intercalating agents, such as cisplatin, are often used, which interact with DNA to form crosslinks. These crosslinks interfere with cell division, which stimulates DNA repair, leading to apoptosis when the damage becomes too severe<sup>138</sup>. Other therapies target the synthesis of nucleotides using antifolates, leading to an inhibition of DNA replication. These agents antagonize the action of folic acid, which takes part in the synthesis of purines and pyrimidines<sup>139</sup>. In these examples, chemotherapy is an alternative way of attacking fast-dividing cells inside the body or treated areas by inflicting stresses to induce cell death. Similar to radiation therapy, traditional chemotherapy is not cell specific in the sense that they do not only attack cancer cells but also fast-dividing healthy cells, like those found in bone marrow, hair follicles and even fetuses<sup>140</sup>.

*Ion beam treatment* shares the same features as radiation therapy. Ion beams are used to induce a large dose of stress inside the cell, aiming to damage DNA. Unlike radiation and chemotherapy, ion beam radiation is not used conventionally and is still under development<sup>141</sup>. Using this technique, a beam of heavy ions (usually carbon) is shot with cell-like precision in the observed malignant cells causing a

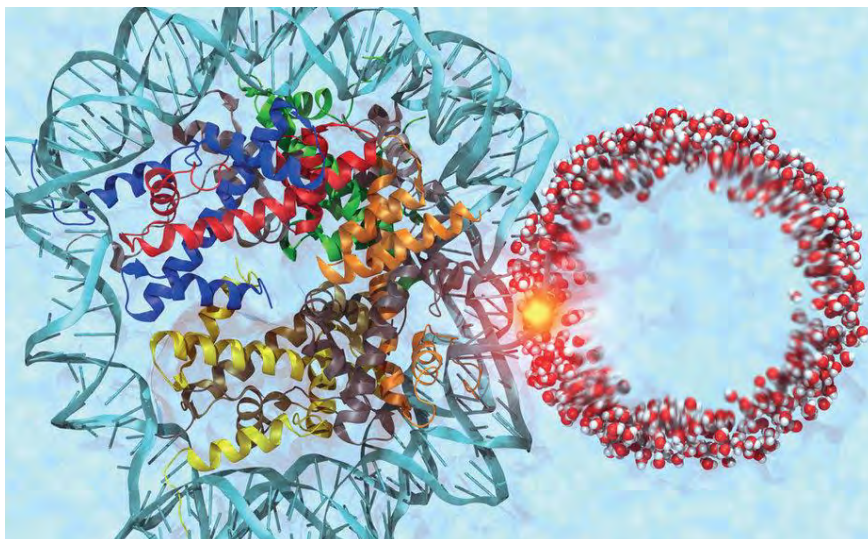


**Figure 1-13. Representation of shockwave induced by ion irradiation.** The heavy ion travels via the axis of the water circle. This releases a pressure next to the nucleosome, creating a shockwave able to damage DNA (yellow dot). Figure adapted from<sup>142</sup>.

shockwave at a specific point in the cytosol around or in the nucleus (see Figure 1-13)<sup>142</sup>. As a result, DNA is damaged, and ROS are created in the cytosol which can further damage and oxidize DNA, leading to apoptosis.

Ion beam radiation is unique as it provides cell-specific treatment, which significantly limits the expected side effects and damage in healthy cells. However, only cancer cells that are identified in the patient can be treated, whereas treating undiscovered cells or metastasis becomes very difficult. Furthermore, due to the severe damage inflicted inside the cells, necrosis is often observed, leading to additional stresses to the treated tissues. In 2016, *in vivo* experiments were performed using carbon ion-beam therapy on eight patients to investigate the long-term effects of this treatment<sup>143</sup>. Although complete therapeutic response was observed in all patients, long-term complications were revealed, like distant metastasis, local reoccurrence of the tumors, and necrosis. This affected four patients and claimed the life of two within the first two years.

*Photodynamic therapy* combines the use of light with photosensitizing agents leading to an oxygen-dependent therapy<sup>144</sup>. First, the photosensitive molecules are incorporated in the targeted cells. Afterwards, light with a specific wavelength is administered, which resonates with the photosensitizer. Finally, the latter transfers



the absorbed energy to molecular oxygen to generate ROS. This action only occurs in the vicinity of the photosensitizer, meaning that the generation of ROS only occurs on the areas that have been exposed to the light. This therapy has proven successful for early stage cancer treatment. However, tumor specificity still proves to be a challenge. In this context, approaches using cancer-associated antibodies can be used so that the photosensitizers are specifically located within cancer cells.

Recently, more studies are conducted to provide selective treatment, where only malignant cells are attacked while their healthy counter parts remain unharmed by the therapy. In this context, the hallmarks of cancer and the knowledge obtained of the envisioned cancerous tissue are taken into account to develop selective treatments. As such, gene-targeted therapies have been developed as a form of *new-generation chemotherapy*. By specifically targeting tumor suppressing factors or attacking oncogenes, the development of specific malignant cells can be controlled or even reversed, leading to apoptosis and tumor shrinkage<sup>145,146</sup>. It should be noted that this differs significantly from conventional chemotherapy as explained above. However, great knowledge of the targeted cancer cells is required for optimal treatment.

All the above-mentioned techniques (with exception for ion beam therapy) suffer from the ever-changing nature of malignant cells which, over time, become immune or resistant to the used technique. In this regard, one is able to destroy the majority of the cancer cells found in a single tumor, while a small part can show resistance to the treatment, leading to a reoccurrence of the initial tumor, which becomes resistant to the anti-cancer therapy used before. Additionally, metastasis forms a big challenge when using area-specific techniques (*i.e.*, radiation, photodynamic and ion-beam therapy). This raises the need for both selective (cancer vs healthy cells) and systemic treatments (whole body) able to damage all malignant cells and, when possible, stimulate healthy tissue, as well as the immune system. Here, again, plasma treatment can hold the key towards an answer.

### *Plasmas for cancer treatment*

By providing the tissue with biologically relevant reactive species, cells will be stressed, initiating anti-tumor responses. In this way, many positive results have already been observed, indicating that plasmas are able to attack a wide range of

cancers tissue without damaging the healthy cells<sup>47,87</sup>. Among the investigated cancer lines are breast cancer<sup>147</sup>, cervical cancer<sup>148</sup>, lung cancer<sup>149</sup>, gastric cancer<sup>150</sup>, leukemia<sup>151</sup>, pancreatic cancer<sup>102</sup>, liver cancer<sup>152</sup>, ovarian cancer<sup>153</sup>, melanoma<sup>154</sup>, neuroblastoma<sup>155</sup>, glioblastoma and colorectal carcinoma<sup>156,157</sup>, *etc.* These studies showed that senescence and apoptosis were the leading, selective, anti-tumor mechanisms at low plasma doses. Moreover, the observed activity was the result of additional reactive oxygen and nitrogen species produced in the plasma. Indeed, this synergy will affect multiple parts of the cell, both stimulating and inhibiting several biochemical pathways. This leads to the inability of the cell to reproduce, eventually causing cell death<sup>38</sup>. Furthermore, plasma treatments have proven to be beneficial against drug resistance of these malignant cells, as the plasma species can interact with specific transmembrane proteins, enhancing conventional anti-cancer treatments<sup>158,159</sup>. In this way, plasma species act together with chemotherapeutic drugs, in a synergistic manner, to overcome drug resistance and to achieve a higher apoptotic rate in tumors. This was clearly demonstrated by Ishaq and coworkers<sup>39</sup>, who observed an increase in apoptotic responses in TRAIL-resistant HT29 colorectal cancer cells, without harming the healthy cells. This was done by using the combined treatment of CAPs with TRAIL (tumor necrosis factor-related apoptosis-inducing ligand)<sup>39</sup>. Another example is the work of Kaushik *et al.*<sup>160</sup>, who combined plasma treatment of blood cancer cells with 2-deoxy-D-glucose, a glycolytic inhibitor (*i.e.*, a metabolic modifier which inhibits the production of energy via aerobic glycolysis, which is essential for many cancerous tissues<sup>161</sup>). Their treatment resulted in a reduction of ATP (adenosine triphosphate) and lactate production, as well as the induction of apoptosis of various blood cancers. This highlights the synergetic effect of plasma treatment with anti-cancer drugs.

### *1-2.3d Plasma-cell interactions*

*In this section, general observations on the impact of plasma treatment on cells will be discussed, with additional information on specific mechanism, that will be indicated by separate titles.*

*Please note that the plasma-cell interactions are still more complex than described in this section, and that other mechanisms can contribute to the biological activity of plasma treatment.*

One of the effects of CAPs most commonly seen during treatment, is the elevation of oxidative species within cells<sup>38,162,163</sup>. However, to the best of our knowledge, the reason for this increase is cell specific and not fully understood. As RONS are unable to directly penetrate the cell-membrane<sup>164,165</sup>, other mechanisms must be present to transfer these species and the accompanied stress in the cell. Three groups of mechanisms can be proposed: (i) active transport of reactive species through transmembrane channels, (ii) chemical modification of the cell membrane, leading to increased permeability (*e.g.*, pore formation) or even a collapse of the membrane, (iii) interactions with membrane-bound proteins leading to stress signaling inside the cell, which can lead to an increase in cellular RONS levels.

#### *Transport of RONS across the cell membrane*

##### Active transport of reactive species through transmembrane channels

In recent years, the transport of small polar reactive species by transmembrane channels, like NO and H<sub>2</sub>O<sub>2</sub>, has been observed<sup>166–168</sup>. The transmembrane channels responsible for this activity were identified as *aquaporins* (AQP), active channels known to transport water molecules through the cell membrane. Within the AQP family, only AQP 1, 3, 8 and 9 have been confirmed to successfully transport H<sub>2</sub>O<sub>2</sub> across the cell membrane. As H<sub>2</sub>O<sub>2</sub> is known to play an active role in cancer and wound treatment, these AQPs became the target of investigation. In 2017, Yan *et al.* investigated the contribution of AQPs in the anti-tumor effect of CAPs on glioblastoma<sup>169</sup>, focusing on AQP 8 and 9. These two transmembrane channels were chosen, as AQP 8 is known to transfer H<sub>2</sub>O<sub>2</sub> efficiently, while AQP 9 was most abundantly found in the investigated glioblastoma (U87MG). In their work, they demonstrated that AQP 8 played a crucial role in the anti-tumor activity. Indeed, when AQP 8 was deactivated in the cell, an inhibition of the anti-glioblastoma capacity of CAP and H<sub>2</sub>O<sub>2</sub> was observed, while this was not the case when blocking AQP 9. However, different cancerous tissues express different levels of AQP activity. It is found that cancer cell with a high proliferation rate express a higher level of AQPs and are thus more susceptible for CAP treatment. Therefore, a good understanding of the transmembrane channels is required, as it will help in understanding the transport of reactive species to and in the cell, and the effect of CAPs during the treatment of cells more in general.

### Transport of reactive species through pores, created upon lipid peroxidation

Although transmembrane channels are able to transport reactive species through the cellular membrane, the majority of the species remain at the outer side of the membrane where they can interact or react with membrane-bound components. One of the most abundantly found molecules in mammalian cell membranes are phospholipids. At this stage, phospholipid peroxidation can occur, when species like OH radicals react with the unsaturated carbon atoms of the phospholipid chains found in the membrane<sup>77,166</sup>. In a recent investigation performed within our group, the behaviour of a phospholipid bilayer, at several rates of phospholipid peroxidation, was studied<sup>77</sup>. In this computational study, we observed the formation of aqueous pores due to the rearrangement of the oxidized phospholipids. This creates a polar channel, enabling the ROS to enter the cell<sup>77</sup>, as illustrated in Figure 1-14. However, this was only encountered in model systems with a reduced cholesterol content compared to the steady-state concentration of healthy cells (usually found in the 40-50% range)<sup>77</sup>. As it is stated that a range of cancerous cells contain a significantly lower concentration of cholesterol in their cell membrane, compared to their healthy counterparts, we expect further accumulation of ROS within these cancer cells<sup>170</sup>. However, it must be mentioned that not all cancer cells contain a lower cholesterol

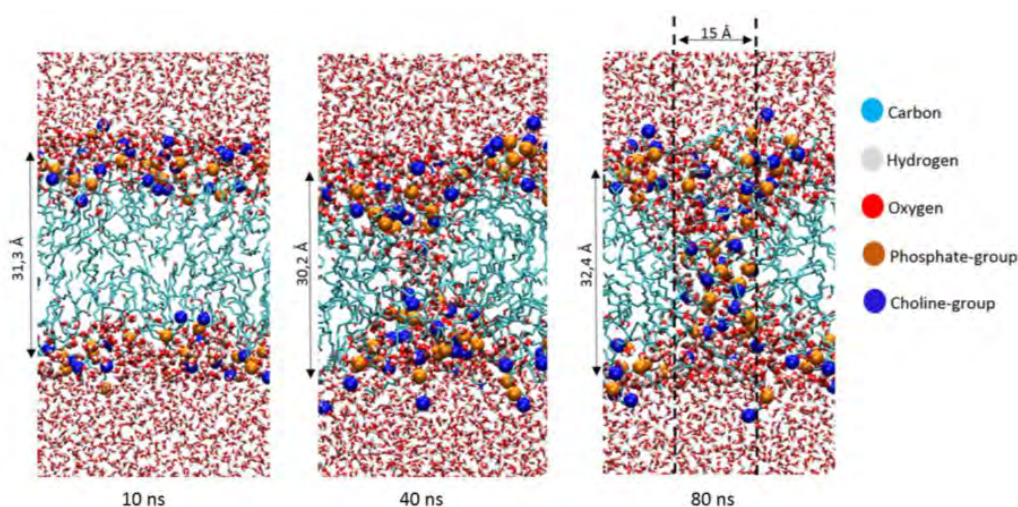


**Figure 1-14. Snapshots of the molecular dynamic simulations showing the formation of pores in the case of 100% oxidized phospholipids.** The introduced oxidation products are aldehydes as a result of lipid peroxidation. Reprinted from<sup>77</sup>.

content in the cell membrane, so this mechanism could only explain the selectivity for some types of cancer cells.

#### RONS interactions with membrane-bound proteins

Next to reactions with the phospholipids, it has been proposed that differences in the redox balance at the outer leaflet of the cell membrane are able to affect cellular signaling pathways of the cell. An important example is the glycoprotein CD44, also known as P-glycoprotein-1<sup>171,172</sup>. CD44 is a membrane-bound receptor that is known to activate the pro-proliferative extracellular regulated kinase (ERK 1/2) and the serine-threonine kinase AKT pathways inside cells (see Figure 1-15). Tanaka *et al.* investigated the impact of PTM treatment on the expression of CD44<sup>172</sup>. Their results indicated that CD44 is significantly downregulated after PTM treatment, compared to the untreated control. This downregulation affected the activation of proliferative signals inside the cell, yielding a reduced expression of the ERK 1/2 and AKT pathways. This reduction in proliferative signals, induces apoptosis in the treated glioblastoma cancer cells (U251SP in this case) and demonstrates that PTMs are able to change the intracellular molecular mechanisms by interacting with the cell membrane, leading to cell death (*cf.* Table 1-A).

#### *Impact of RONS to cellular activity*

##### Chemical modifications caused by RONS

Once reactive species are introduced or generated within the cell, they are able to interact or react with different parts of the cell, which can further stimulate the cellular production of reactive species. Indeed, oxidation of various biomolecular systems is typically observed during plasma treatment. Among the oxidation targets are the phospholipid bilayer, as already mentioned in the previous section, proteins and DNA.

A wide range of experimental studies have shown that reactive species (originating from the cell itself or from plasma treatment) are able to react with DNA, resulting in DNA damage, mutation and even strand breaks<sup>57,173–176</sup>. This DNA damage is usually measured by evaluating the expression of response proteins such as c-Jun N-terminal kinase (JNK), poly (ADP-ribose) polymerase 1 (PARP1) or  $\gamma$ H2AX (histone variant H2AX that is phosphorylated on serine 139)<sup>177,178</sup>.

Irreversible damage (*e.g.*, cross-linking, double strand breaks) can have devastating effects on the treated cells and will lead to the activation of pro-apoptotic factors. More information on the chemical modifications of DNA will be provided in **chapter 4**.

In contrast, the oxidation of proteins is much more complex, given the variety of different proteins and enzymes in the human body<sup>179</sup>. Despite this high number, proteins consist of only 20 different amino acids. In the context of plasma medicine, chemical modifications of amino acids, due to reactions with RONS, are being investigated in order to obtain insight in the oxidation of proteins. Using mass spectrometry (MS), Takai *et al.* was able to deduce the most expected oxidation products of the different amino acids after plasma treatment and the ratio in which these building blocks are targetted<sup>21</sup>. This investigation made clear that plasma-induced oxidation favors sulfur-holding and aromatic amino acids (*i.e.*, methionine, cysteine, tryptophane, phenylalanine and tyrosine). This observation perfectly aligns with multiple independent studies on the plasma treatment of peptides and proteins<sup>106,180–184</sup>. More information on the chemical modifications of peptides and amino acids and their impact on the affected peptides will be presented in **chapter 5**.

Although RONS are able to chemically modify important components of the plasma treated cells, they must be able to diffuse through the cell to reach their targets, thus having a high chance of being scavenged by the multiple antioxidants present in the treated cell (*e.g.*, glutathion, superoxide dismutase, catalase, cytoglobins, cytochrome c, *etc.*). In this context, tumor-selective treatment is partly caused by the difference in the redox balance of cancerous cells compared to normal cells. This manifests both in direct and indirect mechanisms. In the direct mechanism, studies have pointed towards the plasma assisted activation of the antioxidant systems as a response of the affected cells towards the increase in oxidative activities. As a wide range of cancerous cells already contain a higher steady-state concentration of RONS<sup>184–186,187</sup>, the increase in RONS levels, as a result of plasma treatment, can overcome the cellular antioxidant system. As a consequence, these tumorous cells will suffer from damage caused by the chemical modification of proteins, lipids and DNA (as discussed above), which may eventually lead to

apoptosis or even necrosis if the RONS concentration and the consequent chemical damage from the plasma treatment, become too high<sup>157</sup>. As stated before, the reason for the elevated steady-state RONS concentration of cancer cells is not yet fully understood. Possible sources are changes in mitochondrial proteomics due to DNA mutations, hypoxia and anoxia, reduction in the antioxidative responses and errors in the electron transfer chain in the mitochondria as a result of the Warburg effect<sup>161,188,189</sup>.

Finally, the presence of RONS can affect multiple molecular mechanisms and cellular pathways as already mentioned in the above examples and presented in Figure 1-15. In the following subsections, these effects will be explained in a bit more detail.

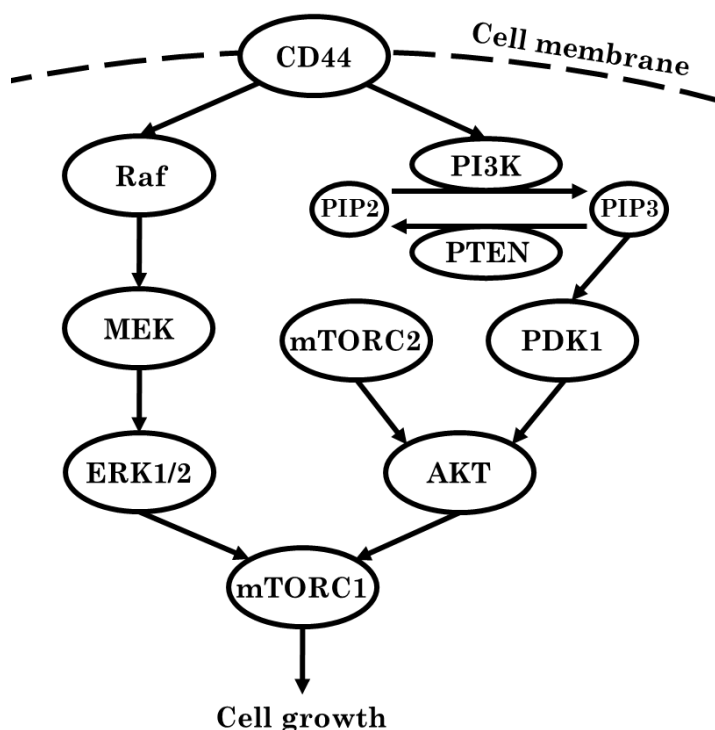


**Figure 1-15. Schematic representation of the proliferative signaling induced by CD44.** This surface receptor transmits proliferative signals downstream to Raf and PI3K, which in turn activates the phosphorylation of ERK1/2 and AKT, respectively. This activates both kinases to promote, *e.g.*, proliferation via mTORC1. Plasma treatment is observed to downregulate CD44 and the expression of AKT, leading to the inhibition of cell growth and the activation of apoptosis.

### Effect of RONS on the inhibition of antioxidants

The antioxidative system can form the target of cancer treatment. Indeed, as cancer cells often contain a higher-than-normal concentration of oxidative species<sup>184–186</sup>, they often contain an elevated expression of antioxidants in order to protect them from oxidative damage. One of the antioxidative systems that has been identified is membrane-associated catalase and superoxide dismutase (SOD)<sup>65,190</sup>. Both act as antioxidants able to detoxify  $\text{H}_2\text{O}_2$ , peroxynitrite (ONOOH) and superoxide ( $\text{O}_2^-$ ), formed inside the cells. As these species are precursors of other reactive species, such as OH radicals, the detoxification of these cellular RONS will protect malignant cell from oxidative damage and therefore apoptosis. The inhibition of catalase and/or SOD can therefore be an efficient way of activating apoptosis in cancer cells.

Bauer has suggested that plasma treatment (CAP) is able to overcome this complex antioxidative system and re-activate apoptosis inside the treated cancer cells<sup>191</sup>. Indeed, both membrane-bound catalase and SOD seem to be deactivated by exogenous singlet oxygen. As a result, an accumulation of  $\text{H}_2\text{O}_2$ , peroxynitrite, HOCl (due to the reaction between  $\text{H}_2\text{O}_2$  and  $\text{Cl}^-$  ions) and superoxide is expected, reactivating the RONS signaling inside the cancer cells and causing apoptosis. As this approach requires extracellular singlet oxygen, for the deactivation of catalase and SOD, CAP can be used to obtain selective treatment of cancer cells.

The necessity for sufficient antioxidant levels in fast growing cells (such as cancer) has been demonstrated as well<sup>192</sup>. In this context, glutathione (GSH) forms an important part for the proliferation of these cells<sup>106,193</sup>. Being an antioxidant, it will be attacked by oxidative species and will therefore be consumed during plasma treatment. In this way, cancer cells will lose their protection against oxidative stress, resulting in the activation of apoptotic pathways inside the treated cancer cells. This insight resulted in the strategy to reduce the GSH levels in cancer cells prior to the anti-cancer treatment<sup>192</sup>.

### Effect of RONS on the ERK1/2 and AKT pathways, inhibiting cell growth and inducing apoptosis

Tanaka *et al.* demonstrated the importance of the PI3K/PTEN-AKT pathway during plasma-cancer treatment, and oncology more in general (*cf.* Figure 1-15



above)<sup>93</sup>. In this scheme, the serine-threonine kinase AKT plays a role in cell proliferation as it is involved in the inhibition of apoptosis. The expression of this kinase is activated by phosphatidylinositol-4,5-bisphosphate 3-kinase (PI3K) through phosphorylation and suppressed by phosphatase and tensin homolog (PTEN). Taken together, the PI3K/PTEN-AKT pathway is involved in the regulation of apoptosis and cell survival as illustrated in Figure 1-15 above. However, many cancer cells contain a shift in this balance by either the overexpression of PI3K or the underexpression of PTEN, both inhibiting apoptosis in the cell by activating the pro-proliferative AKT. Tanaka *et al.*, demonstrated that PTM was able to downregulate the expression of AKT, which activated a cascade of caspase-3 and 7, therefore inducing apoptosis<sup>93</sup>. This was later linked to the oxidative stress encountered by CD44, as explained before. Furthermore, the cytotoxic capacity of PTM was only observed in cancer cells, while their healthy counterparts showed no significant changes after treatment. This suggests potential possibilities for the treatment of glioblastoma and other cancer cell that exhibit an overactivation of the PI3K/PTEN-AKT pathway.

This insight was further expanded when investigating the impact of PTM on the protein kinases mTOR (mammalian target of rapamycin)<sup>172</sup>. The attention was directed to two members of this mTOR family: mTOR complex 2 (mTORC2), which activates AKT by phosphorylation (in addition to PI3K), and mTOR complex 1 (mTORC1), which integrates the signals of AKT and ERK 1/2 for cell proliferation (*cf.* Figure 1-15 above). In this investigation, it was observed that PTM downregulated both kinases (*i.e.*, mTORC1 and 2), resulting in an inhibition of cell proliferation of the treated glioblastoma cells and the induction of apoptosis. The activation of apoptosis was further enhanced due to the downregulation of the so-called Raf kinases (*cf.* Figure 1-15), which are found upstream the ERK 1/2 pathway, and therefore activate proliferation through ERK 1/2 via the so-called Raf-MEK-ERK pathway. The downregulation of both the PI3K/PTEN-AKT and Raf-MEK-ERK pathways results in a inhibition of cell proliferation after plasma treatment. This makes both pathways attractive targets for cancer treatment by reducing the threshold for killing cancer cells by apoptosis.

Effect of RONS on activating the tumor necrosis factor (TNF) family, inducing apoptosis

In 2014, Ishaq *et al.* evaluated the changes in gene expression of over 90 different genes after plasma treatment and noticed significant changes in the tumor necrosis factor (TNF, also known as TNF $\alpha$ ) family<sup>38</sup>. It became clear that the presence of RONS activated apoptosis signal-regulating kinase 1 (ASK1), which is part of the mitogen-activated protein kinases (MAPK) involved in stress-induced apoptosis. These stress signals can arise from, among others, oxidative stress, reactive species, genotoxic agents, endoplasmatic reticulum stress and TNF. ASK1 activates downstream kinases (MKK4/MKK7 and MKK3/MKK6) through phosphorylation. The activation of these down-stream kinases results in the propagation of pro-apoptotic signals via JNK and p38 MAPK kinases, respectively, which both activate caspase-3 and 7, leading to apoptosis. This is schematically depicted in Figure 1-16. Ishaq *et al.* showed that CAP treatment effectively increases the expression of ASK1 in melanoma cells (*i.e.*, Mel-RM, Mel-007, and Mel-JD), which was not found in the control human epidermal melanocytes<sup>38</sup>. More interesting is the fact that this ASK1 activation is ROS dependent. It was demonstrated that including the ROS scavenger N-acetyl-L-cysteine (NAC) significantly reduces the expression of ASK1 and apoptosis (*cf.* Figure 1-16). In addition, DNA damage has been observed because an increase in  $\gamma$ H2AX signals was detected (a marker for DNA damage as mentioned above). However, apoptosis was found to be mediated by TNF, as TNF inhibition resulted in a reduced activation of the stress response protein H2AX, even at the presence of DNA damage. This indicates that TNF plays a pivotal role in the observed activity, in the sense that apoptosis was prevented when inhibiting TNF in the treated cells. Although insight is provided in the role of the TNF-ASK1-JNK/p38MAPK pathway, the exact mechanisms in which RONS activate this response are still unknown and requires further investigation.

In 2015, an interesting discovery has been made by Bundscherer *et al.*, which was focussed in the field of wound healing<sup>187</sup>. They investigated the impact of CAP on different MAPK pathways: MEK-ERK (*cf.* Figure 1-15) and both MKK4/MKK7-JNK and MKK3/MKK6-p38MAPK (*cf.* Figure 1-16). While JNK and p38MAPK are both regulating pro-apoptotic responses (via caspase-3 and 7), ERK is active for pro-

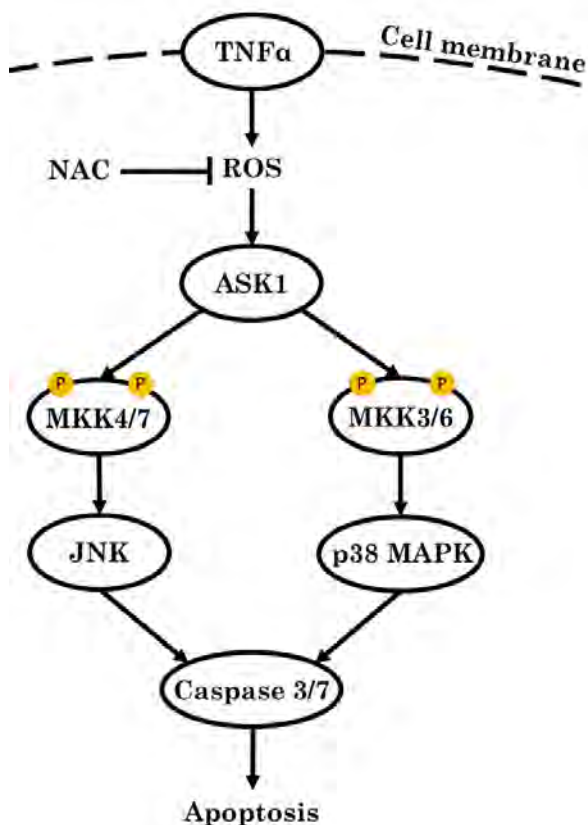


**Figure 1-16. Schematic representation of the pro-apoptotic signaling induced by TNF.** Tumor necrosis factors (TNF, or TNF $\alpha$ ) transmit pro-apoptotic signals downstream to ASK1, which in turn activates the phosphorylation of MKK4/MKK7 and MKK3/MKK6 (indicated by yellow “P”). Upon phosphorylation, these kinases are activated, inducing the activation of caspase-3/7 via JNK and p38 MAPK, respectively. ROS are observed to increase the expression of ASK1, leading to the activation of apoptosis. This was inhibited when using ROS scavenger NAC.

proliferation signals, as already explained above (*cf.* Figure 1-15). Interesting was the fact that the pro-proliferative responses were activated even after short CAP treatment times, by H<sub>2</sub>O<sub>2</sub>, while longer treatment times were required for the activation of JNK 1/2. This might explain why, in plasma medicine, typically proliferation is observed at short treatment times, while apoptosis is activated after longer timescales<sup>194</sup>. This observation, furthermore, highlights the importance of the mentioned MAPK pathways during plasma treatment.

### Effect of ROS on the activation of antioxidants

Although the focus of the above discussion was mainly set on MAPK pathways, the response of cells to plasma treatment is not only governed by the balance of the mentioned pro-apoptotic and pro-proliferative responses. Schmidt *et al.* evaluated the expression of antioxidative response signals during and after plasma treatment and noticed changes in the expression of nuclear factor erythroid-related factor 2 (NRF2)<sup>195</sup>, which activates rescue pathways against oxidative injury and apoptosis<sup>184</sup>. NRF2 is known to regulate genes that encode detoxifying enzymes and antioxidants (*e.g.*, catalase, glutathione (GSH), cytochrome c, superoxide dismutase 1-3 (SOD1-3), heme oxygenase 1 (HMOX1) and NAD(P)H dehydrogenase 1 (NQO1)) as an act against imbalances in the cellular redox homeostasis. This is explained in Figure 1-17. In its passive form, NRF2 is retained in the cellular cytosol by KEAP1 (Kelch-like ECH-associated protein 1). In the presence of oxidizing species, such as ROS, the cysteine residues of KEAP1 are oxidized, which releases NRF2. Upon release,

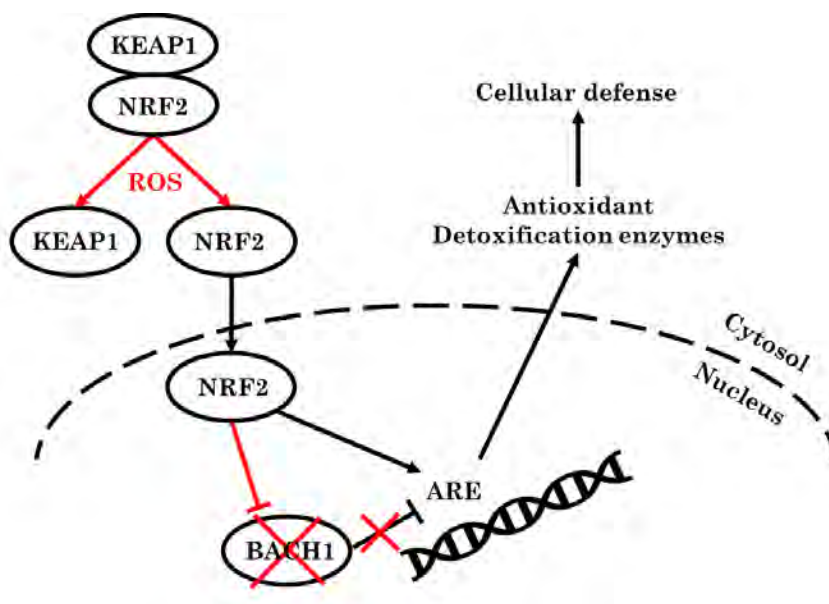


**Figure 1-17. Schematic representation of the activation of NRF2 in the presence of ROS.** Due to the oxidation of KEAP1, NRF2 is able to migrate to the nucleus where it activates the expression of antioxidant response elements (ARE), which are otherwise blocked by BACH1. Antioxidative molecules are expressed to defend against oxidative species. Examples of such molecules are catalase, HMOX1, GSH, cytochrome c and SOD1-3, as explained in the text.

NRF2 migrates to the nucleus and activates the transcription of antioxidant response elements (ARE) (*cf.* Figure 1-17). During basal conditions, this transcription is blocked by NRF2's antagonist, BACH 1 (a transcription regulator protein) which blocks the transcription of ARE. Schmidt observed that CAP treatment resulted in an up-regulation of NRF2 inside the treated cells, coupled with a down-regulation of BACH1<sup>195</sup>. This led to a time-dependent increase in ARE expressions, such as catalase, glutathione, HMOX1 and NQO1. Furthermore, an upregulation of heat shock proteins was encountered as well, suggesting that also thermal and/or chemical stress is induced inside the cell after CAP treatment.

#### Cellular ions contribute to the anti cancer activity of plasma treatment

Work performed in the group of Hara *et al.* shed new light on the anti-cancer capacity of PTM, and of plasmas more in general<sup>196,197</sup>. Using neuroblastoma cells (SH-SY5Y), they evaluated the role of  $Zn^{2+}$  in the observed cell death. The focus was on these ions, as  $Zn^{2+}$  is known to provoke cell death during mitochondrial dysfunction and because the treated neuroblastoma cells contain a higher-than-normal concentration of  $Zn^{2+}$ . It was shown that PTM treatment resulted in a release of  $Zn^{2+}$  in the SH-SY5Y cells which triggered cell death. In addition to the rise in  $Zn^{2+}$  levels, an upregulation of PARP1 (Poly[ADP-ribose] polymerase 1), which acts as a recovery protein for DNA single strand breaks, was observed. PARP1 is often overexpressed in cancer cells due to the inaccurate repair of DNA, leading to mutations and the development of cancer. The activation of PARP1 leads to a depletion of  $NAD^+$  inside by inhibiting hexokinases, which triggers apoptosis. Hexokinases are involved in the activation of glycolysis, which is required to the production of  $NAD^+$ <sup>198</sup>. Although this is no problem for healthy cells (*i.e.*, fibroblasts in the work of Hara *et al.*<sup>197</sup>), it is harmful for cancerous cells due to the Warburg effect<sup>161</sup>. Indeed, many cancer cells rely on glycolysis for energy (production of ATP), which depend on the concentration of free  $NAD^+$  in the cell, while healthy cells mainly depend on oxidative phosphorylation. Therefore, the consumption of  $NAD^+$  by the activation of PARP1 competes with the production of energy of cancer cells leading to energy failure and subsequent cell death. These observations are schematically depicted in Figure 1-18. A similar conclusion was made by Adachi *et al.*<sup>37</sup> who induced DNA damage by plasma treatment. In their work, DNA damage

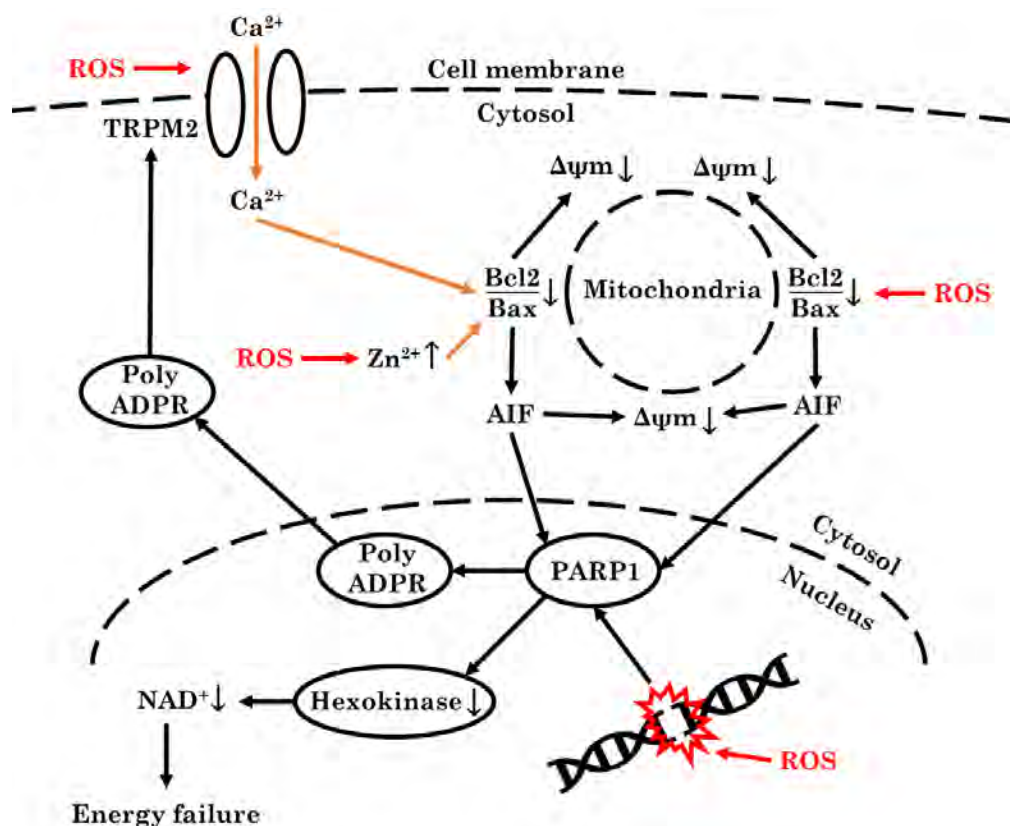


**Figure 1-18.** ROS such as  $\text{H}_2\text{O}_2$ , OH and peroxides (depicted in red) disturb the mitochondrial–nuclear network in various ways. (i) They reduce the mitochondrial membrane potential ( $\Delta\psi_m$ ) leading to mitochondrial dysfunction which activates apoptosis. (ii) They decrease the expression ratio of Bcl2/Bax, which increases the expression of apoptotic induction factors (AIF). This activates PARP1, depleting  $\text{NAD}^+$  and ATP. The consumption of ATP, in turn, leads to energy failure in cancer cells which rely on aerobic glycolysis. The accumulation of PARP1 also results in the generation of ADPR, inducing the activation of TRPM2. This results in a subsequent extracellular  $\text{Ca}^{2+}$  influx and  $\text{Ca}^{2+}$  release from intracellular stores (depicted in orange). (iii) They increase the release of  $\text{Zn}^{2+}$  from intracellular stores (depicted in orange) which leads to mitochondrial dysfunction and as a consequence, apoptosis. (iv) They yield DNA damage which activates PARP1 as a recovery protein.

resulted in the expression of PARP1, which depleted the concentration of  $\text{NAD}^+$  and ATP, leading to energy failure and cell death in lung cancer cells (A549). Moreover, plasma treatment leads to mitochondrial dysfunction (due to reduction of the mitochondrial membrane potential:  $\Delta\psi_m$ ) and the downregulation of the anti-

apoptotic Bcl2, which is located at the outer mitochondrial membrane and which conserves the integrity of this membrane<sup>134,199</sup>. This is also presented in Figure 1-18.

Another ion that plays an important role in the regulation of apoptosis is  $\text{Ca}^{2+}$ . The uptake of  $\text{Ca}^{2+}$  by the cell is regulated by the cation channel TRPM2 (transient receptor potential cation channel, subfamily M, member 2) found in the cell membrane. TRPM2 is triggered by stress signals originating from the cell or by oxidative stress. Adachi *et al.* observed that RONS, generated by plasma treatment, induce mitochondrial injury within A549 cells<sup>37</sup>. Similar as in the work presented by Hara *et al.*, downregulation of Bcl2 was observed, found on the mitochondrial membrane. Interesting is the fact that the antagonist of Bcl2, *i.e.*, Bax, was not upregulated. Like Bcl2, Bax is also found on the mitochondrial membrane and acts by disrupting the integrity of the membrane for the release of the pro-apoptotic signals via cytochrome c. The downregulation of Bcl2 typically results in the release of apoptotic inducing factors (AIF) and activates PARP1<sup>37,200</sup> (*cf.* Figure 1-18).

The fact that Bcl2 and AIF expressions are affected by plasma was confirmed in other studies as well<sup>38,87,173</sup>. The activation of PARP1 resulted in an increase in the expression of polyADP-ribose, depleting  $\text{NAD}^+$  in the affected cells, as also observed during the treatment of A549 cells. Cell injury was further confirmed by the increase in CHOP expression. CHOP are apoptosis regulator proteins which are activated during endoplasmatic reticulum stress, indicating that plasma treatment resulted in stress at both the mitochondria and the nucleus. The increase in polyADP-ribose (polyADPR) levels is translated to the activation of TRPM2 and the subsequent increase in  $\text{Ca}^{2+}$  levels in the cytosol, leading to a further increase in AIF and mitochondrial injury, which induces apoptosis in a caspase-independent fashion (*cf.* Figure 1-18). Indeed, when treating A549 with PTM, Adachi and co-authors did not observe changes in the expression of caspase-3 or 7. Their work suggests that  $\text{H}_2\text{O}_2$  and other RONS are able to inflict mitochondrial injury by decreasing the ratio of Bcl2/Bax, increasing the release of AIF, activating PARP1 and depleting  $\text{NAD}^+$ . This stress network, together with  $\text{H}_2\text{O}_2$ , is able to activate TRPM2 and consequently the uptake of  $\text{Ca}^{2+}$  ions, leading to apoptosis (*cf.* Figure 1-18).

This activity, however, was attenuated by the presence of catalase (a  $\text{H}_2\text{O}_2$  scavenger) in PTM, indicating that  $\text{H}_2\text{O}_2$  indeed plays a crucial role in this pro-

apoptotic mechanism. The exact role of RONS in the downregulation of Bcl2 remains unclear. However, Park *et al.* suggested that ROS affect the methylation status of DNA, affecting the expression of Bcl2 in the cell<sup>34</sup>. The fact that plasma treatment is able to downregulate the expression of Bcl2 creates a new strategy for the treatment of cancer cells suffering from an overexpression of Bcl2, to restore the cell-death responses in the presence of DNA damage<sup>146,201</sup>.

Although not observed in the treatment of A549 lung cancer cells, plasma treatment can induce changes in the expression of the pro-apoptotic Bax as well<sup>38</sup>. Panngom *et al.* investigated the expression of apoptosis in six different cancerous tissues<sup>202</sup> and observed a clear increase in Bax expression after plasma treatment. Additionally, slight increases in caspase-8 expressions were observed as well. Both the expression of Bax and caspase-8 was found to be cell line-dependent. It became indeed clear that the expression of apoptotic factors and mitochondrial vulnerability to plasma treatment greatly depends on the cancer cell line.

#### Effect of RONS on other cell components

It should be noted that other cellular components are affected by the plasma treatment as well and the above sections only discuss several important effects. Multiple studies have demonstrated that a wide range of cellular components are affected by plasma treatment, which can potentially contribute to the observed impact on the cell functionality<sup>38,70,195,203,204</sup>. An important example is p53 which serves as a tumor suppressor, by scanning DNA for inconsistencies and triggering multiple downstream responses, such as DNA repair, cell cycle arrest and even apoptosis<sup>205</sup>. However, around 50% of the cancerous tissues express mutated p53, so these tumor suppressors are attractive candidates for cancer treatment<sup>206</sup>. This is also true for plasma treatment, as p53-mutated cells are expected to contain higher-than-normal ROS levels. Indeed, it has been indicated that plasma treatment demonstrates high selectivity towards p53-mutated or deficient cancer cells<sup>207</sup>.

#### *Biological responses over longer distances*

Next to the direct effect of reactive species to the cellular biology, recent plasma-medicine research is dedicated to other targets in their quest to treat cancer. Among these are the use of low concentrations of RONS to impose noticeable stresses



on the cells found in the treated area in order to activate the immune system. This way, the malignant cells will become visible by the immune cells, triggering an immune response throughout the whole body. This is expected to lead to a so-called ‘vaccination effect’ of the plasma treatment<sup>54</sup>.

Besides the increase in immune responses, biological responses to the treatment are observed over longer distances and depths, and over larger timescales<sup>25,155,157,208,209</sup>. This is interesting given the fact that RONS often have a short lifetime, and the plasma acts on the surface of the treated tissues. An explanation for this observation is the fact that these reactive species trigger biological responses or changes in the adjacent cells that can occur at longer timescales<sup>38,54,56</sup>. Various examples have been given in the discussion above. Furthermore, Graves *et al.* points towards the production of long-lived oxidized biomolecules, similar to the ones found in PTM, which are able to penetrate deeper in the treated tissues and translate stress signals to neighboring cells. This in turn stimulates and affects cell-to-cell communication, and it might also enhance the immune system<sup>54,210,211</sup>. These longer timescale events and responses build up as a result of the initial interactions between the plasma-generated species and the treated area of the tissue. The presence of these species leads to a distortion of the local redox-balance, triggering the oxidation of biochemically important molecules (lipids, proteins, sugars, *etc.*) which, in turn, can change the biological functions of the affected cells and their microenvironment (*e.g.*, membrane pore formation, protein inactivation, stimulation of apoptosis, *etc.*)<sup>20,34,58,77,117,212,213</sup>.

## 1-2.4 Aim of this PhD work

Knowledge on the initial interactions (which start this cascade of biological signaling in the treated tissues), as well as the resulting effects of plasma treatment, are crucial in order to better understand the biological responses towards the treatment. Moreover, insight in the impact of plasma treatment on cellular components (*e.g.*, signaling pathways) can prove to be essential in better understanding and controlling the anti-tumor activity of plasma treatment.

The focus of this PhD thesis was to obtain better insight in the mentioned initial interactions between RONS and the biological material. In this context, the interactions were investigated at the molecular scale using computational methods.

Four systems were considered: sugars, DNA, proteins and water (**chapters 3, 4, 5** and **6**, respectively), where the interactions were investigated using molecular dynamic (MD) simulations. These simulations provide atomic-scale insight in the behavior of the systems of interest. A detailed introduction on the used MD methods will be provided in **chapter 2**. In addition, the generation and accumulation of biologically relevant RONS in water, during plasma treatment, was investigated using a fluid dynamics model that was developed in this work. The model is based on the treatment of water with a kINPen in order to obtain knowledge on the generation of PTL. The details of the model and the results will be discussed in **chapter 7**.



## 1-3 Appendix-1

**Table 1-A. Summary of publication (up to 2017) focusing on the use of PTM as an alternative for plasma cancer therapy.**

Year	Authors	Cell line	Major observations	Ref.
2011	Sato <i>et al.</i>	Cervical cancer (HeLa)	Comparison of the activity of PTM on HeLa cells with the treatment of H <sub>2</sub> O <sub>2</sub> . Comparable inactivation was encountered, which can be inhibited with catalase.	214
2011	Kalghatgi <i>et al.</i>	Mammalian breast cells (MCG10A)	Treatment of cell medium results in the generation of oxidized biomolecules (amino acids hydroperoxides) inducing DNA damage.	46
2011	Chan <i>et al.</i>	Prostate cancer (LNCaP, PC-3 and C4-2)	Effect of extracellular H <sub>2</sub> O <sub>2</sub> on cells. mtDNA damage observed in both cancer and healthy cells. However, cytotoxicity is cell dependent.	215
2012	Vandamme <i>et al.</i>	Glioblastoma (U87) and colorectal cancer (HCT116)	PTM induces cell death <i>in vitro</i> . The cell cycle arrest is promoted, resulting in a reduction of tumor growth.	157
2012	Hoentsch <i>et al.</i>	Epithelial cells (mHepR1)	PTM inhibits the attachment of cells and affects the tight junction protein ZO-1 in a treatment-time dependent manner.	216
2011/ 2012	Tanaka <i>et al.</i>	Glioblastoma (U251SP)	PTM successfully kills cancer cells compared to their healthy counterparts. CD44, AKT and ERK signaling pathways downregulated by PTM	93,172
2014	Yan <i>et al.</i>	Glioblastoma (U87)	Effect of fetal bovine serum (FBS) and temperature on the anti-tumor activity of PTM. FBS and cold temperatures reduces the anti-tumor rate of PTM.	94
2013/ 2014	Utsumi <i>et al.</i>	Ovarian carcinoma (NOS2, TOV21G, ES-2, SKOV3)	Anti-tumor effect of PTM both <i>in vitro</i> and <i>in vivo</i> . Results suggest that ROS hold the key to the anti-tumor effect. Healthy cells are left unharmed after treatment	217,218

2014	Hoentsch <i>et al.</i>	Epithelial cells (mHepR1)	Use of PTM after one week storage to treat cancerous cells. Anti-cancer activity of PTM is successfully stored. Concentration of H <sub>2</sub> O <sub>2</sub> decreases quickly, supporting the hypothesis that organic peroxides are responsible for the activity of PTM.	219
2014	Torii <i>et al.</i>	Gastric cancer (NUGC4, SC-2-NU, MKN28 en MKN45)	PTM is able to induce apoptosis in the studied cancer cells due to ROS uptake.	220
2014/ 2015	Mohades <i>et al.</i>	Human bladder cancer (SCaBER)	The anti-tumor effect of PTM is most pronounced after longer plasma treatments and is H <sub>2</sub> O <sub>2</sub> dependent. Increase in Caspase-3 activity.	221,222
2015	Yan <i>et al.</i>	Glioblastoma (U87), breast cancer (MDA-MB-231 and MCF-7)	Evaluation of different treatment conditions on production of PTM. Larger well, smaller gap and smaller volume enhance anti-tumor activity of PTM. H <sub>2</sub> O <sub>2</sub> is expected to play a major role.	92
2015	Adachi <i>et al.</i>	Lung cancer (A549), liver carcinoma (HepG2) and breast cancer (MCF-7)	Stability of PTM for storage	37
2015/ 2017	Hara <i>et al.</i>	Neuroblastoma (SH-SY5Y)	PTM activates cell death through the release of Zn <sup>2+</sup> ions. Differences in Zn <sup>2+</sup> levels have an impact on the efficiency of PTM.	196,197
2016	Vermeylen <i>et al.</i>	Melanoma (Malm-M3, SK-MEL-28) and glioblastoma (LN229, U87)	Treatment with PTM induces apoptosis in cancer cells. The activity is dependent on the treated cells and used plasma conditions.	223
2016	Yan <i>et al.</i>	Glioblastoma (U87)	Enriching PTM with lysine enhances anti-cancer activity without changing the generation of H <sub>2</sub> O <sub>2</sub> .	111
2016	Boehm <i>et al.</i>	Cervical cancer (HeLa)	Effect of environment on the cytotoxic effect of PTM.	105

2016	Judée <i>et al.</i>	Colorectal cancer (HCT116)	PTM treatment of tumor spheroids indicates a time-dependent shrinkage of the tumor and the protection of DNA damage by catalase	224
2016	Kurake <i>et al.</i>	Glioblastoma (U251SP)	Effect of H <sub>2</sub> O <sub>2</sub> and NO <sub>2</sub> <sup>-</sup> on cancer cells. The anti-tumor effect of H <sub>2</sub> O <sub>2</sub> is synergistically enhanced by the presence of NO <sub>2</sub> <sup>-</sup> . Other effects appear to play a role.	225
2016	Adachi <i>et al.</i>	Lung cancer (A549)	Combining PTM with histone deacetylase enhances cell death during treatment. PTM treatment is further enhanced when the concentration of intercellular Fe(II) is elevated	159,226
2016	Tanaka <i>et al.</i>	Glioblastoma (U251SP)	Produced plasma activated lactate solution for the treatment of glioblastoma. Production of acetyl and pyruvic acid-like groups in PTL resulted in significant anti-tumor activity. Specific functional groups can be used for cancer treatment.	227
2016/ 2017	Mohades <i>et al.</i>	Human bladder cancer (SCaBER)	PTM efficiency is correlated to the concentration of H <sub>2</sub> O <sub>2</sub> and is temporal. Long exposures to PTM results in cell death even for healthy cells. Overall decrease in average cell migration.	113,228
2017	Duan <i>et al.</i>	Liver cancer (HepG2)	PTM treatment of co-culture of malignant and healthy cells. Selectively induces apoptosis in the cancer cells. H <sub>2</sub> O <sub>2</sub> and NO play the key roles in the anti-tumor activity	229
2017	Yan <i>et al.</i>	Glioblastoma (U87)	Aquaporins play a crucial role in the anti-tumor activity of PTM. H <sub>2</sub> O <sub>2</sub> is suggested as key species.	169
2017	Takeda <i>et al.</i>	Gastric cancer (SC-2-NU, AGS and GCIY-EGFP)	Shorter treatment gaps and smaller volumes increase the efficiency of PTM. Reduction in the formation of metastatic nodules in mice.	114

2017	Canal <i>et al.</i>	Bone cancer (SaOS-2)	PTM shows selective treatment towards cancer cells (no damage on stem cells or healthy cells). Role of RONS is crucial	230
------	---------------------	----------------------	--	-----

## 1-4 References

1. Thompson, J. J. XL. Cathode Rays. *Philos. Mag. Ser. 5* **44**, 293–316 (1879).
2. Langmuir, I. Oscillations in ionized gases. *Proc. Natl. Acad. Sci.* **14**, 627–637 (1928).
3. Fridman, A. *Plasma Chemistry*. (Camebridge University Press, 2008).
4. Robert, J. & Rutherford, P. H. *Introduction to Plasma Physics*. (IOP Publishing Ltd, 1995).
5. Bogaerts, A., Neyts, E., Gijbels, R. & Van Der Mullen, J. Gas discharge plasmas and their applications. **57**, 609–658 (2002).
6. Tendero, C., Tixier, C., Tristant, P., Desmaison, J. & Leprince, P. Atmospheric pressure plasmas: a review. *Spectchim. Acta B* **61**, 2–30 (2006).
7. Bárdos, L. & Baránková, H. Cold atmospheric plasma: Sources, processes, and applications. *Thin Solid Films* **518**, 6705–6713 (2010).
8. Fridman, G. *et al.* Applied Plasma Medicine. *Plasma Process. Polym.* **5**, 503–533 (2008).
9. von Woedtke, T., Reuter, S., Masur, K. & Weltmann, K.-D. Plasmas for medicine. *Phys. Rep.* **530**, 291–320 (2013).
10. Kong, M. G. *et al.* Plasma medicine: an introductory review. *New J. Phys.* **11**, 115012 (2009).
11. Nehra, V., Kumar, A. & Dwivedi, H. Atmospheric non-thermal plasma sources. *Int. J. Eng.* **2**, 53–68 (2008).
12. Desmet, T. *et al.* Nonthermal plasma technology as a versatile strategy for polymeric biomaterials surface modification: a review. *Biomacromolecules* **10**, 2351–78 (2009).
13. Arjunan, K., Sharma, V. & Ptasinska, S. Effects of Atmospheric Pressure Plasmas on Isolated and Cellular DNA—a Review. *Int. J. Mol. Sci.* **16**, 2971–3016 (2015).
14. Bartis, E. A. J., Knoll, A. J., Luan, P. & Seog, J. On the Interaction of Cold Atmospheric Pressure Plasma with Surfaces of Bio-molecules and Model Polymers. *Plasma Chem. Plasma Process.* **36**, 121–149 (2016).
15. Laroussi, M., Mohades, S. & Barekzi, N. Killing adherent and nonadherent cancer cells with the plasma pencil. *Biointerphases* **10**, 2940 (2015).



16. van Gils, C. A. J., Hofmann, S., Boekema, B. K. H. L., Brandenburg, R. & Bruggeman, P. J. Mechanisms of bacterial inactivation in the liquid phase induced by a remote RF cold atmospheric pressure plasma jet. *J. Phys. D. Appl. Phys.* **46**, 175203 (2013).
17. Cabiscol, E., Tamarit, J. & Ros, J. Oxidative stress in bacteria and protein damage by reactive oxygen species. *Int. Microbiol.* **3**, 3–8 (2000).
18. Attri, P. *et al.* Effects of atmospheric-pressure non-thermal plasma jets on enzyme solutions. *J. Korean Phys. Soc.* **60**, 959–964 (2012).
19. Attri, P. *et al.* Influence of reactive species on the modification of biomolecules generated from the soft plasma. *Sci. Rep.* **5**, 8221 (2015).
20. Khosravian, N., Kamaraj, B., Neyts, E. C. & Bogaerts, A. Structural modification of P-glycoprotein induced by OH radicals: insights from atomistic simulations. *Sci. Rep.* **6**, 19466 (2016).
21. Takai, E. *et al.* Chemical modification of amino acids by atmospheric-pressure cold plasma in aqueous solution. *J. Phys. D. Appl. Phys.* **47**, 285403 (2014).
22. Tian, W. & Kushner, M. J. Atmospheric pressure dielectric barrier discharges interacting with liquid covered tissue. *J. Phys. D. Appl. Phys.* **47**, 165201 (2014).
23. Bruggeman, P. & Leys, C. Non-thermal plasmas in and in contact with liquids. *J. Phys. D. Appl. Phys.* **42**, 1–28 (2009).
24. Lindsay, A., Anderson, C., Slikboer, E., Shannon, S. & Graves, D. Momentum, heat, and neutral mass transport in convective atmospheric pressure plasma-liquid systems and implications for aqueous targets. *J. Phys. D. Appl. Phys.* **48**, 424007 (2015).
25. Gaur, N. *et al.* Combined effect of protein and oxygen on reactive oxygen and nitrogen species in the plasma treatment of tissue. *Appl. Phys. Lett.* **107**, 103703 (2015).
26. Kong, M. G., Keidar, M. & Ostrikov, K. Plasmas meet nanoparticles—where synergies can advance the frontier of medicine. *J. Phys. D. Appl. Phys.* **44**, 174018 (2011).
27. Wagner, H., Brandenburg, R., Kozlov, K. V., Sonnenfeld, A. & Michel, P. The barrier discharge: basic properties and applications to surface treatment. **71**, 417–436 (2003).
28. Lu, X., Laroussi, M. & Puech, V. On atmospheric-pressure non-equilibrium plasma jets and plasma bullets. *Plasma Sources Sci. Technol.* **21**, 34005 (2012).

29. Golda, J. *et al.* Concepts and characteristics of the ‘COST Reference Microplasma Jet’. *J. Phys. D. Appl. Phys.* **49**, 84003 (2016).
30. Weltmann, K. D. *et al.* Atmospheric-pressure plasma sources: prospective tools for plasma medicine. *Pure Appl. Chem.* **82**, 1223–1237 (2010).
31. Oehmigen, K. *et al.* Estimation of Possible Mechanisms of Escherichia coli Inactivation by Plasma Treated Sodium Chloride Solution. *Plasma Process. Polym.* **8**, 904–913 (2011).
32. Winter, J., Brandenburg, R. & Weltmann, K. Atmospheric pressure plasma jets: an overview of devices and new directions. *Plasma Sources Sci. Technol.* **24**, 64001 (2015).
33. Lim, S. O. *et al.* Epigenetic Changes Induced by Reactive Oxygen Species in Hepatocellular Carcinoma: Methylation of the E-cadherin Promoter. *Gastroenterology* **135**, 2128–2140 (2008).
34. Park, S. *et al.* Differential Epigenetic Effects of Atmospheric Cold Plasma on MCF-7 and MDA-MB-231 Breast Cancer Cells. *PLoS One* **10**, 1–16 (2015).
35. Keidar, M. Plasma for cancer treatment. *Plasma Sources Sci. Technol.* **24**, 33001 (2015).
36. Kisch, T. *et al.* Improvement of cutaneous microcirculation by cold atmospheric plasma (CAP): results of a controlled, prospective cohort study. *Microvasc. Res.* **104**, 55–62 (2016).
37. Adachi, T., Tanaka, H., Nonomura, S., Hara, H. & Kondo, S. Plasma-activated medium induces A549 cell injury via a spiral apoptotic cascade involving the mitochondrial – nuclear network. *Free Radic. Biol. Med.* **79**, 28–44 (2015).
38. Ishaq, M., Evans, M. M. & Ostrikov, K. K. Effect of atmospheric gas plasmas on cancer cell signaling. *Int. J. Cancer* **134**, 1517–28 (2014).
39. Ishaq, M., Han, Z. J., Kumar, S., Evans, M. D. M. & Ostrikov, K. K. Atmospheric-Pressure Plasma- and TRAIL-Induced Apoptosis in TRAIL-Resistant Colorectal Cancer Cells. *Plasma Process. Polym.* **12**, 574–582 (2015).
40. Kaushik, N. K. *et al.* Cytotoxic macrophage-released tumour necrosis factor-alpha (TNF- $\alpha$ ) as a killing mechanism for cancer cell death after cold plasma activation. *J. Phys. D. Appl. Phys.* **49**, 84001 (2016).
41. Collet, G. *et al.* Plasma jet-induced tissue oxygenation: potentialities for new therapeutic strategies. *Plasma Sources Sci. Technol.* **23**, 12005 (2014).

42. Kim, S. J. & Chung, T. H. Plasma effects on the generation of reactive oxygen and nitrogen species in cancer cells in-vitro exposed by atmospheric pressure pulsed plasma jets. *Appl. Phys. Lett.* **107**, 63702 (2015).
43. Graves, D. B. Reactive Species from Cold Atmospheric Plasma: Implications for Cancer Therapy. *Plasma Process. Polym.* **11**, 1120–1127 (2014).
44. Kogelschatz, U. Dielectric-barrier Discharges: their History, Discharge Physics, and Industrial Applications. *Plasma Chem. Plasma Process.* **23**, 1–46 (2003).
45. Weltmann, K. *et al.* Plasma Processes and Plasma Sources in Medicine. *Contrib. to Plasma Phys.* **654**, 644–654 (2012).
46. Kalghatgi, S. *et al.* Effects of non-thermal plasma on mammalian cells. *PLoS One* **6**, e16270 (2011).
47. Schlegel, J., Köritzer, J. & Boxhammer, V. Plasma in cancer treatment. *Clin. Plasma Med.* **1**, 2–7 (2013).
48. Kramer, A. *et al.* Suitability of tissue tolerable plasmas (TTP) for the management of chronic wounds. *Clin. Plasma Med.* **1**, 11–18 (2013).
49. Isbary, G. *et al.* A first prospective randomized controlled trial to decrease bacterial load using cold atmospheric argon plasma on chronic wounds in patients. *Br. J. Dermatol.* **163**, 78–82 (2010).
50. Fridman, G. *et al.* Blood Coagulation and Living Tissue Sterilization by Floating-Electrode Dielectric Barrier Discharge in Air. *Plasma Chem. Plasma Process.* **26**, 425–442 (2006).
51. Emmert, S. *et al.* Atmospheric pressure plasma in dermatology: ulcer treatment and much more. *Clin. Plasma Med.* **1**, 24–29 (2013).
52. Boekema, B. K. H. L., Hofmann, S., van Ham, B. J. T., Bruggeman, P. J. & Middelkoop, E. Antibacterial plasma at safe levels for skin cells. *J. Phys. D. Appl. Phys.* **46**, 422001 (2013).
53. Kuo, S. P., Chen, C.-Y., Lin, C.-S. & Chiang, S.-H. Wound Bleeding Control by Low Temperature Air Plasma. *IEEE Trans. PLASMA Sci.* **38**, 1908–1914 (2010).
54. Miller, V., Lin, A. & Fridman, A. Why Target Immune Cells for Plasma Treatment of Cancer. *Plasma Chem. Plasma Process.* **36**, 259–268 (2016).
55. Ye, F. *et al.* Plasma-activated medium suppresses choroidal neovascularization in mice: a new therapeutic concept for age-related macular degeneration. *Sci. Rep.* **5**, 1–7 (2014).

56. Lu, X. & Reuter, S. Reactive species in non-equilibrium atmospheric-pressure plasmas: generation, transport, and biological effects. *Phys. Rep.* **630**, 1–84 (2016).
57. Dizdaroglu, M. & Jaruga, P. Mechanisms of Free Radical-Induced Damage to DNA. *Free Radic. Res.* **46**, 382–419 (2012).
58. Lackmann, J.-W. *et al.* A dielectric barrier discharge terminally inactivates RNase A by oxidizing sulfur-containing amino acids and breaking structural disulfide bonds. *J. Phys. D. Appl. Phys.* **48**, 494003 (2015).
59. Szili, E. J. *et al.* The hormesis effect of plasma-elevated intracellular ROS on HaCaT cells. *J. Phys. D. Appl. Phys.* **48**, 495401 (2015).
60. Hefny, M. M., Pattyn, C., Lukes, P. & Benedikt, J. Atmospheric Plasma Generates Oxygen Atoms as Oxidizing Species in Aqueous Solutions. *J. Phys. D. Appl. Phys.* **49**, 404002 (2016).
61. Riethmüller, M., Burger, N. & Bauer, G. Redox biology singlet oxygen treatment of tumor cells triggers extracellular singlet oxygen generation, catalase inactivation and reactivation of intercellular apoptosis-inducing signaling. *Redox Biol.* **6**, 157–168 (2015).
62. Grosse-Kreul, S. *et al.* Mass spectrometry of atmospheric pressure plasmas. *Plasma Sources Sci. Technol.* **24**, 44008 (2015).
63. Schneider, S. *et al.* Summarizing results on the performance of a selective set of atmospheric plasma jets for separation of photons and reactive particles. *J. Phys. D. Appl. Phys.* **48**, 444001 (2015).
64. Schmidt-Bleker, A., Winter, J., Bösel, A., Reuter, S. & Weltmann, K.-D. On the Plasma Chemistry of a Cold Atmospheric Argon Plasma Jet with Shielding Gas Device. *Plasma Sources Sci. Technol.* **25**, 15005 (2016).
65. Bauer, G. Increasing the endogenous NO level causes catalase inactivation and reactivation of intercellular apoptosis signaling specifically in tumor cells. *Redox Biol.* **6**, 353–371 (2015).
66. Childress, B. B. & Stechmiller, J. K. Role of Nitric Oxide in Wound Healing. *Biol. Res. Nurs.* **4**, 5–15 (2002).
67. Sen, C. K. & Roy, S. Redox signals in wound healing. *Biochim. Biophys. Acta* **1780**, 1348–1361 (2008).
68. Marengo, B. *et al.* Redox Homeostasis and Cellular Antioxidant Systems: Crucial Players in Cancer Growth and Therapy. *Oxid. Med. Cell. Longev.* **2016**, 16 (2016).

69. Graves, D. B. The emerging role of reactive oxygen and nitrogen species in redox biology and some implications for plasma applications. *J. Phys. D. Appl. Phys.* **45**, 263001 (2012).
70. Sauer, H., Wartenberg, M. & Hescheler, J. Cellular Physiology and Biochemistry Reactive Oxygen Species as Intracellular Messengers During Cell Growth and Differentiation. *Cell. Physiol. Biochem.* **11**, 173–186 (2001).
71. MacMicking, J., Xie, Q. W. & Nathan, C. Nitric oxide and macrophage function. *Annu. Rev. Immunol.* **15**, 323–350 (1997).
72. Nathan, C. F. Secretory Products of Macrophages. *J. Clin. Investig.* **79**, 319–326 (1987).
73. Luo, J. & Chen, A. F. Invited review nitric oxide: a newly discovered function on wound healing. *Acta Pharmacol. Sin.* **26**, 259–264 (2005).
74. Cook, J. A. *et al.* Oxidative Stress, Redox, and the Tumor Microenvironment. *Semin. Radiat. Oncol.* **14**, 259–266 (2004).
75. Mander, P. K., Jekabsone, A. & Brown, G. C. Microglia Proliferation Is Regulated by Hydrogen Peroxide from NADPH Oxidase. *J. Immunol.* **176**, 1046–1052 (2006).
76. Babaeva, N. Y. & Kushner, M. J. Intracellular electric fields produced by dielectric barrier discharge treatment of skin. *J. Phys. D. Appl. Phys.* **43**, 185206 (2010).
77. Van der Paal, J., Neyts, E. C., Verlackt, C. & Bogaerts, A. Effect of lipid peroxidation on membrane permeability of cancer and normal cells subjected to oxidative stress. *Chem. Sci.* **7**, 489 (2016).
78. Yusupov, M., Van der Paal, J., Neyts, E. C. & Bogaerts, A. Synergistic effect of electric field and lipid oxidation on the permeability of cell membranes. *Biochim. Biophys. Acta* **1861**, 839–847 (2017).
79. Lackmann, J. & Schneider, S. Characterization of Damage to Bacteria and Bio-macromolecules Caused by (V)UV Radiation and Particles Generated by a Microscale Atmospheric Pressure Plasma Jet. *Plasma Bio-Decontamination, Med. Food Secur.* (Springer Netherlands, 2011).
80. Folkard, M., Prise, K. M., Turner, C. J. & Michael, B. D. The Production of Single Strand and Double Strand Breaks in DNA in Aqueous Solution by Vacuum UV Photons Below 10 eV. *Radiat. Prot. Dosimetry* **99**, 147–149 (2002).
81. Ehlbeck, J. *et al.* Low temperature atmospheric pressure plasma sources for microbial decontamination. *J. Phys. D. Appl. Phys.* **44**, 13002 (2011).

82. Schneider, S. Separation of VUV/UV photons and reactive particles in the effluent of a He/O<sub>2</sub> atmospheric pressure plasma jet. *J. Phys. D. Appl. Phys.* **44**, 295201 (2011).
83. Weltmann, K. *et al.* Atmospheric Pressure Plasma Jet for Medical Therapy: Plasma Parameters and Risk Estimation. *Contrib. to Plasma Phys.* **49**, 631–640 (2009).
84. Bekeschus, S., Schmidt, A. & von Woedtke, T. The Plasma Jet kINPen—A Powerful Tool for Wound Healing Sander. *Clin. Plasma Med.* **4**, 19–28 (2016).
85. Laroussi, M. & Lu, X. Room-temperature atmospheric pressure plasma plume for biomedical applications. *Appl. Phys. Lett.* **87**, 113902 (2005).
86. Isbary, G. *et al.* Successful and safe use of 2 min cold atmospheric argon plasma in chronic wounds: results of a randomized controlled trial. *Br. J. Dermatol.* **167**, 404–410 (2012).
87. Keidar, M. *et al.* Cold plasma selectivity and the possibility of a paradigm shift in cancer therapy. *Br. J. Cancer* **105**, 1295–301 (2011).
88. MPNS COST Action MP1101: Biochemical Applications of Atmospheric Pressure Plasma Technology. <http://bioplasma.pointblank.ie/>
89. Kelly, S., Golda, J., Turner, M. M. & Schulz-Von Der Gathen, V. Gas and heat dynamics of a micro-scaled atmospheric pressure plasma reference jet. *J. Phys. D. Appl. Phys.* **48**, 444002 (2015).
90. Gorbaney, Y. *et al.* Combining experimental and modelling approach to study the sources of reactive species induced in water by the COST RF plasma jet. *Phys. Chem. Chem. Phys.* **20**, 2797-2808 (2018).
91. Lackmann, J.-W. *et al.* Photons and particles emitted from cold atmospheric-pressure plasma inactivate bacteria and biomolecules independently and synergistically. *J. R. Soc. Interface* **10**, (2013).
92. Yan, D. *et al.* Principles of using Cold Atmospheric Plasma Stimulated Media for Cancer Treatment. *Sci. Rep.* **5**, 18339 (2015).
93. Tanaka, H. *et al.* Plasma-Activated Medium Selectively Kills Glioblastoma Brain Tumor Cells by Down-Regulating a Survival Signaling Molecule, AKT Kinase. *Plasma Med.* **1**, 265–277 (2011).
94. Yan, D. *et al.* Controlling plasma stimulated media in cancer treatment application. *Appl. Phys. Lett.* **105**, 224101 (2014).
95. Becker, K. H., Schoenbach, K. & Eden, J. G. Microplasmas and applications. *J. Phys. D. Appl. Phys.* **39**, R55–R70 (2006).

96. Weltmann, K. & von Woedtke, T. for plasma applications to medicine and biology Plasma medicine—current state of research and medical application. *Plasma Phys. Control. Fusion* **59**, 14031 (2017).
97. Kim, J. Y., Ballato, J. & Kim, S. Intense and Energetic Atmospheric Pressure Plasma Jet Arrays. *Plasma Process. Polym.* **9**, 253–260 (2012).
98. Fang, Z., Ruan, C., Shao, T. & Cheng, Z. Two discharge modes in an atmospheric pressure plasma jet array in argon. *Plasma Sources Sci. Technol.* **25**, 01LT01 (2016).
99. Uchida, G., Nakajima, A., Ito, T., Takenaka, K. & Kawasaki, T. Effects of nonthermal plasma jet irradiation on the selective production of H<sub>2</sub>O<sub>2</sub> and NO<sub>2</sub> in liquid water. *J. Appl. Phys.* **120**, 203302 (2016).
100. Ito, T., Uchida, G., Nakajima, A., Takenaka, K. & Setsuhara, Y. Control of reactive oxygen and nitrogen species production in liquid by nonthermal plasma jet with controlled surrounding gas. *Jpn. J. Appl. Phys.* **56**, 014AC06 (2017).
101. Van Boxem, W. *et al.* Anti-Cancer Capacity of Plasma-Treated Pbs: Effect of Chemical Composition on Cancer Cell Cytotoxicity. *Sci. Rep.* **7**, 16478 (2017).
102. Partecke, L. I. *et al.* Tissue tolerable plasma (TTP) induces apoptosis in pancreatic cancer cells in vitro and in vivo. *BMC Cancer* **12**, 473–483 (2012).
103. Pacher, P., Beckman, J. S. & Liaudet, L. Central Control of Breathing in Mammals: Neuronal Circuitry, Membrane Properties, and Neurotransmitters. *Physiol. Rev.* **87**, 315–424 (2007).
104. Ryu, Y. *et al.* Effects of Background Fluid on the Efficiency of Inactivating Yeast with Non-Thermal Atmospheric Pressure Plasma. *PLoS One* **8**, 1–9 (2013).
105. Boehm, D., Heslin, C., Cullen, P. J. & Bourke, P. Cytotoxic and mutagenic potential of solutions exposed to cold atmospheric plasma. *Sci. Rep.* **6**, 21464 (2016).
106. Klinkhammer, C. *et al.* Elucidation of Plasma-Induced Chemical Modifications on Glutathione and Glutathione Disulphide. *Sci. Rep.* **7**, 13828 (2017).
107. Görlach, A. Reactive Oxygen Species (ROS) and the Cellular Redox State - from Toxicity to Signaling. *Antioxid. Redox Signal.* **7**, 1398–1404 (2005).
108. Yang, C. *et al.* Selective modification of apoB-100 in the oxidation of low density lipoproteins by myeloperoxidase in vitro. *J. Lipid Res.* **40**, 686–698 (1999).

109. Cadet, J. & Wagner, J. R. DNA Base Damage by Reactive Oxygen Species, Oxidizing Agents, and UV Radiation. *Cold Spring Harb. Perspect. Biol.* **5**, 1–18 (2013).
110. Gebicki, S. & Gebicki, J. M. Formation of peroxides in amino acids and proteins exposed to oxygen free radicals. *Biochem. J.* **749**, 743–749 (1993).
111. Yan, D., Nourmohammadi, N., Talbot, A., Sherman, J. H. & Keidar, M. The strong anti-glioblastoma capacity of the plasma-stimulated lysine-rich medium. *J. Phys. D. Appl. Phys.* **49**, 274001 (2016).
112. Naïtali, M., Kamgang-youbi, G., Herry, J., Bellon-Fontaine, M.-N. & Brisset, J.-L. Combined Effects of Long-Living Chemical Species during Microbial Inactivation Using Atmospheric Plasma-Treated Water. *Appl. Environ. Microbiol.* **76**, 7662–7664 (2010).
113. Mohades, S., Laroussi, M. & Maruthamuthu, V. Moderate plasma activated media suppresses proliferation and migration of MDCK epithelial cells. *J. Phys. D. Appl. Phys.* **50**, 185205 (2017).
114. Takeda, S. *et al.* Intraperitoneal Administration of Plasma-Activated Medium: Proposal of a Novel Treatment Option for Peritoneal Metastasis From Gastric Cancer. *Ann. Surg. Oncol.* **24**, 1188–1194 (2017).
115. Traylor, M. J. *et al.* Long-term antibacterial efficacy of air plasma-activated water. *J. Phys. D. Appl. Phys.* **44**, 472001 (2011).
116. Ma, R. *et al.* Non-thermal plasma-activated water inactivation of food-borne pathogen on fresh produce. *J. Hazard. Mater.* **300**, 643–651 (2015).
117. Circu, M. L. & Aw, T. Y. Reactive oxygen species, cellular redox systems, and apoptosis. *Free Radic. Biol. Med.* **48**, 749–62 (2010).
118. Heinlin, J. *et al.* Plasma applications in medicine with a special focus on dermatology. *J. Eur. Acad. Dermatology Venereol.* **25**, 1–11 (2011).
119. Yoon, S., Park, S., Yoon, S. Y., Yun, C. & Chung, A. Sustained Production of H<sub>2</sub>O<sub>2</sub> Activates Pro-matrix Metalloproteinase-2 through Receptor Tyrosine Kinases/Phosphatidylinositol 3-Kinase/NF-κB Pathway. *J. Biol. Chem.* **277**, 30271–30282 (2002).
120. Cianchi, F. *et al.* Inducible Nitric Oxide Synthase Expression in Human Colorectal Cancer Correlation with Tumor Angiogenesis. *Am. J. Pathol.* **162**, 793–801 (2003).
121. Brown, G. C. Nitric oxide regulates mitochondrial respiration and cell functions by inhibiting cytochrome oxidase. *FEBS Lett.* **369**, 136–139 (1995).
122. Sen, C. K. Wound healing essentials: Let there be oxygen. *Wound Repair Regen.* **17**, 1–18 (2009).



123. Adler, S. C. & Kent, K. J. Enhancing wound healing with growth factors. *Facial Plast. Surg. Clin. North Am.* **10**, 129–146 (2002).
124. Chiang, B. *et al.* Enhancing skin wound healing by direct delivery of intracellular adenosine triphosphate. *Am. J. Surg.* **193**, 213–218 (2007).
125. Venezia, R. A., Orrico, M., Houston, E., Yin, S. M. & Naumova, Y. Y. Lethal Activity of Nonthermal Plasma Sterilization Against Microorganisms. *Infect Control Hosp. Epidemiology* **29**, 430–436 (2008).
126. Daeschlein, G. *et al.* Antibacterial Activity of an Atmospheric Pressure Plasma Jet Against Relevant Wound Pathogens in vitro on a Simulated Wound Environment. *Plasma Process. Polym.* **7**, 224–230 (2010).
127. Maisch, T. *et al.* Decolonisation of MRSA, *S. aureus* and *E. coli* by Cold-Atmospheric Plasma Using a Porcine Skin Model in vitro. *PLoS One* **7**, e34610 (2012).
128. Heinlin, J. *et al.* Randomized placebo-controlled human pilot study of cold atmospheric argon plasma on skin graft donor sites. *Wound Repair Regen.* **21**, 800–807 (2013).
129. Isbary, G. *et al.* Cold atmospheric argon plasma treatment may accelerate wound healing in chronic wounds: results of an open retrospective randomized controlled study in vivo. *Clin. Plasma Med.* **1**, 25–30 (2013).
130. Tiede, R. *et al.* Plasma Applications: a Dermatological View. *Contrib. to Plasma Phys.* **54**, 118–130 (2014).
131. Oh, J. *et al.* How plasma induced oxidation, oxygenation, and de-oxygenation influences viability of skin cells. *Appl. Phys. Lett.* **203701**, 203701 (2016).
132. Hirschberg, J. *et al.* Influence of excitation pulse duration of dielectric barrier discharges on biomedical applications. *J. Phys. D. Appl. Phys.* **46**, 165201 (2013).
133. Alberts, B. *et al.* *Molecular Biology of The Cell*. (Garland Science, Taylor & Francis Group, 2008).
134. Hanahan, D. & Weinberg, R. A. Hallmarks of cancer: the next generation. *Cell* **144**, 646–74 (2011).
135. Goodspeed, A., Heiser, L. M., Gray, J. W. & Costello, J. C. Tumor-Derived Cell Lines as Molecular Models of Cancer Pharmacogenomics. *Mol. Cancer Res.* **14**, 3–14 (2015).
136. Zeman, E., Schreiber, E. & Tepper, J. *Basics of Radiation Therapy*. (Elsevier Inc., 2013).

137. Side Effects of Radiation Therapy. *American Society of Clinical Oncology* (2017). at <<https://www.cancer.net/navigating-cancer-care/how-cancer-treated/radiation-therapy/side-effects-radiation-therapy>>
138. Johnstone, T. C., Kogularamanan, S. & Lippard, S. J. The Next Generation of Platinum Drugs: Targeted Pt(II) Agents, Nanoparticle Delivery, and Pt(IV) Prodrugs. *Chem. Rev.* **116**, 3436–3486 (2016).
139. Hagner, N. & Joerger, M. Cancer chemotherapy: targeting folic acid synthesis. *Cancer Manag. Res.* **2**, 293–301 (2010).
140. Side Effects of Chemotherapy. *American Society of Clinical Oncology* (2017). at <<https://www.cancer.net/navigating-cancer-care/how-cancer-treated/chemotherapy/side-effects-chemotherapy>>
141. Schardt, D., Elsässer, T. & Schulz-ertner, D. Heavy-ion tumor therapy: physical and radiobiological benefits. *Rev. Mod. Phys.* **82**, 383–425 (2010).
142. Surdutovich, E., Yakubovich, A. V. & Solov'yov, A. V. Biodamage via shock waves initiated by irradiation with ions. *Nature* **3**, 1–6 (2013).
143. Nobusuke, J. O., Shoko, H. & Shoji, T. Treatment outcome of ion beam therapy in eight patients with head and neck cancers. *Eur. Arch. Otorhinolaryngol.* **273**, 4397–4402 (2016).
144. Dolmans, D. E. J. G. J., Fukumura, D. & Jain, R. K. Photodynamic therapy for cancer. *Nat. Rev. Cancer* **3**, 380–387 (2003).
145. Semenza, G. L. Targeting HIF-1 for Cancer Therpay. *Nat. Rev.* **3**, 721 (2003).
146. Vanneman, M. & Dranoff, G. Combining Immunotherapy and Targeted Therapies in Cancer Treatment. *Nat. Rev. Cancer* **12**, 237–251 (2014).
147. Kim, S. J., Chung, T. H., Bae, S. H. & Leem, S. H. Induction of apoptosis in human breast cancer cells by a pulsed atmospheric pressure plasma jet. *Appl. Phys. Lett.* **97**, 23702 (2010).
148. Ahn, H. J. *et al.* Atmospheric-pressure plasma jet induces apoptosis involving mitochondria via generation of free radicals. *PLoS One* **6**, e28154 1-7 (2011).
149. Panngom, K. *et al.* Preferential killing of human lung cancer cell lines with mitochondrial dysfunction by nonthermal dielectric barrier discharge plasma. *Cell Death Dis.* **4**, e642 1-8 (2013).
150. Sagawa, T. *et al.* Argon plasma coagulation for successful treatment of early gastric cancer with intramucosal invasion. *Gut* **52**, 334–9 (2003).
151. Barekzi, N. & Laroussi, M. Dose-dependent killing of leukemia cells by low-temperature plasma. *J. Phys. D. Appl. Phys.* **45**, 422002 (2012).

152. Zhang, X., Li, M., Zhou, R., Feng, K. & Yang, S. Ablation of liver cancer cells in vitro by a plasma needle. *Appl. Phys. Lett.* **93**, 021502 (2008).
153. Iseki, S. *et al.* Selective killing of ovarian cancer cells through induction of apoptosis by nonequilibrium atmospheric pressure plasma. *Appl. Phys. Lett.* **100**, 113702 (2012).
154. Arndt, S. *et al.* Cold atmospheric plasma, a new strategy to induce senescence in melanoma cells. *Exp. Dermatol.* **22**, 284–289 (2013).
155. Walk, R. M. *et al.* Cold atmospheric plasma for the ablative treatment of neuroblastoma. *J. Pediatr. Surg.* **48**, 67–73 (2013).
156. Vandamme, M. *et al.* Antitumor Effect of Plasma Treatment on U87 Glioma Xenografts: Preliminary Results. *Plasma Process. Polym.* **7**, 264–273 (2010).
157. Vandamme, M. *et al.* ROS implication in a new antitumor strategy based on non-thermal plasma. *Int. J. Cancer* **130**, 2185–94 (2012).
158. Köritzer, J. *et al.* Restoration of sensitivity in chemo-resistant glioma cells by cold atmospheric plasma. *PLoS One* **8**, e64498 (2013).
159. Adachi, T., Kano, A., Nonomura, S., Kamiya, T. & Hara, H. Histone deacetylase inhibitors stimulate the susceptibility of A549 cells to a plasma-activated medium treatment. *Arch. Biochem. Biophys.* **606**, 120–127 (2016).
160. Kaushik, N. *et al.* Non-thermal plasma with 2-deoxy-D-glucose synergistically induces cell death by targeting glycolysis in blood cancer cells. *Sci. Rep.* **5**, 1–11 (2015).
161. Warburg, O. & Dickens, F. *The Metabolism of Tumours*. (Constable and Company Limited, 1930).
162. Yan, X. *et al.* Plasma-Induced Death of HepG2 Cancer Cells: Intracellular Effects of Reactive Species. *Plasma Process. Polym.* **9**, 59–66 (2012).
163. Ninomiya, K. *et al.* Evaluation of extra- and intracellular OH radical generation, cancer cell injury, and apoptosis induced by a non-thermal atmospheric-pressure plasma jet. *J. Phys. D: Appl. Phys.* **46**, 425401 (2013).
164. Möller, M. N., Lancaster, J. R. & Denicola, A. in *Free Radical Effects on Membranes* **61**, 23–42 (2008).
165. Van der Paal, J., Verheyen, C., Neyts, E. C. & Bogaerts, A. Hampering Effect of Cholesterol on the Permeation of Reactive Oxygen Species through Phospholipids Bilayer: Possible Explanation for Plasma Cancer Selectivity. *Sci. Rep.* **7**, 39526 (2016).
166. Bienert, G. P. & Chaumont, F. Aquaporin-facilitated transmembrane diffusion of hydrogen peroxide. *Biochim. Biophys. Acta* **1840**, 1596–1604 (2014).

167. Almasalmeh, A., Krenc, D., Wu, B. & Beitz, E. Structural determinants of the hydrogen peroxide permeability of aquaporins. *FEBS J.* **281**, 647–656 (2014).
168. Herrera, M., Hong, N. J. & Garvin, J. L. Aquaporin-1 Transports NO Across Cell Membranes. *Hypertension* **48**, 157–164 (2006).
169. Yan, D. *et al.* The role of aquaporins in the antiglioblastoma capacity of the cold plasma-stimulated medium. *J. Phys. D. Appl. Phys.* **50**, 55401 (2017).
170. Van Blitterswijk, W. J., De Veer, G., Krol, J. H. & Emmelot, P. Comparative lipid analysis of purified plasma membranes and shed extracellular membrane vesicles from normal murine thymocytes and leukemic GRSL cells. *Biochim. Biophys. Acta* **688**, 495–504 (1982).
171. Senbanjo, L. & Chellaiah, M. CD44: a Multifunctional Cell Surface Adhesion Receptor is a Regulator of Progression and Metastasis of Cancer Cells. *Front. Cell Dev. Biol.* **5**, 1–6 (2017).
172. Tanaka, H. *et al.* Cell survival and proliferation signaling pathways are downregulated by plasma- activated medium in glioblastoma brain tumor cells. *Plasma Med.* **2**, 207–220 (2012).
173. Kim, G. J., Kim, W., Kim, K. T. & Lee, J. K. DNA Damage and Mitochondria Dysfunction in Cell Apoptosis Induced by Nonthermal Air Plasma. *Appl. Phys. Lett.* **96**, 21502 (2010).
174. Cadet, J. & Wagner, J. R. Oxidatively Generated Base Damage to Cellular DNA by Hydroxyl Radical and One-Electron Oxidants: Similarities and Differences. *Arch. Biochem. Biophys.* **557**, 47–54 (2014).
175. Nowicka, A., Kowalczyk, A., Sek, S. & Stojek, Z. Oxidation of DNA Followed by Conformational Change after OH Radical Attack. *Anal. Chem.* **85**, 355–361 (2012).
176. Shao, C., Saito, M. & Yu, Z. Formation of Single- and Double-Strand Breaks of pBR322 Plasmid Irradiated in the Presence of Scavengers. *Radiat. Environ. Biophys.* **38**, 105–109 (1999).
177. Van Meter, M. *et al.* JNK Phosphorylates SIRT6 to Stimulate DNA Double-Strand Break Repair in Response to Oxidative Stress by Recruiting PARP1 to DNA Breaks. *Cell Rep.* **16**, 2641–2650 (2016).
178. Rogakou, E. P., Pilch, D. R., Orr, A. H., Ivanova, V. S. & Bonner, W. M. DNA Double-stranded Breaks Induce Histone H2AX Phosphorylation on Serine 139. *J. Biol. Chem.* **273**, 5858–5868 (1998).
179. Wilhelm, M. *et al.* Mass-spectrometry-based draft of the human proteome. *Nature* **509**, 582–587 (2014).

180. Topala, I. & Nagatsu, M. Capillary plasma jet: a low volume plasma source for life science applications. *Appl. Physcis Lett.* **106**, 54105 (2015).
181. Lackmann, J. *et al.* A dielectric barrier discharge terminally inactivates RNase A by oxidizing sulfur-containing amino acids and breaking structural disulfide bonds. *J. Phys. D. Appl. Phys.* **48**, 494003 (2015).
182. Takai, E., Kitano, K., Kuwabara, J. & Shiraki, K. Protein Inactivation by Low-temperature Atmospheric Pressure Plasma in Aqueous Solution. *Plasma Process. Polym.* **9**, 77–82 (2012).
183. Espino, J. A. & Jones, L. M. In Cell Footprinting Coupled with Mass Spectrometry for the Structural Analysis of Proteins in Live Cells. *Anal. Chem.* **87**, 7971–7978 (2015).
184. Trachootham, D., Alexandre, J. & Huang, P. Targeting cancer cells by ROS-mediated mechanisms: a radical therapeutic approach *Nat. Rev. Drug Discov.* **8**, 579–91 (2009).
185. Toyokuni, S., Okamoto, K., Yodoi, J. & Hiai, H. Persistent oxidative stress in cancer. *FEBS Lett.* **358**, 1–3 (1995).
186. Ogasawara, M. & Zhang, H. Redox regulation and its emerging roles in stem cells and stem-like cancer cells. *Antioxid. Redox Signal.* **11**, 1107–1122 (2009).
187. Bundscherer, L. *et al.* Non-thermal plasma treatment induces MAPK signaling in human monocytes. *Open Chem.* **13**, 606–613 (2015).
188. Costa, A., Scholer-Dahirel, A. & Mechta-Grigoriou, F. The role of reactive oxygen species and metabolism on cancer cells and their microenvironment. *Semin. Cancer Biol.* **25**, 23–32 (2014).
189. Kalghatgi, S. U. *et al.* Mechanism of blood coagulation by nonthermal atmospheric pressure dielectric barrier discharge plasma. *IEEE Trans. PLASMA Sci.* **35**, 1559–1566 (2007).
190. Bauer, G. Targeting extracellular ROS signaling of tumor cells. *Anticancer Res.* **34**, 1467–82 (2014).
191. Bauer, G. The Antitumor Effect of Singlet Oxygen. *Anticancer Res.* **36**, 5649–5663 (2016).
192. Markovic, J., Garcia-Gimenez, J. L., Gimeno, A., Vina, J. & Pallardo, F. V. Role of glutathione in cell nucleus. *Free Radic. Res.* **44**, 721–733 (2010).
193. Weiss, M. *et al.* Cold Atmospheric Plasma Treatment Induces Anti-Proliferative Effects in Prostate Cancer Cells by Redox and Apoptotic Signaling Pathways. *PLoS One* **10**, e0130350 (2015).

194. Yusupov, M., Lackmann, J.-W., Razzokov, J., Stapelmann, K. & Bogaerts, A. Impact of plasma oxidation on structural features of human epidermal growth factor. *Plasma Process. Polym.* **submitted** (2018).
195. Schmidt, A. *et al.* Non-thermal Plasma Activates Human Keratinocytes by Stimulation of Antioxidant and Phase II Pathways. *J. Biol. Chem.* **290**, 6731–6750 (2015).
196. Hara, H., Taniguchi, M., Kobayashi, M., Kamiya, T. & Adachi, T. Plasma-activated medium-induced intracellular zinc liberation causes death of SH-SY5Y cells. *Arch. Biochem. Biophys.* **584**, 51–60 (2015).
197. Hara, H., Sueyoshi, S., Taniguchi, M., Kamiya, T. & Adachi, T. Differences in intracellular mobile zinc levels affect susceptibility to plasma-activated medium- induced cytotoxicity. *Free Radic. Res.* **51**, 306–315 (2017).
198. Andrabi, S. A. *et al.* Poly(ADP-ribose) polymerase-dependent energy depletion occurs through inhibition of glycolysis. *Proc. Natl. Acad. Sci. USA* **111**, 10209–10214 (2014).
199. Gillies, L. A. & Kuwana, T. Apoptosis regulation at the mitochondrial outer membrane. *J. Cell. Biochem.* **115**, 632–40 (2014).
200. Lee, H. C. & Wei, Y. H. Oxidative Stress, Mitochondrial DNA Mutation, and Apoptosis in Aging. *Exp. Biol. Med.* **232**, 592–606 (2007).
201. Sawyers, C. Targeted cancer therapy. *Nature* **432**, 294–297 (2004).
202. Panngom, K., Baik, K. Y., Ryu, Y. H., Uhm, H. S. & Choi, E. H. Differential responses of cancer cell lines to non-thermal plasma from dielectric barrier discharge. *Curr. Appl. Phys.* **13**, S6–S11 (2013).
203. Hou, J. *et al.* Non-thermal plasma treatment altered gene expression profiling in non-small-cell lung cancer A549 cells. *BMC Genomics* **16**, 435 (2015).
204. Kim, C.-H. *et al.* Induction of cell growth arrest by atmospheric non-thermal plasma in colorectal cancer cells. *J. Biotechnol.* **150**, 530–8 (2010).
205. Hager, K. & Gu, W. Understanding the non-canonical pathways involved in p53-mediated tumor suppression. *Carcinogenesis* **35**, 740–746 (2014).
206. Hainaut, P. & Hollstein, M. p53 and human cancer: the first ten thousand mutations. *Adv. Cancer Res.* **77**, 81–137 (2000).
207. Ma, Y. *et al.* Non-thermal atmospheric pressure plasma preferentially induces apoptosis in p53-mutated cancer cells by activating ROS stress-response pathways. *PLoS One* **9**, e91947 (2014).

208. Kaushik, N. K., Attri, P., Kaushik, N. & Choi, E. H. A preliminary study of the effect of DBD plasma and osmolytes on T98G brain cancer and HEK non-malignant cells. *Molecules* **18**, 4917–28 (2013).
209. Hong, S.-H., Szili, E. J., Jenkins, A. T. A. & Short, R. D. Ionized gas (plasma) delivery of reactive oxygen species (ROS) into artificial cells. *J. Phys. D. Appl. Phys.* **47**, 362001 (2014).
210. Graves, D. B. Reactive Species from Cold Atmospheric Plasma: Implications for Cancer Therapy. *Plasma Process. Polym.* **11**, 1120–1127 (2014).
211. Graves, D. B. Oxy-nitroso shielding burst model of cold atmospheric plasma therapeutics. *Clin. Plasma Med.* **2**, 38–49 (2014).
212. Ishaq, M., Evans, M. D. M. & Ostrikov, K. Atmospheric pressure gas plasma-induced colorectal cancer cell death is mediated by Nox2–ASK1 apoptosis pathways and oxidative stress is mitigated by Srx–Nrf2 anti-oxidant system. *Biochim. Biophys. Acta - Mol. Cell Res.* **1843**, 2827–2837 (2014).
213. Kalghatgi, S., Friedman, G., Fridman, A. & Clyne, A. M. Endothelial cell proliferation is enhanced by low dose non-thermal plasma through fibroblast growth factor-2 release. *Ann. Biomed. Eng.* **38**, 748–57 (2010).
214. Sato, T., Yokoyama, M. & Johkura, K. A key inactivation factor of HeLa cell. *J. Phys. D. Appl. Phys.* **44**, 372001 (2011).
215. Chan, S. W. *et al.* Mitochondrial DNA damage is sensitive to exogenous H<sub>2</sub>O<sub>2</sub> but independent of cellular ROS production in prostate cancer cells. *Mutat. Res.* **716**, 40–50 (2011).
216. Hoentsch, M., von Woedtke, T., Weltmann, K.-D. & Nebe, B. J. Time-dependent effects of low-temperature atmospheric-pressure argon plasma on epithelial cell attachment, viability and tight junction formation in vitro. *J. Phys. D. Appl. Phys.* **45**, 25206 (2012).
217. Utsumi, F. *et al.* Effect of Indirect Nonequilibrium Atmospheric Pressure Plasma on Anti-Proliferative Activity Against Chronic Chemo-Resistant Ovarian Cancer Cells in Vitro and in Vivo. *PLoS One* **8**, 1–10 (2013).
218. Utsumi, F. *et al.* Selective cytotoxicity of indirect nonequilibrium atmospheric pressure plasma against ovarian clear-cell carcinoma. *Springerplus* **3**, 398 (2014).
219. Hoentsch, M. *et al.* Persistent Effectivity of Gas Plasma-Treated, Long Time-Stored Liquid on Epithelial Cell Adhesion Capacity and Membrane Morphology. *PLoS One* **9**, e104559 (2014).
220. Torii, K. *et al.* Effectiveness of plasma treatment on gastric cancer cells. *Gastric Cancer* **18**, 635–643 (2015).

221. Mohades, S., Laroussi, M., Sears, J., Barekzi, N. & Razavi, H. Evaluation of the effects of a plasma activated medium on cancer cells. *Phys. Plasmas* **22**, 122001 (2015).
222. Mohades, S., Barekzi, N. & Laroussi, M. Efficacy of Low Temperature Plasma against SCaBER Cancer Cells. *Plasma Process. Polym.* **11**, 1150–1155 (2014).
223. Vermeulen, S. *et al.* Cold atmospheric plasma treatment of melanoma and glioblastoma cancer cells. *Plasma Process. Polym.* **13**, 1195–1205 (2016).
224. Judée, F., Fongia, C., Ducommun, B. & Yousfi, M. Short and long time effects of low temperature plasma activated media on 3D multicellular tumor spheroids. *Sci. Rep.* **6**, 21421 (2016).
225. Kurake, N. *et al.* Cell survival of glioblastoma grown in medium containing hydrogen peroxide and/or nitrite, or in plasma-activated medium. *Arch. Biochem. Biophys.* **605**, 102–108 (2016).
226. Adachi, T., Nonomura, S., Horiba, M., Hirayama, T. & Kamiya, T. Iron stimulates plasma-activated medium-induced A549 cell injury. *Sci. Rep.* **6**, 20928 (2016).
227. Tanaka, H., Nakamura, K., Mizuno, M., Ishikawa, K. & Takeda, K. Non-thermal atmospheric pressure plasma activates lactate in Ringer's solution for anti-tumor effects. *Nat. Publ. Gr.* **6**, 1–11 (2016).
228. Mohades, S., Barekzi, N., Razavi, H., Maruthamuthu, V. & Laroussi, M. Temporal evaluation of the anti-tumor efficiency of plasma-activated media. *Plasma Process. Polym.* **13**, 1206–1211 (2016).
229. Duan, J., Lu, X. & He, G. The selective effect of plasma activated medium in an in vitro co-culture of liver cancer and normal cells. *J. Appl. Phys.* **121**, 13302 (2017).
230. Canal, C. *et al.* Plasma-induced selectivity in bone cancer cells death. *Free Radic. Biol. Med.* **110**, 72–80 (2017).





## **2 Methodology Molecular Dynamics**



## 2-1 Computational research – An introduction

During the last decades, computer simulations have become a well-established and important scientific research method. Thanks to the increasing calculation capacity of computers, simulations are nowadays not only used in the fields of physics, chemistry and biology, but also in psychology, economics, medicine, climate science, astronomy, engineering, sociology and decision theory. Moreover, they found their way into people's everyday life with weather forecasting and video games as two of the main examples.

One of the first appearances of computational experiments dates from World War II where two mathematicians, *i.e.*, John Von Neumann and Stanislaw Ulam, used Monte Carlo simulations (an algorithm based on random numbers) to investigate the behavior of neutrons in different materials<sup>1-3</sup>. It depicts the clear advantages of computer simulations. As an experimental approach was too costly and the events were too short and too complicated for an analytical approach, simulations would provide an excellent solution. Furthermore, computer simulations enable one to investigate only a single parameter at a time and at high resolution (both in space and time), providing insight which is very difficult or even impossible to obtain experimentally. In addition, simulations do not require any safety, health or waste regulations as is often the case in, for instance, medical, environmental and chemical research fields. Finally, simulations can be performed at conditions close to their experimental counterparts, leading to a direct correlation between the two approaches. The combination of these advantages makes computational research a powerful method for elucidating the underlying processes in experimental observations and to retrieve insight and information on numerous phenomena.

A wide range of computational methods and techniques exist, all having their own typical capabilities and limitations. To date, two families of simulations are used to investigate various aspects and properties of both plasma and biomolecules, and their interactions. The first group contains atomic scale simulations including quantum mechanical (QM) techniques, such as the density functional theory (DFT) and (post-)Hartree-Fock<sup>4-10</sup>, and molecular dynamics (MD) simulations<sup>11-18</sup>. The second group contains macroscopic simulations such as chemical kinetic and hydrodynamics (HD) models<sup>19-22</sup>. These techniques are very distinct, and the

utilization of these methods is determined by the research question at hand. An introduction to macroscopic scale simulations, as well as details on the techniques used in this thesis, are presented in **chapter 7**.

QM simulations are typically used to obtain fundamental chemical information on the atomistic scale. Using these methods, one is able to acquire energy differences between different conformers or products, detailed molecular geometries, thermodynamic properties, transition states, *etc.*<sup>23</sup>. QM simulations use a basic source of information, such as the electron density (in case of DFT) or the wave functions (for Hartree-Fock) to calculate all properties and the total energy of the molecular system of interest<sup>23</sup>. Although these methods are able to describe the system with great precision and detail, they are very time consuming. This limits the calculation to relatively small dimensions (*i.e.*, up to 100 atoms). Therefore, to be able to investigate biological systems at a larger scale (lipids, proteins, DNA, hormones, *etc.*), computationally ‘cheaper’ methods are required. For these research questions, MD simulations (nanometer to sub-micrometer and nanosecond-microsecond scales) are better suited<sup>24</sup>.

MD simulations are based on solving the laws of motion, describing the trajectory for each particle in the phase space. This way, both the static and dynamic properties of a system can be investigated at the atomic scale. Because of this, MD forms the method of choice to study interactions and reactions in biological systems. When the forces are derived from a classical force field, the technique is referred to as classical MD, while it is called *ab initio* MD when the forces are derived from electronic structure calculations. It is important to realize that MD simulations are deterministic. This means that the results are solely dependent on the used parameters. The simulation parameters are in this case the initial positions, velocities and the used interatomic potential (see **section 2-2** for more information).

Plasma chemistry and HD models, are suited to describe, *e.g.*, the interactions between the plasma and treated objects, as well as the behavior of the plasma itself, on a macroscopic scale. In the context of plasma medicine, non-plasma materials are usually represented by dielectric matter, characterized with the appropriate conductivities and permittivities so that it can represent biological tissue, *e.g.*, cell membranes, biofilms, *etc.*<sup>21</sup>.

In this thesis, the reactivity of plasma-generated reactive species towards various essential biomolecules (glucose, DNA, peptides and amino acids) was investigated. To this end, MD simulations were used to elucidate the interactions in various situations in **chapters 3, 4** and **5**. In addition, the behavior of the plasma-generated species in and in contact with liquids was investigated on the macroscopic scale, as described in **chapter 7**. For this study, a fluid model was built and utilized.

*The molecular dynamics techniques used in this thesis will be described in more detail in the following **sections 2-2**. A detailed description on the used fluid models can be found in **chapter 7**.*



## 2-2 Molecular dynamics

### 2-2.1 Introduction

MD simulations calculate the time-dependent trajectory of every particle in a N-body system (where N stands for the number of particles that are considered in the calculation). This is done by integrating the laws of motion, considering the forces that act on each particle. On the atomic scale, particles can be defined by a single atom or a (part of a) molecule. When multiple atoms form a particle, the term *pseudo-atom* is used. We define two groups of MD simulations: *ab initio* or quantum mechanical MD simulations (qMD), where the forces are commonly obtained using *ab initio* calculations<sup>25,26</sup>, and classical MD simulations (cMD), where forces are obtained from an interatomic potential—the force field<sup>27–30</sup>.

Here, particles are approximated by classical particles. In this context, classic means that particles obey the laws of classical physics, such as the laws of Newton. This is a good approximation for a wide range of systems. However, we know that particles at the atomic scale obey the laws of quantum mechanics, following the Schrödinger equation. However, as solving the Schrödinger equation involves solving for the wave functions (containing  $4N_e$  variables;  $N_e$  = number of electrons), this equation can only be solved for the simplest systems and becomes too complex for larger molecules. In order to find a solution for these larger systems, the Born-Oppenheimer approximation can be applied<sup>31</sup>. This approximation separates the electronic part and the nuclear part of a system in such a way that atomic interactions can be calculated using an interatomic potential based on the positions of the nuclei.

### 2-2.2 Classical MD – ReaxFF

#### 2-2.2a Introduction

The classical trajectories are calculated based on the forces that act on each particle as a result of the immediate environment (*i.e.*, surrounding particles). For a system composed of atoms with spatial coordinates  $R_N^{t=0} = \{r_1, r_2, r_3, \dots, r_N\}$ , the forces are derived from an adequate interatomic interaction potential ( $V(\mathbf{r}^N)$ ). The forces and subsequent accelerations of each particle are calculated in the following manner:



$$\mathbf{F}_i = -\nabla V(\mathbf{r}^N) \quad [2-1]$$

$$\mathbf{a}_i = \frac{\mathbf{F}_i}{m_i} \quad [2-2]$$

$\mathbf{F}_i$  represents the forces acting on particle  $i$  as a function of the position of all other particles  $j$  at timestep  $t$ .  $\mathbf{a}_i$  is the acceleration of particle  $i$  with mass  $m_i$ , as a consequence of the forces acting on this particle.

However, as the potential energy  $V$  is a function of  $3N$  variables, the equations of motion are integrated numerically. Various numerical algorithms –*integrators*– were developed to integrate these equations to determine the positions,  $\mathbf{R}_N^{t+\Delta t}$ , and momenta,  $\mathbf{P}_N^{t+\Delta t}$ , after every timestep. For this purpose, the used integrator should be characterized by the following criteria: energy and momentum are conserved (implying a good stability); computationally efficient and permitting long time steps for integration (keeping the calculation time as low as possible); time-reversible and able to conserve the phase space volume.

### 2-2.2b Integration methods

One of the most popular integrators is the Verlet integrator<sup>32</sup>. The Verlet algorithm is commonly used in MD simulations due to its stability and simplicity. It was first introduced by the French physicist Loup Verlet in 1967 in order to integrate the equations of Newton for a two-body Lennard-Jones type potential<sup>32</sup>. The Verlet integrator can be derived from the Taylor expansions of the positions  $\mathbf{r}_i^{(t+\Delta t)}$  and  $\mathbf{r}_i^{(t-\Delta t)}$ :

$$\mathbf{r}_i^{(t+\Delta t)} = \mathbf{r}_i^{(t)} + \mathbf{v}_i^t \Delta t + \frac{\mathbf{f}_i^{(t)}}{2m_i} \Delta t^2 + \frac{\Delta t^3}{3!} \frac{\partial^3 \mathbf{r}_i}{\partial t^3} + O(\Delta t^4) \quad [2-3]$$

$$\mathbf{r}_i^{(t-\Delta t)} = \mathbf{r}_i^{(t)} - \mathbf{v}_i^t \Delta t + \frac{\mathbf{f}_i^{(t)}}{2m_i} \Delta t^2 - \frac{\Delta t^3}{3!} \frac{\partial^3 \mathbf{r}_i}{\partial t^3} + O(\Delta t^4) \quad [2-4]$$

When adding the two equations, one obtains the basic formula for this integrator:

$$\mathbf{r}_i^{(t+\Delta t)} = 2\mathbf{r}_i^{(t)} - \mathbf{r}_i^{(t-\Delta t)} + \frac{\mathbf{f}_i^{(t)}}{m_i} \Delta t^2 + O(\Delta t^4) \quad [2-5]$$

The velocities are not explicitly considered in this equation but are often needed for the calculation of system properties such as the kinetic energy. The calculation of these properties at time  $t$  can pose as a challenge as this requires the positions to be known at time  $t+\Delta t$ . This problem can be solved using either the velocity Verlet algorithm (see below) or by using the following expression, obtained after subtracting in the two Taylor expansions mentioned above:

$$\mathbf{p}_i^{(t)} = \frac{m_i}{2\Delta t} (\mathbf{r}_i^{(t+\Delta t)} - \mathbf{r}_i^{(t-\Delta t)}) + O(\Delta t^2) \quad [2-6]$$

Both equations, [2-5] and [2-6], contain a local error,  $O$ , which is in the order of  $\Delta t^4$  and  $\Delta t^2$ , respectively. As the global error is determined by the biggest contribution, being  $\Delta t^2$ , the Verlet algorithm is known as a second-order integrator. Additionally, the presence of both terms  $\mathbf{r}^{(t+\Delta t)}$  and  $\mathbf{r}^{(t-\Delta t)}$  results in a time-reversible algorithm, which is one of the requirements of an integrator as stated before. To limit the contribution of  $O(\Delta t^2)$ , the time step,  $\Delta t$ , can be reduced<sup>33</sup>.

From the above equations, both  $R_N^{t+\Delta t}$  and  $P_N^t$  are calculated at different time steps, *i.e.*,  $t+\Delta t$  and  $t$ , respectively. As the velocity is needed to determine the kinetic energy of the system (used to control and verify the temperature for instance), this forms a significant disadvantage of this algorithm. To circumvent this problem, multiple variations of the Verlet algorithm were developed, such as the leap-frog algorithm, velocity Verlet integration or Beeman's algorithm<sup>33</sup>.

The leap-frog algorithm is based on explicitly calculating the velocities at  $t+1/2\Delta t$  which are in turn used to determine the position,  $R_N$ , at  $t+\Delta t$ <sup>33</sup>. This way, the velocity is calculated to *leap* over the positions, after which the position *leaps* over the velocity. In order to compute  $R_N$  and  $P_N$  at the same time step,  $t$ , the velocities are approximated as the average between  $\mathbf{v}_i^{t-1/2\Delta t}$  and  $\mathbf{v}_i^{t+1/2\Delta t}$ .

The velocity Verlet algorithm is very similar to the leap-frog algorithm except that the positions and velocities are calculated at the same time value. This is done using two steps: Calculate the velocity at  $t+1/2\Delta t$ , based on  $\mathbf{v}_i^t$  and use this value to calculate the position at  $t+\Delta t$ .

$$\mathbf{v}_i^{(t+1/2\Delta t)} = \mathbf{v}_i^{(t)} + \frac{\mathbf{a}_i^t}{2} \Delta t \quad [2-7]$$

$$\mathbf{r}_i^{(t+\Delta t)} = \mathbf{r}_i^{(t)} + \mathbf{v}_i^{t+1/2\Delta t} \Delta t \quad [2-8]$$

Afterwards, the forces at  $t+\Delta t$  are determined, based on the  $\mathbf{r}_i^{t+\Delta t}$ , which can then be used to obtain  $\mathbf{a}_i^{t+\Delta t}$  and, from that,  $\mathbf{v}_i^{t+\Delta t}$ :

$$\mathbf{v}_i^{(t+\Delta t)} = \mathbf{v}_i^{(t+1/2\Delta t)} + \frac{\mathbf{a}_i^{(t+\Delta t)}}{2} \Delta t \quad [2-9]$$

Beeman's algorithm is closely related to the expressions used in the velocity Verlet integrator. This method results in a better conservation of  $P_N$  and energy but with significantly higher computational cost. This increase in calculation time combined with the fact that the velocity Verlet algorithm shows excellent energy conservation over time, and the ability to calculate the kinetic and potential energy simultaneously, makes the velocity Verlet scheme the integrator of choice in most MD simulations, as well as in this work.

### 2-2.2c MD molecular system

In order to describe global properties of the simulated system, molecular dynamics simulations are performed in a suitable thermodynamic ensemble<sup>33,34</sup>. Ensembles can be described as the probability distribution for the states of a system in the context of statistical mechanics. An ensemble consists of a large number of states, *i.e.*, *microstates*, in which the system can potentially be found. Within a given ensemble, the various thermodynamical (macroscopically observable) properties of a system in thermodynamic equilibrium can be calculated (*i.e.*, all physical properties are independent of time). Physical quantities are defined as the weighted average over all microstates of the system, called *ensemble averages*, which should correspond to experimental observables. The ensemble average of a quantity  $A$  is defined as:

$$\langle A \rangle_{\text{ens}} = \iint \mathrm{d}\mathbf{p}^N \mathrm{d}\mathbf{r}^N A(\mathbf{p}^N, \mathbf{r}^N) \rho(\mathbf{p}^N, \mathbf{r}^N) \quad [2-10]$$

The probability density distribution is in the canonical ensemble given by:

$$\rho(\mathbf{p}^N, \mathbf{r}^N) = \frac{\exp[-H(\mathbf{p}^N, \mathbf{r}^N)/k_B T]}{\iint \mathrm{d}\mathbf{p}^N \mathrm{d}\mathbf{r}^N \exp[-H(\mathbf{p}^N, \mathbf{r}^N)/k_B T]} \quad [2-11]$$

where  $H(p^N, r^N)$  is the system Hamiltonian,  $k_B$  is the Boltzmann constant, and  $T$  is the system temperature. In contrast, an MD simulation travels through phase space and as such, it generates naturally the appropriate weighting of the observable according to the probability distribution. In MD, we thus compute the time average of  $A$  as:

$$\langle A \rangle_{\text{time}} = \lim_{\tau \rightarrow \infty} \frac{1}{\tau} \int_{t=0}^{\tau} A(p^N(t), r^N(t)) dt \approx \frac{1}{M} \sum_{t=1}^M A(p^N, r^N) \quad [2-12]$$

$A(p^N, r^N)$  corresponds to the instantaneous value for the quantity  $A$ ,  $\tau$  represents the simulation time and  $M$  the total number of time steps. In an ergodic system at thermodynamic equilibrium, the time average of  $A$  corresponds to the ensemble average, and thus corresponds to the experimental observable. The latter is known as the *Ergodic hypothesis*.

There are four thermodynamic ensembles which are widely used in MD simulations: the *microcanonical ensemble* (NVE), the *canonical ensemble* (NVT), *isothermal–isobaric ensemble* (NPT) and *grand-canonical ensemble* ( $\mu$ VT)<sup>33,34</sup>. A microcanonical ensemble corresponds to an isolated system where the total number of simulated particles,  $N$ , the volume of the system,  $V$ , and the total energy,  $E$ , are kept constant. When representing a system, which is able to exchange energy with its environment, the system can reside in states that belong to the canonical ensemble. In addition to  $N$  and  $V$ , in the canonical ensemble also  $T$  (instead of  $E$ ) of the observed system is kept constant. In practice, this is realized by using an external heat bath to which the system couples, and which is simulated by using a thermostat<sup>35,36</sup> (e.g., Berendsen, Nosé-Hoover, Bussi, *etc.*). When a system at constant pressure is considered, the isothermal-isobaric ensemble results, where, next to a thermostat, also a barostat is employed in the MD simulation. In contrast to an NVE or NVT ensemble, the volume of the system,  $V$  –not to be confused with the interatomic potential– can fluctuate in order to keep the pressure constant. Finally, grand-canonical ensembles are appropriate when considering a system where particles are introduced or removed from the system, kept at constant pressure and temperature, during the computation. In this case, the variables kept constant are temperature, pressure and chemical potential. More information about ensembles used in MD can be found in<sup>33,34</sup>.

*In this work, all simulations are carried out in the NVT ensemble, representing closed systems found at constant temperature and volume.*

### 2-2.2d Thermostat

Thermostats are used to allow the MD system to generate a statistical ensemble at a specific and constant temperature, including the canonical ensemble, the grand canonical ensemble and the isobaric-isothermal ensemble. In this way, one can perform simulations closer to experimental conditions. An extensive overview on the algorithms of thermostats can be found in<sup>37</sup>. In this investigation, the Berendsen, Bussi and Nosé-Hoover thermostat were used.

The Berendsen thermostat rescales the velocities in each step proportional to the difference in temperature<sup>38</sup>. This effectively corresponds to adding and removing energy from the system in such a way that the total temperature remains constant. The velocity of every atom  $i$  is manipulated using a scaling factor  $\lambda$ :

$$v'_i = \lambda v_i \quad [2-13]$$

$$\lambda = \sqrt{1 + \frac{\Delta t}{\tau} \left( \frac{T_c}{T_t} - 1 \right)} \quad [2-14]$$

$T_c$  and  $T_t$  are the temperature of the heat bath and the temperature of the system at time step  $t$ , respectively.  $\tau$  is the coupling parameter which determines how strong the coupling is between the system and the heat bath. A  $\Delta t/\tau$  value of 0.1 ps is typically used.

Unlike the Berendsen thermostat, the Bussi thermostat uses a properly chosen scaling factor<sup>36</sup>. It can be seen as an extension of the Berendsen thermostat, adding a random force to assure a correct distribution of the kinetic energy. Here, the scaling factor  $\alpha$  is determined by a canonical equilibrium distribution. As a consequence, the factor is not solely dependent on the properties of the system, in contrast to  $\lambda$ , but is obtained from the gamma distribution. This way, the Bussi thermostat preserves the simple nature of the Berendsen thermostat but is able to describe a well-defined canonical ensemble.

The Nosé-Hoover thermostat considers the heat bath as an integral part of the system. This is done by introducing an artificial friction term,  $s$ , to the systems which

couples the system with a heat bath by introducing or releasing heat from the system. In this way, the total energy of the system is kept constant.  $s$  is controlled by an artificial mass term  $Q$ . The choice of  $Q$  regulates the effectiveness of this thermostat where large values for  $Q$  leads to weak coupling. More information can be found in<sup>39</sup>.

### *2-2.2e Boundary conditions*

As stated before, particles in MD can be defined as atoms, groups of atoms or whole molecules. In this thesis, particles are defined as atoms. From the basics, we know that forces in MD simulations are a function of the particle coordinates (*i.e.*,  $3N$ , where  $N$  is the number of particles). As every particle corresponds to a single atom, the calculations have to consider three times the number of atoms in the system as variables. In order to obtain results in a reasonable amount of time, MD systems are typically limited to  $10^2$ - $10^7$  particles depending on the used method (see below). This means that, when linking with a macroscopic situation, only a microscopic piece of the system can be investigated. As a result, the simulation will strongly depend on how atoms, at or near the borders of the simulation box, are treated. How do we describe the particles at the border of the system?

The boundary conditions depend on the system to be investigated. Three types of boundary conditions are commonly used in MD simulations<sup>33</sup>: free boundary conditions (FBC), reflective boundary conditions (RBC) and periodic boundary conditions (PBC).

FBC are typically used when the border of the system can be neglected or to investigate molecules or clusters in vacuum. Because of this, no mathematical conditions are applied on the edge of the simulated box. RBC refer to boundaries that simply reflect all particles impacting the border of the simulation box, by inverting the momentum of the impacting particles. PBC are used to mimic an infinite system while keeping the number of particles limited. The principle of PBC is illustrated in Figure 2-1. When a particle, like particle A in Figure 2-1, moves through the boundary, it will be replaced by a replica of that same particle A at the opposite side of the box. This means that the simulated system is surrounded by endless copies of itself in all six directions ( $x$ ,  $-x$ ,  $y$ ,  $-y$ ,  $z$ ,  $-z$ ) and every linear combination of these directions. Furthermore, this also means that all particles will not only interact with every particle in the simulated

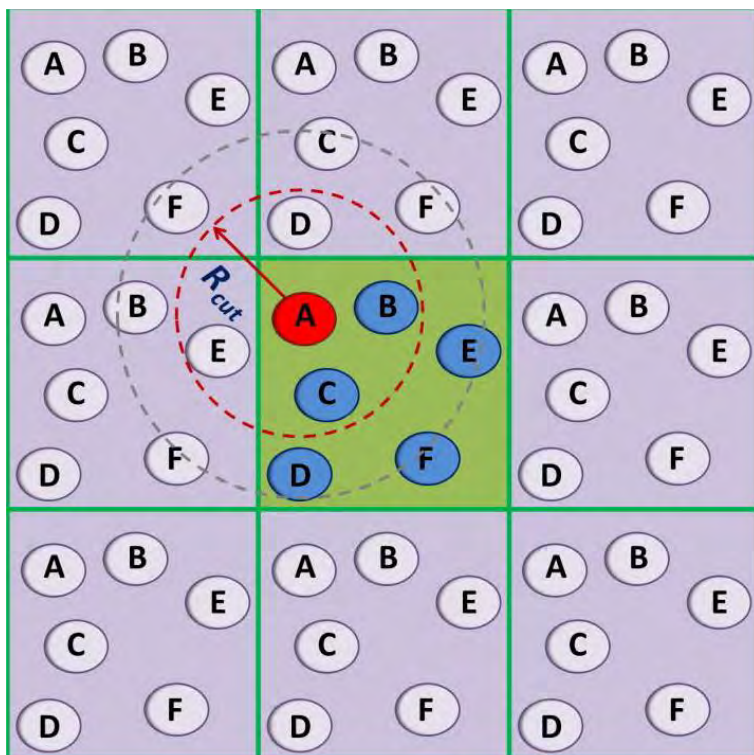


**Figure 2-1. Schematic representation of the principles of periodic boundary conditions.** Copies of the green cell are seen around the cell in all four directions (six directions for 3D systems). A visualization of the cut-off distance is given for particle A in the original cell (red circle). If this distance was larger (grey circle), particle A would be able to interact with multiple copies of particles B, C, D, E and F.

box but also with their copies in the neighboring cells. One therefore needs to employ a minimal box size, taking into account the so-called *cut-off distance* of the interaction potential. The cut-off distance,  $R_{cut}$ , refers to the maximum distance in which two particles are able to interact with each other (repel or attract). However, it is important that each particle is unable to interact with its own copy or multiple copies of the same particle in order to avoid artefact interactions. To overcome this, the dimensions of the simulation box must always be greater than  $2R_{cut}$ . This is known as the *minimum image criterion*.

### 2-2.2f Interatomic potentials

As explained at the beginning of **section 2-2.2**, the forces acting on the particles are calculated as the negative gradient of the interatomic potential. This

interatomic potential must be able to represent all possible atomic interactions for the system of interest. In order to investigate biomolecules, the interactions between a multitude of chemical elements need to be described by the used force field (*e.g.*, H, C, O, N, S, P, *etc.*). Two types of force fields can be discerned: *reactive force fields* and *non-reactive force fields*.

Unlike its non-reactive counterpart, reactive force fields are able to describe changes in the binding structure of the molecular system. This means that one is able to investigate bond formation and dissociation during the course of the MD simulation. This provides the user with the ability to investigate the reactivity of the system of interest. However, this also means that the connectivity of the system needs to be recalculated every time step, which results in a steep increase in calculation time. In the non-reactive case, the neighbors of each particle remain unchanged. This means that, when using a non-reactive force fields, only the region around the harmonic minimum of the potential can be considered. Another contrast between the two types of force fields is the fact that reactive force fields usually represent only a limited number of elements, while non-reactive force fields are typically more generic.

Depending on the research question at hand, a particular force field is used. Reactive force fields can be used to investigate the reactivity of a system and (unknown) chemical processes. Non-reactive force fields, in contrast, are typically used to investigate dynamic and static properties of the system over a longer period, as these calculations are generally much faster.

*We are specifically interested in the oxidation processes that might occur because of the treatment of biological tissue with cold atmospheric pressure plasmas. For this purpose, we used reactive force fields to investigate the atomic system.*

### **2-2.2g Reactive force fields**

Reactive force fields can be divided in two groups: force fields that use a reaction cutoff distance, and empirical force fields. *Reaction cutoff force fields* use an imaginary switch, which is implemented to simulate bond formation or dissociation reactions. These methods rely on the distance between two reactive particles. If the distance between these particles is smaller than the cutoff distance, the bond is



formed. This results in sudden bond formation or dissociation interactions and is suited for polymerization reactions. These force fields have been used by, *e.g.*, Wu *et al.*, Lin *et al.* and Bermejo *et al.*, investigating the polymerization of various organic molecules<sup>40–42</sup>. Other examples of cutoff distance force fields are the *Breakable Quartic Bond Potential* and the *Reflected Weeks-Chandler-Andersen Potential*<sup>43</sup>.

The second class of reactive force fields are known as empirical force fields. These force fields are able to describe chemical reactions more smoothly and yield a continuous transition between the bonded and non-bonded state. Hence, these force fields can be used to investigate reaction mechanisms and evaluate transition states. Examples of such force fields are the Stillinger-Weber potential<sup>44</sup>, embedded atom method (EAM)<sup>45</sup>, the Finnis-Sinclair potential<sup>46</sup>, the Abell-Tersoff-Brenner potential<sup>47</sup> and the ReaxFF potential<sup>27</sup>. The first potential is based on the many-body-method where the interatomic interactions are described by a combination of many-body terms (in the case of the Stillinger-Weber potential, a combination of the two-body and three-body terms is used). The last three examples are bond-order potentials where both the Abell-Tersoff-Brenner and ReaxFF potentials are based on the relations of Abell<sup>48</sup>. Bond-order potentials are based on the idea that chemical bonds are dependent on the bonding environment (angle, bond length and number of bonds).

For investigating the expected oxidation of biochemical molecules, the reaction mechanisms and transition states of reactions, both known and unknown, are crucial. Therefore, the use of empirical reactive force fields is preferred. In this context, only the Abell-Tersoff-Brenner potential and ReaxFF potential are able to investigate interactions with biochemical molecules. Other potentials, which were mentioned above, have been designed for the investigation of either silicon-based materials (Stillinger-Weber potential) or metals (EAM) and either yield a very low transferability or do not describe the necessary elements needed for investigating biomolecules. The Abell-Tersoff-Brenner potential was initially designed for the simulation of carbohydrates but was extended by Ni *et al.*<sup>49</sup> to describe H/C/O materials, while the original Tersoff potential was developed for silicon as well. Compared to the ReaxFF potential, it has the advantage of being simple, containing  $\pm 100$  parameters. However, the Abell-Tersoff-Brenner potential is unable to

accurately describe the energy profiles of reactions. Together with the fact that a wide variety of Reax force fields has been developed, able to describe an extensive range of elements, makes the ReaxFF potential the method of choice in the investigation of the oxidation of biomolecules (containing not only H, C and O but also N, S and P) for classical MD.

### 2-2.2h ReaxFF potential

As stated above, the *Reax force field* (ReaxFF) is an empirical and classical force field, able to describe long range interactions (van der Waals and Coulomb interactions). It was introduced by van Duin in 2001 for hydrocarbons<sup>27</sup>. In the past 15 years, ReaxFF has become one of the most parametrized reactive force fields able to describe a large part of the periodic table of the elements. For instance, this force field was used to investigate the chemistry of polymers<sup>50,51</sup>, combustion<sup>52,53</sup>, catalysis<sup>54</sup>, metals<sup>55,56</sup> and metal oxides<sup>57–59</sup>, biomolecules<sup>12,60–62</sup>, *etc.*

The ReaxFF potential energy is divided in multiple partial energy contributions accounting for the bond energy, the energy of the lone electron pairs, energy contributions for over- and undercoordination, valence angle energy, torsion energy, penalty energy, H-bond energy, conjugation energy, and energy contributions for van der Waals and Coulomb interactions. In practice, this means that the potential energy is described by the bond energy which is corrected using attractive and repulsive terms.

$$E_{system} = E_{bond} + E_{lp} + E_{over} + E_{under} + E_{val} + E_{tors} + E_{pen} + E_{H-bond} + E_{conj} + E_{vdw} + E_{cou} \quad [2-15]$$

In ReaxFF, the potential energy between a pair of atoms is dependent on the bond order, which is directly obtained from the interatomic distance. The combined equation contains 58 parameters where the details and the expression can be found in<sup>27</sup>.

The necessary parameters for the partial energy contributions are usually derived from quantum mechanical calculations like DFT using a, preferably large, set of molecules, known as the *training set*. As the results of MD simulations are strongly dependent on the derived forces, it is clear that these results strongly depend

on the capability of the force field to describe the investigated system. Therefore, it is necessary to use a force field which has been parametrized with a training set that contains all chemical structures (*e.g.*, functional groups, specific chemical bonds, *etc.*) and elements as present in the investigated system.

- For the investigation of D-glucose (**chapter 3**), the parameters derived by Rahaman<sup>63</sup> were used. These parameters are able to accurately describe the interactions between C/H/O and N atoms in structures which closely represent sugars. Hence the use of this force field.
- For the investigation of DNA and nucleotides, a more advanced parameter set was used (**chapter 4**). We employed parameters derived by Monti<sup>64</sup> which were modified in order to describe the interactions between C/H/O/N and P atoms in amino acids and nucleotides. This was done in collaboration with the group of Prof. Van Duin.

## 2-2.3 Quantum mechanical MD - DFTB

### 2-2.3a Introduction

The use of classical force fields enables one to describe relatively large systems (both reactive and non-reactive) over relatively long time scales ( $10^{-12}$ - $10^{-7}$  s)<sup>24</sup>. This, however, comes at the price of having to use classical force fields. This becomes clear when interactions and reaction energies are involved in the research question. As already pointed out, when discussing the nature of reactive force fields and reactive MD, the results of MD simulations are highly dependent on the accurate calculation of the potential energies and the forces. Therefore, the use of specific force fields is only encouraged when investigating systems which are very closely related to the used training set of that particular force field. In the course of this research, the currently available force fields were unable to accurately describe particular systems and their properties. In this respect, I would like to direct the reader to the conclusion of **chapter 4**. This observation prompted us to use more accurate methods.

*Ab initio* calculations form without a doubt the benchmark for simulation methods but are computationally very expensive and can only be used for the investigation of small and simple systems (up to  $\sim 10^3$  atoms)<sup>24</sup> as stated before. This

category of calculations represents the other side of the accuracy–computational speed compromise (*ab initio* vs empirical methods). For the systems investigated in this thesis, *ab initio* methods, such as DFT, are not the method of choice, given the often-high number of atoms required. Systems which cannot be represented by the use of empirical force fields and which are simultaneously too large to be calculated using DFT, were investigated using a semi-empirical technique, called Density-Functional based Tight-Binding (DFTB).

### *2-2.3b Density-functional based tight-binding*

DFTB is a computational technique to perform MD simulations in a similar way as, for example, ReaxFF. However, the big difference lies in the calculation of the required energies and therefore the obtained forces. DFTB relies on the tight-binding scheme. In tight-binding models, the ionic potentials are described as being very strong in such a way that the electrons are tightly bound to a single atom without feeling the influence of other atoms, essentially forming atomic orbitals (hence the name *tight-binding scheme*)<sup>65,66</sup>. This will result in a relatively simple description of the wave function and an electron energy close to the ionization energy. As such, the method is able to rapidly and qualitatively calculate the electronic structure for condensed matter and crystals, but it will fail for other systems, such as biomolecules, due to the lack of electron-electron interactions. Furthermore, much like classical MD, the results are highly dependent on the parametrization and the transferability to various systems. These issues and the, sometimes difficult, parametrization can be avoided using more complex computational methods based on this tight-binding scheme. A few successful implementations include Density Functional Theory parametrized Tight-Binding<sup>67</sup>, Hartree-Fock based Tight-Binding<sup>68</sup> and Density-Functional based Tight-Binding. In the latter, the Hamiltonian matrix elements are calculated using a non-orthogonal basis of atomic orbitals<sup>25,69</sup>.

*In this thesis, I only focused on density-functional based tight-binding. For this reason, DFTB will be described in more detail in this section.*

DFTB uses a series expansion of the Kohn-Sham total energy used in DFT calculations, where only the valence orbitals are taking into account. The latter

approximation is known as the *frozen-core approximation*. When one replaces the charge densities with a superposition of an input density and a small fluctuation,  $n'o + \delta n'$ , while neglecting the higher-order terms, the following general expression for the energy of the system can be written<sup>25,70</sup>:

$$E_0^{TB} = \sum_i^{\text{occ}} \langle \psi_i | \hat{H}_0 | \psi_i \rangle + E_{\text{rep}} \quad [2-16]$$

In this expression, the energy of the system,  $E_0^{TB}$ , represents a sum (over all the occupied Kohn-Sham orbitals) over the energy contributions that only depend on the input density,  $n_0$ , together with the core-core repulsion.  $E_{\text{rep}}$  represents the pairwise repulsive and short ranged interactions, which can easily be derived using the results of self-consistent LDA calculations (*Local-Density Approximation*)<sup>23,25</sup>. This results in an  $E_0^{TB}$  which only depends on one- and two-body contributions. This approach, known as zeroth-order DFTB, is able to accurately describe a wide range of chemical bonds for systems where a superposition of overlapping atom-like densities serves as a good approximation<sup>25</sup>.

However, problems arise when charges are introduced to the system for the formation of chemical bonds, *i.e.*, between two different atom types. This required the implementation of a self-consistent field algorithm without sacrificing the simplicity and the efficient nature of zeroth-order DFTB. This implementation is known as the second-order DFTB or Self-Consistent-Charge-DFTB (SCC-DFTB)<sup>25</sup>. In this approach, the second term of the series expansion of the Kohn-Sham total energy is included, unlike in the case of zeroth-order DFTB. Taking this second term into account, the following general expression for the total energy of the system can be derived<sup>25</sup>:

$$E_2^{TB} = \sum_i^{\text{occ}} \langle \psi_i | \hat{H}_0 | \psi_i \rangle + \frac{1}{2} \sum_{\alpha,\beta}^N \gamma_{\alpha\beta} \Delta q_\alpha \Delta q_\beta + E_{\text{rep}} \quad [2-17]$$

$$\gamma_{\alpha\beta} = \frac{1}{|\vec{R}_\alpha - \vec{R}_\beta|} - e^{-\tau_\alpha(\vec{R}_\alpha - \vec{R}_\beta)} \left( \frac{\tau_\beta^4 \tau_\alpha}{2(\tau_\alpha^2 - \tau_\beta^2)} - \frac{\tau_\beta^6 - 3\tau_\beta^4 \tau_\alpha^2}{(\tau_\alpha^2 - \tau_\beta^2)^3 (\vec{R}_\alpha - \vec{R}_\beta)} \right) - e^{-\tau_\beta(\vec{R}_\alpha - \vec{R}_\beta)} \left( \frac{\tau_\alpha^4 \tau_\beta}{2(\tau_\beta^2 - \tau_\alpha^2)} - \frac{\tau_\alpha^6 - 3\tau_\alpha^4 \tau_\beta^2}{(\tau_\beta^2 - \tau_\alpha^2)^3 (\vec{R}_\alpha - \vec{R}_\beta)} \right) \quad [2-18]$$

In spite of its rather complicated formulation, the second term of  $E_2^{TB}$  is solely dependent on the charges of both atoms  $\alpha$  and  $\beta$  ( $q_\alpha$  and  $q_\beta$ , respectively) and the so-called electron repulsion function,  $\gamma_{\alpha\beta}$ <sup>69</sup>.  $\gamma_{\alpha\beta}$  in turn is only dependent on the distance between the two atoms and their respective Hubbard parameters  $U_i = 0.3125 \tau_i$  ( $\tau_i$  is known as the normalized Slater-type spherical charge density), which is related to the chemical hardness<sup>71</sup>. This way, a self-consistent scheme is realized based on the second-order expansion of the Kohn-Sham total energy, able to describe the charge-dependent behavior in function of the distance. Using SCC-DFTB one is able to reproduce geometries of large molecular structures<sup>25,72</sup>, as well as the relative energies of peptides and hydrogen bonding<sup>73,74</sup>. More information about SCC-DFTB can be found in the work of Elstner *et al.*<sup>25</sup>.

Despite the many successes of second-order DFTB, several limitations are still found. A few examples are the overestimation of the heats of formation, the often-poor representation of radicals and the inability to describe certain modes of vibration well enough. Furthermore, calculations are limited by the inability of changing the chemical hardness (needed when simulating ions compared to their neutral counterpart). In order to improve the DFTB scheme, an additional term of the series expansion of the Kohn-Sham total energy can, again, be considered, as proposed by Gaus *et al.*<sup>69</sup>. Adding the third term of the Taylor expansion to SCC-DFTB results in the formation of the third-order DFTB scheme, or DFTB3. When treating the function of the total energy in a similar way as for the second-order expression, the derivatives of the  $\gamma_{ij}$  functions, with respect to the charges,  $\Gamma_{ij}$ , are introduced.

$$E_3^{TB} = \sum_i^{\text{occ}} \langle \psi_i | \hat{H}_0 | \psi_i \rangle + \frac{1}{2} \sum_{\alpha,\beta}^N \gamma_{\alpha\beta} \Delta q_\alpha \Delta q_\beta + \frac{1}{3} \sum_{\alpha,\beta} \Delta q_\alpha^2 \Delta q_\beta \Gamma_{\alpha,\beta} + E_{\text{rep}} \quad [2-19]$$

$$\begin{aligned} \Gamma_{\alpha,\beta} &= \left. \frac{\delta \gamma_{\alpha\beta}}{\delta q_\alpha} \right|_{q_\alpha^0} = \left. \frac{\delta \gamma_{\alpha\beta} \delta U_\alpha}{\delta U_\alpha \delta q_\alpha} \right|_{q_\alpha^0} \quad \text{with } \alpha \neq \beta \\ \Gamma_{\alpha,\alpha} &= \left. \frac{\delta \gamma_{\alpha\alpha}}{\delta q_\alpha} \right|_{q_\alpha^0} = \left. \frac{1}{2} \frac{\delta \gamma_{\alpha\alpha} \delta U_\alpha}{\delta U_\alpha \delta q_\alpha} \right|_{q_\alpha^0} \end{aligned} \quad [2-20]$$

$\Gamma_{\alpha\beta}$  implements the ability to calculate the chemical hardness of atoms in different charged states. Furthermore, the third-order derivation will not only be able to describe the charge dependent atomic electron-electron repulsion, but also the calculation of proton affinities and charge transfers. A full description of DFTB3 can be found in the work of Gaus *et al.*<sup>69</sup>.

The use of the above-mentioned energy equations results in a vast increase in computational cost in contrast to, *e.g.*, ReaxFF. For this reason, systems smaller than  $10^3$  atoms can be investigated over a timescale of  $10^{-10}$  s within a reasonable calculation time.

## 2-3 References

1. Aspray, W. *John von Neumann and the Origins of Modern Computing*. (The MIT Press, 1990).
2. Von Neumann, J. IFORS' Operational Research Hall of Fame. *Int. Trans. Oper. Res.* **13**, 85–90 (2006).
3. Ulam, S. John von neumann. *Bull. Am. Math. Soc.* **64**, 1–49 (1958).
4. Rauk, A., Yu, D. & Armstrong, D. A. Toward Site Specificity of Oxidative Damage in Proteins: C-H and C-C Bond Dissociation Energies and Reduction Potentials of the Radicals of Alanine, Serine, and Threonine Residues - an ab initio Study. *J. Am. Chem. Soc.* **7863**, 208–217 (1997).
5. McGillen, M. R., Percival, C. J., Shallcross, D. E. & Harvey, J. N. Is hydrogen abstraction an important pathway in the reaction of alkenes with the OH radical? *Phys. Chem. Chem. Phys.* **9**, 4291–300 (2007).
6. Ji, Y. J., Xia, Y. Y., Zhao, M. W., Huang, B. D. & Li, F. Theoretical study of the OH reaction with cytosine. *J. Mol. Struct. THEOCHEM* **723**, 123–129 (2005).
7. Szymusiak, H. & Zieliński, R. Bond dissociation enthalpy of phenolic antioxidants. *Polish J. Food Nutr. Sci.* **12**, 129–135 (2003).
8. Codorniu-Hernández, E., Hall, K. W., Ziemianowicz, D., Carpendale, S. & Kusalik, P. G. Aqueous production of oxygen atoms from hydroxyl radicals. *Phys. Chem. Chem. Phys.* **16**, 26094 (2014).
9. Codorniu-hern, E. & Kusalik, P. G. Insights into the Solvation and Mobility of the Hydroxyl Radical in Aqueous Solution. *J. Chem. Theory Comput.* **7**, 3725–3732 (2011).
10. Codorniu-Hernández, E. & Kusalik, P. G. Mobility Mechanism of Hydroxyl Radicals in Aqueous Solution via Hydrogen Transfer. *J. Am. Chem. Soc.* **134**, 532–538 (2012).
11. Abolfath, R. M., Carlson, D. J., Chen, Z. J. & Nath, R. A Molecular Dynamics Simulation of DNA Damage Induction by Ionizing Radiation. *Phys. Med. Biol.* **58**, 7143–7157 (2013).
12. Yusupov, M. *et al.* Inactivation of the endotoxic biomolecule lipid A by oxygen plasma species: a reactive molecular dynamics study. *Plasma Process. Polym.* **12**, 162–171 (2014).
13. Yusupov, M. *et al.* Plasma-Induced Destruction of Bacterial Cell Wall Components: a Reactive Molecular Dynamics Simulation. *J. Phys. Chem. C* **117**, 5993–5998 (2013).



14. Khosravian, N., Kamaraj, B., Neyts, E. C. & Bogaerts, A. Structural modification of P-glycoprotein induced by OH radicals: insights from atomistic simulations. *Sci. Rep.* **6**, 19466 (2016).
15. Van der Paal, J., Neyts, E. C., Verlackt, C. & Bogaerts, A. Effect of lipid peroxidation on membrane permeability of cancer and normal cells subjected to oxidative stress. *Chem. Sci.* **7**, 489 (2016).
16. Verlackt, C. C. W. *et al.* Atomic-scale insight into the interactions between hydroxyl radicals and DNA in solution using the ReaxFF reactive force field. *New J. Phys.* **17**, 103005 (2015).
17. Sprou, D., Young, M. A. & Beveridge, D. L. Molecular Dynamics Studies of Axis Bending in d(G5-(GA4T4C)2-C5) and d(G5-(GT4A4C)2-C5): Effects of Sequence Polarity on DNA Curvature. *J. Mol. Biol.* **285**, 1623–1632 (1999).
18. Vernier, P. T. *et al.* Electroporating fields target oxidatively damaged areas in the cell membrane. *PLoS One* **4**, e7966 (2009).
19. Van Gaens, W. & Bogaerts, A. Kinetic Modelling for an Atmospheric Pressure Argon Plasma Jet in Humid Air. *J. Phys. D. Appl. Phys.* **46**, 275201 (2013).
20. Bogaerts, A., Eckert, M., Mao, M. & Neyts, E. Computer modelling of the plasma chemistry and plasma-based growth mechanisms for nanostructured materials. *J. Phys. D. Appl. Phys.* **44**, 174030 (2011).
21. Tian, W. & Kushner, M. J. Atmospheric pressure dielectric barrier discharges interacting with liquid covered tissue. *J. Phys. D. Appl. Phys.* **47**, 165201 (2014).
22. Lindsay, A., Anderson, C., Slikboer, E., Shannon, S. & Graves, D. Momentum, heat, and neutral mass transport in convective atmospheric pressure plasma-liquid systems and implications for aqueous targets. *J. Phys. D. Appl. Phys.* **48**, 424007 (2015).
23. Atkins, P. & Friedman, R. *Molecular Quantum Mechanics*. (Oxford University Press, 2008).
24. Neyts, E. C., Yusupov, M., Verlackt, C. C. & Bogaerts, A. Computer simulations of plasma–biomolecule and plasma–tissue interactions for a better insight in plasma medicine. *J. Phys. D. Appl. Phys.* **47**, 293001 (2014).
25. Elstner, M. *et al.* Self-consistent-charge density-functional tight-binding method for simulations of complex materials properties. *Phys. Rev. B* **58**, 7260–7268 (1998).
26. Car, R. Unified Approach for Molecular Dynamics and Density-Functional Theory. *Phys. Rev. Lett.* **55**, 2471–2474 (1985).

27. van Duin, A. C. T., Dasgupta, S., Lorant, F. & Goddard, W. A. ReaxFF: a Reactive Force Field for Hydrocarbons. *J. Phys. Chem. A* **105**, 9396–9409 (2001).
28. Abraham, M. J. *et al.* GROMACS: High performance molecular simulations through multi-level parallelism from laptops to supercomputers. *Softw. X* **1**, 19–25 (2015).
29. Pronk, S. *et al.* GROMACS 4.5: a high-throughput and highly parallel open source molecular simulation toolkit. *Bioinformatics* **29**, 845–854 (2013).
30. Case, D. A. *et al.* The Amber Biomolecular Simulation Programs. *J. Comput. Chem.* **26**, 1668–1687 (2005).
31. Born, M. & Oppenheimer, R. Zur Quantentheorie der Molekeln. *Ann. Phys.* **74**, 457–484 (1927).
32. Verlet, L. Computer Experiments on Classical Fluids. I. Thermodynamical Properties of Lennard-Jones Molecules. *Phys. Rev.* **159**, 159 (1967).
33. Allen, M. P. & Tildesley, D. J. *Computer Simulation of Liquids*. (Oxford University Press, 1991).
34. Erpenbeck, J. J. & Wood, W. W. in *Statistical Mechanics Part B: Time-Dependent Processes* 1–40 (Springer US, 1977).
35. Rühle, V. Berendsen and Nose-Hoover Thermostats. 1–4 (2007).
36. Bussi, G., Donadio, D. & Parrinello, M. Canonical sampling through velocity rescaling. *J. Chem. Phys.* **126**, 14101 (2007).
37. Hünenberger, P. H. Thermostat algorithms for molecular dynamics simulations. *Adv. Polym. Sci.* **173**, 105–147 (2005).
38. Berendsen, H. J. C., Postma, J. P. M., van Gunsteren, W. F., Di Nola, A. & Haak, J. R. Molecular dynamics with coupling to an external bath. *J. Chem. Phys.* **81**, 3684 (1984).
39. Evans, D. J. & Holian, B. L. The Nosé-Hoover thermostat. *J. Chem. Phys.* **83**, 4069 (1998).
40. Lin, B., Boinske, P. T. & Halley, J. W. A molecular dynamics model of the amorphous regions of polyethylene oxide. *J. Chem. Phys.* **105**, 1668 (1996).
41. Wu, C. & Xu, W. Atomistic molecular modelling of crosslinked epoxy resin. *Polymer (Guildf)*. **47**, 6004–6009 (2006).
42. Bermejo, J. S. & Ugarte, C. M. Chemical Crosslinking of PVA and Prediction of Material Properties by Means of Fully Atomistic MD Simulations. *Macromol. Theory Simulations* **18**, 259–267 (2009).

43. Farah, K., Müller-Plathe, F. & Böhm, M. C. Classical reactive molecular dynamics implementations: state of the art. *ChemPhysChem* **13**, 1127–1151 (2012).
44. Stillinger, F. H., Thomas, A., Laboratories, T. B. & Hill, M. Computer simulation of local order in condensed phases of silicon. *Phys. Rev. B* **31**, 5262–5271 (1985).
45. Daw, M. S., Foiles, S. M. & Baskes, M. I. The Embedded-Atom Method: a Review of Theory and Applications. *Mater. Sci. Reports* **9**, 251–310 (1993).
46. Finnis, M. W. & Sinclair, J. E. A simple empirical N-body potential for transition metals. *Philos. Mag. Part A* **50**, 45–55 (1984).
47. Brenner, D. W. The Art and Science of an Analytic Potential. *Phys. Status Solidi B Basic Solid State Phys.* **23**, 23–40 (2000).
48. Abell, G. C. Empirical Chemical Pseudopotential Theory of Molecular and Metallic Bonding. *Phys. Rev. B* **31**, 6184–6196 (1985).
49. Ni, B., Lee, K.-H. & Sinnott, S. B. A Reactive Empirical Bond Order (REBO) Potential for Hydrocarbon–Oxygen Interactions. *J. Phys. Condens. Matter* **16**, 7261–7275 (2004).
50. Odegard, G. M. *et al.* Predicting Mechanical Response of Crosslinked Epoxy Using ReaxFF. *Chem. Phys. Lett.* **591**, 175–178 (2014).
51. Chenoweth, K., Cheung, S., van Duin, A. C. T., Goddard, W. A. & Kober, E. M. Simulations on the Thermal Decomposition of a Poly(dimethylsiloxane) Polymer Using the ReaxFF Reactive Force Field. *J. Am. Chem. Soc.* **127**, 7192–7202 (2005).
52. Chenoweth, K., van Duin, A. C. T. & Goddard, W. A. ReaxFF Reactive Force Field for Molecular Dynamics Simulations of Hydrocarbon Oxidation. *J. Phys. Chem. A* **112**, 1040–1053 (2008).
53. Chen, B., Diao, Z. & Lu, H. Using the ReaxFF Reactive Force Field for Molecular Dynamics Simulations of the Spontaneous Combustion of Lignite with the Hatcher Lignite Model. *Fuel* **116**, 7–13 (2014).
54. Somers, W., Bogaerts, A., van Duin, A. C. T. & Neyts, E. C. Plasma Species Interacting with Nickel Surfaces: Toward an Atomic Scale Understanding of Plasma-Catalysis. *J. Phys. Chem. C* **116**, 20958–20965 (2012).
55. Sanz-Navarro, C. F. *et al.* Molecular Dynamics Simulations of Carbon-Supported Ni Clusters Using the Reax Reactive Force Field. *J. Phys. Chem. C* **112**, 12663–12668 (2008).

- 
56. Cheung, S., Deng, W. Q., van Duin, A. C. T. & Goddard, W. A. ReaxFF(MgH) Reactive Force Field for Magnesium Hydride Systems. *J. Phys. Chem. A* **109**, 851–859 (2005).
  57. Huygh, S., Bogaerts, A., van Duin, A. C. T. & Neyts, E. C. Development of a ReaxFF Reactive Force Field for Intrinsic Point Defects in Titanium Dioxide. *Comput. Mater. Sci.* **95**, 579–591 (2014).
  58. Raymand, D., van Duin, A. C. T., Spangberg, D., Goddard III, W. A. & Hermansson, K. Water Adsorption on Stepped ZnO Surfaces from MD Simulation. *Surf. Sci.* **604**, 741–752 (2010).
  59. Aryanpour, M., van Duin, A. C. T. & Kubicki, J. D. Development of a Reactive Force Field for Iron-Oxyhydroxide Systems. *J. Phys. Chem. A* **114**, 6298–6307 (2010).
  60. Yusupov, M., Neyts, E. & Bogaerts, A. Atomic-scale simulation of reactive oxygen species interacting with bacterial cell walls. *New J. Phys.* **14** 093043 (2012).
  61. Yusupov, M. *et al.* Atomic-scale simulations of reactive oxygen plasma species interacting with bacterial cell walls. *New J. Phys.* **14**, 093043 (2012).
  62. Van der Paal, J., Aernouts, S., van Duin, A. C. T., Neyts, E. C. & Bogaerts, A. Interaction of O and OH Radicals With a Simple Model System for Lipids in the Skin Barrier: a Reactive Molecular Dynamics Investigation for Plasma Medicine. *J. Phys. D. Appl. Phys.* **46**, 395201 (2013).
  63. Rahaman, O., van Duin, A. C. T., Goddard III, W. A. & Doren, D. J. Development of a ReaxFF Reactive Force Field for Glycine and Application to Solvent Effect and Tautomerization. *J. Phys. Chem. B* **115**, 249–261 (2011).
  64. Monti, S. *et al.* Exploring the Conformational and Reactive Dynamics of Biomolecules in Solution Using an Extended Version of the Glycine Reactive Force Field. *Phys. Chem. Chem. Phys.* **15**, 15062–77 (2013).
  65. Paxton, A. T. An Introduction to the Tight Binding Approximation – Implementation by Diagonalisation. *Methods* **42**, 145–176 (2009).
  66. Slater, J. C. & Koster, G. F. Simplified LCAO Method for the Periodic Potential Problem. *Phys. Rev.* **94**, 1498–1524 (1954).
  67. Cohen, R. E., Mehl, M. J. & Papaconstantopoulos, D. A. Tight-binding Total-Energy Method for Transition and Noble Metals. *Phys. Rev. B* **50**, 694–697 (1994).
  68. Artacho, E. & Yndurain, F. Nonparametrized Tight-Binding Method for Local and Extended Defects in Homopolar Semiconductors. *Phys. Rev. B* **44**, 6169–6187 (1991).

- 69. Gaus, M., Cui, Q. & Elstner, M. DFTB3: Extension of the Self-Consistent-Charge Density-Functional Tight-Binding Method (SCC-DFTB). *J. Chem. Theory Comput.* **7**, 931–948 (2011).
- 70. Foulkes, W. M. C. & Haydock, R. Tight-Binding Models and Density-Functional Theory. *Phys. Rev. B* **39**, 12520–12536 (1989).
- 71. Parr, R. G. & Pearson, R. G. Absolute Hardness: Companion Parameter to Absolute Electronegativity. *J. Am. Chem. Soc.* **105**, 7512–7516 (1983).
- 72. Sattelmeyer, K. W., Tirado-Rives, J. & Jorgensen, W. L. Comparison of SCC-DFTB and NDDO-Based Semiempirical Molecular Orbital Methods for Organic Molecules. *J. Phys. Chem. A* **110**, 13551–13559 (2014).
- 73. Otte, N., Scholten, M. & Thiel, W. Looking at Self-Consistent-Charge Density Functional Tight Binding from a Semiempirical Perspective. *J. Phys. Chem. A* **111**, 5751–5755 (2007).
- 74. Seabra, G. D. M., Walker, R. C. & Roitberg, A. E. Are Current Semiempirical Methods Better than Force Fields? A Study from the Thermodynamics Perspective. *J. Phys. Chem. A* **113**, 11938–11948 (2009).

## **3 Molecular Dynamics Simulations: D-Glucose**

This chapter served as a way to develop the necessary know-how of the code and MD simulations more in general, as well as knowledge on the expected reactions and behavior of biomolecules during treatment.



## 3-1 Introduction

### 3-1.1 Saccharides

Sugars, or saccharides, form one of the four basic building blocks of cells, next to fatty acids, amino acids and nucleotides<sup>1</sup>. Saccharides are formed out of a combination of C, H and O, generally following the  $(\text{CH}_2\text{O})_n$  structure. Three main groups of saccharides can be classified: polysaccharides, oligosaccharides and monosaccharides. The monosaccharides form the building blocks of all sugars.

Monosaccharides are connected to each other by a glycosidic bond as a result of a condensation reaction (see Figure 3-1)<sup>1</sup>. The number of monosaccharides within a single sugar polymer determines whether this molecule is called an oligosaccharide or a polysaccharide. Here, we follow the general rule which dictates that saccharides containing more than nine glycosidic bonds (or ten monosaccharides) are called polysaccharides, while smaller chains are oligosaccharides.

Glucose is one of the best known monosaccharides, together with fructose and galactose, as these are the three main sugars which are absorbed into the blood stream during digestion<sup>2,3</sup>. The chemical structures of these sugars are given in Figure 3-2. There are slight differences between these structures (*e.g.*, changes in

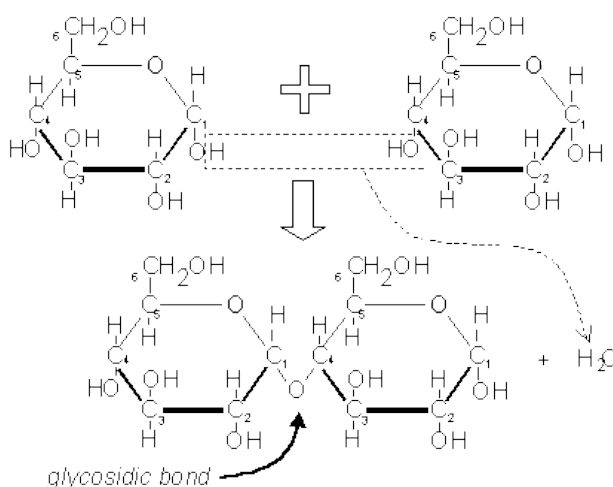


**Figure 3-1. Condensation reaction of glucose, forming the disaccharide maltose.** This reaction results in the formation of a 1-4 glycosidic bond (carbon 1 and 4 of both glucose molecules are connected). Taken from <http://www.mrothery.co.uk/biochm/biochmnotes.htm>.



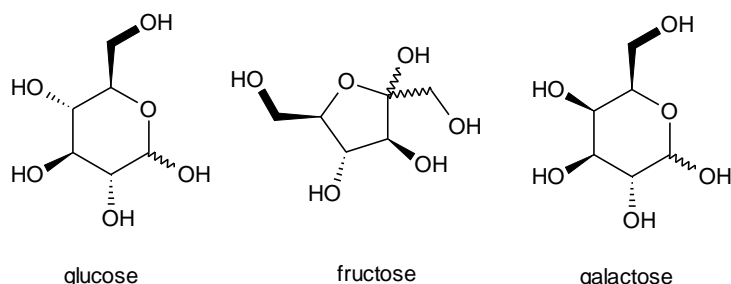



**Figure 3-2. Chemical structure of glucose (left), fructose (middle) and galactose (right).**

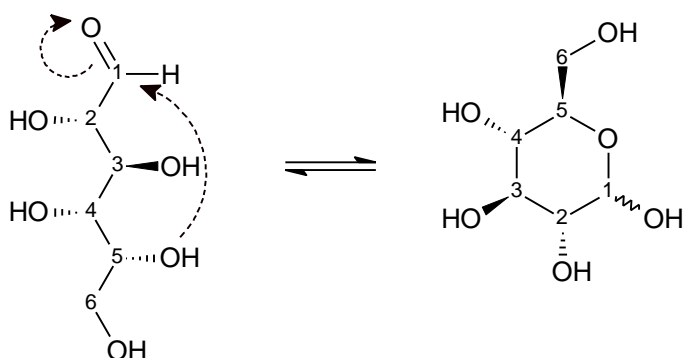


**Figure 3-3. Equilibrium between the open structure and ring structure of monosaccharides.** In this figure it is depicted in the case of an aldose, leading to the formation of glucose. This also happens to ketoses, to form, *e.g.*, fructose. In this case the C-2 of the open chain contains the C=O (ketone) instead of C-1.

the chiral centers or the number of C-atoms in the ring). The monosaccharides mentioned in Figure 3-2 all contain a ring structure. Although usually found in a ring formation, monosaccharides can be found in an open chain formation as well (in the case of glucose, more than 97% of the monomers exists in a ring conformer in aqueous solution) (see Figure 3-3)<sup>1-3</sup>. There is a balance between the two conformations in solution, as depicted in Figure 3-3.

Next to the chain-ring balance, monosaccharides (with at least six carbon atoms) are also known to exist as ketose (*i.e.*, containing a ketone in the open structure; such as fructose) or as aldose (*i.e.*, containing an aldehyde in the open structure; like glucose in Figure 3-3) conformation. Moreover, note that different possible ring formations can be formed for one given sugar chain (indicated by the  in the right panel of Figure 3-3 for C-1). From the chain conformation, it is

clear that different stereoisomers exist, resulting in a different three-dimensional orientation. In the case of glucose, two different stereoisomers are distinguished: D- and L-glucose. Both stereoisomers are enantiomers, meaning that they are each other's mirror image. Although they are enantiomers, D-glucose is more abundantly found in biochemistry compared to its L-stereoisomer.

The combination of all the above-mentioned balances and stereoisomers results in a very wide range of different monosaccharides with the same basic formula  $(\text{CH}_2\text{O})_n$ . Therefore, it is not surprising that more than a multiple thousand different oligosaccharides are known in biochemistry. An overview can be found in the book of Anderson *et al.*<sup>2</sup>.

### 3-1.2 Impact of plasma treatment

Found in almost every aspect of a cell, saccharides take part in a wide range of biochemical activities, from the storage of energy and supporting the immune system to acting as structural support of macromolecules or biofilms<sup>3</sup>.

- Sugars play a crucial part in the delivery of energy to cells. Cellular energy is temporarily stored within the biochemical high-energy compounds adenosine-triphosphate (ATP) and nicotinamide adenine dinucleotide (NADH). The production of ATP, as well as NADH, is a result of, *e.g.*, glycolysis which degrades glucose into pyruvate. The resulting release of energy is then used to produce ATP and NADH. Afterwards, pyruvate will degrade further towards either  $\text{CO}_2$  (via the reaction with  $\text{O}_2$ ), known as aerobic glycolysis, or lactic acid, referred to as anaerobic glycolysis.
- Saccharides often provide structural support within several biochemical macromolecules. A few examples are the ribose-rings forming the backbone of a DNA or RNA strand (see **chapter 3**) and polysaccharides found in multiple important macromolecules located in cell membranes (*e.g.*, Lipid-A and peptidoglycan found in Gram-negative and -positive bacteria, respectively).
- Saccharides are often found on the cell membrane, connected to proteins and lipids (forming glycoproteins and glycolipids) which are recognized by carbohydrate-binding proteins such as white blood cells and antibodies. This

recognition is essential in cell-to-cell communication and the detection of micro-organisms like bacteria and fungi<sup>1,4</sup>.

As a result, it is clear that plasma-generated species will come in contact with these biomolecules during plasma treatment, which may lead to chemical modifications, possibly changing the biochemical functions of the affected saccharides (*e.g.*, oxidative damage on DNA or Lipid-A<sup>5,6</sup>). However, only limited data is available on the oxidation of monosaccharides and it is mainly limited to glucose. In this context, oxidation of this sugar leads to an increase in the expression of ketones (C=O) and the opening of the glucose-ring<sup>7-9</sup>.

Given the slight differences in the chemical structures of different monosaccharides, only one was selected for the investigation presented in this chapter. Indeed, these differences mainly involve orientation or the number of functional groups, while different types of monosaccharides share the same chemical groups and environments. To investigate the interactions between plasma-generated species and sugars, D-glucose was chosen as the model system, as it is also mainly investigated experimentally. Combined with the relatively easy structure of this monomer, this makes D-glucose an excellent system to be investigated with MD.

In addition to the computational work, the treatment of D-glucose was investigated in collaboration with the research group of Prof. Dr. Jan Benedikt of the University of Bochum in Germany for experimental validation. This research group used the so-called X-plasma jet, as discussed in *section 1-2.2a*, to investigate the impact of different plasma components on this simple hydrocarbon in solution and as a dried droplet.

In the computational work, we only investigated the interactions between reactive oxygen species (ROS) and D-glucose, *i.e.*, O, OH, HO<sub>2</sub> and H<sub>2</sub>O<sub>2</sub>, for two reasons. (i) The force field used for ReaxFF (*cf.* **section 3-2**) was unable to accurately describe reactive nitrogen species (RNS). (ii) The experimental results were obtained using a He/O<sub>2</sub> plasma jet, greatly limiting the number of RNS produced in the plasma.

## 3-2 Computational setup

Reactive MD simulations were performed using the ReaxFF potential from van Duin *et al.*<sup>10</sup> combined with the C/H/O/N parameters derived by Rahaman *et al.*<sup>11</sup>. Before starting the impact simulations, the molecular systems were equilibrated at room temperature (*i.e.*, 300 K) in the canonical ensemble (temperature and volume were kept constant: NVT) using a Bussi thermostat with a coupling constant of 100.0 fs. Simulations were performed for 100 ps (unless specified otherwise). The used simulation times were large enough to stabilize the molecular structures at the given temperature, *i.e.*, the total energy of the system remains constant as a function of time. For all simulations, *i.e.*, thermalization and subsequent impact simulations, periodic boundary conditions and a time step of 0.25 fs was used. The maximum displacement of the simulated particles between two time steps was 0.01 Å.

Two different systems were investigated in correlation with the experiments done at the Ruhr-Universität of Bochum, supervised by Prof. Dr. Jan Benedikt: D-glucose in aqueous solution and D-glucose as an amorphous bulk (*i.e.*, the dried droplets). In practice, three different systems were considered for the simulations:

- vacuum simulations: D-glucose in vacuum with a single ROS (O, OH, HO<sub>2</sub>, H<sub>2</sub>O<sub>2</sub>) to obtain quick insight in the expected interactions.

Simulations were performed in a 25 x 25 x 25 Å<sup>3</sup> box where the D-glucose molecule and the ROS were placed randomly with a minimum distance of 10 Å, to avoid van der Waals interactions at the start of the simulation (see top-left in Figure 3-4). The initial velocity of the molecular system corresponds to 300 K. Results indicated that only O and OH react with the glucose molecule within the simulated timescale. Both were found to interact in a very similar manner.

- aqueous solution simulations: D-glucose in a water box containing only a single ROS (OH or O).

D-glucose was incorporated in a 25 x 25 x 25 Å<sup>3</sup> water box. Water molecules were removed within a radius of 3.5 Å (corresponding to a weak hydrogen bond) of the D-glucose molecule. This resulted in a molecular system with 1 D-glucose and 490 H<sub>2</sub>O molecules, ensuring a density of 1 mg/ml at a pressure of 1 atm.

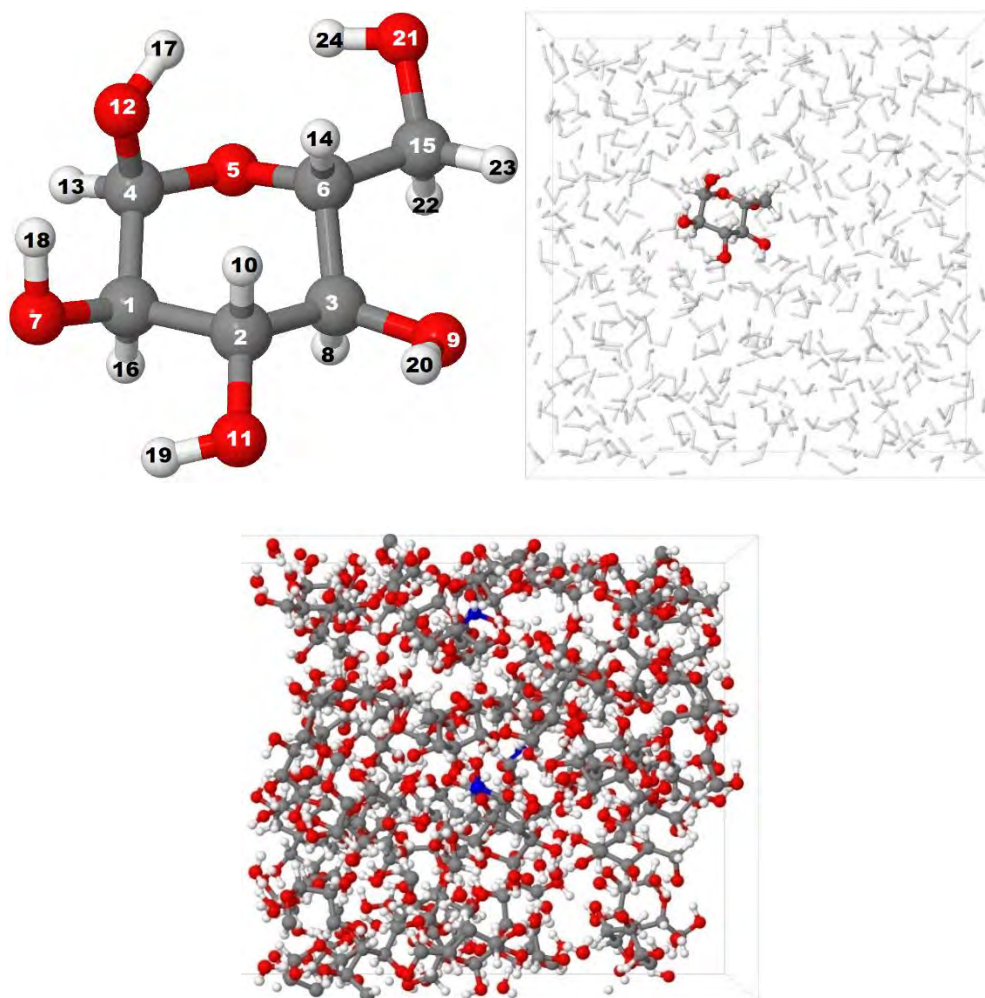


**Figure 3-4. 3D model of D-glucose systems used in the simulations.** Top left) Model of D-glucose in vacuum: the carbon (grey), oxygen (red) and hydrogen (white) atoms are indicated with their respective atom number from the simulation, as they are used in the description of the reaction schemes below (see schemes 3-1 – 3-8). Top right) Model of D-glucose in solution: water molecules are depicted using a light grey stick-representation, for sake of clarity. Bottom) Model of the amorphous bulk containing a D-glucose-water ratio of 1:1. The Z-axis is positioned in the horizontal direction (the full box is cut to only display the amorphous structure). The atoms colored in blue represent the fixed atoms in the amorphous structure to prevent drifting during the calculations.

An example of the resulting structure in case of OH is given in the top-right of Figure 3-4. Furthermore, a single water molecule was replaced by a reactive species (by removing one or two of the H atoms) at a minimum distance of 10 Å away from the D-glucose molecule.

- amorphous D-glucose simulations: dried amorphous D-glucose (1:1 sugar-water) with ten OH radicals.

Results from the University of Bochum pointed out that the experimental dried D-glucose droplets contain water in a 1:1 glucose-water ratio\*. Hence, the amorphous system in this work contains a ratio of 1:1 sugar-water as well. This amorphous structure was made by a random addition of D-glucose and water molecules (1:1) in a simulation box of  $25 \times 25 \times Z \text{ \AA}^3$ , periodic in the first and second dimension for the formation of a periodic D-glucose structure. The Z dimension was simulated as a reflective border and was chosen to be long enough to ensure 50 D-glucose and water molecules to be added with a minimum distance of  $1.6 \text{ \AA}$  from already existing molecules in the box. After the addition of  $\approx 50$  molecules of both species, the molecular structure was able to coagulate during an MD simulation in an isothermal-isobaric ensemble (NPT: constant pressure and temperature, 0 Pa and 300 K, respectively) up to the point where an amorphous structure was formed. Note that this was a spontaneous process where no artificial forces were used to create the amorphous structure. Indeed, the interactions between the molecules, simulated by the ReaxFF code, were sufficient for the coagulation of the structure as depicted in the bottom of Figure 3-4. Finally, the simulation box was reduced to a Z-length of  $70 \text{ \AA}$ , D-glucose structure was kept in position by fixing three random atoms (blue atoms in Figure 3-4). OH radicals were positioned at the far end of the Z-axis ( $Z \geq 50 \text{ \AA}$ ).

Initial results indicated that O radicals reacted with water, upon impact, leading to the formation of two OH radicals<sup>12</sup>.



Due to reaction 3-1, simulations in solution were only performed for OH radicals. However, results of a later investigation (presented in **chapter 6**) have indicated that atomic O is found to be stable in liquid. This was further supported by

---

\* Personal communication

experimental study performed by Hefny *et al.*<sup>13</sup>. Because this insight was not yet obtained during this the work presented in this chapter, the interactions between O and D-glucose in solution was not investigated as explained above (*cf.* reaction 3-1).

## 3-3 Results and discussion

### 3-3.1 Experimental results

Experiments were performed in the group of Prof. Dr. Jan Benedikt at the Ruhr-Universität Bochum. The plasma source used for the treatment of glucose was the so-called X-jet, which has the capability of shielding the treated surface from several plasma-generated components (*i.e.*, photons or reactive particles). The principle has been depicted in Figure 1-6 in *section 1-2.2a*. The plasma is operated with 1.4 standard liter per minute helium flow rate with 8.4 standard cubic centimeter of O<sub>2</sub> gas per minute (0.6% of the He flow rate). The maximum O atom density ( $8 \times 10^{14} \text{ cm}^{-3}$ ) in the effluent is obtained with these conditions at 4 mm distance from the position of the liquid surface<sup>14</sup>.

Experiments were performed on two systems: D-glucose dissolved in water (0.05% glucose solution) and a dried droplet of this solution. Surprisingly, 10-minute-long treatment of the solution left the glucose molecules largely unmodified. Comparing the measured Fourier-transform infrared (FTIR) spectra of the untreated molecule with the treated one only revealed a slight increase in C=O double bonds, indicating the formation of carbonyl or carboxyl groups. This points towards the oxidation of the hydroxyl groups found in the chemical structure of glucose (results not shown). However, more subtle changes could not be revealed due to the relatively large noise on the FTIR signals. In order to increase the resolution of the obtained spectra, to study the possible modifications in more detail, 45-min-long treatments were performed. The FTIR spectra of the 45-min treatment is depicted in the Figure 3-5. Here, again an increase in the signals at  $1730 \text{ cm}^{-1}$  is observed, which indicates an increase in C=O, originating from carbonyl or carboxyl groups. Slight increases in other characteristic signals (*e.g.*,  $\sim 3200 \text{ cm}^{-1}$  and  $\sim 1100 \text{ cm}^{-1}$ ) are the result of the subtraction of the background spectra.

The spectra in Figure 3-5 result from the combined jet (both plasma-generated reactive species and photons are permitted to reach the solution). Identical treatments were performed for both the particle- (photons do not reach the solution) and UV-jet (reactive species do not reach the solution) in order to investigate the role of both plasma-generated components in the observed oxidation of D-glucose. Results



of both treatments are depicted in Figure 3-6 (particle-jet on the top and UV-jet at the bottom). The spectra indicate that the observed oxidation (the increase in carbonyl groups on the chemical structure of D- glucose) is the result of the plasma-generated reactive species. However, the UV-jet does not significantly change the chemical structure of glucose. This points towards the important role of reactive species (most likely the ROS) in the oxidation mechanisms of this monosaccharide. Results from the treatment of the dried droplets only indicated a significant etching of the substrate while no clear chemical modifications were observed from FTIR (results are obtained from personal communication and are not shown in this thesis)\*.<sup>1</sup>

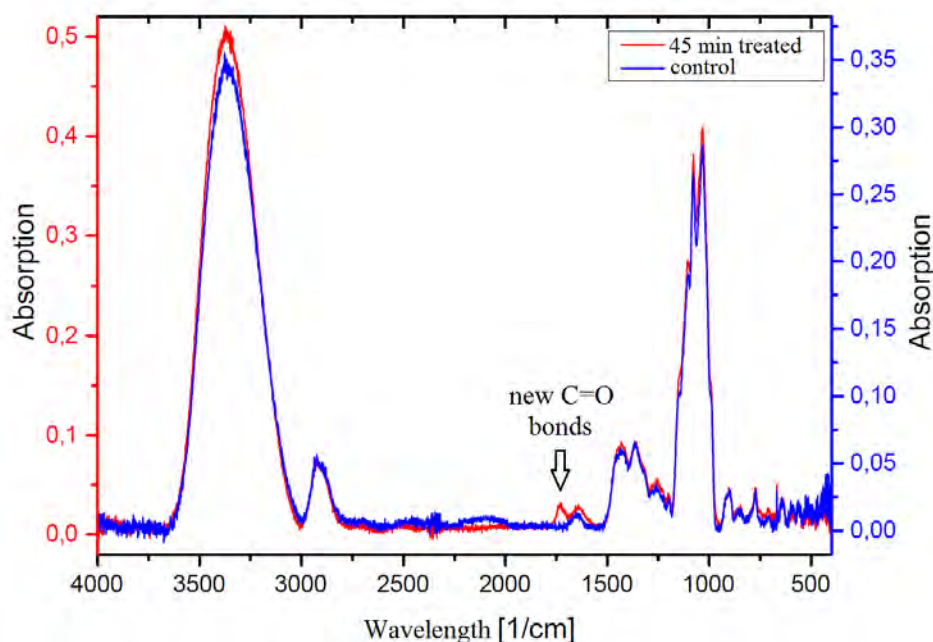


**Figure 3-5.** FTIR spectra obtained after the plasma treatment of D-glucose in aqueous solution for 45 minutes with the combined jet. Comparing the treated sample (red spectra) with the untreated sample (blue) reveals a clear increase of the signals corresponding to C=O functional groups.

\* Poster presented at COST TD-1208 in Lisbon (2014)

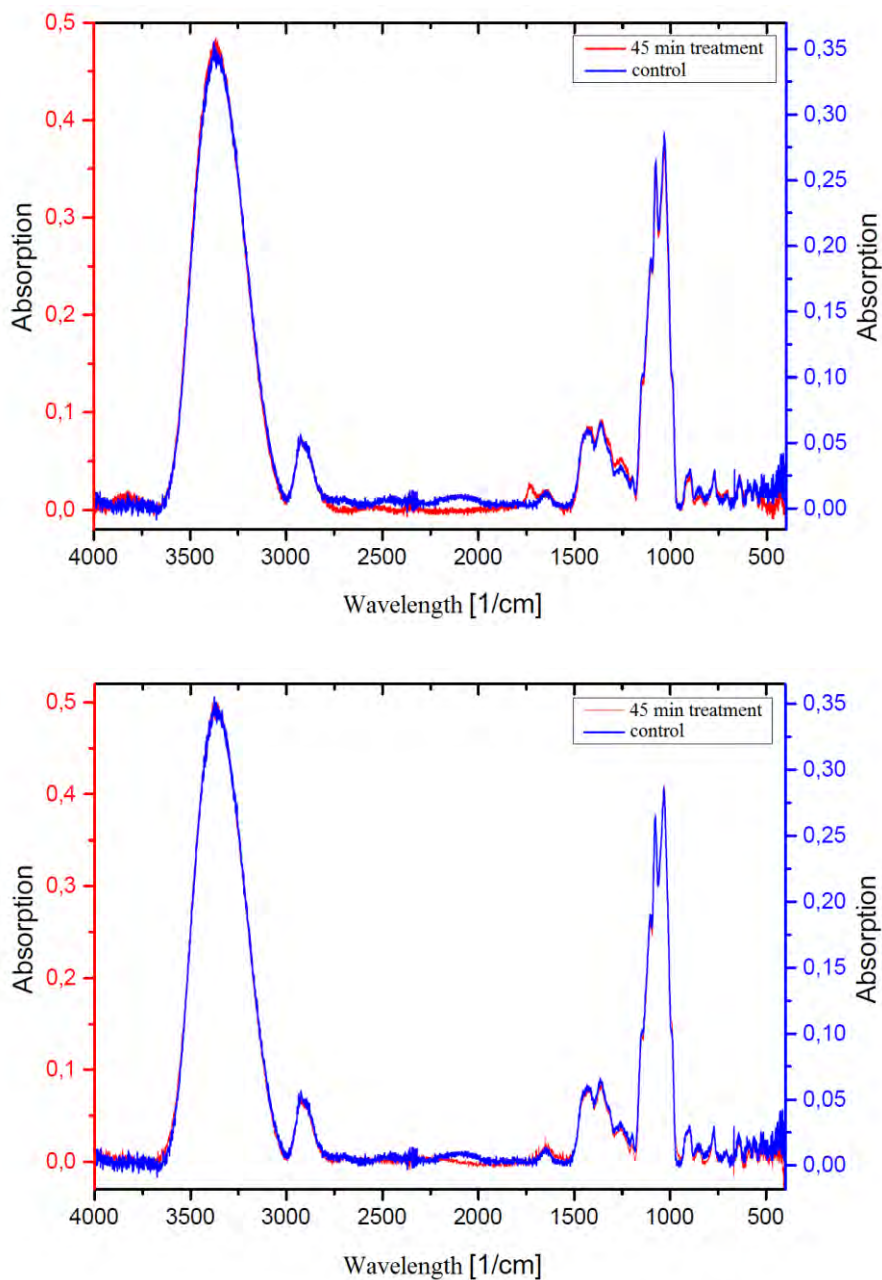


**Figure 3-6. FTIR spectra obtained after the plasma treatment of D-glucose in aqueous solution for 45 minutes with the particle jet (top) and UV-jet (bottom).** Comparing the treated sample (red spectra) with the untreated sample (blue) reveals a clear increase of the signals corresponding to C=O functional groups after the treatment of the solution with the particle jet while the UV-jet has no significant effect on the chemical structure of the sugar molecules.

## 3-3.2 Computational results

### 3-3.2a Vacuum

#### *OH radical*

Given the small number of atoms in every vacuum system (24 atoms of glucose + 1 OH radical), numerical simulations were computationally “cheap”, leading to the possibility to perform a large number of different runs in a limited amount of time. Consequently, 1000 different impact simulations, on D-glucose in vacuum, were performed over a time scale of 100 ps using a canonical ensemble (NVT).

From the 1000 simulations, ergo 1000 OH radicals, 4.3% showed no reaction after 100 ps. Within the remaining simulations, H-abstractions were observed within the given simulation time. A total of eight different reaction schemes could be detected, which can be divided in three reaction groups:

- (i) H-abstraction from OH-groups directly connected to the oxane ring. This was observed in 79.8% of the cases.
- (ii) H-abstraction from the oxane ring (11.0% of all encountered reactions).
- (iii) H-abstraction from the  $-\text{CH}_2\text{OH}$  side-group (9.2% of all simulated reactions).

The fact that the mentioned H-atoms can be abstracted by OH radicals has been observed using electron spin resonance studies performed by Gilbert *et al.*<sup>15</sup>. However, the authors could not deduce a clear order in the encountered H-abstractions.

The time evolution of the H-abstractions is given in Figure 3-7. This graph summarizes the number of H-abstractions (in percentage) as a function of simulation time (in ps) for all 1000 simulations. From Figure 3-7 it is clear that hydrogen 17 (H-17; see Figure 3-4 for nomenclature) is most favored for abstraction by OH radicals, followed by H-19, H-18, H-20 and H-24. This is in agreement with oxidation literature in that sense that H-17 is often the initial target during various oxidation processes on glucose (*e.g.*, catalysis, aerobic oxidation, enzymatic oxidation)<sup>7-9</sup>. In literature on glucose oxidation, H-17 is abstracted to form a C=O double bond, which eventually opens the oxane ring during further oxidation steps<sup>7-9</sup>. The formation of

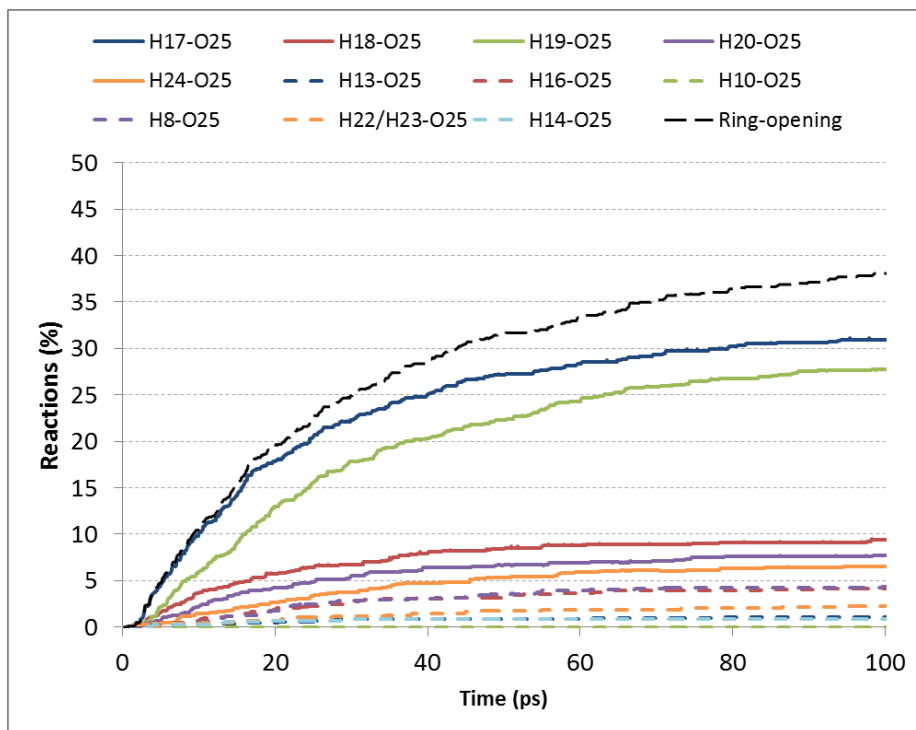


**Figure 3-7. Time evolution of H-abstraction over 100 ps.** These values are taken from all OH impacts. The atom numbers are depicted in Figure 3-4.

C=O was also observed during the experimental treatment, as explained in **section 3-3.1**. However, the decrease in ether bonds (C-O-C due to the ring opening) was not observed after plasma treatment (*cf.* Figure 3-5).

The five mentioned hydrogens (*i.e.*, H-17, H-19, H-18, H-20 and H-24) are all part of OH-groups (reaction group 1 and 3, as explained above). The dashed lines in Figure 3-7 represent hydrogen atoms bound directly to the oxane ring (reaction group 2). This clearly shows that hydroxyl groups are favored for H-abstraction over the other H-atoms located on the oxane ring. The black dashed line represents the number of D-glucose molecules where the oxane ring opened, *i.e.*, dissociation of the C-O-C ether bond, as a result of the H-abstraction (38.1% of the glucose molecules).

#### *Reaction group 1: H-abstraction from ring bound OH-groups*

Three reaction schemes were observed, which involved an OH-group on the oxane ring of D-glucose: one where no further bond formation/dissociation reactions took place after the H-abstraction (Scheme 3-1) and two involving a ring opening

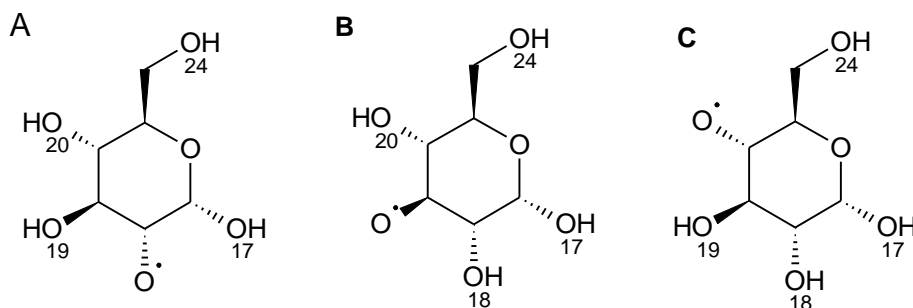
(Scheme 3-2 and Scheme 3-3). The abstraction of H-18, H-19 and H-20 did not lead to further reactions within the remaining D-glucose radical, see Scheme 3-1.

However, if H-17 is abstracted, the ring opens as a result of a homolytic C-O-C bond dissociation (Scheme 3-2), consistent with literature on glucose oxidation<sup>7-9</sup>, as already discussed above. The homolytic breaking of bond C4-O5 results in the formation of an aldehyde and an oxygen radical. The reaction depicted in Scheme 3-3 was only observed once within the 1000 simulations. Due to its very low probability, this reaction will not be considered throughout the rest of the discussion.

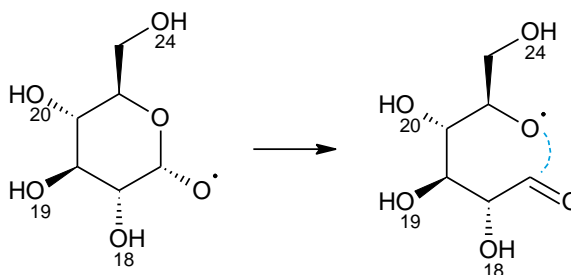
*Reaction group 2: H-abstraction from the oxane ring*

Hydrogen abstraction from the oxane ring can occur at the five different carbon atoms present in the ring, but was only observed in 11% of the impact simulations. From the five possible hydrogen abstractions only four were observed in these simulations (H-10 was never abstracted during the 1000 impact simulations). Abstraction from the oxane ring gave rise to three possible reaction pathways as depicted in Scheme 3-4, Scheme 3-5 and Scheme 3-6.

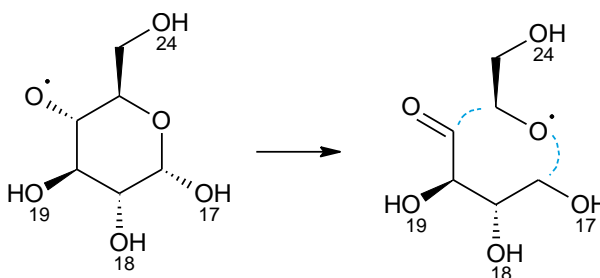
First, a hydrogen atom was abstracted from C-1 of the oxane ring, as depicted in the left of Scheme 3-4. This hydrogen abstraction reaction was followed by the homolytic dissociation of the neighboring C-O-C ether bond leading to the formation of a C=C double bond and a D-glucose oxygen radical. The depicted ether bond dissociation leads to the opening of the glucose ring, and was seen in 52% of the simulations after the abstraction of this specific hydrogen atom.



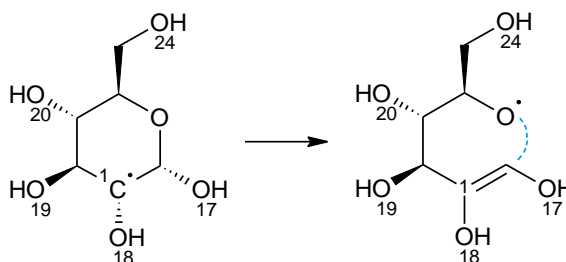
**Scheme 3-1. Schematic representation of the resulting radical after the abstraction of H-atoms 18 (left), 19 (middle) and 20 (right) from an OH group of the ring.** These abstraction reactions did not lead to further bond formation or dissociation events in the remaining D-glucose radical. H-atoms are numbered consistent with Figure 3-4 above.



**Scheme 3-2. Schematic representation of the reaction scheme after the abstraction of hydrogen from O-12 upon impact of one OH radical.** This abstraction is followed by a homolytic dissociation of the neighboring C-O-C bond of the oxane ring, which leads to the opening of the ring and the formation of an aldehyde. The homolytic bond breaking is depicted by the dashed blue line. H-atoms are numbered consistent with Figure 3-4.



**Scheme 3-3. Schematic representation of the reaction scheme after the abstraction of H-20.** This reaction results in the opening of the oxane ring, the formation of an aldehyde and desorption of HO-CH<sub>2</sub>-CH=O. The homolytic dissociation events are represented by the dashed blue lines. H-atoms are numbered consistent with Figure 3-4.

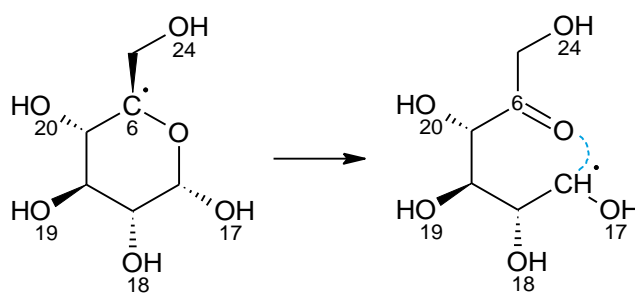


**Scheme 3-4. Schematic representation of the reaction scheme occurring after the hydrogen atom was abstracted from C-1, by an OH radical (left).** The existence of the tertiary C-1 radical led to the homolytic dissociation of the C-O-C bond resulting in the formation of a C=C double bond and a stable oxygen radical (right). The homolytic bond dissociation is depicted in a dashed blue line. H-atoms are numbered consistent with Figure 3-4.

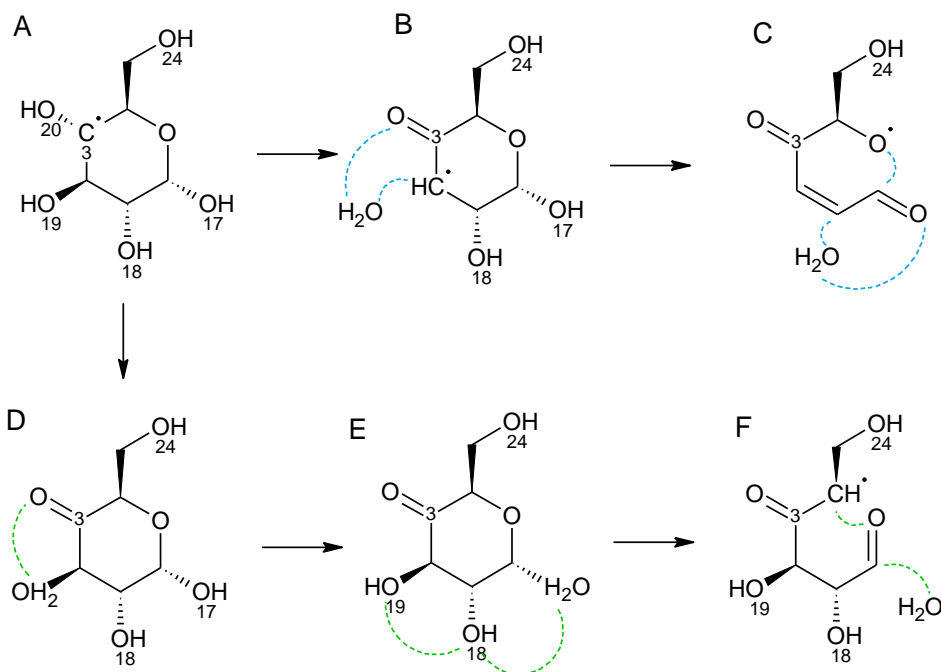
Second, if the H-14 is abstracted, a tertiary carbon radical is formed, as shown in Scheme 3-5. This was followed by the homolytical breaking of the neighboring C-O-C ether bond for the formation of a C=O double bond and a secondary carbon radical, leading to the opening of the glucose ring. This reaction always took place after the abstraction of this specific hydrogen atom.

Finally, H-8, H-16 and H-13 were found to be abstracted as well, which led to further reactions in 15.1% of the cases after abstraction. Two reaction pathways were encountered, both leading to the opening of the oxane ring (depicted in Scheme 3-6 after abstraction of H-8, as an example model). Although both reaction pathways start from the same principle, *i.e.*, the formation of a C=O double bond by an intramolecular H-abstraction, the reaction mechanism shown in Scheme 3-6-ABC only occurred after abstraction of H-8 while the second reaction (Scheme 3-6-ADEF) is observed after the abstraction of either of the three above-mentioned hydrogen atoms.

In reaction pathway A-C, the OH group, bound to the neighboring carbon atom, abstracts a hydrogen atom of O-9, leading to the desorption of a water molecule, the formation of a C=O double bond and a tertiary C-2 radical in the ring (as seen in structure B of Scheme 3-6). Consequently, a second reaction can be observed where a hydrogen atom was abstracted from O-12 by the neighboring OH group, again leading to the desorption of yet another water molecule. Simultaneously, a homolytic



**Scheme 3-5. Schematic representation of the reaction scheme occurring after hydrogen was abstracted from C-6, of the oxane ring, by an OH radical (left).** The existence of the tertiary C-6 radical led to the dissociation of the neighboring C-O-C bond for the formation of a C=O double bond and a tertiary C-4 radical (right). The homolytic bond dissociation event is depicted in a dashed blue line. H-atoms are numbered consistent with Figure 3-4.



**Scheme 3-6. Schematic representation of the reaction scheme occurring after a hydrogen atom was abstracted from C-3, by OH radical (A), as an example of the possible reactions after the abstraction of the ring H-atoms.** A-C only occurred after abstraction of H-8. The abstraction can lead to a hopping event of H-20 to O-11 which will desorb as water. A C=C double bond is formed after a similar desorption event of the neighboring O-7 after the abstraction of H-17. This results in the formation of a C=O double bond, after the loss of a C-O-C bond, and one C=C double bond. D-F can occur after abstraction of either H-8, H-13 or H-16. The abstraction will also lead to an H-hopping event, starting with H-20. After the H-abstraction by O-12, a desorption of this oxygen atom as water occurs along with the dissociation of the C-O-C bond, leading to the formation of a C=O double bond. The homolytic bond dissociation reactions are depicted in a dashed blue line for A-C and a dashed green line for D-F. H-atoms are numbered consistent with Figure 3-4.

dissociation of the C-O-C bond, resulting in the opening of the ring occurs, giving rise to an aldehyde and a bonded oxygen radical (structure C of Scheme 3-6). In the second reaction pathway D-F, intramolecular H-abstraction events occur, leading to the formation of a C=O double bond. However, instead of the desorption of a water molecule, intramolecular H-abstractions keep on occurring, as seen in structure E, until the point where O-12 contains a second hydrogen atom. –The intramolecular H-abstraction reactions will be called H-hopping in this discussion– At this given moment, water desorbs homolytically, resulting in the formation of a double bonded C4-O5 and a tertiary carbon radical (structure F of Scheme 3-6).

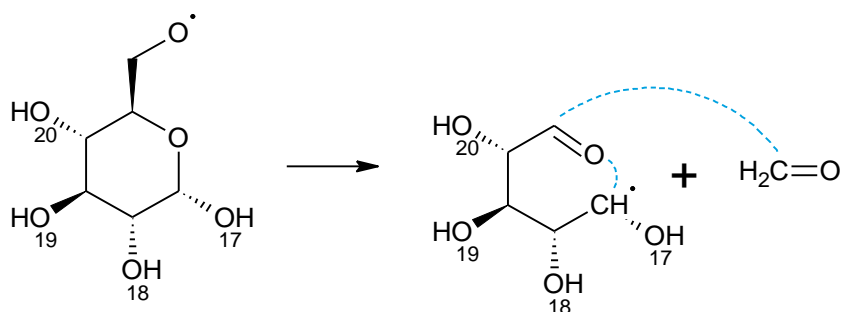


Note that the latter reaction pathway was found after the abstraction of either H-8, H-16 or H-13. The reaction from structure B to structure C was observed only in a very small number of cases compared to the reaction from structure D to structure F (2% and 12.9%, respectively, compared to the total sum of the abstraction of H-8, H-16 and H-13).

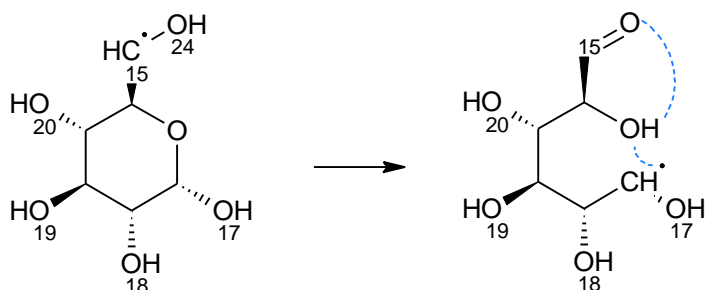
*Reaction group 3: H-abstraction from the  $-CH_2OH$  side chain*

Hydrogen abstraction reactions on the hydroxyl group, as well as on  $-CH_2-$  were observed as depicted in Scheme 3-7 and Scheme 3-8, respectively. The abstraction of H-24 leads to a stable D-glucose radical as no further bond formation and dissociation events were observed throughout the simulations. However, one follow-up reaction was observed in a single simulation (as depicted in Scheme 3-7). Firstly, the C-C bond, connecting the side chain to the ring, dissociated leading to a tertiary carbon radical on the oxane ring and the desorption of a formaldehyde molecule ( $CH_2=O$ ). Secondly, the C-O-C bond of the ring dissociated homolytically leading to the opening of the oxane ring and the formation of a C=O double bond, using the already existing radical on this particular carbon atom, and the formation of another tertiary carbon radical. The latter reaction was observed only once and will not be considered throughout the rest of the discussion from this point.

When a hydrogen atom from the  $-CH_2-$  group was abstracted, the reaction as shown in Scheme 3-8 occurred. The oxygen atom from the oxane ring abstracts the



**Scheme 3-7.** Schematic representation of the reaction scheme which follows the abstraction of a hydrogen atom by the impact of one OH radical (left). After the hydrogen abstraction two homolytic bond dissociation events occurred simultaneously (depicted by the dashed blue line) (right). H-atoms are numbered consistent with Figure 3-4.



**Scheme 3-8. Schematic representation of the reaction scheme after the abstraction of the H-22 or H-23 on C-15 (left).** An intramolecular H-abstraction reaction results in the formation of a C=O double bond and the homolytic dissociation of the oxane ring, leading in turn to the formation of a tertiary carbon radical (right). The bond dissociation/formation events are represented by the dashed blue line. H-atoms are numbered consistent with Figure 3-4.

hydrogen from the hydroxyl group on the  $-\text{CH}_2\text{OH}$  side chain. This resulted in the formation of a C=O aldehyde and the dissociation of the C-O-C bond of the oxane ring. This breaking leads to the formation of another tertiary carbon radical at C-4. This reaction occurred after every hydrogen abstraction, by an OH radical, at this specific position.

#### *O atoms*

Impact reactions of D-glucose with O atoms were conducted and investigated over a course of 500 ps. A longer simulation time, compared to the 100 ps of the OH impact simulations, was chosen to ensure that all reactions are captured, as preliminary results showed that O atoms mostly react at two different sites with the hydrocarbon molecule, while OH radicals only reacted on a single site. Compared to the OH simulations, only 50 different runs were performed to give a primary view on the expected reactions. The reason for this will become clear in the discussion given below.

Unlike the simulations with OH radicals, reactions with O atoms resulted in a vast range of reaction schemes leading to a mixture of reaction products with no clear trend. Indeed, the combination of two different reactions results in a wide range of possible oxidation products after 500 ps. A few of the observed oxidation products are depicted in Figure 3-8. However, the interactions of O with D-glucose always led to two H-abstraction reactions, similar as in the OH impact simulations. The order

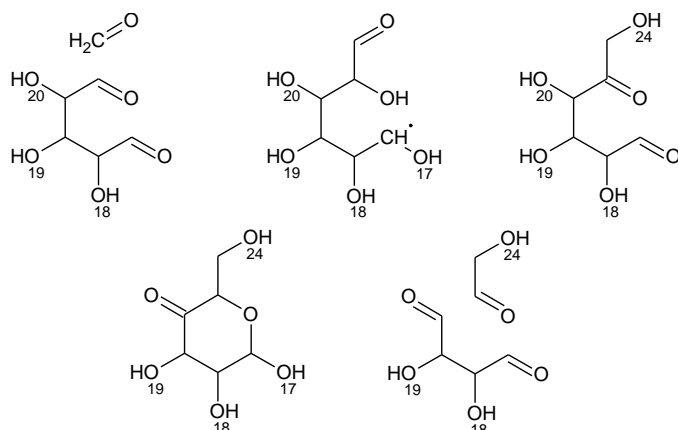


**Figure 3-8. Examples of reaction products after the impact of a single O radical in vacuum.** H-atoms are numbered consistent with Figure 3-4.

in which hydrogen atoms are favored for abstraction remains similar to the order seen during the OH radical impacts. This becomes clear when looking at the time evolutions of the hydrogen abstractions for the 50 cases, as displayed in Figure 3-9 and in Table 3-1. The graph in Figure 3-9 represents the time and number of hydrogens abstracted by O, summed over the 50 simulations (*i.e.*, total of 100 H-abstractions). H-17 and H-19 are found to be abstracted the most (indicated in red in Table 3-1) along with, and unlike in the case of the OH radicals, H-20 and H-24. However, when one looks at the H-abstractions more closely, H-20 and H-24 are mostly the second hydrogen to be abstracted (indicated in blue in Table 3-1). This is not visible in Figure 3-9 but is shown in Table 3-1. Given the fact that Table 3-1 is drawn from a limited number of simulations, *i.e.*, 50 runs, a comparison between O impacts and OH impacts in vacuum remains speculative.

Given the fact that one H-abstraction can lead to eight different reactions (described in the section on the behavior of the OH radicals), a second hydrogen abstraction can result in a vast range of reaction products. Not all reactions and oxidation products will be shown in this thesis but examples of the most found reaction products are given in Figure 3-8. Reaction products mostly contain ketone and aldehyde groups (C=O), as also observed by the experimental results of Figure 3-5. Due to the chaotic nature of these reactions, driven by the two H-abstractions, as well as the fact that the H-abstractions resemble the OH simulations, a limited number of simulations, *i.e.*, 50, were performed in vacuum.

**Table 3-1. Summary of hydrogens abstracted by O atoms, taken from a total of 50 simulations where every O atom abstracted two hydrogens of D-glucose.**

H-atom number	First abstraction (%)	Second abstraction (%)
H-8	4.5	6.8
H-10	0	4.5
H-13	6.8	0
H-14	0	11.4
H-16	11.4	4.5
<b>H-17</b>	<b>31.8</b>	11.4
H-18	9.1	4.5
<b>H-19</b>	<b>15.9</b>	6.8
<b>H-20</b>	9.1	<b>18.2</b>
H-22	2.3	11.4
H-23	2.3	2.3
<b>H-24</b>	6.8	<b>18.2</b>

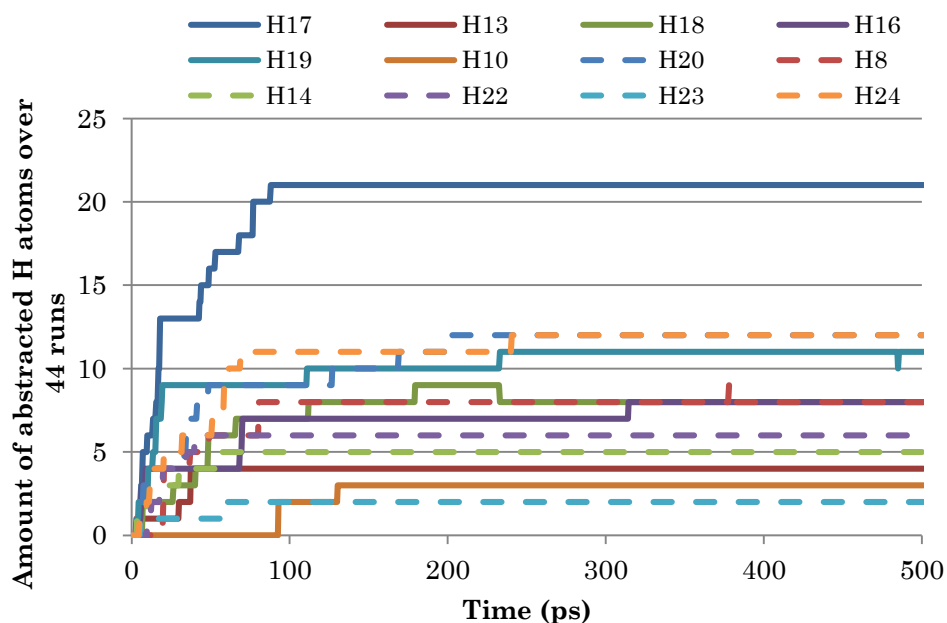


**Figure 3-9. Time evolution of hydrogen abstraction by O radicals over a course of 500 ps.** These values are taken from 50 O impacts (100 H-abstractions). The atom numbers are depicted in Figure 3-1.

### 3-3.2b *D-glucose in aqueous solution*

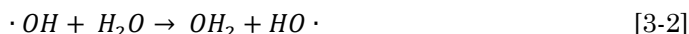
Two sets of simulations, resulting in a total of 250 simulations, were performed using the structure as depicted in the top right of Figure 3-4:

set 1: containing 50 simulations for 100 ps

set 2: containing 200 simulations for 250 ps

The initial geometry consisted of one D-glucose molecule in 489 H<sub>2</sub>O molecules (to represent a density of 1 g/ml) plus one OH radical in a box of 25 x 25 x 25 Å<sup>3</sup>. The simulations were performed at 300 K. Note that one water molecule of the 490 initial molecules has been modified to form one OH radical. After 100 ps only 18 out of the 50 simulations in set 1 showed a reaction between an OH radical and the D-glucose molecule, while 125 reactions (out of 200) were observed over a course of 250 ps in set 2.

Considering the vast number of atoms needed in the simulations, the calculation time increases dramatically with simulation time, leading to the choice of limiting the simulation time to 250 ps. The vast increase in reaction time has two reasons. (i) The propagation of OH radicals in water was a result of consecutive H-abstraction reactions (*cf.* reaction 3-2), forming consecutive OH radicals as described by Yusupov *et al.*<sup>12</sup>; therefore, the pathway of the radical through the water box can be approximated by a random walk in which the free path length is the average distance between the water molecules.



Here, it is important to state that this behavior was strongly present in the simulations using ReaxFF, but was hardly detected when using DFTB (see **chapter 5** and **chapter 6**). This indicates that the reactivity of reaction 3-2 is most likely overestimated by the used classical force field. (ii) The presence of water molecules most likely stabilized the introduced OH radical, shielding the organic compound, thus reducing the reactivity of OH towards D-glucose. Therefore, it is not surprising that the average time for the OH radical to reach the D-glucose and react was significantly longer compared to the reactions in vacuum. This explains why only

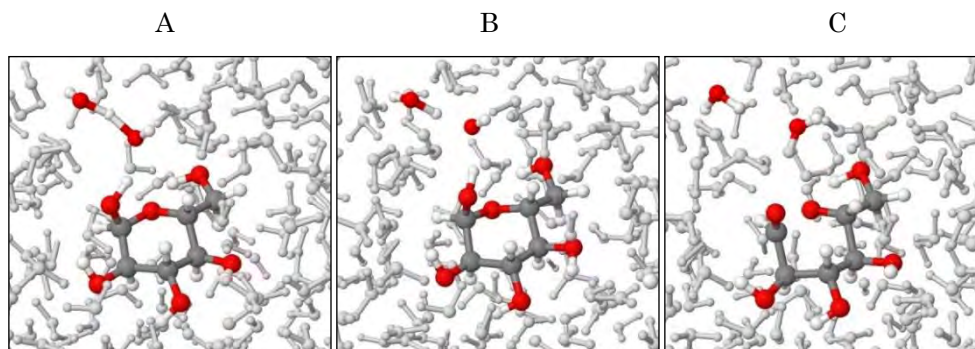


**Figure 3-10. Three frames of the simulation depicting the H-abstraction at oxygen atom 12 of D-glucose leading to the opening of the oxane ring.** The OH radical is mostly found physically bound to a water molecule (as seen in figure A) resulting in a H-abstraction of water, which gives a new OH radical (seen in figure B). When the distance and position between the OH radical and D-glucose are optimal, H-abstraction occurs (figure C) followed by the reaction pathway shown in Scheme 3-2. The same color codes are used as in Figure 3-4. Water is depicted in a light grey color.

143 reactions, out of 250 simulations, were found during the simulation timescale (18 and 125 for sets 1 and 2, respectively). In all the 143 reacting runs, the introduced OH radical abstracted an H-atom from a hydroxyl group (reaction group 1 and 3 of *section 3-3.2a*) after which the remaining D-glucose radical remained stable, as shown in Figure 3-10 and the left molecule in Scheme 3-7. However, 13.3% of the cases gave a reaction identical to Scheme 3-2, where the H-17 was abstracted, leading to the opening of the oxane ring, and therefore a decrease in C-O-C ether bonds. After the breakage of the D-glucose by H-abstraction, a stable glucose radical remained. Some cases were found where an intramolecular H-abstraction took place, which is called a H-hopping event in this thesis. However, in most cases a water molecule (not necessarily the newly formed water molecule after the H-abstraction) interacted with the lone electron of the D-glucose radical forming an H-bond, but this never led to a reaction between the two molecules. It is important to note that even though only one reaction scheme has been encountered, it was the only reaction found in vacuum after the abstraction of either H-17, H-18, H-19, H-20 and H-24 (excluding the reactions which only happened once in the 1000 vacuum simulations). Therefore, it is clear that the possible reactions after H-abstraction in aqueous solution perfectly match the reactions found in vacuum, for the same H-abstractions. When comparing the relative order of favored hydrogens for abstraction, with the

**Table 3-2. Percentage of H-abstraction of a specific H-atom over the 250 simulations.**

Abstracted hydrogen atom	Percentage of abstraction over 143 runs (of the total 250)
H-17	13.3%
H-18	17.7%
H-19	22.1%
H-20	37.1%
H-24	9.7%

1000 simulations in vacuum, there is a slight shift noticeable, in the sense that H-17 was no longer the most favored hydrogen atom for abstraction, unlike H-19, as shown in Table 3-2. Moreover, a steep rise in the relative occurrence of the abstraction of H-20 was observed, compared to the vacuum simulations. This contradicts literature on the oxidation of glucose<sup>7-9</sup>. However, it is important to note that mechanisms presented in literature lead towards the opening of the ring, forming a ketone (C=O). This was only observed to happen when H-17 was abstracted during the simulations in solution. In this context, it is well possible that other hydrogen atoms are targeted experimentally, but that this does not directly lead towards the observed reaction products. Furthermore, literature on glucose oxidation often uses catalysts (*e.g.*, enzymes, Au, PdBi catalyst), changing the chemical environment during reactions.

### 3-3.2c *D-glucose in amorphous surface*

The impact of OH radicals on the surface of an amorphous structure at 300 K was simulated. This structure consists of  $\pm 55$  D-glucose and  $\pm 55$  water molecules, covering a volume of roughly  $23 \times 23 \times 25 \text{ \AA}^3$ , as shown in the bottom Figure 3-4. After thermalizing the structure at 300 K in an NVT ensemble, it was exposed to ten OH radicals over a time of 100 ps (for five different simulations). Similar to the O impact simulations in vacuum, a wide range of oxidation products was observed, as multiple OH radicals are able to interact with a single D-glucose molecule. In this discussion, the more general observations will be presented instead of describing every simulation and reaction product separately. From the five independent simulations, or 50 OH impacts, all OH radicals reacted through H-abstraction

reactions upon impact on the surface of the structure, leading to the following general observations:

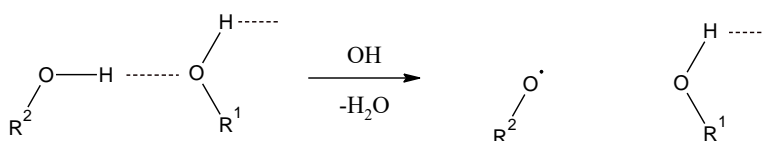
- Radical reactions, caused by either OH or the created glucose radicals, were located only in the first 6.7 Å of the structure, averaged over the five simulations. This is depicted in the right figures of **Appendix-3**
- Given the fact that D-glucose has a radius of roughly 6.9 Å, it is clear that only the first two layers in the structure are affected by the radicals during the simulations of ten OH radicals each. This phenomenon is explained by the immediate reactions that take place upon impact on the surface. Therefore, a very low penetration depth of the radicals in the system is expected.
- H-abstractions have led to the formation of C=O double bonds as a consequence of the reactions observed during the vacuum impact simulations. It should be noted that multiple H-abstractions with the same glucose molecule can occur, leading to a wide range of reaction products, as seen in *section O atoms*.
- All reaction products remained physically attached to the surface, *i.e.*, no etching has been noticed during these simulations at 300 K, unlike observed after plasma treatment experimentally (*cf. section 3-3.1*). However, some reaction products, as a result of H-abstraction reactions, were only found to be (very) weakly bound to the surface. On average, during the simulations, D-glucose molecules are connected to the structure with three hydrogen bonds (number taken from manual assessment), while the weakly bound reaction products are connected with only one or even no H-bonds on the surface of the structures. The absence of desorption can be explained by the existing vacuum around the surface of the amorphous bulk structure. As absolutely no driving forces, favoring desorption, are present during the simulation, the reaction products will remain at the surface due to weak (polar) interactions with D-glucose and water molecules, preventing the detachment of the resulting oxidized structures.

These simulations showed only chemical modifications, whereas no modified

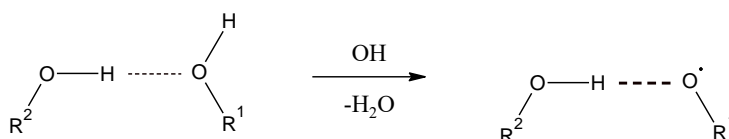


molecules desorbed from the surface. Assuming that experimental plasma treatment can lead to non-reactive impacts, it is evident that physically weakly bound molecules can desorb as a consequence of these bombardments by for example  $O_2$ ,  $H_2O$  molecules or the feeding gas, or due to an increase in temperature on the treated surface. Considering this assumption, ten new simulations have been performed where the structure is exposed to ten consecutive OH radicals. After every radical reaction, the structure was investigated for weakly bound reaction products, which are capable of desorbing and were removed from the surface, followed by the next OH impact simulation, over a course of ten OH impacts (examples of removed structures are depicted in blue in Figure 3-11). Over the course of the ten simulations, 12 glucose radicals were removed, resulting in a desorption rate of 0.12 D-glucose molecules per OH radical. Note that desorption only occurred for small molecules ( $O=CH_2$ ,  $O=CH-CH=O$ , *etc.*) and broken D-glucose rings. In addition, the results show that H-abstraction events were able to either destabilize a particular D-glucose molecule at the surface, by decreasing the average number of H-bonds, or stabilize a particular D-glucose molecule, by strengthening one or multiple H-bonds to this molecule. It should be noted that not all broken structures were found to desorb. A case was found where the broken structures migrated from the surface to the second layer. However, small ketones/aldehydes ( $O=CH_2$ ,  $O=CH-CH=O$ , *etc.*) were found to float over the surface and are considered to be able to desorb.

Destabilization:



Stabilization:



In this investigation, only OH radicals were considered, while experimental plasma treatment exposes the substrate to a mixture of different ROS, like  $\text{H}_2\text{O}_2$ ,  $\text{HO}_2$ ,  $^1\text{O}_2$  and O, which further complicates the experimental system. These impact simulations were not considered, as reactions with  $\text{H}_2\text{O}_2$  and  $\text{HO}_2$  require a significantly longer time scale compared to OH. Furthermore, the simulation of  $^1\text{O}_2$  requires the calculation of excited states, which cannot be accurately described by the used classical force field. Finally, O was not considered due to the fact that our knowledge at that moment stated that O forms OH in aqueous solution. However, as  $\text{H}_2\text{O}_2$  and  $\text{HO}_2$  have a significant longer half-life compared to OH, it can be expected that these species are able to penetrate the droplet and invoke reactions at layers deeper than 6.7 Å.

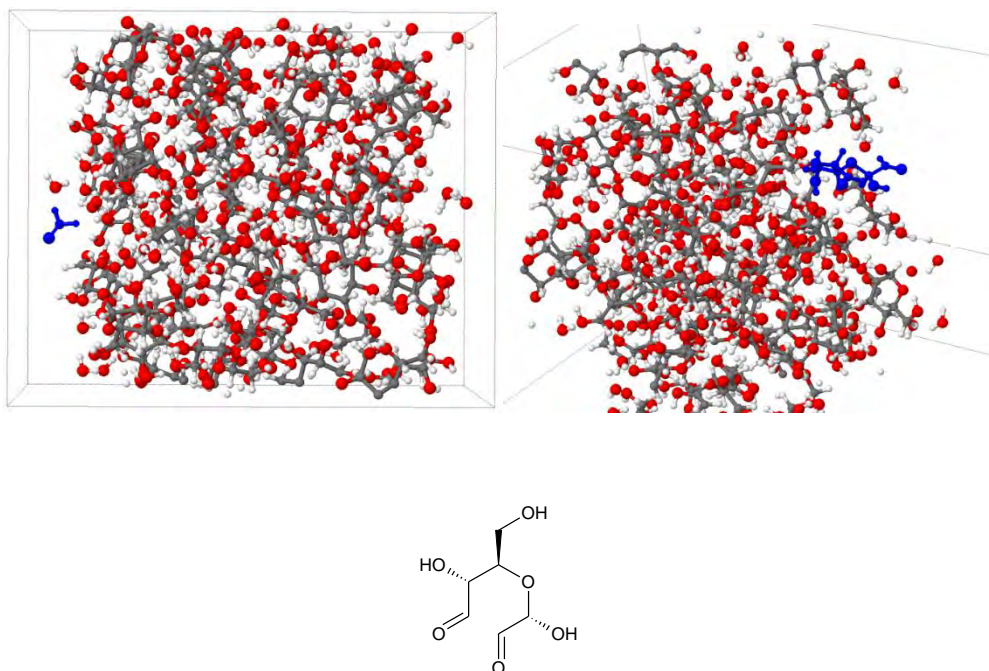


**Figure 3-11. Examples of weakly bound reaction products after OH impacts which were removed.** Left: formaldehyde ( $\text{O}=\text{CH}_2$ ) was often found to float over the surface. Right: The reaction product depicted in the bottom figure was found to be bound by a single hydrogen bond at the surface. The mentioned molecules are depicted in blue.



### 3-4 Concluding remarks

In this chapter, we tried to elucidate the oxidation of D-glucose using MD simulations. Our results were supported by experiments performed in the group of Prof. Dr. Jan Benedikt at the Ruhr-Universität of Bochum. In the computational side of this work, classical molecular dynamic simulations were performed based on a C/H/O force field. Three different systems were evaluated: in vacuum, in solution and amorphous D-glucose. In the experiments, the X-jet (as presented in *section 1-2.2a*) was used to treat D-glucose in solution and in a dried droplet (containing a 1:1 water/D-glucose ratio).

From the MD simulations, it became clear that both OH and O radicals reacted with D-glucose through H-abstraction reactions, while only weak attractive interactions were observed with H<sub>2</sub>O<sub>2</sub> and HO<sub>2</sub>. The majority of abstracted hydrogen atoms belonged to a hydroxyl group (bound to the ring or to the side chain of the glucose molecule). During the simulations in vacuum, ring opening, through the loss of the ether group (C-O-C), was observed in all the cases where the hydrogen abstraction led to further reactions within the remaining glucose radical. This led to the increase in C=O double bonds and the decrease in C-O-C bonds. Furthermore, impact simulations with a single O radical led to two different hydrogen abstractions, in similar ways as seen after impacts of OH radicals. The loss of two hydrogen atoms per D-glucose molecule gave rise to a vast range of reaction products containing different ketone and aldehyde groups (*i.e.*, increase in C=O bonds). However, as O radicals were found to react with water molecules, creating two OH radicals, O radicals were not considered during the simulations in solution or amorphous bulk.

Reactions and reaction products encountered during the simulations in solution were identical to those found in vacuum. Here, again, an increase in C=O double bonds and a decrease of the oxane rings (C-O-C) was encountered. However, a difference in the statistical order of favored hydrogens for H-abstraction reactions was found. A significant decrease in the number of broken oxane rings was observed, *i.e.*, the decrease in C-O-C bonds was more pronounced in vacuum. As the molecular system in solution represents the experimental conditions far better than the vacuum system, the results of the former are considered to give a more realistic representation of the expected radical chemistry between OH and D-glucose.

OH radical impacts on amorphous D-glucose (D-glucose/water 1:1) at 300 K resulted in H-abstractions, leading to the formation of C=O double bonds and the decrease in C-O-C ether bonds (oxane ring), as seen in the simulations in solution and vacuum as well. The simulations predicted chemical modification of the first two layers of the structure by either strengthening the hydrogen bonds, which keeps the glucose molecules stable on the surface, or by destabilizing the interactions of particular D-glucose molecules. In the latter case, desorption of the resulting ketones and aldehydes (after OH impact) can be assumed. Moreover, small reaction products ( $\text{O}=\text{CH}_2$ ,  $\text{O}=\text{CH}-\text{CH}=\text{O}$ , *etc.*) were found to float over the surface which were able to desorb. The desorption rate was found to be 0.12 D-glucose molecules per OH radical (for a total of 100 radicals).

Interestingly, the increase in C=O double bonds (*i.e.*, carbonyl or carboxyl groups) has been observed by the experimental studies as well, which was attributed to the interactions with ROS, in agreement with the simulated results. During the experimental treatment of a D-glucose solution, only the increase of carbonyl groups has been observed. Although the decrease in ether bonds (C-O-C) is much less pronounced during the simulations in solution, a decrease in the FTIR spectra should be expected. The fact that this phenomenon was not observed can be attributed to the difference between the simulated and experimental conditions. Indeed, only fast reacting ROS were considered in this computational investigation (*i.e.*, O and OH), while other ROS like  $\text{H}_2\text{O}_2$ ,  $\text{HO}_2$  and  $^1\text{O}_2$  were not simulated but are expected to play a role in the experimental observations. During the experiments, a clear etching was observed, which can be linked to the 0.12 D-glucose loss of the amorphous structure per OH impact. However, it should be noted that the experimental gas flow rate, temperature and longer time scales can have a significant effect on the observed etching rate. Surprising was the fact that no chemical modifications were noticed after the experimental treatment of the dried droplet, while modified D-glucose could bind to the surface of the amorphous bulk or even migrate deeper inside the structure during the simulations.

D-glucose was the monosaccharide of choice in this investigation. However, as other monosaccharides, like fructose and galactose, contain the same chemical groups and environment, similar results are expected when treating these simple

sugars with plasma. The situation becomes more complex when considering oligosaccharides and polysaccharides due to the presence of the glycosidic bond.

Taken together it is clear that plasma-generated reactive oxygen species are indeed capable of inducing chemical modifications in saccharides. However, to achieve this, rather harsh oxidative environments are required. This is, first of all, clearly visible when considering the experimental results presented above: small increase in the C=O signal after 45 min treatment and the absence of significant chemical modifications after the treatment of the dried droplet. Secondly, from the simulations, a significant reduction in the amount of observed oxidation products occurred in solution, raising the need for more oxidizing species in such systems.

The fact that harsh oxidative environments are required for significant oxidation of saccharides is also in agreement with observations reported in literature, as the direct oxidation of glucose often requires the use of various catalysts (*e.g.*, enzymes, Au or Pd/Bi catalysts)<sup>7-9</sup>. Although the oxidation of saccharides has hardly been investigated, saccharide-containing biomolecules have been the subject of multiple plasma-related studies. An important example is DNA<sup>6,16,17</sup>. As will be explained in more detail in **chapter 4**, DNA consists of nucleobases situated on ribose rings, which are connected to each other with phosphate groups. From extensive literature<sup>6,16,17</sup>, it is clear that oxidizing species like OH radicals favor nucleobases, and to a lesser extent the connection between the ribose rings, compared to the ribose ring itself. However, it should be noted that the ribose rings, situated in DNA, do not contain free hydroxyl group, which formed the most targeted sites of oxidation in the results presented in this chapter.

Furthermore, the observed modifications have also been encountered in other studies, both computational and experimental. An important example is the oxidation of lipopolysaccharides. These molecules form an important part in the construction of bacterial cell walls<sup>18,19</sup>. Using X-ray photoelectron spectroscopy, a clear increase in C=O groups, as well as a decrease in C-O-C ether bonds, could be observed<sup>18</sup>. This was further supported by classical MD simulations done by Yusupov *et al.* who observed the breaking of the pyranose ring as a result of oxidation<sup>19</sup>.

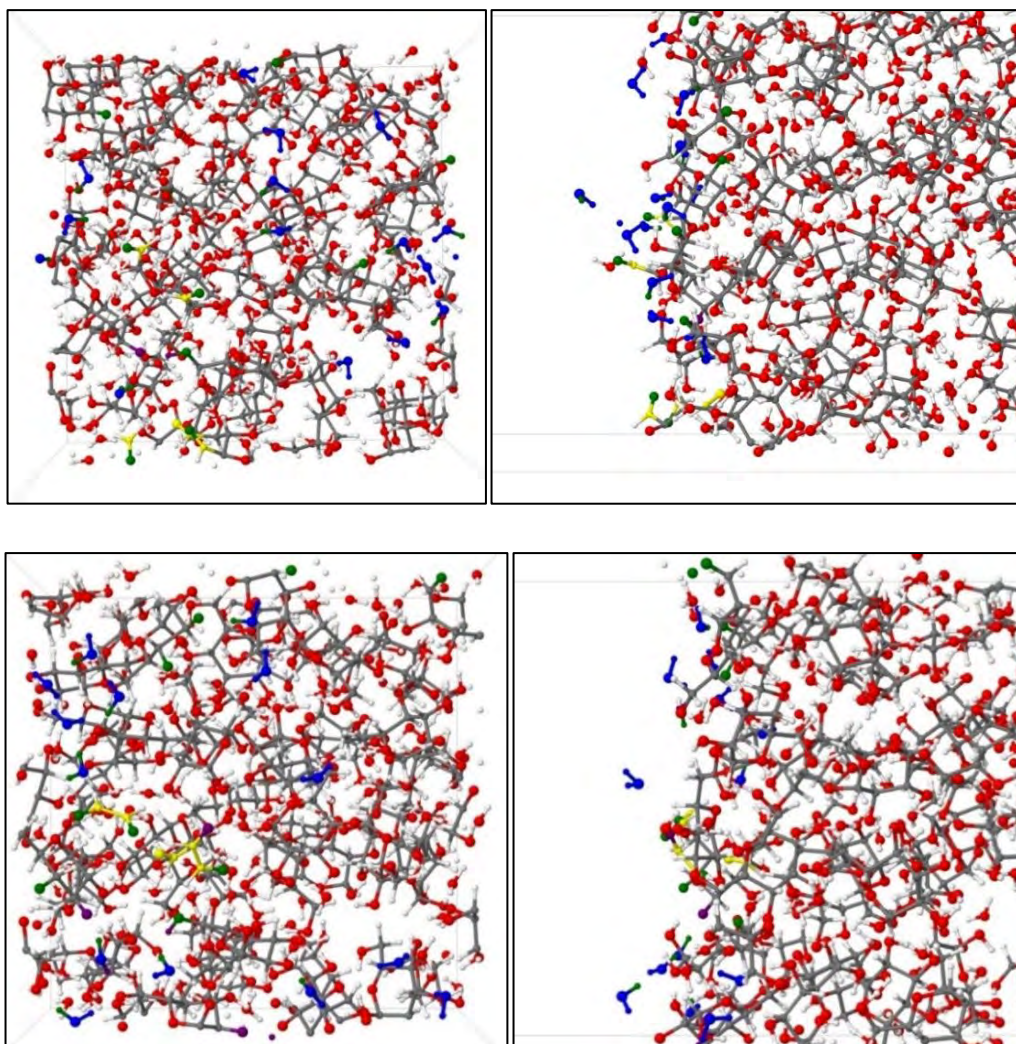


### 3-5 Appendix-3

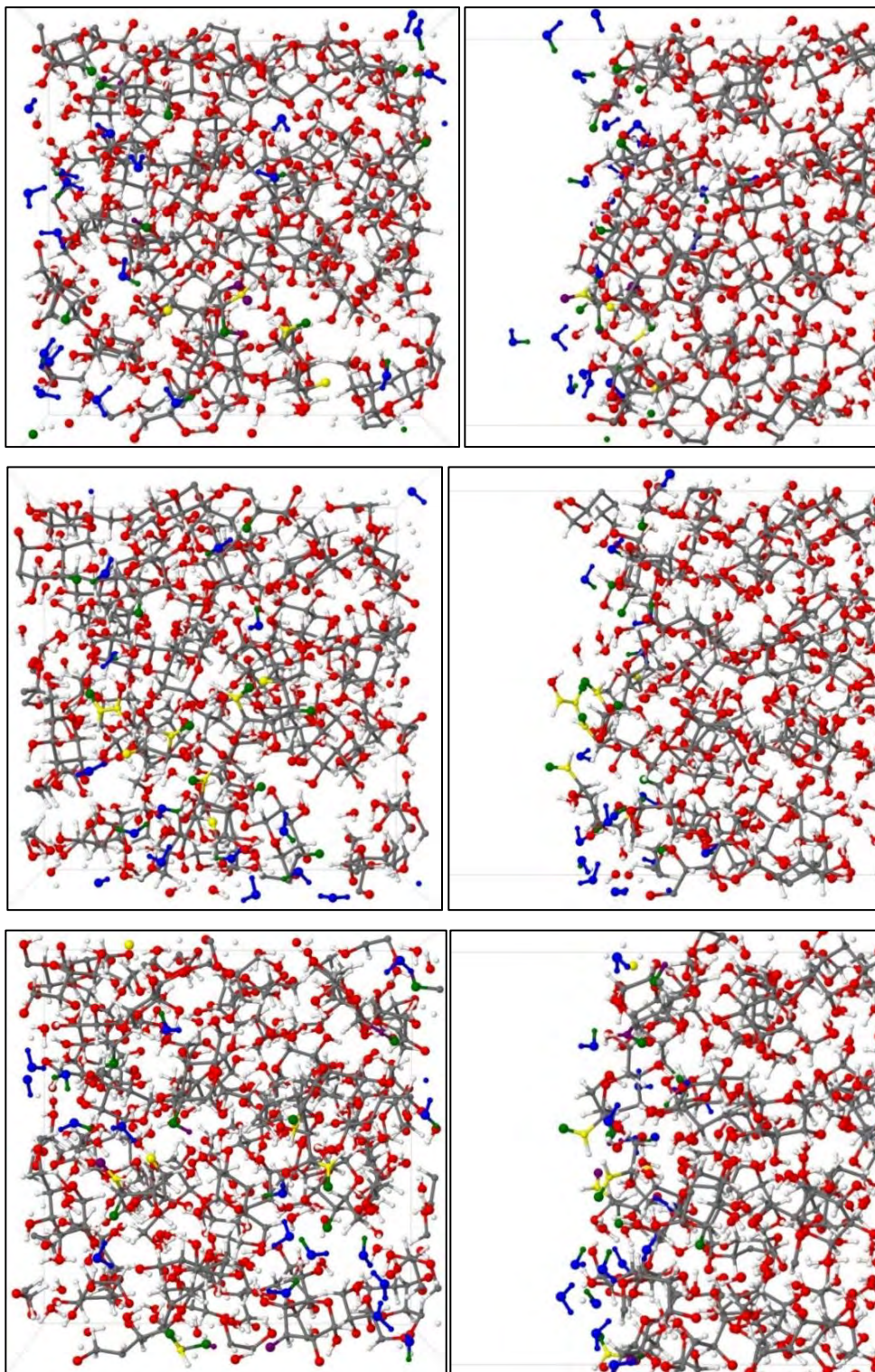
**Figure 3-A. The five impact simulations on amorphous D-glucose/water (1:1) are given in following figures.** Every simulation system consists of  $\pm 55$  D-glucose and  $\pm 55$  water molecules at 300 K. Every simulation contains 10 OH radicals for impact. From every simulation two pictures were taken: Front-view (z-axis; left), Right-side view (x-axis; right, OH impact initiated at left side).

**Color code:**

Oxygen atoms (red); Carbon atoms (grey); Hydrogen atoms (white); OH radicals + OH formed after abstraction of hydrogen from water (blue); R-H break/H-abstraction from D-glucose directly abstracted by OH (green); C-C / C-O bond breakage (yellow); R-H break/H-abstraction by another D-glucose radical for stabilization purposes (purple)







## 3-6 References

1. Alberts, B. *et al.* *Molecular Biology of The Cell*. (Garland Science, Taylor & Francis Group, 2008).
2. Anderson, L. *et al.* *Advances in Carbohydrate Chemistry and Biochemistry*. (Elsevier B.V., 2004).
3. Elliott, W. H. & Elliott, D. C. *Biochemistry and Molecular Biology*. (Oxford University Press, 2009).
4. Lindberg, A. L. F. A., Wollin, R., Bruse, G., Ekwall, E. & Svenson, S. B. in *Bacterial Lipopolysaccharides* (1983).
5. Yusupov, M. *et al.* Inactivation of the endotoxic biomolecule lipid A by oxygen plasma species: a reactive molecular dynamics study. *Plasma Process. Polym.* **12**, 162–171 (2014).
6. Verlackt, C. C. W. *et al.* Atomic-scale insight into the interactions between hydroxyl radicals and DNA in solution using the ReaxFF reactive force field. *New J. Phys.* **17**, 103005 (2015).
7. Besson, M., Lahmer, F., Pierre, G., Fuertes, P. & Flèche, G. Catalytic Oxidation of Glucose on Bismuth-Promoted Palladium Catalysts. *J. Catal.* **152**, 116–121 (1994).
8. Comotti, M., Pina, C. D., Falletta, E. & Rossi, M. Aerobic Oxidation of Glucose with Gold Catalyst: Hydrogen Peroxide as Intermediate and Reagent. *Adv. Synth. Catal.* **348**, 313–316 (2006).
9. Beltrame, P., Comotti, M., Della, C. & Rossi, M. Aerobic oxidation of glucose I. Enzymatic catalysis. *J. Catal.* **228**, 282–287 (2004).
10. van Duin, A. C. T., Dasgupta, S., Lorant, F. & Goddard, W. A. ReaxFF: a Reactive Force Field for Hydrocarbons. *J. Phys. Chem. A* **105**, 9396–9409 (2001).
11. Rahaman, O., van Duin, A. C. T., Goddard III, W. A. & Doren, D. J. Development of a ReaxFF Reactive Force Field for Glycine and Application to Solvent Effect and Tautomerization. *J. Phys. Chem. B* **115**, 249–261 (2011).
12. Yusupov, M. *et al.* Reactive Molecular Dynamics Simulations of Oxygen Species in a Liquid Water Layer of Interest for Plasma Medicine. *J. Phys. D. Appl. Phys.* **47**, 25205 (2014).

13. Hefny, M. M., Pattyn, C., Lukes, P. & Benedikt, J. Atmospheric Plasma Generates Oxygen Atoms as Oxidizing Species in Aqueous Solutions. *J. Phys. D. Appl. Phys.* **49**, 404002 (2016).
14. Ellerweg, D., von Keudell, A. & Benedikt, J. Microplasma Jets Emanating Into Ambient Air. *Plasma Sources Sci. Technol.* **21**, 34019 (2012).
15. Gilbert, B. C., King, D. M. & Thomas, C. B. Radical Reaction of Carbohydrates. Part 2. An Electron Spin Resonance Study of the Oxidation of D-Glucose and Related Compounds with the Hydroxyl Radical. *J. Chem. Soc.* **2**, 1186–1199 (1981).
16. Dizdaroglu, M. & Jaruga, P. Mechanisms of Free Radical-Induced Damage to DNA. *Free Radic. Res.* **46**, 382–419 (2012).
17. Cadet, J. & Wagner, J. R. Oxidatively Generated Base Damage to Cellular DNA by Hydroxyl Radical and One-Electron Oxidants: Similarities and Differences. *Arch. Biochem. Biophys.* **557**, 47–54 (2014).
18. Bartis, E. A. J., Graves, D. B., Seog, J. & Oehrlein, G. S. Atmospheric pressure plasma treatment of lipopolysaccharide in a controlled environment. *J. Phys. D. Appl. Phys.* **46**, 312002 (2013).
19. Yusupov, M. *et al.* Plasma-Induced Destruction of Bacterial Cell Wall Components: Reactive Molecular Dynamics Simulation. *J. Phys. Chem. C* **117**, 5993–5998 (2013).

# 4 Molecular Dynamics Simulations: DNA

The majority of this chapter has been published in Verlacket, C. C. W. *et al. New J. Phys.* **17**, 103005 (2015)<sup>1</sup>.



## 4-1 Introduction

Deoxyribonucleic acid, or simply DNA, forms the essence of every living cell and the respective organisms. DNA holds the genetic code of all components of each cell. In other words, it carries the instructions needed for the (re)production, development and functioning of all living cells. DNA is a macromolecule consisting of a sequence of deoxyribonucleotides. Deoxynucleotides form simple biochemical structures, composed of the monosaccharide deoxyribose, a phosphate group (to connect the ribose molecules together) and a nitrogen-based nucleobase. A total of four different nucleobases are known to be found in DNA: adenine (A), cytosine (C), guanine (G) and thymine (T), which form four nucleotides, dAMP, dCMP, dGMP and dTMP, respectively, as displayed in Figure 4-1.

DNA is usually a combination of two nucleotide chains, which are connected to each other by hydrogen bonds. This leads to the formation of a double helix, Figure 4-2. Three different double helix formations are known in biochemistry:

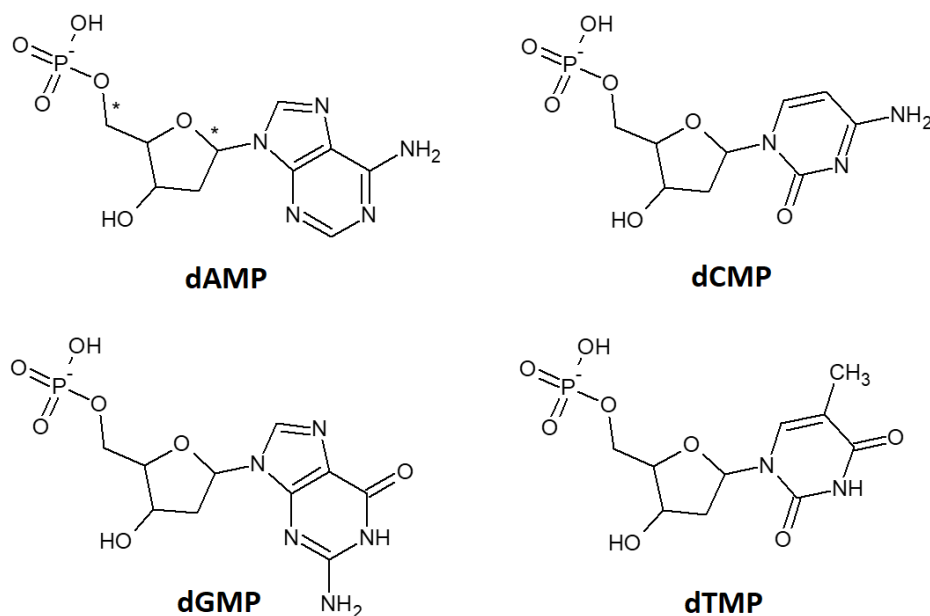


**Figure 4-1. Chemical structures of the four deoxyribonucleotides:** deoxyadenosine monophosphate (dAMP), deoxycytidine monophosphate (dCMP), deoxyguanosine monophosphate (dGMP) and deoxythymidine monophosphate (dTMP). The asterisk on dAMP indicates bonds with an underestimated bond order, as found in the results of test simulations (see text).

A-DNA, B-DNA and Z-DNA, see top Figure 4-2. The conformation of DNA is highly dependent on the hydration levels of the cells. A-DNA is only observed in dehydrated cells, at hydration levels where the cell becomes non-functional. Furthermore, B-DNA is most abundant in cells functioning under physiological

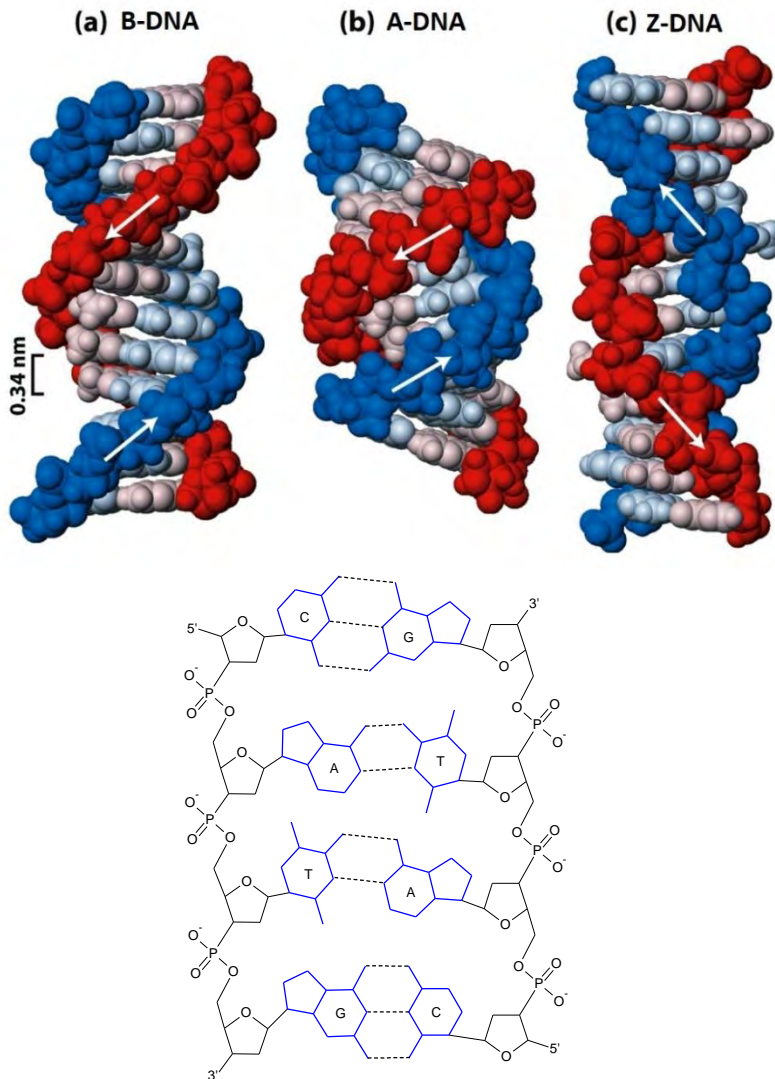


**Figure 4-2. Schematic representation of the three different DNA double helices: B-DNA (a), A-DNA (b) and Z-DNA (c).** The two DNA strands both have a different color: red and blue. The bottom figure depicts the different H-bonds between complementary nucleotide, which keep both DNA strands together: three H-bonds between cytosine and guanine; two H-bonds between thymine and adenine. Top figure obtained from *Molecular Cell Biology: Sixth Edition* (2008), W. H. Freeman and Company.

conditions, while Z-DNA is typically encountered to relieve torsional strain in the DNA double strand during transcription. In addition, Z-DNA is believed to be present at positions where the nucleotides are methylated (*i.e.*, chemical modification of cytosine, which changes the activity of the corresponding DNA code)<sup>2</sup>. The relative large change in DNA conformation between B-DNA and Z-DNA makes it possible for Z-DNA specific proteins and enzymes to interact with this biomolecule to trigger specific biological pathways.

As already stated, the two DNA strands are connected with each other through a network of hydrogen bonds. This occurs between two complementary nucleobases at opposite single strands. As such, two combinations are optimal for double strand formation: A-T and C-G, forming two and three hydrogen bonds, respectively. These two possible connections are depicted in the bottom panel of Figure 4-2. Other combinations (*e.g.*, A-G, G-G or T-C) result in a poor connection at that given point and will be repaired by the specific repair proteins, known as Mut proteins (*i.e.*, MutS, MutH and MutL)<sup>3-5</sup>. This highlights an additional function of the complementary nature of the double strand: the protection of the genetic code of each cell, since mismatches can be detected and will activate biochemical repair mechanisms. This will not be possible when the genetic code was stored in a single stranded formation. Moreover, possible chemical modifications of individual nucleotides (*e.g.*, oxidation, amination, *etc.*) can be recognized and repaired to, again, correspond with the complementary nucleotide of the opposite single strand<sup>4,6-8</sup>. Despite this protection mechanism, the genetic code is not 100% secured, as the presence of mismatching nucleotide couples, or certain chemical modifications resembling other nucleotides, may result in a wrong repair response. This basically results in the ‘restoration’ of the opposite nucleotide, instead of the mismatching one, resulting in a change in the genetic code –mutations<sup>7,8</sup>.

It is clear that DNA plays a crucial role in the existence of cells and organisms, serving as the data-base for cellular productions, behaviour and action against certain signals. A mutation or change in this genetic code can therefore be potentially lethal to the cell, as certain important processes might change<sup>3,4</sup>. As a result, the protection of the genetic sequence is of utmost importance to the cell. To achieve this, DNA is preserved in certain organelles inside every cell –the nucleus and the



mitochondria—protecting them against potential harmful chemicals. Especially nuclear DNA (nDNA) is heavily protected inside cells. During the non-replicative stages, nDNA is wound up around proteins, called histones, and stored as chromatin. However, during DNA transcription, *i.e.*, copying the DNA code to produce proteins, DNA is unwound for transcription proteins to read the DNA code, making it vulnerable for damage. This is an important target for many conventional anti-cancer therapies given the fast dividing nature of cancer cells (*cf.* 1-2.3c). Additionally, mitochondrial DNA (mtDNA) is prone to oxidative stress as mitochondria often produce reactive oxygen species, *e.g.*, superoxide ions, as a byproduct during the production of ATP, which is the source of energy for many cellular activities. Here, an important antioxidant, known as superoxide dismutase, protects DNA by transforming super oxide to  $\text{H}_2\text{O}_2$  (which is further degraded by catalase) or molecular oxygen<sup>9</sup>.

Yet, the protection of cellular DNA is not flawless. Indeed, experimental results have shown that reactive species (originating from the cell itself, as already mentioned, or from plasma treatment) are able to interact with DNA, resulting in DNA damages, mutation and single or double strand breaks<sup>10–13</sup>. Indeed, as plasma treatment increases the level of oxidative species in the affected cells, it is able to modify DNA. As a crucial part of living cells, insight in the oxidation processes is necessary to obtain an understanding in the cellular responses towards plasma treatment and oxidative stress more in general (proliferation, apoptosis, activation or inhibition of certain pathways, *etc.*).

In this chapter we utilized classical reactive MD simulations, based on the ReaxFF potential, given the size of the system, to elucidate the molecular scale interactions and reactions of various reactive oxygen species (*i.e.*, OH radicals,  $\text{HO}_2$  radicals and  $\text{H}_2\text{O}_2$  molecules) with DNA in aqueous solution. In this way, we obtain knowledge on the origins of important oxidative DNA lesions (such as double strand breaks), which can trigger apoptosis in mammalian cells.

## 4-2 Computational setup

Similar as in **chapter 3**, the interactions between DNA and ROS were investigated using the ReaxFF potential of van Duin *et al.*<sup>14</sup>. O atoms were not taken into account, as the simulations were only performed in aqueous solution. As observed in **chapter 3**, O atoms abstract an H-atom of water molecules upon impact with the solution, creating two OH radicals. This has also been observed and reported by Yusupov *et al.*<sup>15</sup>. However, in a later investigation (presented in **chapter 6**), the stability of O in liquid water has been confirmed using DFTB calculations. As this investigation was performed prior to the DFTB calculations on O in water, atomic O has not been considered in this work (*cf.* **chapter 6**) due to the abovementioned reasons.

In order to simulate DNA systems, the modified force field developed by Monti<sup>16,\*</sup> was used, containing parameters for C/H/O/N/P atoms, optimised for amino acids, peptides and nucleotides. A dodecamer, with the following sequence: ‘3-GCGTTTAAAGCG-5’ (see Figure 4-3), was used for the present study. Note that the aim of this study was to investigate the reactions between ROS and the nucleotides in a single strand and its consequences to the DNA molecule as a whole. For this reason, the exact nucleotide sequence of the simulated DNA molecule holds little value for the current study. As reactive MD simulations are quite time-consuming, and depend on the number of atoms in the system, a compromise had to be made between DNA string length and calculation time. Therefore, the DNA dodecamer, containing 12 base pairs, was used to investigate the migration of the reactive species towards the biomolecule and the subsequent reactions.

The DNA string was placed in a periodic rectangular cuboid with dimensions 33 Å x 33 Å x 48 Å. The remaining volume of the simulation box was filled with water molecules (approaching a density of 1 g/ml), providing a simple model for DNA found in the nucleoplasm/cytosol of living cells. As the force field only describes interactions among C/H/O/N/P atoms accurately, no additional atoms were included (*e.g.*, counter ions to compensate for the negative phosphate groups). On one hand, this guarantees a more reliable chemistry in the simulation of the DNA-water system.

---

\* Personal communication

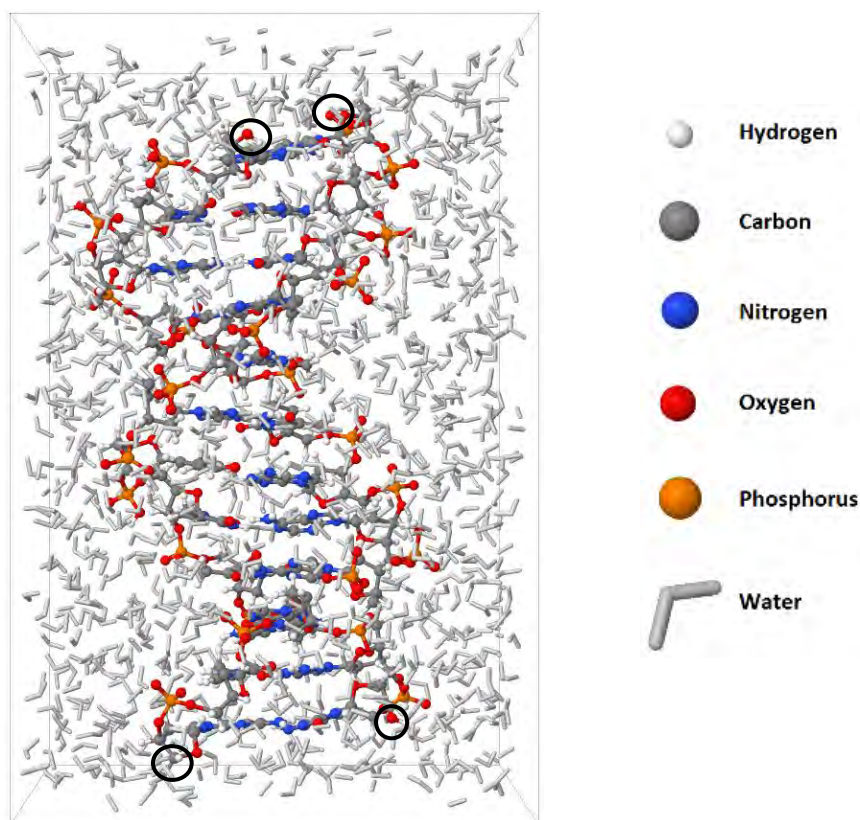


**Figure 4-3. Snapshot of the dodecamer in water, as used for the simulations.** The added OH groups, forming the end points of every single strand, are indicated by the black circles.

On the other hand, the phosphate groups of DNA are typically negatively charged. In solution, this is compensated by counter ions. However, as the used force field is not capable of describing these counter ions, they are not included in the simulations. Despite the lack of ions during the simulations, we expect that the negative charge is shielded, due to the presence of the water molecules, and will therefore have little effect on the simulated system. Furthermore, given the low number of water molecules present, the effect of pH has not been included in the current model system. Hydroxyl groups were added to the two ends of both DNA strands, replacing the missing phosphate group while preserving the O-atoms of the end nucleotides. The introduced OH groups are indicated by a black circle in Figure 4-3. Reactions at either one of these four end points are thus not considered in the results, *i.e.*, reactions at the resulting OH groups (*e.g.*, H-abstractions) as well as the adjacent

**Table 4-1. Average simulated bond orders (BO) found in dAMP after NVT at 300 K for 500 ps, in vacuum and in solution, compared to *ab initio* values.** The two C-O bonds which differ significantly from the initial values are highlighted. The initial values are deduced from the built-in dAMP structure in Gaussian09. Numbering is presented in Figure 4-4 below.

Bond	BO vacuum	BO solution	Initial BO
P1-O2	1.3	1.5	1.5
P1-O3	1.3	1.5	1.5
P1-O4	1.1	1.1	1.2
P1-O34	1.1	1.1	0.7
O4-C5	0.4	0.6	1.0
C5-C8	0.9	1.0	1.0
C8-O10	0.9	1.2	1.0
C8-C27	0.6	0.8	1.0
O10-C11	0.5	0.6	1.0
C11-N13	1.0	1.2	0.8
C11-C29	1.0	1.0	1.0
N13-C14	1.0	1.1	1.2
C14-N16	1.1	1.2	1.4
N16-C17	1.1	1.3	1.2
C17-C18	1.0	1.2	1.3
C17-C26	0.9	1.0	1.3
C18-N19	1.1	1.2	1.2
C18-N22	1.1	1.2	1.3
N22-C23	1.2	1.2	1.3
C23-N25	1.2	1.3	1.4
N25-C26	1.2	1.4	1.3
C26-N13	0.9	1.1	1.0

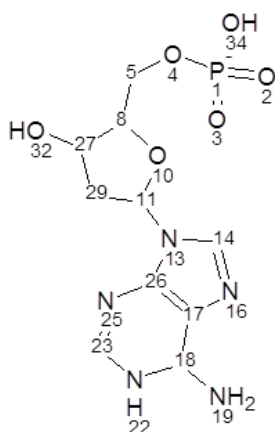


**Figure 4-4. Chemical structure of deoxyadenosine monophosphate (dAMP), labelled with atom numbers.**

atoms (*e.g.*, bond breaks and formations) are neglected.

Prior to the impact simulations in solution, test simulations with the individual nucleotides were performed both in vacuum and in solution, to verify the accuracy of the employed force field for our purposes. The results are summarized in Table 4-1. Overall, correct bond orders are found, over 50 independent simulations, for all bonds in the system, with the exception of two specific bond orders: C-OPO<sub>3</sub> and C-OC (indicated by an asterisk in dAMP in Figure 4-1), both having a bond order of around 0.6, instead of 1.0. This corresponds to an average bond length of 1.75 Å, instead of the expected 1.45 Å<sup>17</sup>. As a result, we expect a lower threshold for reactions with the introduced OH radicals for these bonds during the simulations. Indeed, the test simulations showed that the O4-C5 bond takes part in specific reactions (nomenclature is presented in Figure 4-4). However, the other bond (O10-C11) never interacted with the introduced radicals in the test simulations, nor in the simulations performed to investigate the reaction pathways. Hence, the reactivity of the specific reaction on C-OPO<sub>3</sub> is most likely overestimated by the used force field, but it cannot be discarded as being improbable and will be considered during the discussion.

Before starting the impact simulations, the molecular systems were equilibrated at room temperature (*i.e.*, 300 K) for 300 ps in the canonical ensemble (temperature and volume were kept constant: NVT), using a Nosé-Hoover thermostat with coupling constant of 25.0 fs. We used the following procedure for the equilibration: The system was first slowly heated from 0 K to room temperature for 100 ps, after which the system was stabilized at 300 K for 200 ps. This simulation time was enough to stabilize the molecular structures at the given temperature, *i.e.*, the total energy of the system remained constant as a function of time. For all further simulations, *i.e.*, thermalization and subsequent impact simulations, a time step of 0.25 fs was used.

Fifteen independent simulations were performed, by randomly placing ten ROS around the biomolecule. As also observed in a previous study from our group<sup>15</sup>, the trajectory of every molecule can roughly be approximated by a random walk, where the average distance between the water molecules can be seen as the mean free path of the radical. Because of this behavior, the impact simulations were carried out for 500 ps, enabling the system to perform as many impact reactions as possible

within a reasonable calculation time. In the case of OH, 15 additional impact simulations were carried out due the high reactivity of the OH radicals. In practice, this means that the output of the first set of simulations was used as the new starting point for the follow-up simulations, where ten new OH radicals are introduced. In this way, the 20 possible impact reactions (*i.e.*, interaction with two times ten OH radicals) are spread over 1000 ps, giving the structure some time to stabilize after every reaction, while increasing the chance of multiple impact reactions to happen on the single nucleotides, which can then be investigated further.



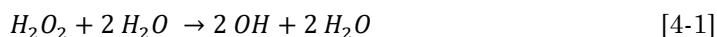
## 4-3 Results

### 4-3.1 H<sub>2</sub>O<sub>2</sub> and HO<sub>2</sub>

A total of 15 independent simulations were performed containing ten ROS (either HO<sub>2</sub> or H<sub>2</sub>O<sub>2</sub>). In contrast to the OH radical impact simulations, a selected number of ROS was positioned relatively close to the biomolecule to elucidate whether reactions can be expected. Indeed, as H<sub>2</sub>O<sub>2</sub> and HO<sub>2</sub> have a significantly longer lifetime compared to OH, more time is often required to observe reactions with the biomolecule during the simulations. Furthermore, this was necessary given the short simulation times of a few hundred ps, as well as the clear decrease in reactivity of these species compared to OH radicals<sup>18</sup>.

#### 4-3.1a H<sub>2</sub>O<sub>2</sub>

H<sub>2</sub>O<sub>2</sub> molecules were never found to react directly with the biomolecule. However, in a single case, the formation of OH radicals was encountered, which in turn was able to abstract an H from the dodecamer:



Reaction 4-1 was discarded from the results given the fact that the dissociation of H<sub>2</sub>O<sub>2</sub> requires additional energy (Fe<sup>2+</sup> catalyst or UV excitation<sup>19,20</sup>). Because of this, it was highly unlikely that reaction 4-1 would spontaneously happen experimentally and was probably caused by a spike in the calculated energy. However, although the reactivity was overestimated by the used force field, the formation of OH radicals by the dissociation of H<sub>2</sub>O<sub>2</sub> is a well-known observation within plasma medicine (as a result of the Fenton reaction<sup>19</sup> or photo-dissociation<sup>20</sup>) and can play a very important role in DNA oxidation, as plasma-generated OH radicals are unable to reach DNA due to their extremely short life-time<sup>18</sup>. The reactions with OH radicals will be discussed in **section 4-3.2**.

#### 4-3.1b HO<sub>2</sub>

Using similar conditions as the impact simulations with H<sub>2</sub>O<sub>2</sub>, HO<sub>2</sub> radicals were found to react mainly with other HO<sub>2</sub> molecules or water in 4 and 65% of the cases, respectively:





This resulted in the formation of  $H_2O_2$ ,  $O_2^-$  and  $H_3O^+$ . The formation of  $H_2O_2$  in water has been covered in the work of Bielski<sup>21</sup>. However, from 4-3.1a, it was clear that hydrogen peroxides will not react further with the DNA dodecamer. The resulting ions were observed to react further, in rare cases (7%), with the biomolecule through the protonation of various ketones found in the dodecamer. Given the fact that the pKa value of  $HO_2$  is around 4.88, the deprotonation of  $HO_2$  (*i.e.*,  $O_2^-$ ) is expected to be a dominant process at the physiological acidity of pH 7.3<sup>21</sup>. Although  $HO_2/O_2^-$  is known to cause DNA damage, as it forms one of the major oxidants in mitochondria (as explained in **section 4-1**), no reaction between  $O_2^-$  and DNA was encountered. We expect that longer time scales, or the presence of other reactants, are required for chemical modifications to occur.

## 4-3.2 OH radicals

Simulations were divided in two groups: the first 500 ps, where the first set of ten OH radicals were introduced in the simulated system; and the last 500 ps (adding up to 1000 ps), where a second set of ten OH radicals was introduced, aiming to observe later-stage oxidation products.

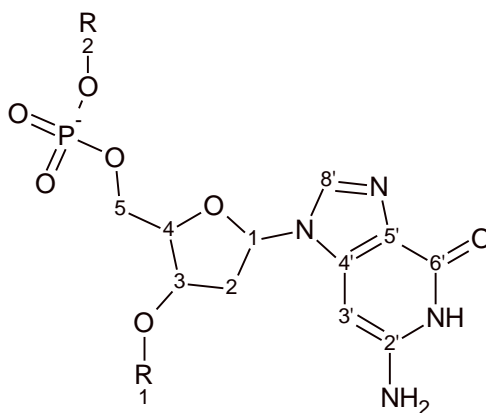
### 4-3.2a Dodecamer DNA simulations: 0 – 500 ps

In the first part of the simulations (*i.e.*, first 500 ps), a distinct set of reactions has been identified, including both H-abstractions and OH addition reactions. In total, 65 reactions were observed, neglecting those that occurred at the end points of the DNA molecule due to the reasons mentioned in **section 4-2**. These reactions are summarized, along with their corresponding number of occurrence, in Figure 4-5. Three different types of reactions, on both the ribose-phosphate backbone and the nucleobases, were identified.

The first type is the H-abstraction reaction of the amines found in the nucleobases, *i.e.*, the primary amine in dAMP, dCMP and dGMP; and the secondary amine in the 6-ring of dGMP and dTMP (*cf.* Figure 4-1). These two reactions are displayed in Figure 4-6 and Figure 4-7, respectively, for dGMP as an example. Both

reactions result in a radical within the purine ring (for dAMP and dGMP) or pyrimidine ring (for dCMP and dTMP). In turn, the resulting radical can lead to a series of intermolecular H-abstractions, enabling further reactions in the corresponding nucleotides. As these H-atoms were often part of the H-bond structure between the two DNA strands, it is well possible that they affected this H-bond system. Indeed, a subsequent H-abstraction could occur from the complementary nucleobase by the radical, enabling further reactions within the DNA molecule.

The abstraction of H-atoms from these amines has also been proposed by Abolfath *et al.*<sup>22</sup>, at least for secondary amines. Using QM/MM calculations on guanine in water, they observed the abstraction of H-atoms from the secondary amine and noticed a strong affinity of OH radicals towards the H-atom of the primary amine, making this atom a potential target for abstraction reactions as well, despite



Reaction	Frequency
H-abstraction of primary amine	7
H-abstraction of secondary amine	3
OH addition on C-8' adenine	21
OH addition on C-8' guanine	31
Addition-elimination on C5-O	3

**Figure 4-5. Schematic representation of dGMP as an example for the nomenclature used in the table and the discussion above.** In the table, an overview of the reactions observed between the OH radicals and the nucleotides of the dodecamer DNA helix in water, within a simulation time of 500 ps, is presented, along with the number of occurrence. Primary amine corresponds to the  $-NH_2$  group found on dAMP, dCMP and dGMP. Secondary amine corresponds to the  $R_2NH$  group found in the pyrimidine ring of dGMP and dTMP.

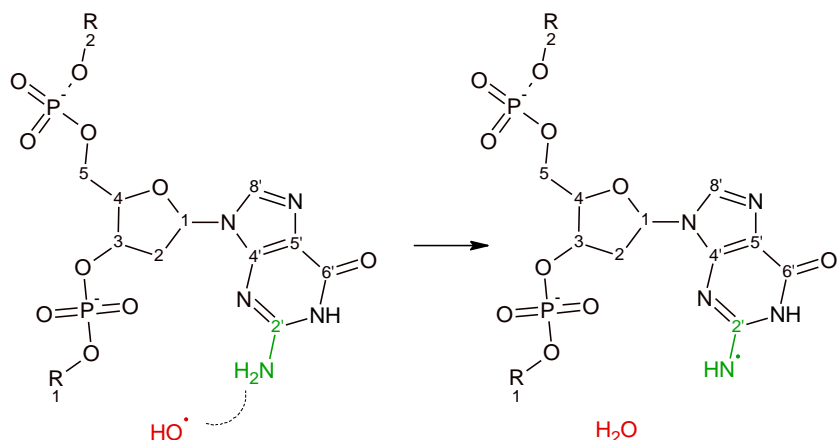


**Figure 4-6. H-abstraction reaction caused by an OH radical at a primary amine found on dGMP.** R<sub>1</sub> and R<sub>2</sub> correspond to the preceding and following nucleotide, respectively.

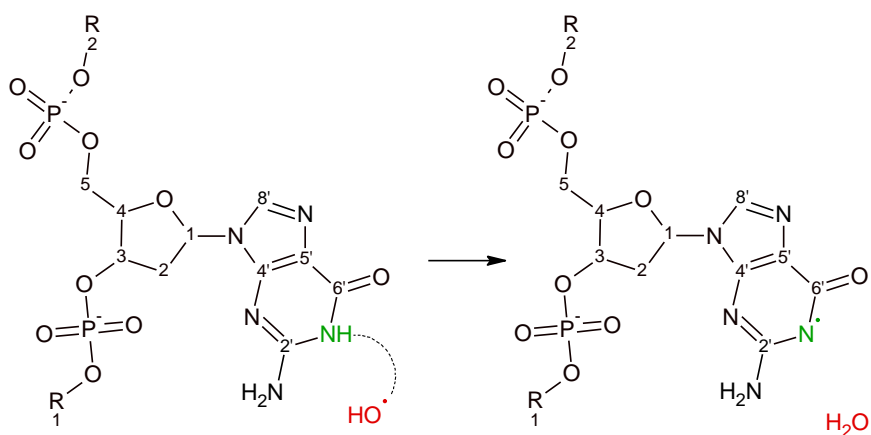


**Figure 4-7. H-abstraction reaction caused by an OH radical at a secondary amine found on the purine 6-ring of dGMP.** R<sub>1</sub> and R<sub>2</sub> correspond to the preceding and following nucleotide, respectively.

the fact that the actual H-abstraction was not observed. However, the abstraction of H-atoms from the primary amine has been encountered experimentally by Chatgililoglu *et al.*<sup>23</sup>, as well as by Mundy *et al.* using *ab initio* MD simulations<sup>24</sup>. Their observations suggested a low probability for the H-abstraction reaction from the secondary amine. Our results correspond well with the discussed studies as they also predict a lower probability for H-abstraction from the secondary amines (*cf.* Figure 4-5).

The second type of reaction, which was abundantly observed in the

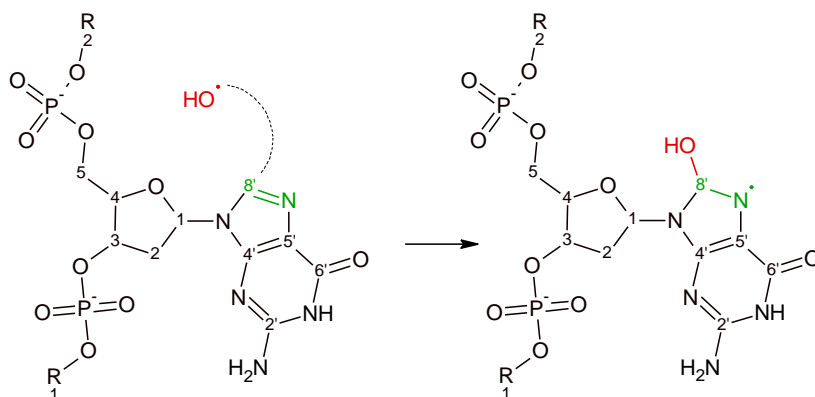


**Figure 4-8. Addition of an OH radical on C-8' of dGMP.** This reaction results in the formation of an 8-OH-guanine adduct radical. R<sub>1</sub> and R<sub>2</sub> correspond to the preceeding and following nucleotide, respectively.

simulations (*cf.* Figure 4-5), was the addition of an OH radical at the C-8' position on the purine ring of dAMP and dGMP. This reaction yields the formation of the 8-hydroxy-purine-adduct radicals (8-OH-Ade● or 8-OH-Gua●, respectively). This results in a radical in the purine ring, as depicted in Figure 4-8 for dGMP, as an example. This reaction is the first step towards the formation of the well-known 8-oxo-guanine (8-O-Gua) and 2,6-diamino-4-hydroxy-5-formamido-pyrimidine (FapydG)<sup>25</sup>. These reaction pathways are among the most studied oxidative processes on DNA and are widely used as a marker for DNA oxidation by ROS, described in multiple studies, for both dAMP and dGMP<sup>12,26–33</sup>. Multiple reaction pathways, with the 8-OH-adduct radicals, have been proposed in several studies and are summarized by Dizdaroglu *et al.*<sup>28</sup>. One of the proposed reaction pathways continues with a H-abstraction of the C8'-H from the adduct radical, resulting in the formation of an 8-hydroxy-purine, forming the enol-form of 8-oxo-purine (both structures are keto-enol tautomers). A second pathway continues with the opening of the purine 5-ring, followed by a reduction (*i.e.*, H donation from other molecules in the surrounding nucleoplasma or cytosol, such as acids, other ROS or biomolecules), forming FapydG and FapydA, for dGMP and dAMP, respectively. The formation of these products may lead to the inability of various proteins to interact with the DNA strands and are a target for incorrect repair, causing DNA mutations<sup>27–29</sup>. Indeed, it has been proven experimentally that the introduction of 8-hydroxy-guanine or 8-hydroxy-adenine can result in DNA point mutations: G → A and A → G/C<sup>27,29</sup>. Moreover, another

experimental study performed by Kuchino *et al.* confirms the introduction of all four nucleotides after DNA synthesis when 8-hydroxy-guanine was embedded in the parent DNA double helix<sup>34</sup>.

Random DNA mutations can lead to severe damage, *e.g.*, changing the coding sequence of key proteins, which may lead to apoptosis<sup>35</sup>. The existence of FapydG and FapydA in DNA has also been suggested to cause the inhibition of DNA synthesis, thus being potentially lethal to the cell<sup>28</sup>. As the first steps in the reaction pathways of these mutagenic and toxic lesions have been observed in our simulations, apoptosis can be expected when more time is given to the cell.

The final reaction pathway, predicted by the simulations, was the addition of the OH radical on C-5 of any nucleotide, leading to a broken C5-O bond and thus the desorption of the phosphate group attaching the two nucleotides together, as illustrated in Figure 4-9. Although this reaction was only observed a few times (*cf.* Figure 4-5), it forms a very important reaction, because it can lead to single strand breaks (SSB) as observed in the simulations. The latter is a reversible oxidation pathway in DNA, but combined with a second SSB at the opposite single strand, in close vicinity, it results in double strand breaks (DSB). In this way, the DNA double helix is irreversibly cleaved in two parts. Among the main antitumor responses, single and double strand breaks are widely considered as triggers for apoptosis<sup>10,13,36–41</sup>, forming the main goal of plasma cancer treatment.

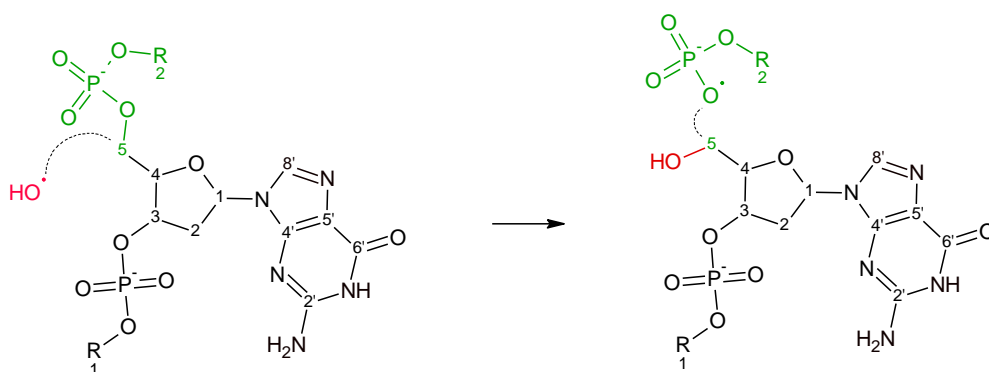
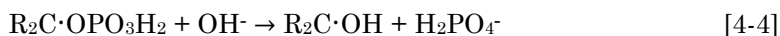


**Figure 4-9. Addition-elimination reaction where an OH radical binds with C-5 at the sugar-phosphate backbone, resulting in the breaking of the C-O bond and the desorption of the phosphate group, *i.e.*, SSB.  $R_1$  and  $R_2$  correspond to the preceeding and following nucleotide, respectively.**

DSBs can be triggered by either two separate SSBs on both strands in close vicinity, or by radical transfer after one SSB. In the latter case, the radical present in the broken chain reacts with the opposite single strand, leading to a second SSB, and thus resulting in a DSB<sup>41</sup>. Many research groups tried to estimate the maximum distance between the two separate SSBs in order to trigger DSBs, pointing towards values varying from 20 to 57 base pairs<sup>13</sup>. As our simulations contained only 12 base pairs, DSBs are expected if SSBs were found on both strands despite their position. However, in this case study, not more than a single SSB has been encountered in a single simulation. Combined with the fact that the resulting radical after SSBs never came into contact with the opposite single strand during the 500 ps simulation time, no DSBs were observed in this set of simulations. This is most likely due to the limited simulation time, as SSBs are not abundantly found during the performed simulations. Indeed, as will be discussed later, DSBs have been observed in our simulations during the subsequent 500 ps (for a total of 1 ns).

In literature, SSBs are triggered by H-abstraction reactions by OH radicals with the ribose H-atoms<sup>28,37,42</sup>. Here, SSBs occurred when, for example, O<sub>2</sub> interacts with the formed ribose radical, generating a peroxide. Our simulations, however, suggested a different mechanism, as depicted in Figure 4-9. The interaction with the C5-O bond was favored above the H-atoms connected to the same carbon atom. This can be caused by an underestimation of the C-OPO<sub>3</sub> bond strength, as discussed in Table 4-1, due to the reduced bond order. In spite of the difference in the reaction pathway, we believe that an addition-elimination reaction should not be completely discarded, as it has also been reported in previous studies<sup>43</sup>. Indeed, Samuni *et al.*<sup>43</sup> reviewed the possibility of the following overall reaction 4-4:



Note that, prior to the addition-elimination reaction (albeit with OH<sup>-</sup>), a H-abstraction took place, resulting in the formation of the C-radical. Despite the mentioned difference in reaction pathways, we believe that the SSBs observed in our simulations can play a critical role in the oxidation of DNA molecules caused by OH radicals in solution, and that they affect the stability of the structure of this biomolecule.

### 4-3.2b Dodecamer DNA simulations: 500 – 1000 ps

After the introduction of ten additional OH radicals per simulation run (*i.e.*, after the first 500 ps), the simulations continued for an additional 500 ps. This resulted in similar reactions as discussed above, combined with two new phenomena: breaking the purine 5-rings (in the case of dGMP) and two SSBs in opposite strands within a single run (*i.e.*, a single dodecamer DNA molecule).

The break of the dGMP purine ring is depicted in Figure 4-10. An OH radical abstracted the H-atom of the alcohol group introduced by the reaction shown in Figure 4-8. This reaction led to the homolytic dissociation of the adjacent N-C8' bond, resulting in the formation of both an aldehyde and another radical within the structure (see Figure 4-10). Results in literature indicated that FapydG is formed after an intermolecular rearrangement of the H-atoms and a H-abstraction by the 8-OH-Gua●<sup>28</sup>. However, in results presented here, no H-abstraction by the 8-OH-Gua● has been encountered as no suitable H-sources were present in the system. Furthermore, due to the absence of these H-sources, the H-rearrangements (*e.g.*, keto-enol conversion, as suggested by Dizdaroglu *et al.*<sup>28</sup>) could not be observed. Despite this, the reaction as illustrated in Figure 4-10 does point out the necessary H-abstraction-part for the rearrangements for the formation of FapyG. We believe

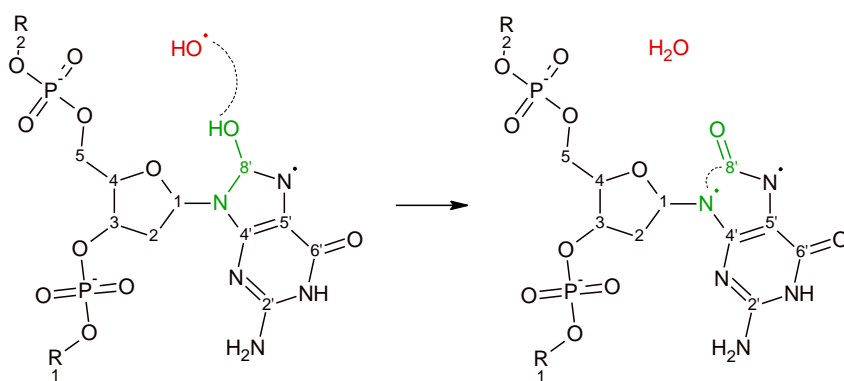


**Figure 4-10. H-abstraction reaction of 8-OH-guanine in dGMP as formed by the reaction displayed in Figure 4-8.** The abstraction of the alcohol H-atom leads to the homolytic break-up of the N-C8' bond, resulting in an N-radical and an aldehyde group (ring opening). The N-radical may in turn abstract an H-atom from surrounding H-donors, possibly leading to the formation of FapydG<sup>28</sup>. R<sub>1</sub> and R<sub>2</sub> correspond to the preceding and following nucleotide, respectively.

that, when suitable H-sources would be present and the system would be given enough time, FapyG would most likely be formed during the simulations.

As mentioned above, the simulations for the additional 500 ps also showed SSBs at opposite strands within a single DNA molecule (see Figure 4-11 for an example found in the simulations), so that a DSB can be expected when enough time is given, as discussed above. Figure 4-11 depicts a snapshot of part of the dodecamer, as found in one of the simulations, containing three SSBs on different strands (*i.e.*, two on the grey single strand and one on the purple single strand). The SSBs are displayed in green (dark green for the grey single strand and light green for the purple single strand). Multiple SSBs have been observed in two of the 15 independent simulations (*i.e.*, three in each case), similar to the situation depicted in Figure 4-11. However, they did not (yet) result in DSBs as a consequence of simulation time and box-size. Indeed, loose DNA single strand ends can migrate away from the complementary single strand, breaking the H-bond system over time. When both strands are broken within 20-57 base pairs<sup>13</sup>, a DSB will eventually occur when enough H-bonds, between the two helices, are broken. As two of the 15 independent simulations of the dodecamer showed multiple SSBs, it is expected that a DSB will occur when enough time and space is given to the simulated system. In Figure 4-11, the two SSBs at one single strand occur at a distance of two and six base pairs away from the SSB at the opposite single strand.

In another simulation run, the reaction depicted in Figure 4-12 was observed. This reaction involves the transfer of a radical (*e.g.*, ribose radical), giving rise to the alternative pathway of DSB, as suggested in literature<sup>13,41</sup>. Indeed, when enough time was given to the structure, the resulting alcohol group, after the first SSB, was able to interact with the C5-O bond at the opposite single strand. Similar as discussed in the case of SSBs, our simulations describe the double strand break by an addition-elimination reaction. When the alcohol H-atom was abstracted, a reaction between the two strands took place where the C5-O bond was broken, yielding the formation of an ether and yet another phosphate radical, hence transferring the radical site from the first single strand to the other one, resulting in the second SSB. This thus leads to the point where both strand are broken.

As the results suggested a different pathway for the formation of SSBs (see



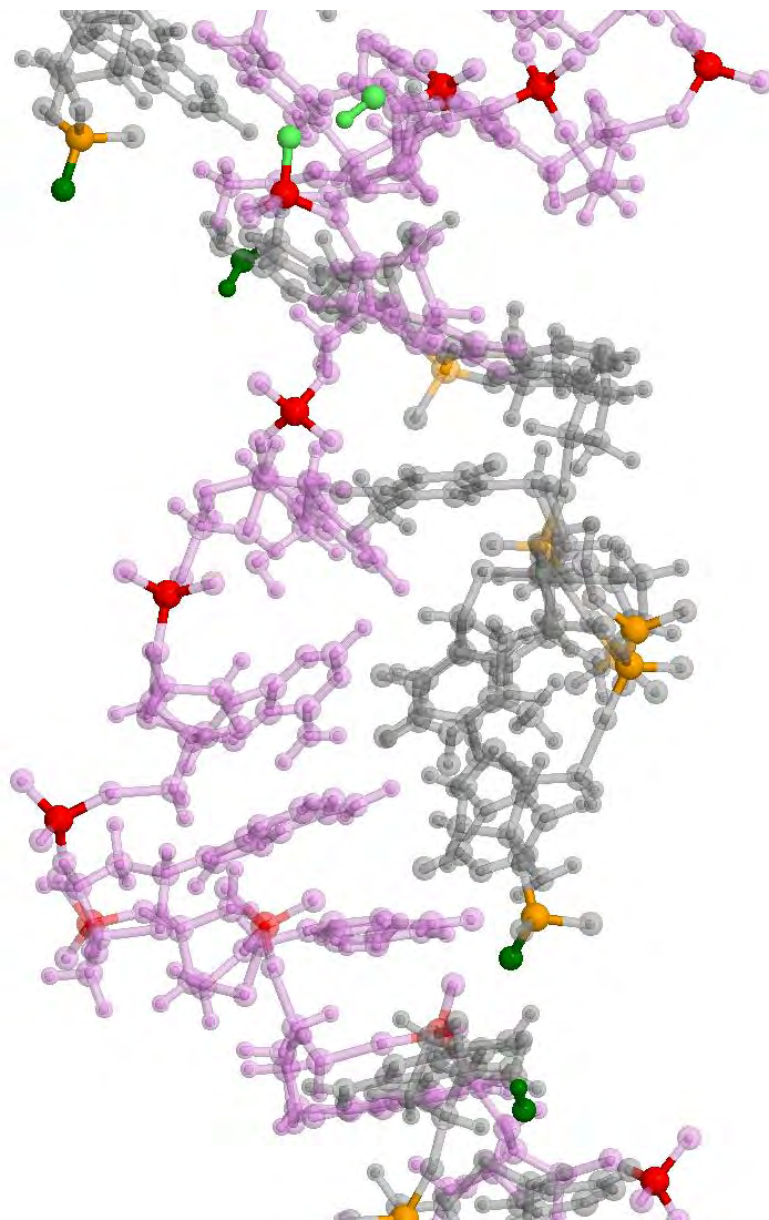


**Figure 4-11.** 3D snapshot of a part of the dodecamer after the impact of 20 OH radicals for 1000 ps. The DNA molecule is depicted in slightly transparent grey and purple (representing both strands); phosphorus atoms of the first and second single strand are displayed in red and orange, respectively, for sake of clarity; the three SSBs, which can eventually lead to a DSB, if enough time is given to the system, are depicted in green, *i.e.*, the corresponding phosphate O-atom on one hand and the added OH radical on the other hand. Two SSBs are found on the grey single strand and one on the purple single strand (depicted in a lighter green). The two SSBs on the grey single strand, in this particular simulation run, occurred at a distance of two and six base pairs away from the SSB at the purple single strand.

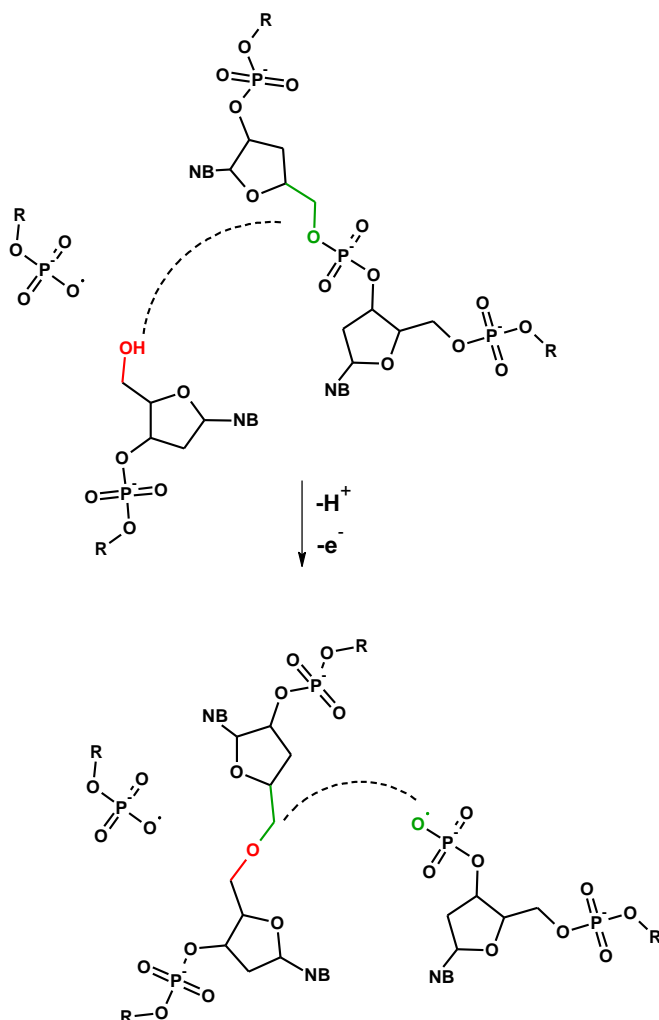


**Figure 4-12. Reaction between two DNA strands when one has been broken by the addition of an OH radical, as depicted in Figure 4-9 (SSB).** This reaction results in yet another SSB, in the opposite single strand, which may lead to a DSB. The nucleobase are depicted as *NB*. R correspond to the preceeding and following nucleotides connected by phosphodiester bonds to the displayed structure.

discussion above), it is well possible that, due to the overestimated C-OPO<sub>3</sub> bond length, the reaction pathway described in Figure 4-12 is more favourable in the simulations than what can be expected in the experimental observations. However, studies in literature<sup>13,41</sup> explicitly mentioned the reaction of the resulting radical of the first single strand, due to SSB, with the opposite single strand, which will trigger DSB. We believe that these radical reactions can therefore also result in a connection between the two opposite strands, similar as seen in our results (Figure 4-12, *i.e.*, the

two opposite strands are here connected via an ether group). This can, nonetheless, have devastating consequences to the cell if left unrepaired, due to severe distortion of the helical structure. Moreover, if the bond, connecting the two strands, would be broken again, similar consequences as described above for multiple SSBs are expected, for this type of DSBs.

In a final remark, it is important to note that several oxidation reactions reported in literature have not been encountered in our simulations. An example is the addition of OH radicals on  $sp^2$  carbon atoms of pyrimidines (dTMP or dCMP)<sup>44,45</sup>. Ji *et al.* investigated the interaction of OH radicals and thymine using *ab initio* DFT calculations and concluded that the additions of OH on 6-C and 5-C are energetically the most favored reactions between OH and pyrimidine nucleobases, with yields of 60 and 30%, respectively, corresponding to experimental values. These observations suggest a decrease in the overall simulated reactivity in this model, compared to experimental and *ab initio* studies. However, it is not the aim of this work to describe all possible reactions but rather to give dynamic insight in DNA oxidation from the viewpoint of (reactive) molecular dynamics. With respect to this, and to our opinion, it is clear that the observed reactions point towards the most relevant oxidation products which can be expected when considering an aqueous solution containing only OH or  $H_2O_2$  and a dodecamer, without increasing the complexity of the system. Moreover, a high rate of DNA oxidation, introducing a wide range of oxidation products on a limited length-scale, may distort the system too much, resulting in an unrealistic representation of our system.

## 4-4 Conclusion

In this chapter, the interactions of three ROS (*i.e.*,  $\text{H}_2\text{O}_2$ ,  $\text{HO}_2$  and  $\text{OH}$ ) with DNA helices in solution were investigated by means of reactive molecular dynamics simulations, using the ReaxFF potential. This investigation pointed towards  $\text{OH}$  as the most important oxidizing agent, resulting in the formation of several oxidation products, which are also found in experimental and *ab initio* studies. In particular, the first steps in the formation of 8-oxo-guanine and 8-oxo-adenine, which are known as markers for oxidative stress in cells, H-abstraction of amines, and DNA single and double strand breaks, as a result of an addition-elimination reaction, were predicted. Additionally, two mechanisms for double strand breaks have been discussed, (i) resulting from two independent single strand breaks at opposite strands within a DNA molecule, and (ii) due to a radical transfer from a resulting product, after a first SSB, which reacts with the opposite, intact single strand. However, only the second mechanism has been observed, but we expect that the first mechanism would be observed as well, at longer calculation times, and in a larger simulation box (enabling the broken strands to migrate away from each other, breaking the H-bridge system between them). Finally, the effects of the oxidative damage on the helical structure have been investigated, indicating a clear deformation of the structure due to new interactions between the resulting oxidation products and the simulated biomolecule, which may trigger pro-apoptotic factors within the treated cells.

Besides  $\text{OH}$  radicals, the interaction of  $\text{H}_2\text{O}_2$  and  $\text{HO}_2$  with DNA has been investigated. Both species were found to be largely non-reactive towards the introduced DNA dodecamer within the simulated timescales. Indeed, we found that they reacted with the DNA helices only in rare cases, leading to the protonation of various ketones found in the biomolecule. Furthermore, suspicious behavior has been observed during the simulations, where the force field enabled reactions resulting in oxidation products, which are experimentally unknown or behaved in an incorrect way. In this context, the dissociation of  $\text{H}_2\text{O}_2$  after a few tens of ps in aqueous solution was observed. This is likely caused by a spike in the calculated energy, enabling the dissociation of the O-O bond of hydrogen peroxide. Additionally, while oxidative damage by  $\text{HO}_2/\text{O}_2^-$  was expected, no such phenomena were encountered during the simulated timescale, indicating that either longer timescales or other reactants are

required for the oxidation of DNA to occur.

It is important to note that the situation is more complex than provided in this study, as several later-stage oxidation products that have been observed in literature were not investigated here, due to the limited time- and space-scale, as well as due to the absence of the needed reactants (one example is the peroxidation in the presence of O<sub>2</sub>). Furthermore, combining the experience obtained from this particular research, we must conclude that this research is at the limits of what is possible with the classical MD approach (*cf.* **section 2-2.2**). When more complex systems are investigated, more accurate methods are required to obtain reliable results. This was, however, not possible in this case due to the high number of simulated atoms. Indeed, as water is needed for the stabilisation of the DNA double helix, the number of atoms increases beyond the limitations of more accurate methods like DFTB (*cf.* **2-2.3**).

## 4-5 References

1. Verlackt, C. C. W. *et al.* Atomic-scale insight into the interactions between hydroxyl radicals and DNA in solution using the ReaxFF reactive force field. *New J. Phys.* **17**, 103005 (2015).
2. Carvalho, A. T. P. *et al.* Understanding the Structural and Dynamic Consequences of DNA Epigenetic Modifications: Computational Insights into Cytosine Methylation and Hydroxymethylation. *Epigenetics* **9**, 1604–1612 (2015).
3. Elliott, W. H. & Elliott, D. C. *Biochemistry and Molecular Biology*. (Oxford University Press, 2009).
4. Alberts, B. *et al.* *Molecular Biology of The Cell*. (Garland Science, Taylor & Francis Group, 2008).
5. Marinus, M. G. DNA Mismatch Repair. *EcoSal Plus* **5**, 1–62 (2014).
6. Lee, H. C. & Wei, Y. H. Oxidative Stress, Mitochondrial DNA Mutation, and Apoptosis in Aging. *Exp. Biol. Med.* **232**, 592–606 (2007).
7. Lutsenko, E. A., Carcamo, J. M. & Golde, D. W. Vitamin C Prevents DNA Mutation Induced by Oxidative Stress. *J. Biol. Chem.* **277**, 16895–16899 (2002).
8. Shibutani, S., Takeshita, M. & Grollman, A. P. Insertion of Specific Bases During DNA Synthesis Past the Oxidation-Damaged Base 8-oxodG. *Nature* **349**, 431–434 (1991).
9. Imlay, J. A. Cellular Defenses Against Superoxide and Hydrogen Peroxide. *NIH Public Access* **77**, 755–776 (2011).
10. Kim, G. J., Kim, W., Kim, K. T. & Lee, J. K. DNA Damage and Mitochondria Dysfunction in Cell Apoptosis Induced by Nonthermal Air Plasma. *Appl. Phys. Lett.* **96**, 21502 (2010).
11. Cadet, J. & Wagner, J. R. Oxidatively Generated Base Damage to Cellular DNA by Hydroxyl Radical and One-Electron Oxidants: Similarities and Differences. *Arch. Biochem. Biophys.* **557**, 47–54 (2014).
12. Nowicka, A., Kowalczyk, A., Sek, S. & Stojek, Z. Oxidation of DNA Followed by Conformational Change after OH Radical Attack. *Anal. Chem.* **85**, 355–361 (2012).
13. Shao, C., Saito, M. & Yu, Z. Formation of Single- and Double-Strand Breaks of pBR322 Plasmid Irradiated in the Presence of Scavengers. *Radiat. Environ. Biophys.* **38**, 105–109 (1999).

14. van Duin, A. C. T., Dasgupta, S., Lorant, F. & Goddard, W. A. ReaxFF: a Reactive Force Field for Hydrocarbons. *J. Phys. Chem. A* **105**, 9396–9409 (2001).
15. Yusupov, M. *et al.* Reactive Molecular Dynamics Simulations of Oxygen Species in a Liquid Water Layer of Interest for Plasma Medicine. *J. Phys. D. Appl. Phys.* **47**, 25205 (2014).
16. Monti, S. *et al.* Exploring the Conformational and Reactive Dynamics of Biomolecules in Solution Using an Extended Version of the Glycine Reactive Force Field. *Phys. Chem. Chem. Phys.* **15**, 15062–77 (2013).
17. Arnott, S., Dover, S. D. & Wonacott, A. J. Least-Squares Refinement of the Crystal and Molecular Structures of DNA and RNA from X-ray Data and Standard Bond Lengths and Angles. *Acta Crystallogr. Sect. B Struct. Crystallogr. Cryst. Chem.* **25**, 2192–2206 (1969).
18. Pacher, P., Beckman, J. S. & Liaudet, L. Central Control of Breathing in Mammals: Neuronal Circuitry, Membrane Properties, and Neurotransmitters. *Physiol. Rev.* **87**, 315–424 (2007).
19. Imlay, J. A., Chin, S. M. & Linn, S. Toxic DNA Damage by Hydrogen Peroxide Through the Fenton Reaction in Vivo and in Vitro. *Science*. **240**, 640–642 (1988).
20. Zhang, D. H. & Zhang, J. Z. H. Quantum Mechanical Calculation for Photodissociation of Hydrogen Peroxide. *J. Chem. Phys.* **98**, 6276 (1993).
21. Bielski, B. H. J., Cabelli, D. E. & Arudi, R. L. Reactivity of HO<sub>2</sub>/O<sub>2</sub><sup>-</sup> Radicals in Aqueous Solution. *J. Phys. Chem. Ref. Data* **14**, 1041 (1985).
22. Abolfath, R. M. *et al.* Multiscale QM/MM Molecular Dynamics Study on the First Steps of Guanine Damage by Free Hydroxyl Radicals in Solution. *J. Phys. Chem. A* **116**, 3940–5 (2012).
23. Chatgililoglu, C., D’Angelantonio, M., Guerra, M., Kaloudis, P. & Mulazzani, Q. G. A Reevaluation of the Ambident Reactivity of the Guanine Moiety Towards Hydroxyl Radicals. *Angew. Chem. Int. Ed. Engl.* **48**, 2214–2217 (2009).
24. Mundy, C., Colvin, M. & Quong, A. Irradiated Guanine: a Car-Parrinello Molecular Dynamics Study of Dehydrogenation in the Presence of an OH Radical. *J. Phys. Chem. A* **106**, 10063–10071 (2002).
25. Dizdaroglu, M., Kirkali, G. & Jaruga, P. Formamidopyrimidines in DNA: Mechanisms of Formation, Repair, and Biological Effects. *Free Radic. Biol. Med.* **45**, 1610–21 (2008).

26. Cadet, J., Douki, T., Ravanat, J.-L. & Di Mascio, P. Sensitized Formation of Oxidatively Generated Damage to Cellular DNA by UVA Radiation. *Photochem. Photobiol. Sci.* **8**, 903–911 (2009).
27. Jena, N. R. & Mishra, P. C. Mechanisms of Formation of 8-Oxoguanine due to Reactions of One and Two OH\* Radicals and the H<sub>2</sub>O<sub>2</sub> Molecule with Guanine: a Quantum Computational Study. *J. Phys. Chem. B* **109**, 14205–18 (2005).
28. Dizdaroglu, M. & Jaruga, P. Mechanisms of Free Radical-Induced Damage to DNA. *Free Radic. Res.* **46**, 382–419 (2012).
29. Harańczyk, M., Miller, J. H. & Gutowski, M. Differences in Electrostatic Potential around DNA Fragments Containing Adenine and 8-oxo-adenine. An Analysis Based on Regular Cylindrical Projection. *J. Mol. Graph. Model.* **26**, 282–9 (2007).
30. Kamiya, H. & Miura, H. 8-Hydroxyadenine (7, 8-dihydro-8-oxoadenine) Induces Misincorporation in in vitro DNA Synthesis and Mutations in NIH 3T3 cells. *Nucleic Acids Res.* **23**, 2893–2899 (1995).
31. Munk, B. H., Burrows, C. J. & Schlegel, H. B. Exploration of Mechanisms for the Transformation of 8-hydroxy guanine Radical to FAPyG by Density Functional Theory. *Chem. Res. Toxicol.* **20**, 432–44 (2007).
32. Wang, Y. J., Ho, Y. S., Lo, M. J. & Lin, J. K. Oxidative Modification of DNA Bases in Rat Liver and Lung During Chemical Carcinogenesis and Aging. *Chem. Biol. Interact.* **94**, 135–45 (1995).
33. Wood, M. L., Dizdaroglu, M., Gajewski, E. & Essigmann, J. M. Mechanistic Studies of Ionizing Radiation and Oxidative Mutagenesis: Genetic Effects of a Single 8-hydroxyguanine (7-hydro-8-oxoguanine) Residue Inserted at a Unique Site in a Viral Genome. *Biochemistry* **29**, 7024–32 (1990).
34. Kuchino, Y., Mori, F., Kasai, H., Inoue, H. & Iwai, S. Misreading of DNA Templates Containing 8-Hydroxydeoxyguanosine at the Modified Base and at Adjacent Residues. *Nature* **327**, 77–80 (1987).
35. Alberts, B. DNA, Chromosomes, and Genomes. *Mol. Biol. Cell* (2008).
36. Alkawareek, M. Y., Gorman, S. P., Graham, W. G. & Gilmore, B. F. Potential Cellular Targets and Antibacterial Efficacy of Atmospheric Pressure Non-Thermal Plasma. *Int. J. Antimicrob. Agents* **43**, 154–60 (2014).
37. Dharmadhikari, A. K., Bharambe, H., Dharmadhikari, J. A., D'Souza, J. S. & Mathur, D. DNA Damage by OH Radicals Produced Using Intense, Ultrashort, Long Wavelength Laser Pulses. *Phys. Rev. Lett.* **112**, 138105 (2014).



38. Folkard, M., Prise, K. M., Turner, C. J. & Michael, B. D. The Production of Single Strand and Double Strand Breaks in DNA in Aqueous Solution by Vacuum UV Photons Below 10 eV. *Radiat. Prot. Dosimetry* **99**, 147–149 (2002).
39. Uhm, H. S., Choi, E. H., Cho, G. S. & Hwang, D. H. Influence of Reactive Oxygen Species on the Sterilization of Microbes. *Curr. Appl. Phys.* **13**, S30–S35 (2013).
40. Leduc, M., Guay, D., Coulombe, S. & Leask, R. L. Effects of Non-thermal Plasmas on DNA and Mammalian Cells. *Plasma Process. Polym.* **7**, 899–909 (2010).
41. Siddiqi, M. & Bothe, E. Single- and Double-Strand Break Formation in DNA Irradiated in Aqueous Solution: Dependence on Dose and OH radical Scavenger Concentration. *Radiat. Res.* **112**, 449–463 (1987).
42. Bryant-friedrich, A. C. in *Fate of DNA Sugar Radicals, in Advances in Molecular Toxicology* **4**, 127–155 (James Fishbein Ed.; Elsevier: New York, 2010).
43. Samuni, A. & Neta, P. Hydroxyl Radical Reaction with Phosphate Esters and the Mechanism of Phosphate Cleavage. *J. Phys. Chem.* **77**, 2425–2429 (1973).
44. Yadav, A. & Mishra, P. C. Reactivities of Hydroxyl and Perhydroxyl Radicals Toward Cytosine and Thymine: a Comparative Study. *Int. J. Quantum Chem.* **113**, 56–62 (2013).
45. Ji, Y., Xia, Y., Zhao, M., Li, F. & Huang, B. Reactions of  $\cdot\text{OH}$  with Thymine Studied using Density Functional Theory. *Int. J. Quantum Chem.* **101**, 211–218 (2005).

## 5 Molecular Dynamics Simulations: Peptides

The data presented in this chapter is based on the articles published in Verlackt, C. C. W. *et al. J. Phys. Chem. C* **121**, 5787–5799 (2017)<sup>1</sup>, Klinkhammer, C. *et al. Sci. Rep.* **7**, 13828 (2017)<sup>2</sup> and Lackmann J.-W. *et al. Sci. Rep.* **submitted**<sup>3</sup>.



## 5-1 Small peptides angiotensin and bradykinin

### 5-1.1 Introduction

To date, knowledge on the interactions of RONS with peptides and proteins remains limited. Topala *et al.* reported the easy oxidation of bovine serum albumin (BSA) and methionine upon treatment with a He capillary plasma jet<sup>4</sup>. In addition, Lackmann *et al.* investigated the use of both a microscale atmospheric pressure plasma jet ( $\mu$ -APPJ) –known to be able to oxidize the highly sensitive GapDH (glyceraldehyde 3-phosphate dehydrogenase)<sup>5</sup>– and a dielectric barrier discharge (DBD) for the inactivation of the protein RNase A<sup>6</sup>. In their work, they observed the direct and irreversible inactivation of the highly stable protein RNase A after plasma treatment with a DBD, which normally would require harsh conditions, *e.g.*, heating the structure to 90 °C. The DBD treatment resulted in chemical modifications of the cysteine groups of RNase A, resulting in the inhibition of disulfide bond formation, which is necessary for the reactivation of this protein. No comparable effects were achieved with the  $\mu$ -APPJ setup. The difference in reactivity between the two plasma sources was attributed to different types of reactive species reaching the proteins. More specifically, the DBD was able to transport a high concentration of hydroxyl radicals (OH) and atomic oxygen (O) to the sample, while these species were largely absent at the surface during the  $\mu$ -APPJ treatment.

To better understand the plasma-protein interactions, MD simulations were performed, combining both DFTB, and non-reactive MD calculations. This was done to provide molecular-scale understanding of the expected oxidation processes for two small peptides, *i.e.*, angiotensin fragment 1-7 and bradykinin, serving as simple model systems for proteins. We specifically look at the interactions between the peptides and OH radicals, being representative for the RONS created by the plasma<sup>7</sup>. We focus on OH radicals, because previous studies, and the results presented in the previous chapters, have indicated that OH radicals are most reactive towards the biomolecular structures<sup>7–9</sup>, able to react within the limited timescales (*i.e.*, picosecond ranges for DFTB). In **chapter 6**, the stability and importance of atomic O is evaluated using DFTB. However, the work presented in this chapter was performed before the work of **chapter 6**. Because of this, and because earlier simulations within

our group had revealed that O atoms were not very stable in water<sup>10</sup>, we did not consider the interactions of O with the biomolecules investigated in this chapter. The interactions are investigated in the presence of water and molecular oxygen, as proteins and peptides are usually found in aerobic conditions during treatment. Furthermore, the presence of O<sub>2</sub> might play an important role in the propagation of radical oxidation of biomolecules<sup>11,12</sup>. To validate the computational investigation, we collaborated with the Biomolecular & Analytical Mass Spectrometry (BAMS) research group supervised by Frank Sobott at the University of Antwerp, and the Research Department Plasmas with Complex Interactions supervised by Prof. Dr. Jan Benedikt at the Ruhr-Universität Bochum. Experimental studies were performed in these groups, treating the model peptides with a  $\mu$ -APPJ, after which the oxidation and possible structural changes were investigated.

## 5-1.2 Computational setup

Figure 5-1 illustrates the chemical structure of both peptides investigated. In this representation, the amino acid side chains are depicted in red for the sake of clarity. The investigated peptides represent angiotensin fragment 1-7 (a hormone responsible for vasoconstriction, called peptide A in this work) and bradykinin (an inflammatory mediator, called peptide B in this work), respectively. Both peptides have the advantage of being relatively small –with a size best suited for the calculations– and containing enough variation in the structure (*i.e.*, type of amino acids) without being too complex. Furthermore, these peptides are relatively easy to purchase, for experimental validation of the computations, and they have already been the subject of various studies in literature<sup>13,14</sup>.

The chemical reactions between OH radicals and both model peptides were investigated using reactive MD simulations (which will be referred to as *impact simulations*) utilizing the DFTB method. Preliminary simulations pointed out that the oxidation reactions are initiated by OH radicals, followed by an interaction with molecular oxygen. This observation inspired us to perform our computational study in three steps:

- (i) A total of 75 impact simulations, each containing two OH radicals, were performed using the DFTB method. This was performed for each peptide (A

- and B) in the presence of water molecules, in order to elucidate the expected oxidation sites.
- (ii) Based on the information about the most targeted reaction sites, further oxidation processes were investigated using the respective amino acids in the presence of molecular oxygen.
  - (iii) Subsequently, the most common oxidation products were implemented in the peptides to investigate their effect on the structural behavior using a non-reactive force field (GROMACS).

This approach is necessary, given the nature of the employed reactive MD simulations, *i.e.*, DFTB, which is a quite time-consuming calculation method. Indeed, we chose to investigate the further oxidation processes in step (ii) on isolated amino acids rather than on every oxidized peptide observed in step (i), in order to limit the necessary calculation expenses and to guarantee the occurrence of later-stage oxidation reactions at the sites of interest. In fact, if these calculations would be performed on the oxidized peptides of step (i), only a very small fraction of the

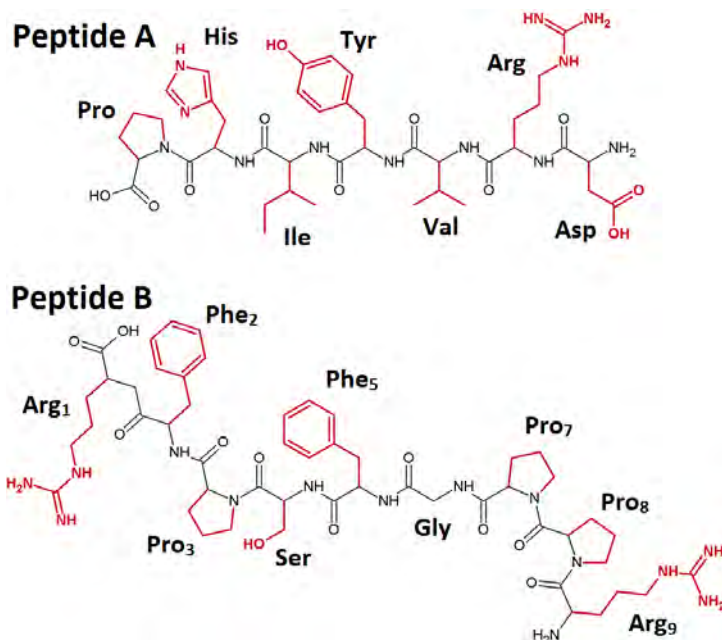


**Figure 5-1. Chemical structure of the peptides considered for the reactive MD simulations: angiotensin fragment 1-7 (called peptide A) and bradykinin (peptide B).** In this representation, the amino acid side chains are depicted in red.

introduced species would react with the amino acids of interest (*i.e.*, which were targeted in the previous step).

In step (i), we treated isolated peptides in each impact simulation. Given the size of the peptides, positioning the structure inside a water box or inside a water-shell would surpass the size limitation of the used method, *i.e.*,  $10^3$  atoms, as stated in *section 2-2.3a*. However, to account for the effect of surrounding water molecules on the interactions, and thus to better mimic reality, we introduced the OH radicals in an aqueous sphere (an example is presented in Figure 5-2). In this way, the radicals are surrounded by water molecules at the moment of impact, without the need to have water molecules surrounding the complete peptide.

In step (ii), we considered isolated amino acids, where the OH radicals (or  $O_2$  molecules) were not surrounded by water. This might affect the reactivity to some extent. Indeed, OH radicals will have a lower chemical hardness in solution, resulting in an overall lower reactivity towards biomolecules<sup>15</sup>. This behavior has been

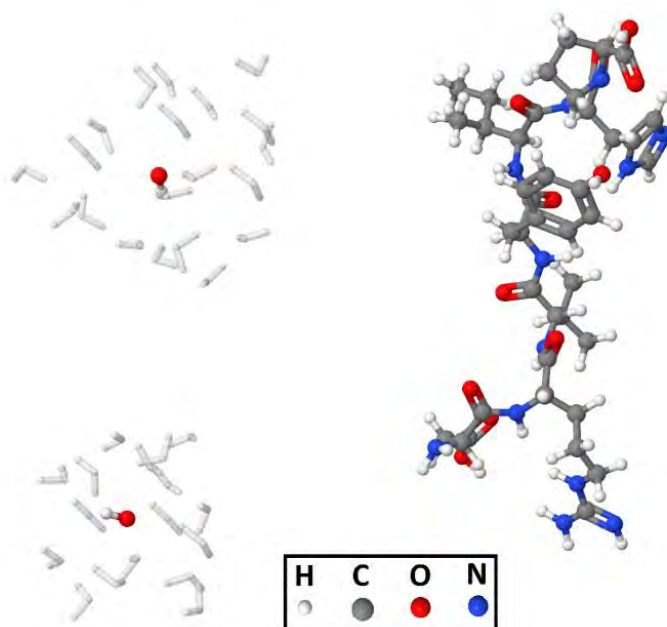


**Figure 5-2. Snapshot of the initial 3D structure of peptide A as used in the impact simulations.** Two OH radicals are placed inside a water shell, to ensure no initial interactions with the peptide and to mimic the effect of the surrounding water molecules on the interaction process during the impacts.

observed during the peptide impact simulations and also in our earlier studies presented in **chapter 3** and **chapter 4**<sup>8</sup>. However, the purpose of this step was to obtain information on every possible oxidation product, rather than to obtain a statistically valid distribution of products. The obtained oxidation products were compared to experimental data from literature, to reveal which are the most common and expected oxidation products to be used in the third step of this investigation (see below).

For both the peptide and amino acid impact simulations, a simulation time of 10 ps was chosen, to ensure that chemical reactions occur within the timescale of the simulation while maintaining reasonable calculation times. The impact simulations were performed in a canonical ensemble (temperature and volume were kept constant, NVT) using a Berendsen thermostat with a coupling constant of 100 fs<sup>16</sup>. All simulations were performed using periodic boundary conditions for a cubic box with dimensions of 25 x 25 x 25 Å for the amino acids, and 40 x 40 x 40 Å for the peptides. Prior to the impact simulations, all systems were equilibrated at room temperature for 100 ps using similar simulation conditions. All impact simulations were performed using a time step for integration of 0.25 fs.

Finally, the obtained oxidation products of step (ii), *i.e.*, the impact simulations on the most targeted amino acids, were introduced to the respective peptide and used to perform non-reactive MD simulations in water, step (iii), to obtain insight into the effects of the oxidation products on the structural behavior of each peptide. The non-reactive MD simulations were performed using the GROMACS 5.1.2 package<sup>17,18</sup>. Six different structures were prepared for each peptide: the native structure, three structures containing a single oxidized amino acid, one structure containing two oxidized amino acids and one containing three oxidized amino acids (as determined from the reactive MD simulations; see details in the *section 5-1.4c* below). All structures were dissolved in a 40 x 40 x 40 Å box containing TIP3P water molecules, and periodic boundary conditions were applied on all three dimensions. The native and oxidized structures were equilibrated at 300 K and 1 atm using the Nosé-Hoover thermostat and Parrinello-Rahman barostat. The Particle Mesh Ewald (PME) method was used to treat the long-range electrostatic interactions. A total simulation time of 1 μs was used with a time step of 1 fs. A principal component analysis (PCA),



also known as essential dynamics, was used for analyzing the structural modifications. During a PCA, a covariance matrix is built, which embodies the collinearity of atomic motions for each pair of atoms. This matrix, in turn, is diagonalized, and the sum of the eigenvalues is a measure for the total mobility of the analyzed system, while the eigenvectors describe the collective motion of the particles.

### 5-1.3 Experimental details

*The experiments were performed by Dr. D. Dewaele from the Biomolecular & Analytical Mass Spectrometry research group.*

A microscale atmospheric pressure plasma jet ( $\mu$ -APPJ) operated in He/O<sub>2</sub> gas mixture was used to treat the liquid samples (Figure 5-3). It is a capacitively coupled microplasma jet consisting of two stainless-steel electrodes (length 30 mm, width 1 mm) with 1 mm interelectrode distance, and the electrode gap is confined on both sides by quartz glass plates. A discharge is generated in the volume of 1 x 1 x 30 mm<sup>3</sup> by applying a radio-frequency voltage (13.56 MHz, root mean square voltage 230 V,

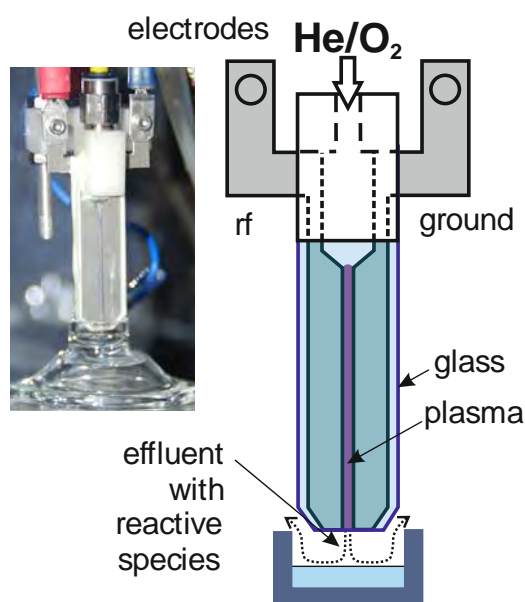


**Figure 5-3.** Photograph and scheme of the  $\mu$ -APPJ used in the treatment of the test solutions.

absorbed power  $P_{\text{plasma}} < 1$  W) to one electrode, while the other one is grounded (see Figure 5-3). This electrode configuration and corresponding dimensions resemble very closely the recently introduced plasma-jet reference discharge, the COST-Jet<sup>19</sup>. The plasma is operated with 1.4 standard liter per minute helium flow with 8.4 standard cubic centimeter of O<sub>2</sub> gas per minute (0.6% of the He flow). A maximum O atom density ( $8 \times 10^{14} \text{ cm}^{-3}$ ) in the effluent is obtained at these conditions at 4 mm distance at the position of the liquid surface<sup>20</sup>.

Angiotensin fragment 1-7 and bradykinin were obtained from Sigma-Aldrich (Bornem, Belgium). Reverse osmosis water was prepared using a Silex water filtering system from Eurowater (Nazareth-Ekeren, Belgium). 7.5 M ammonium acetate solution was purchased from Sigma-Aldrich (Bornem, Belgium). Acetonitrile (ACN; HPLC grade for analysis) and formic acid (FA; 99+%) were obtained from Acros Organics (Geel, Belgium). Samples were diluted to a concentration of 1 mg/mL and 400  $\mu\text{L}$  aliquots were placed in glass vials. The final concentration of the plasma-treated samples was determined after exposure, since the gas jet resulted in some solvent evaporation.

The effect of the plasma treatment was studied using an ESI-Q-TOF Synapt G2 HDMS T-wave ion mobility (IM) mass spectrometer (Waters, Wilmslow/UK). Samples were diluted to 5  $\mu\text{M}$  in ammonium acetate and introduced into the instrument by nano-electrospray ionization (ESI) in positive ion mode, using gold-coated borosilicate capillaries made in-house (capillary voltage 1.25-1.5 kV). Adduct formation was monitored under denaturing conditions (50:50:1 H<sub>2</sub>O:ACN:FA) and in TOF mode, while IM measurements were done using native-like solution conditions (100 mM aqueous ammonium acetate pH 6.9) in IM mode. The sample and extraction cone voltage were set in the range of 20-40 V and 0.5-1.0 V, and source and desolvation temperatures were 50 °C and 150 °C, respectively. Vacuum pressures were: backing 2.46 mbar, source  $1.79 \times 10^{-3}$  mbar, trap  $6.2 \times 10^{-2}$  mbar and transfer cell  $6.3 \times 10^{-3}$  mbar. For the IM experiments the following parameters were used: He and IM cell gas flow 180 and 90 mL/min; DC bias 45 V, wave height 40 V and wave velocity 700 m/s. The mass range was set to 50-2000 Da. External calibration up to 2000  $m/z$  was performed with NaI/CsI solution. Data acquisition was performed using MassLynx (version 4.1).

## 5-1.4 Results and Discussion

### 5-1.4a Peptide impact simulations

The first step in this investigation was performed to gain insight in the most favored sites for initiating the chemical modifications in both peptides upon OH radical impact. This was done by performing 75 independent impact simulations for each peptide, as described in the computational setup. After 10 ps, 41 and 49% of the OH radicals have reacted with peptide A and B, respectively. The results of the impact simulations are summarized in Table 5-1 and Figure 5-4.

During the simulations, the OH radicals mainly reacted through H-abstraction reactions. The H-atoms in the peptides that are mostly prone to abstraction, by the OH radicals, are presented by the red spheres in Figure 5-4. The intensity of the red color is a measure for the number of H-abstraction reactions that were observed on that particular site. The OH radicals mainly targeted the hydroxyl group of serine (Ser) in peptide B, and of aspartic acid (Asp) and tyrosine (Tyr) in peptide A (see

**Table 5-1. Summary of the observed oxidations and the amino acids that were targeted by the OH radicals introduced during the peptide impact simulations.** The percentages correspond to the number of oxidation reactions that occur at the respective amino acid, compared to the total number of reactions observed (not including reactions on both terminals of the peptide). *Val* represents the amino acid valine. *np*: not present in the peptide.

Amino acid oxidized	Percentage of oxidation (%) Compared to the total number of reactions observed	
	Peptide A	Peptide B
<b>Arg</b>	9	<b>Arg<sub>1</sub></b> 4 <b>Arg<sub>9</sub></b> 22
<b>Asp</b>	34	np
<b>Gly</b>	np	3
<b>His</b>	18	np
<b>Ile</b>	2	np
<b>Phe</b>	np	<b>Phe<sub>2</sub></b> 10 <b>Phe<sub>5</sub></b> 0
<b>Pro</b>	18	<b>Pro<sub>3</sub></b> 14 <b>Pro<sub>7</sub></b> 4 <b>Pro<sub>8</sub></b> 12
<b>Ser</b>	np	19
<b>Tyr</b>	20	np
<b>Val</b>	0	np

intense red spheres on the mentioned amino acids in Figure 5-4). In addition, also the most right arginine (Arg<sub>9</sub>) of peptide B, and proline (Pro) in both peptides, are attacked in high numbers by the introduced OH radicals. Finally, H-abstraction reactions have also been observed on Arg<sub>1</sub> in peptide B and on both the aromatic amino acids, *i.e.*, histidine (His) in peptide A and phenylalanine (Phe<sub>2</sub>) in peptide B, albeit to a lesser extent (indicated by the light red spheres on the mentioned amino acids). The percentage of oxidation is summarized in Table 5-1. Besides H-abstraction, also some OH addition reactions are observed, but only for peptide B (*i.e.*, 3% of the reactions), and the C-atoms that are subject to these OH addition reactions are indicated by green spheres in Figure 5-4. This reaction was, however, only observed on Phe<sub>2</sub> of peptide B. The side chains and peptide backbone where no OH reactions took place are depicted in transparent blue and grey, respectively. These results indicate that the OH radicals favor (i) the hydroxyl and carboxyl groups found in both peptides, as well as (ii) the side chains of the amino acids in both peptides. From Table 5-1, it becomes clear that in the case of peptide A, reactions were mainly observed to happen on Asp, followed by Tyr, Pro and His, and finally Arg and isoleucine (Ile). The order of oxidation for Tyr, His, Arg and Ile is in agreement with experimental observations<sup>6,12,21</sup>. Takai *et al.* investigated the oxidation of every individual amino acid as a result of plasma jet treatment<sup>21</sup>. They reported that chemical modifications were mostly encountered on amino acids containing a sulfur atom or aromatic group, such as Tyr and His, while the concentration of oxidized Arg and Ile was significantly lower compared to Tyr and His, in agreement with our simulations. Furthermore, Stadtman reported that Tyr, His and Arg are indeed among the amino acids that are susceptible for oxidation by ROS<sup>12</sup>, while Ile has not been mentioned, supporting the low reactivity observed in our simulations. Moreover, the oxidation of Tyr and His has also been encountered in a recent study by Lackmann *et al.*<sup>6</sup>.

In the simulations, Pro and Asp are affected by the OH radicals more often than initially expected. In the case of Asp, this is a result of the presence of the carboxyl group, one of the main targets of the impacting species. This functional group is expected to be deprotonated in aqueous solution at pH  $\approx$  7 (pKa value of 3.86). Given the low number of water molecules present during the simulations, we

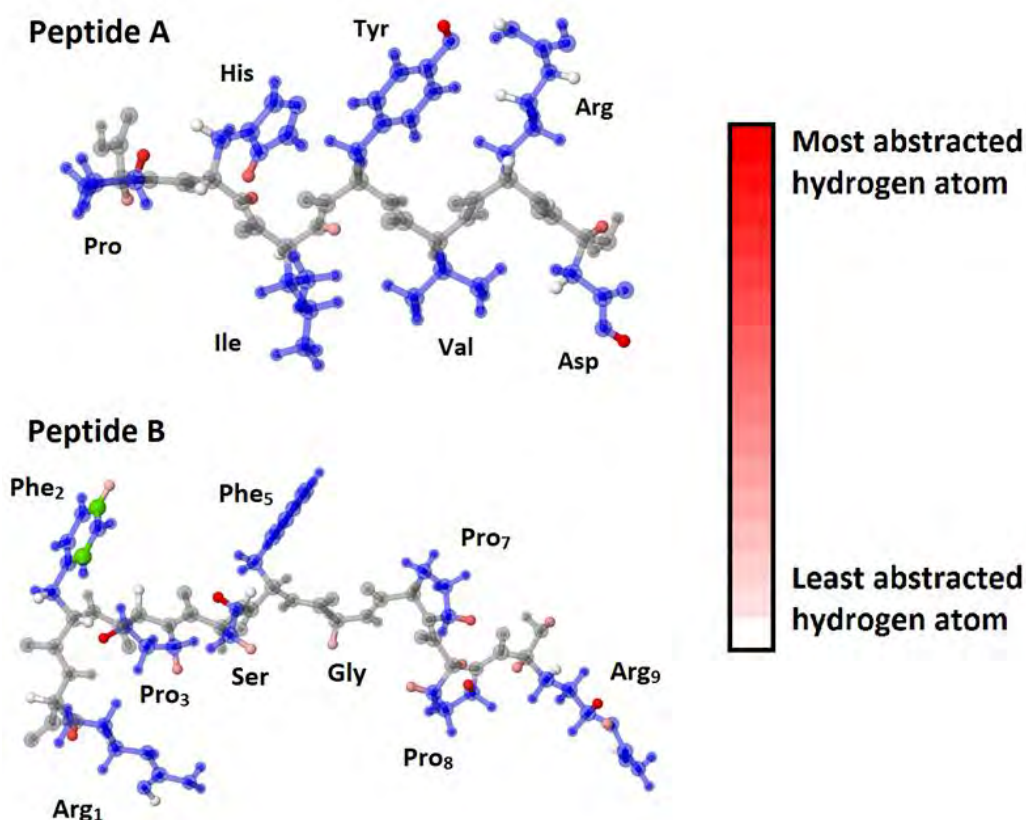


**Figure 5-4. Snapshot of the 3D representation of the oxidation sites in both peptides.** The H-atoms most prone to H-abstraction reactions are depicted as red solid spheres, using a scale ranging from pale to intense red, representing the range from least abstracted to most abstracted H-atoms. The green spheres indicate the positions where OH addition reactions were observed. Atoms which did not react with OH radicals are depicted in transparent blue (for the side chains) or grey (for the peptide backbone).

decided to investigate the neutral equivalent of the peptide, instead of the deprotonated variant, similar to the terminal carboxyl group. Furthermore, the high hydrophilicity of the carboxyl group makes it easier for the OH radicals, residing inside an aqueous shell, to come in contact with Asp. This significantly increases the chance of oxidation. In the case of Pro, we observed that peptide A folds into a specific 3D structure during the simulation. This structure leads to a relatively large potential contact surface for the targeted Pro with the solution, which possibly explains the higher-than-expected number of observed reactions, surpassing the number of reactions on His. This 3D structure is depicted in Figure 5-5.

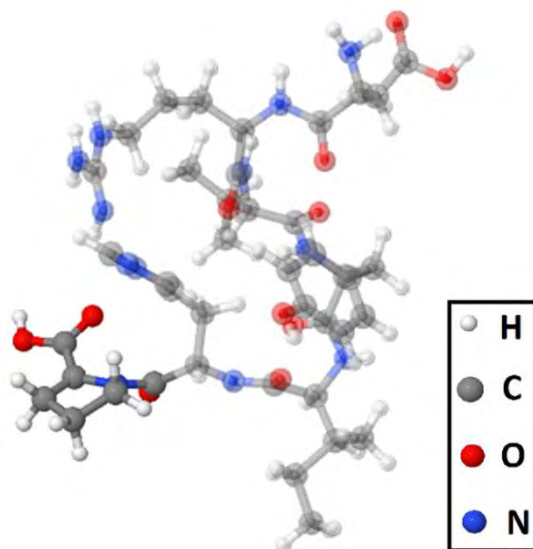


**Figure 5-5. Snapshot of peptide A after 10 ps.** Proline is found to have a relatively large contact surface with the solution. This might explain the higher number of observed reactions, compared to experiments. Proline is represented by the solid spheres while the remaining peptide is depicted using semi-transparent spheres, for the sake of clarity.

For peptide B, most OH reactions took place on Pro (mostly Pro<sub>3</sub> and Pro<sub>8</sub>), Arg (Arg<sub>9</sub>, and in rare cases Arg<sub>1</sub>), Ser, Phe<sub>2</sub> and glycine (Gly). The order of Pro, Arg and Gly is in line with observations reported in literature<sup>12,21</sup>. Indeed, while Pro and Arg are known to be susceptible to ROS oxidation, the reactions with Gly are rarely encountered experimentally. However, the observed oxidation rate of Phe is significantly lower compared to experimental reports<sup>12,21</sup>. Being an aromatic amino acid, Phe is known to be even more susceptible to oxidation than Pro and Arg, and comparable to Tyr<sup>21</sup>. The lower reactivity, observed in the simulations, might be the result of the impact conditions, where aqueous spheres around the OH radicals are introduced, while the peptide itself is not dissolved (in order to avoid excessive calculations times). Before the introduced OH radicals can interact with the peptide, the amino acids must first come in contact with the aqueous shell. Given the apolar nature of Phe, one can expect that the interaction with the water shell is less favored, compared to, for example Arg, Pro and even Tyr. Moreover, as Phe is able to occupy a larger phase space compared to Pro, *i.e.*, being more flexible, while Pro is more fixed in the peptide structure, the repulsion from the impacting water-radical droplets is expected to be more pronounced in the case of Phe. This can explain the lower number

of observed oxidation reactions with Phe. Finally, Ser appears more reactive than expected from literature, which can be explained by the high hydrophilicity compared to its environment, similar to Asp for peptide A, making it easier for the OH radicals to come in contact with the hydroxyl group of Ser.

The differences in the observed reactivity for Phe and Ser (in peptide B), as well as for Asp (in peptide A) illustrate the importance of the chemical environment of the amino acids for oxidation by ROS. This importance has recently been reported by Espino *et al.*<sup>22</sup>, who observed, among others, a surprisingly high oxidation rate of Asp, which was attributed to the fact that this amino acid is a marker for solvent accessibility<sup>23</sup>. The influence of the chemical environment is especially clear when comparing the difference in reactivity of the same amino acids occurring more than once in the peptide (*i.e.*, Pro, Arg and Phe in peptide B). Indeed, Table 5-1 clearly illustrates a significantly higher number of oxidations of Phe<sub>2</sub> compared to Phe<sub>5</sub>, of Pro<sub>3</sub> and Pro<sub>8</sub> vs Pro<sub>7</sub>, as well as of Arg<sub>9</sub> compared to Arg<sub>2</sub>. Here, the hydrophilicity of neighboring side chains clearly influences the rate of oxidation observed.

The observation that the OH radicals react slightly faster with peptide B than with peptide A (*i.e.*, 49% vs 41%) correlates with experimental data obtained after

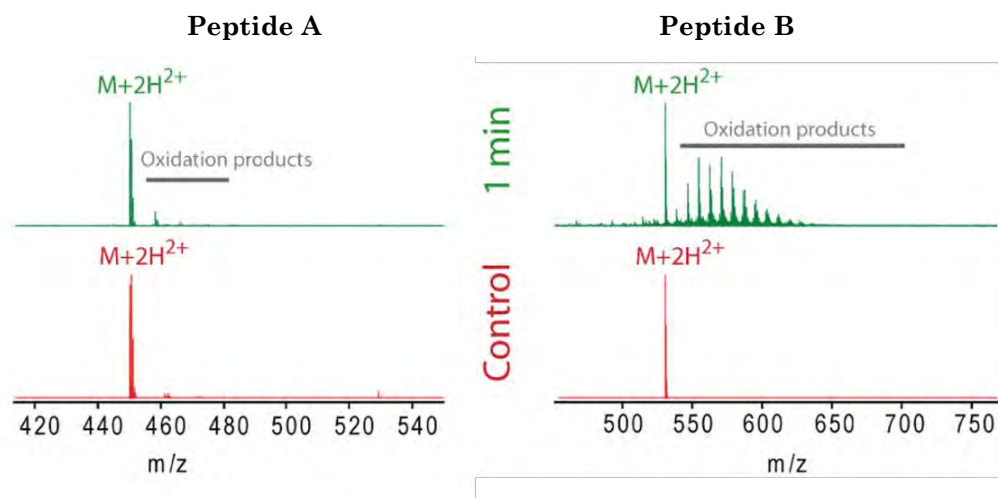


**Figure 5-6.** ESI mass spectra of peptide A and peptide B under denaturing conditions, after 1 min of plasma treatment using a  $\mu$ -APPJ. Covalent adducts appear at  $m/z$  values higher than the peptide mass, with each major peak corresponding to  $n$  additional oxygen masses ( $n \times 16$  Da). While peptide A shows predominantly only one oxygen adduct ( $n = 1$ ), peptide B gets oxidized up to  $>10$  times under the same conditions.

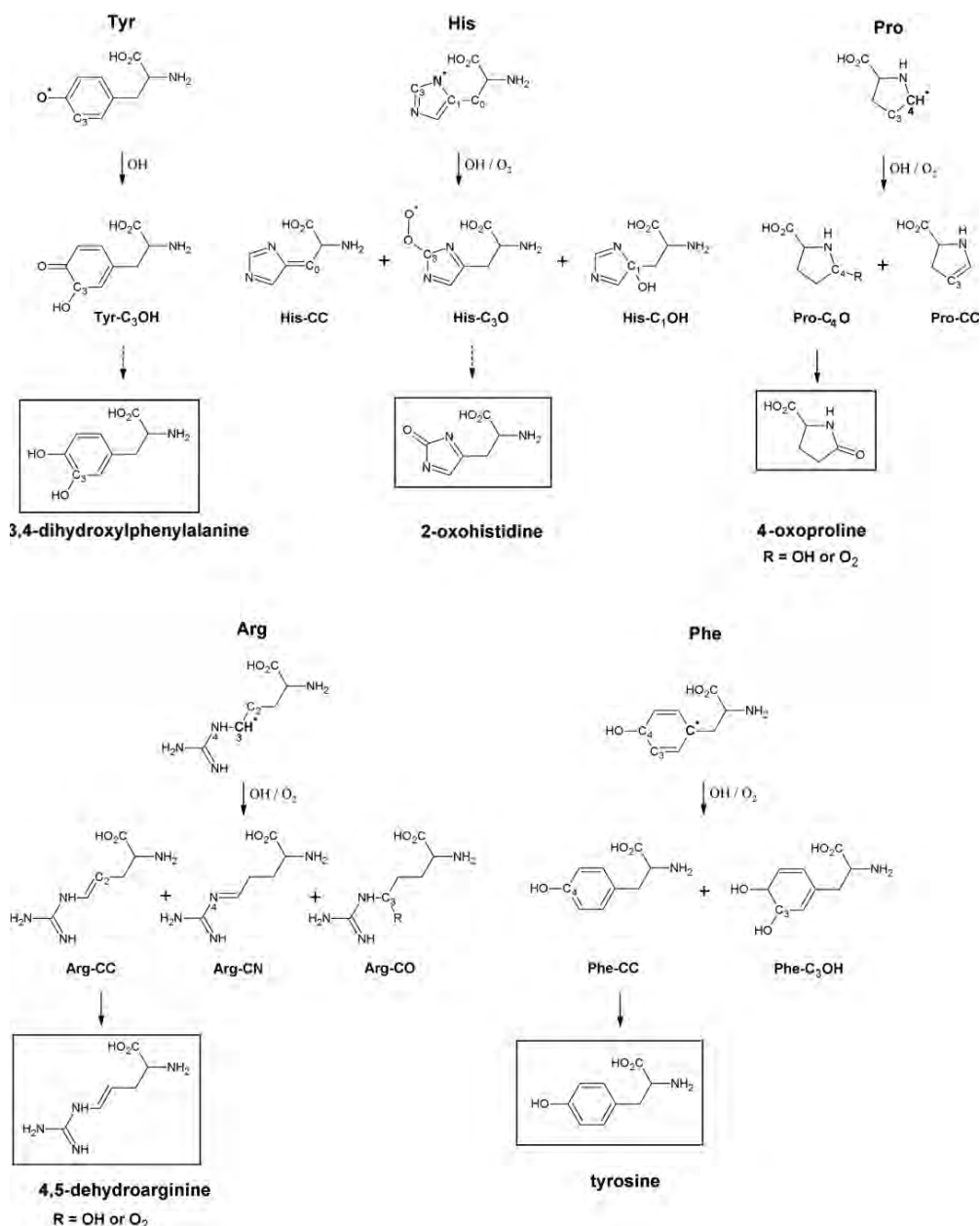
plasma treatment of both model peptides. Figure 5-6 illustrates the obtained mass-spectra of both model peptides after 1 min treatment using the  $\mu$ -APPJ. The difference in both spectra after plasma treatment is very striking. It is clear that peptide B is indeed more prone to oxidation. This can be attributed to the increase in peptide flexibility after later stage oxidation of proline (as bradykinin contains three proline groups), enhancing oxidation. Indeed, overoxidation of proline leads to the opening of its ring structure after which the characteristic bends in the backbone disappear<sup>12,21</sup>, making the peptide more flexible.

### 5-1.4b Amino acid impact simulations

Based on the knowledge obtained from the peptide impact simulations, the most targeted amino acids, *i.e.*, three for each peptide, were selected for investigating the further oxidation processes of these amino acids. Keeping in mind the comparison with literature (see above), we selected Tyr, His and Pro for peptide A, and Phe<sub>2</sub>, Pro<sub>1</sub> and Arg<sub>1</sub> for peptide B (see Scheme 5-1). More specifically, the further oxidation of Tyr was investigated after the abstraction of the hydroxylic hydrogen atom; for His, further oxidation was studied after the abstraction of the N-bound hydrogen atom; for Arg, after the abstraction of the C<sub>3</sub>-bound hydrogen atom; for Phe, after the addition of the OH radical on position C<sub>4</sub> in the ring; and for Pro (occurring in both peptides A and B) after the abstraction of the C<sub>4</sub>-bound hydrogen atom. Their further oxidation processes were simulated by introducing either an O<sub>2</sub> molecule or another OH radical to the amino acid in vacuum. Asp was not considered in these further oxidation simulations, given the fact that the oxidation is focused on the carboxyl group by abstracting the H-atom, which is absent in aqueous solution at pH  $\approx$  7, as discussed in 5-1.4a.

For every case, ten independent impact simulations were performed in a system containing only a single oxygen species (*i.e.*, either OH or O<sub>2</sub>). A summary of the observed reactions is presented in Scheme 5-1. Introducing the mentioned species to the amino acid radicals resulted in either H-abstraction adjacent to the initial reaction site (from *section 5-1.4a*), leading to the formation of a C=C or C=N double bond, or addition of the OH radical or O<sub>2</sub> molecule on the radical site. The specific reactions observed for each of the amino acid radicals are explained below in more detail, along with the most probable follow-up reactions. The formation of 3,4-





**Scheme 5-1.** Observed reactions between the amino acid radicals, formed in the peptide impact simulations (see 5-1.4a), and the introduced oxygen species, *i.e.*, either OH or O<sub>2</sub>, as well as the later stage oxidation products, either obtained from the simulations (solid arrow) or proposed from experiments in literature (dashed arrows). The latter could not be observed in the simulations, as it would require conditions far beyond the limitations of DFTB. The reactions displayed for Tyr, His and Arg are related to peptide A, while those for Phe, Pro and Arg are connected to peptide B. For each amino acid, a single (later stage) oxidation product was chosen, indicated in rectangular boxes, to be used in the non-reactive MD simulations (see below). Note that O<sub>2</sub> did not react with the Tyr-radical within the simulated timescale.

dihydroxyphenyl alanine and 2-oxohistidine (see Scheme 5-1) was not simulated as this requires much larger timescales and more complex molecular systems, beyond the limitations of DFTB. However, below we motivate why they should arise from the amino acid radicals observed in our simulations. Hence, these final products are also depicted in Scheme 5-1, because they will be used in the later non-reactive MD simulations (see 5-1.4c).

The Tyr radical reacts with OH through an addition reaction on the C<sub>3</sub> atom, positioned next to the hydroxyl functional group. This results in the formation of Tyr-C<sub>3</sub>OH (top left Scheme 5-1). It is noteworthy that, within the timescale of 10 ps, no chemical reaction occurred with O<sub>2</sub>, showing the stability of the initial amino acid radical during these calculations. Although reactions on aromatic structures progress slowly during the simulations, the formation of Tyr-C<sub>3</sub>OH was observed multiple times. Furthermore, the illustrated addition reaction is a well-known result of tyrosine oxidation and is in excellent agreement with the literature, resulting in the precursor for 3,4-dihydroxyphenylalanine (DOPA)<sup>12,21,24–28</sup>. DOPA will be formed after a H-abstraction from neighboring biomolecules or H-donors by Tyr-C<sub>3</sub>OH. However, this could not be simulated in this work, as the required timescale exceeds the capabilities of DFTB. Indeed, after the H-abstraction of Tyr, no consecutive H-abstraction was observed during the peptide impact simulations, supporting the need for longer simulation times.

The His radical was able to react with both OH radicals and O<sub>2</sub> molecules, resulting in the formation of three distinct products: His-CC, His-C<sub>3</sub>O and His-C<sub>1</sub>OH (see Scheme 5-1 for nomenclature). Firstly, His-CC results from H-abstraction of C<sub>0</sub> adjacent to the ring structure, by OH radicals. His-C<sub>1</sub>OH results from OH addition on the tertiary C<sub>1</sub> in the imidazole ring structure, but it was observed less frequently than the formation of His-CC. Finally, O<sub>2</sub> molecules react through addition on the N=C-N carbon atom in the ring (C<sub>3</sub>), resulting in the formation of a peroxy radical (His-C<sub>3</sub>O). Peroxyl radicals are known to undergo a number of reactions, resulting in the formation of hydroxyl and carbonyl derivatives<sup>24,28,29</sup>. Among these reaction products is the formation of 2-oxohistidine, a well-known product of histidine oxidation<sup>12,21,27–29</sup>. In order to acquire 2-oxohistidine, a number of reduction processes with either Fe<sup>2+</sup> in the presence of H<sup>+</sup>, or reduction through additional H-abstraction

reactions from neighboring H-sources are required<sup>12</sup>. Simulating the reduction of His-C<sub>3</sub>O therefore requires both significantly longer timescales (similar to the formation of DOPA) and more complex molecular systems (necessary to introduce the H-sources or perform metal-catalyzed reactions), which are beyond the capabilities of the DFTB method used. However, as 2-oxohistidine is observed to be the major oxidation product of His<sup>12,27–29</sup>, it is used for the non-reactive simulations for peptide A, as described in the next section.

The Pro radical shows reactions with both OH radicals and O<sub>2</sub> molecules, similar to His. Both oxygen species interact with the radical through either an addition reaction on C<sub>4</sub>, resulting in the formation of Pro-C<sub>4</sub>O (adding either a peroxide or a hydroxyl group on the pyrrolidine ring), or a H-abstraction reaction on C<sub>3</sub>, leading to the formation of Pro-CC (*cf.* Scheme 5-1). Although the oxidation of Pro was not so often investigated in literature, it is known to result in an increase in the oxygen content in the pyrrolidine ring structure, forming, among others, 2-pyrrolidone, 4- or 5-hydroxyproline and 4-oxoproline<sup>12,21,30</sup>. As 2-pyrrolidone is a product after peptide-bond cleavage, and the addition of oxygen species has been encountered on the C<sub>4</sub> of Pro during the simulations (Pro-C<sub>4</sub>O in Scheme 5-1), we have chosen to include 4-oxoproline in the non-reactive MD simulations for both peptides A and B (see next section). Note that the formation of 4-oxoproline was only encountered during our simulations when Pro-C<sub>4</sub>O was formed after an OH addition (R = OH in Scheme 5-1). Similar to 2-oxohistidine, further reactions with the observed Pro-C<sub>4</sub>O peroxide, as a result of an O<sub>2</sub> addition (R = O<sub>2</sub>), were not simulated as the required conditions exceed the capabilities of DFTB.

Introducing oxygen species in the vicinity of the Arg radical results in the formation of multiple oxidation products. During the simulations, both OH radicals and O<sub>2</sub> molecules were able to abstract a H atom from the C<sub>2</sub> and N<sub>4</sub> atoms adjacent to the radical. This leads to the formation of Arg-CC and Arg-CN, respectively (*cf.* Scheme 5-1). Next to the H-abstraction reactions, addition reactions on C<sub>3</sub> were also encountered during the simulations, leading to the formation of Arg-CO. The oxidation at this particular position is in line with known oxidation products of Arg, *e.g.*, glutamic semi-aldehydes and the formation of double bonds<sup>12,21</sup>. For the last step of this investigation, Arg-CC, or 4,5-dehydroarginine (*cf.* Scheme 5-1), was chosen for

peptide B, as the formation of this double bond is observed in experimental research<sup>21</sup> using only mild oxidative stress.

Finally, Phe radicals were observed to react both with OH radicals and O<sub>2</sub> molecules to form Phe-CC, after a H-abstraction by either oxygen species, thus restoring the aromatic system, or Phe-C<sub>3</sub>OH, upon addition of an OH radical on C<sub>3</sub> (*cf.* Scheme 5-1). The restoration of the aromatic system, after the H-abstraction, results in the formation of tyrosine and has been observed both experimentally as well as during previous computational studies<sup>21,27,31</sup>. Therefore, tyrosine will be introduced in the non-reactive MD simulations for peptide B.

#### 5-1.4c Non-reactive MD simulations

Based on the peptide impact simulations, and the subsequent individual amino acid impact simulations, six structures were identified for both peptides A and B, to be investigated with the longer timescale non-reactive MD simulations (*cf.* Table 5-2). These structures include the native structures (called A-Nat and B-Nat, respectively), three structures per peptide containing a single oxidation product (A-Tyr, A-His, A-Pro, B-Phe, B-Arg and B-Pro), one structure per peptide containing two oxidation products (A-ox2 and B-ox2, respectively) and one containing three oxidation products (A-ox3 and B-ox3, respectively). For these modified structures, the indicated amino acids of the native structure were replaced by their respective oxidation products as depicted in Scheme 5-1. The structures were dissolved in a 40 x 40 x 40 Å water box and simulated for 1 μs. The results of these non-reactive MD simulations are illustrated in Figure 5-7. Here, the PCA analyses of all structures, plotting the projection of the first eigenvector of the analysis (representing the direction of the highest motion) versus the projection of the second eigenvector (representing the second highest motion) are presented. These graphs give a representation of the total phase space that each peptide is able to occupy. In Table 5-3, we also list the covariance values, *i.e.*, the sum of the eigenvalues, for each structure, providing a numerical representation of the total motility of the respective structures. In the left two graphs of Figure 5-7, the introduction of a single oxidation product is compared with the native structure for both peptides A and B, while in the right two graphs of Figure 5-7 the effect of introducing an increasing number of oxidation products is shown.

**Table 5-2. Summary of the peptide structures used for the non-reactive MD simulations.** Six structures were investigated for both peptides A and B: the native structure, three peptides containing a single oxidation product, a peptide containing a combination of two oxidation products and a peptide containing the combination of all three oxidation products.

	Peptide A		Peptide B	
	AA oxidized <sup>b</sup>	Name	AA oxidized <sup>b</sup>	Name
<b>Native <sup>a</sup></b>	-	A-Nat	-	B-Nat
<b>1 oxidation product</b>	Tyr	A-Tyr	Phe <sub>2</sub>	B-Phe
	His	A-His	Pro <sub>8</sub>	B-Pro
	Pro	A-Pro	Arg <sub>9</sub>	B-Arg
<b>2 oxidation products</b>	Tyr His	A-ox2	Phe <sub>2</sub> Pro <sub>8</sub>	B-ox2
<b>3 oxidation products</b>	Tyr His Pro	A-ox3	Phe <sub>2</sub> Pro <sub>8</sub> Arg <sub>9</sub>	B-ox3

(a) Native structure as depicted in Figure 5-1.

(b) The mentioned amino acids (AA) were replaced by their respective oxidation product, as given in Scheme 5-1.

The results in Figure 5-7 indicate that even a single oxidation product can affect the overall structural behavior of the peptide in which it is introduced, albeit to a low extent. This is apparent for A-Tyr compared to A-Nat. For peptide A, a significant reduction of the phase space is observed when Tyr is replaced with 3,4-dihydroxyphenylalanine, *i.e.*, the oxidation product of Tyr. This is also obvious when comparing the covariance value of both structures (9.53 nm<sup>2</sup> versus 16.22 nm<sup>2</sup>). This observation points towards a more rigid structure after the oxidation of Tyr, which can affect the overall behavior of the host protein. Indeed, as the local structure of the protein (in the vicinity of the oxidized Tyr) changes due to oxidation, so will the interactions with other proteins or receptors on and inside cells. As such, the observed oxidation product can enhance or hinder the protein activity, which greatly depends on the protein considered. However, for the other oxidation products the effect on the peptide structure is much less pronounced. Although the projections of the eigenvectors suggest some slight changes in the phase space, the covariance

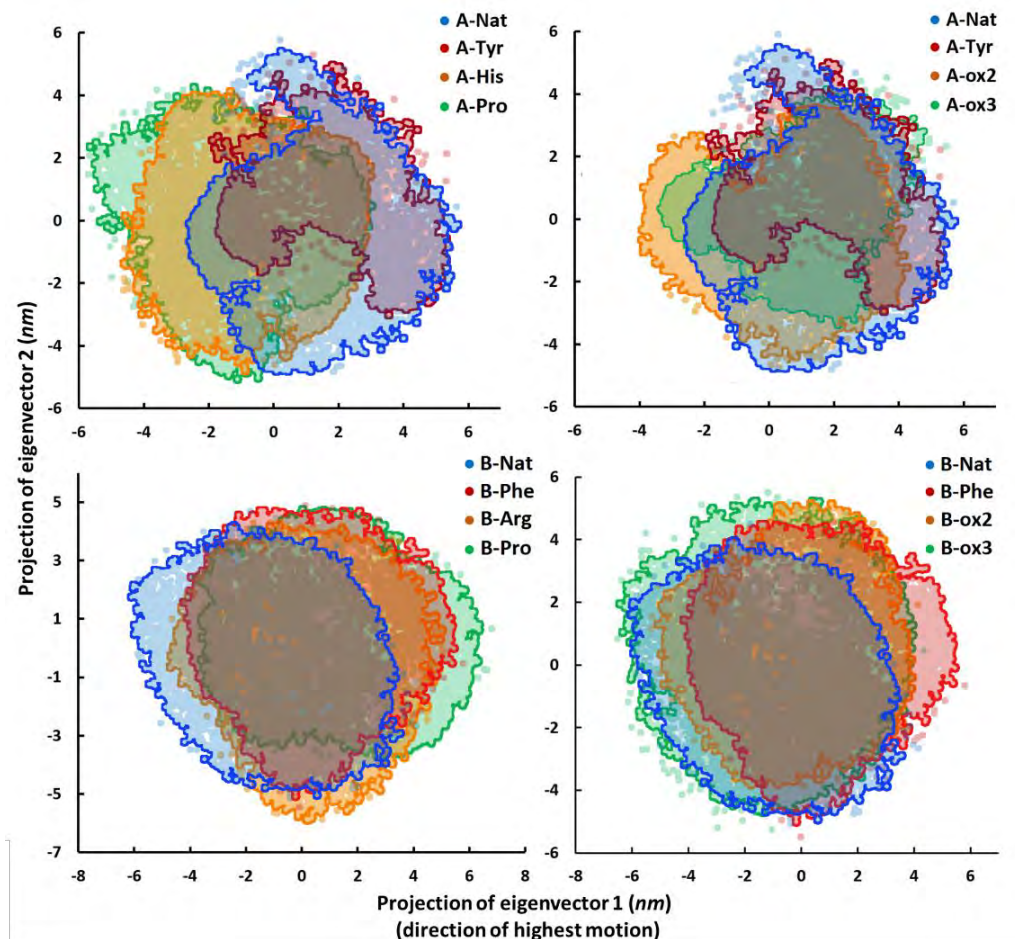


**Figure 5-7. Results of the Principal Component Analysis (PCA) performed on each structure after 1  $\mu$ s.** In the left two graphs, the PCA results are shown for the native structures (A-Nat and B-Nat, respectively) compared to the structures containing one of the three oxidation products, as summarized in Table 5-2. In the right two graphs the PCA results are shown for the native structures compared to the structures containing an increasing number of oxidized amino acids (comparing the phase space that is occupied by peptides with 0, 1, 2 or 3 oxidation products).

values are considered equal. We were not able to perform a statistical analysis of the covariance values due to the major computational cost required for such calculations. However, in order to obtain a measure for the fluctuation of the covariance values, simulations of four structures (A-Nat, A-Tyr, A-ox2, A-ox3) were repeated a second time. This allows us to verify both the changes in phase space of A-Tyr, as well as the limited effect of further oxidation (A-ox2 and A-ox3). Covariance values similar

**Table 5-3. Summary of the covariance values (in nm<sup>2</sup>) after 1  $\mu$ s for the native structures and each of the modified structures of both peptides A and B.**

Peptide A		Peptide B	
Structure	Covariance value ( $\pm 2 \text{ nm}^2$ )	Structure	Covariance value ( $\pm 2 \text{ nm}^2$ )
A-Nat	16.22	B-Nat	22.68
A-Tyr	9.53	B-Phe	27.12
A-His	18.18	B-Arg	25.97
A-Pro	18.68	B-Pro	25.71
A-ox2	20.06	B-ox2	24.30
A-ox3	16.05	B-ox3	26.89

**Table 5-4. Covariance values of the repeated simulations on A-Nat, A-Tyr, A-ox2 and A-ox3.** Simulations were repeated to obtain insight in the fluctuation of the calculated covariance values.

Peptide A	
Structure	Covariance value ( $\pm 2 \text{ nm}^2$ )
A-Nat	15.87
A-Tyr	7.59
A-ox2	20.68
A-ox3	17.04

to those reported in Table 5-3 were obtained. The result is presented in Table 5-4. Comparing these results with the ones listed in Table 5-3, an overall fluctuation of  $\pm 2 \text{ nm}^2$  was observed. Therefore, this number is used here as a measure for the fluctuation, when comparing the covariance values of the investigated structures. Based on this number, the calculated covariance values of the oxidized structures (with exception of A-Tyr) are considered to be equal compared to their native counterparts. This indicates that slight changes in the overall structure can be expected, without a change in the flexibility as well as the average size of the peptide.

The absence of significant changes in the flexibility and average size is supported by experimental data, obtained with ion mobility mass spectrometry (IM-MS) for the two peptides after 1 min of plasma treatment, as presented in Figure 5-8<sup>32,33</sup>. In order to obtain experimental insight into the global structural effects of peptide oxidation, four extracted IM-MS profiles are shown and compared: the native structure in the control (*i.e.*, untreated) sample ( $M + 2\text{H}^{2+}$ , red); the native

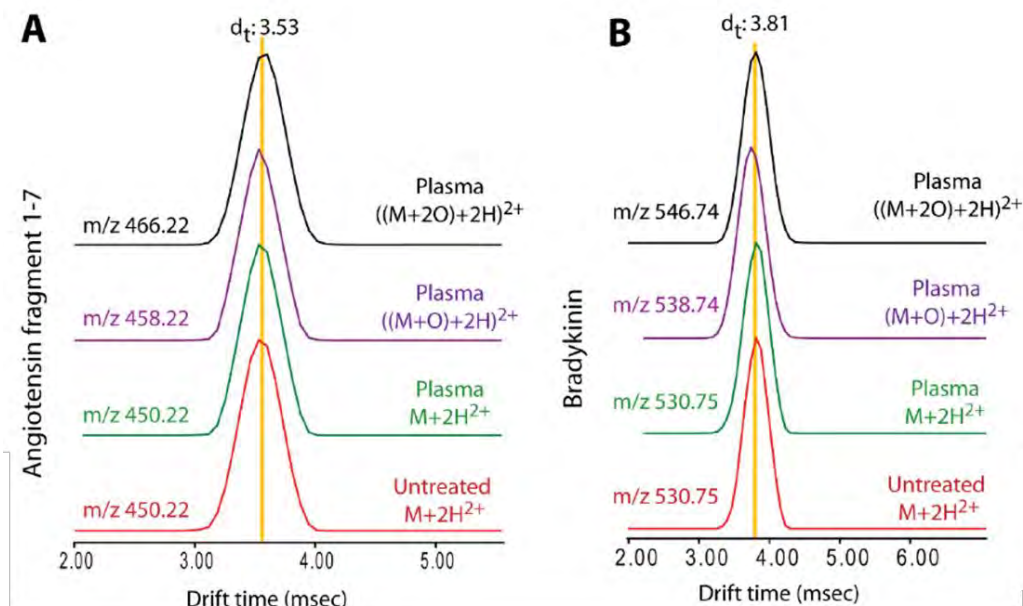


**Figure 5-8. Extracted ion mobility profiles of (A) peptide A and (B) peptide B after 1 min of plasma treatment.** No significant differences are found for the overall size and shape of the peptides with and without up to two oxygen adducts.

structure in a treated sample ( $M + 2H^{2+}$ , green); the structure containing one additional oxygen atom ( $M+O + 2H^{2+}$ , purple), and the structure containing two additional oxygen atoms ( $M+2O + 2H^{2+}$ , black). Comparing the signals, we observed no significant change in drift time when the peptides (both peptide A and B) are oxidized after plasma treatment. The drift time in IM-MS characterizes ions based on their rotationally averaged size and shape (collision cross section), as well as intrinsic flexibility (conformational space, via the width of the mobility peaks). Therefore, the results suggest that oxidation has no noticeable effect on the overall 3D structure or folding state of the peptide, which is in agreement with the results of the PCA of Figure 5-7 and Table 5-3.

As the results of both the PCA and IM-MS experiments show no major structural differences between the oxidized peptides and the native peptides, we also compared the average structures of the peptides after 1  $\mu$ s in solution, in order to obtain additional insight in the 3D structures. These structures are depicted in Figure 5-9. In these figures the average position of every atom, compared to the center of mass, is depicted. Note that this does not represent a physical molecule, but



rather a visualization of the most likely positions of each atom in this molecule (for example: As the phenyl ring of Phe is only able to rotate around its axis, the average structure will illustrate all atoms to be on that axis). In Figure 5-9, the backbone is shown in grey, while the unmodified side chains are depicted in blue. The red, yellow and green side chains represent the amino acids that were considered for oxidation, as specified in Table 5-2.

From the native peptides A and B, a certain 3D configuration is obtained from calculations (*cf.* Figure 5-9, black boxes). On one hand, peptide A appears to exhibit

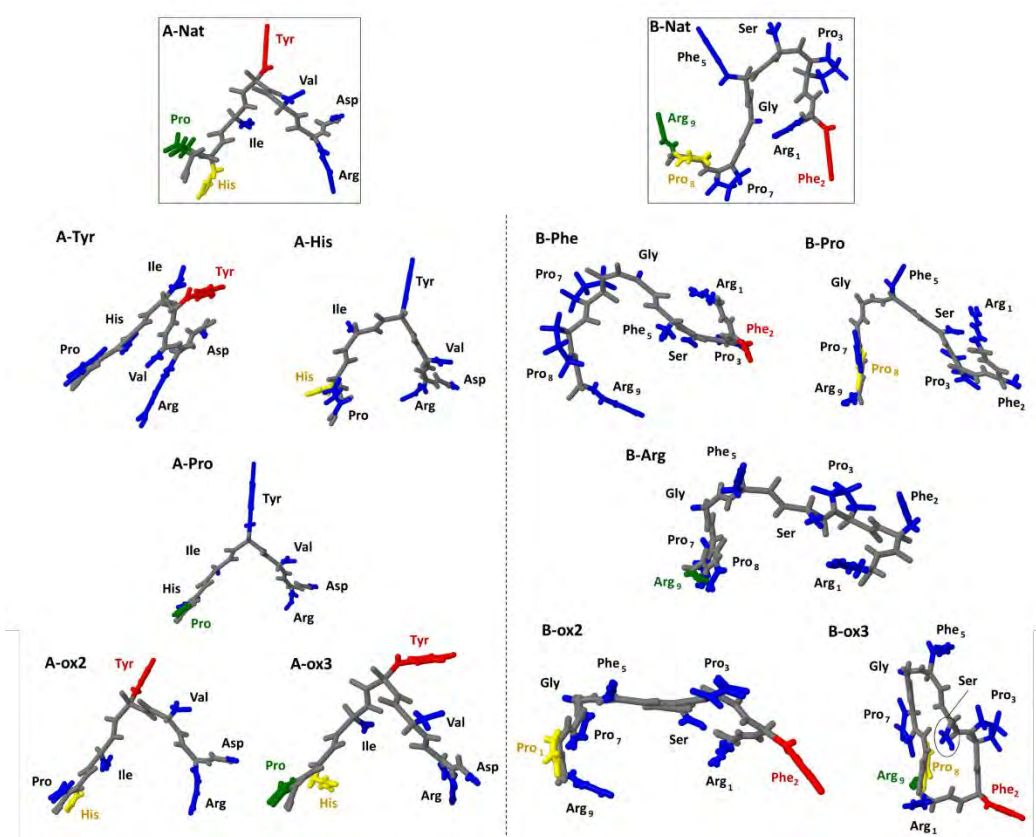


**Figure 5-9. Representation of the average structures of the native peptides (black boxes) and their oxidized structures.** On the left side, the structures of peptide A are shown, on the right side the structures of peptide B. The peptide backbone is depicted in grey using a stick model in all structures. Un-oxidized side chains are depicted in blue. Red indicates the oxidation of Tyr for peptide A and Phe for peptide B. Yellow indicates the oxidation of His for peptide A and Pro for peptide B. Green indicates the oxidation of Pro for peptide A and Arg for peptide B.

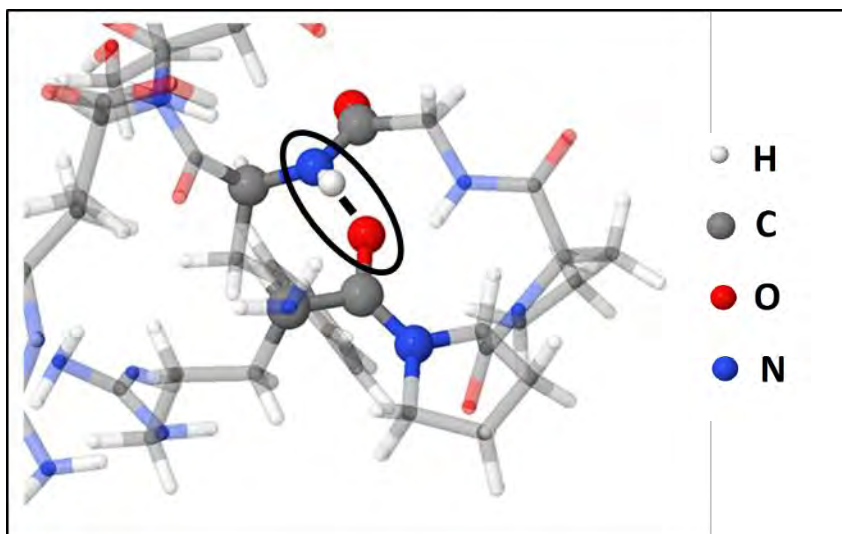


**Figure 5-10.** Example of a site where the intrapeptide interaction is observed in peptide B (indicated by a black line in the circle). The interacting site is depicted using solid spheres while the remaining peptide of the snapshot is shown using a semitransparent stick model.

a more linear configuration with a distinctive bend around Val-Tyr-Ile. This conformation has also been found using NMR and circular dichroism by Lula *et al.*<sup>13</sup>. On the other hand, peptide B shows a more random conformation, with interactions between the H- and O-atoms of different amides in the backbone, found throughout the simulation. An example of such interactions is presented in Figure 5-10.

Oxidation of some amino acids in the peptides has an impact on the structural properties and therefore also on the conformation of the peptides. This could not be clearly deduced from the PCA or the IM-MS spectra, but it is obvious from the average positions of all atoms in the oxidized peptides, which are also illustrated in Figure 5-9. When comparing the modified structures with their native counterparts, it becomes clear that even a single oxidized amino acid can significantly affect the average conformation. In most cases, this results in a more compact environment where the oxidized amino acid shows a stronger interaction with the peptide backbone, reducing the local surface area. For example, the introduction of 4-oxoproline or 2-oxohistidine results in a slightly higher affinity of the introduced oxidized amino acids for the backbone and neighboring side chains, leading to a more condensed conformation at the site of oxidation itself (see A-His, A-Pro and B-Pro,

compared to the native structures in Figure 5-9). However, the general effect is, again, most pronounced for the oxidation of A-Tyr. The increase in affinity with the backbone of Tyr in this modified peptide A results in an additional bend in the peptide, leading to a more folded structure. This observation is, however, much more subtle in the case of A-ox2 and A-ox3. Indeed, although the oxidized amino acids are found closer to the peptide (His, Pro as well as Tyr), the folding of the conformation (as seen in A-Tyr) is prevented in the case of these higher oxidation degrees. The reliability of the obtained structures has been tested by simulating the initial structures of A-Nat, A-Tyr, A-ox2 and A-ox3 a second time for 1  $\mu$ s (results are shown in Figure 5-11), and very similar average conformations were obtained; hence, identical observations could be made, supporting the results and the discussion made above. A similar conclusion can be drawn for peptide B, where the oxidations of Pro and Arg result in a more compact conformation at the respective sites, similar to A-Pro and A-His. However, compared to peptide A, a higher degree of oxidation has a much more pronounced effect on the structure (*cf.* Figure 5-9, B-ox2 and B-ox3). The reason for the more pronounced differences of B-ox2 and B-ox3, however, remains unclear and might be a result of a more random 3D structure, as this effect has not been observed during the PCA. Indeed, if the peptide is more flexible during the MD simulations, this will have a larger effect on the average structure. In this case, we expect that the introduction of more than one oxidation product reduces the stability of the conformation of peptide B, increasing both the number of interactions with the solution and the fluctuation of the 3D structure. As a result, the obtained average structures differ more from the native peptide.

Literature has indicated that oxidation of proteins results in significant protein deformation, leading to either protein accumulation (*i.e.*, the formation of aggregates of several proteins) or the loss of the 3D structure<sup>34</sup>. From the average structures presented above, we observe an increase in affinity between the oxidized amino acids and the peptide backbone. This increase in affinity can, besides causing changes in protein activities, also be linked with the experimentally observed aggregation of proteins, as a result of more and stronger intermolecular interactions. Protein aggregation tends to be insoluble as well as resistant to metabolic activities and is associated with cell death in many diseases (Alzheimer's and amyloid diseases,

Parkinson's disease, *etc.*)<sup>35</sup>. In contrast, accumulation is prevented in unstressed cells as a result of cellular enzymatic activities. As the oxygen content increases, so will the hydrophilicity, which results in a higher contact surface with the solution. Because of this, important disulfide bonds and amino acids are more available for oxidation, leading to a further loss of the structure and activity, and even fragmentation, finally destroying the affected protein<sup>6,34</sup>.

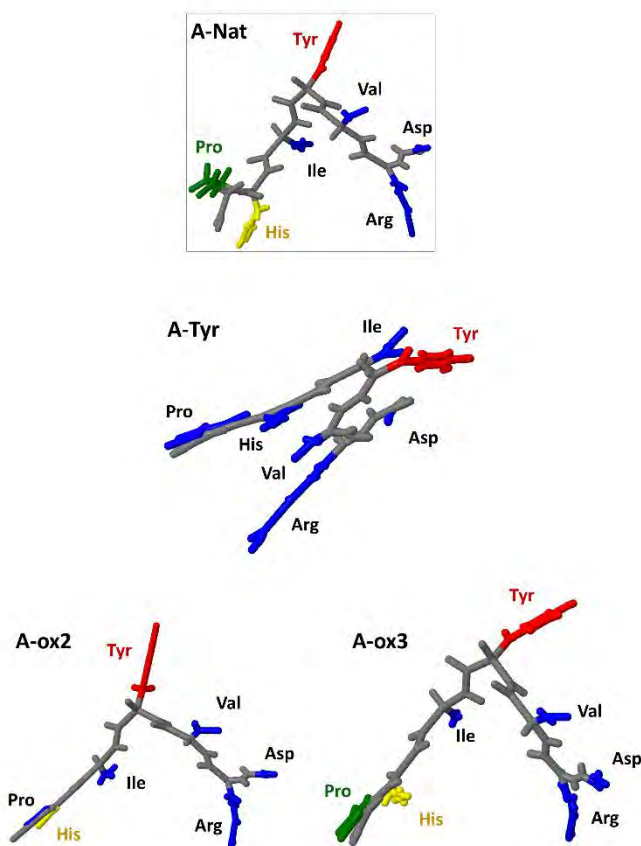


**Figure 5-11. Representation of the average structures of the native peptide A (grey box) and peptide A containing an increasing number of oxidized amino acids (A-Tyr, A-ox2 and A-ox3, respectively).** The peptide backbone is depicted in grey using a stick model in all structures. Un-oxidized amino acid side chains are depicted in blue. Red, yellow and green indicate the oxidation of Tyr, His and Pro, respectively. These average structures are obtained from the second batch of long-term MD calculations in order to verify the repeatability of the simulations.



## 5-2 Cysteine as a reference for plasma-induced modifications

### 5-2.1 Introduction

As stated in **section 1-2.2**, cold atmospheric pressure plasmas can be generated using various sources like jets, DBDs and other setups. Furthermore, a wide range of feed gases or gas admixtures, such as noble gases with molecular gas mixtures or ambient air, can be used. While the large variability of plasma sources creates the possibility of using different conditions for different applications, in order to optimize the treatment, it also complicates the comparison of various plasma sources, as well as treatment conditions to each other. This is especially important in the field of plasma medicine as, next to the range of working conditions, the biological targets vary widely.

In this section, the treatment of a simple model system with both the COST-jet and kINPen11 is compared. In this context, cysteine was chosen as a target as it has been presented as a biological model target for plasma treatment<sup>36</sup>. Although it is a rather small molecule, it contains three chemical functional groups with high biological relevance. Because of this, investigating the chemical modifications induced by plasma treatment provides insight into the effect of such treatment on various biological samples. On one hand, and as already stated in **section 1-2.2**, the COST-jet has been developed as a standard plasma source to compare the performance of different plasma jets on a common basis<sup>19</sup>. On the other hand, the kINPen11 is identical to the commercially available kINPenMed® albeit it is not certified. The kINPen11 consists of two electrodes, *i.e.*, a central pin electrode with diameter of 1 mm surrounded by a grounded electrode (*cf.* Figure 1-8D). It uses argon as working gas and is widely used in experiments<sup>37–42</sup>, and even in clinical studies<sup>43–45</sup>. The COST-jet has a simple design made of two plate electrodes (*cf.* Figure 5-3) which can use both argon and helium as working gas.

A combined approach of both MD simulations and experiments is used to investigate the relevance of various feed gas compositions and their effect on chemical modifications introduced in a biological model substrate. This allows us to elucidate the impact of various plasma sources on a common sample, comparing

different plasmas by their impact on biological samples. This work was performed in collaboration with the Biomedical Applications of Plasma Technology group of the Ruhr-Universität Bochum and the Leibniz Institute for Plasma Science and Technology. This part will mainly focus on the computational results. For more details on the experimental data, the reader is referred to<sup>3</sup>.

## 5-2.2 Computational setup

The interactions between RONS (*i.e.*, H<sub>2</sub>O<sub>2</sub>, OH, O<sub>2</sub>, O<sub>3</sub> and NO) and cysteine were investigated using the density-functional based tight-binding (DFTB) method. The interactions with O in solution were not investigated for the reasons explained in **section 5-1.1**.

Prior to the MD impact simulations, a cysteine molecule was introduced in a 20 x 20 x 20 Å<sup>3</sup> cubic simulation box filled with equilibrated water molecules. An example is depicted in Figure 5-12. In order to eliminate any stresses, which are a result of introducing the biochemical structure in the solution, the system was further equilibrated at room temperature for 10 ps using a canonical ensemble (where the temperature and volume are kept constant, NVT). A single reactive species was introduced per simulation by replacing a water molecule with the

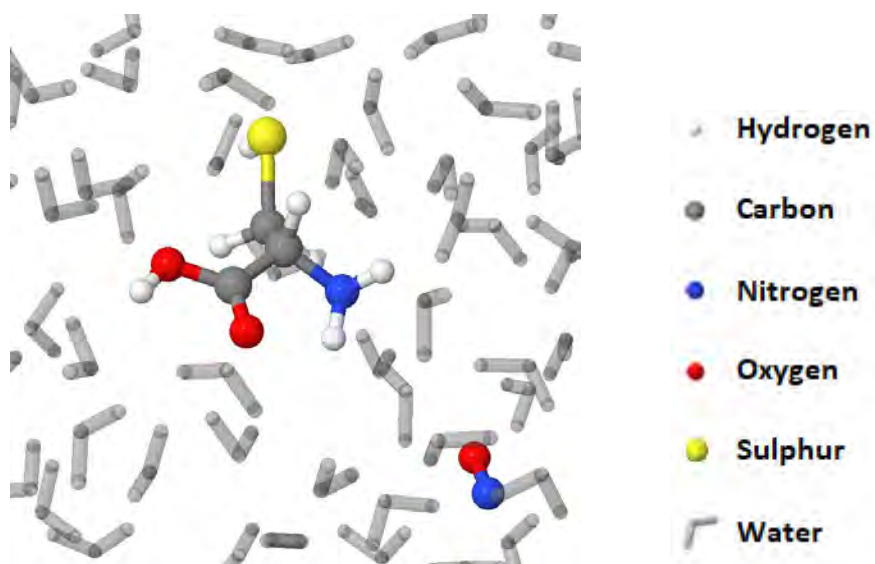


**Figure 5-12. Snapshot of cysteine in solution serving as input for the performed MD calculations.** In addition to the introduction of cysteine in the water box, a single water molecule was replaced by an NO radical.

reactive species (minimum distance of 5 Å to the biomolecule to avoid initial interactions). All impact simulations were performed at room temperature using a Berendsen thermostat with a coupling constant of 100 fs and using periodic boundary conditions. The time scale of 10 ps was chosen as such for reactions to happen. Furthermore, all simulations were performed using a time step for integration of 0.25 fs. Every interaction has been simulated using 50 independent runs. It is important to note that the effect of pH and charges has not been considered during the simulations given the very small dimensions and the limited number of water molecules in the simulated systems.

### 5-2.3 Simulations of cysteine reacting with RONS

To gain insight into potential reactions causing cysteine modification, DFTB simulations of cysteine interacting with several reactive species, known to be generated by plasmas, were performed. The reactive species considered are hydroxyl radicals (OH), hydrogen peroxide (H<sub>2</sub>O<sub>2</sub>), molecular oxygen (O<sub>2</sub>), ozone (O<sub>3</sub>) and nitrogen oxide (NO) in solution. Singlet delta oxygen (O<sub>2</sub> (<sup>1</sup>Δ<sub>g</sub>)), which is also an interesting species, as it is produced by various plasma sources, cannot be investigated using DFTB as the calculated species are defined by the number of (un)paired electrons, which results in O<sub>2</sub> in the ground state.

An overview of the simulated reactions, together with the most pronounced oxidation products that were observed during these calculations, are presented in Figure 5-13, Figure 5-14 and Figure 5-15. Over the course of 10 ps, the oxidation of cysteine was initiated by a reaction with either OH or NO radicals, while only weak attractive interactions were encountered between cysteine and H<sub>2</sub>O<sub>2</sub>, O<sub>2</sub> or O<sub>3</sub>. In this context, OH and NO radicals interacted with cysteine leading to the formation of the cysteine adduct radicals (2) to (6), as illustrated in the top of Figure 5-13. Oxidation was mainly initiated on the thiol group of cysteine where the abstraction of the H-atom resulted in the formation of product (6), or Cys-(-H), while the formation of product (5), Cys-SOH<sub>2</sub>, and product (7), Cys-SNO, are formed after an addition reaction of OH and NO, respectively. In the case of the OH radicals, the addition reaction was preferred over the H-abstraction. Indeed, in 50% of the observed reactions, OH was found to add on the molecules, while H- abstraction reactions were only found in 30% of the total number of reactions. It should be noted that these are



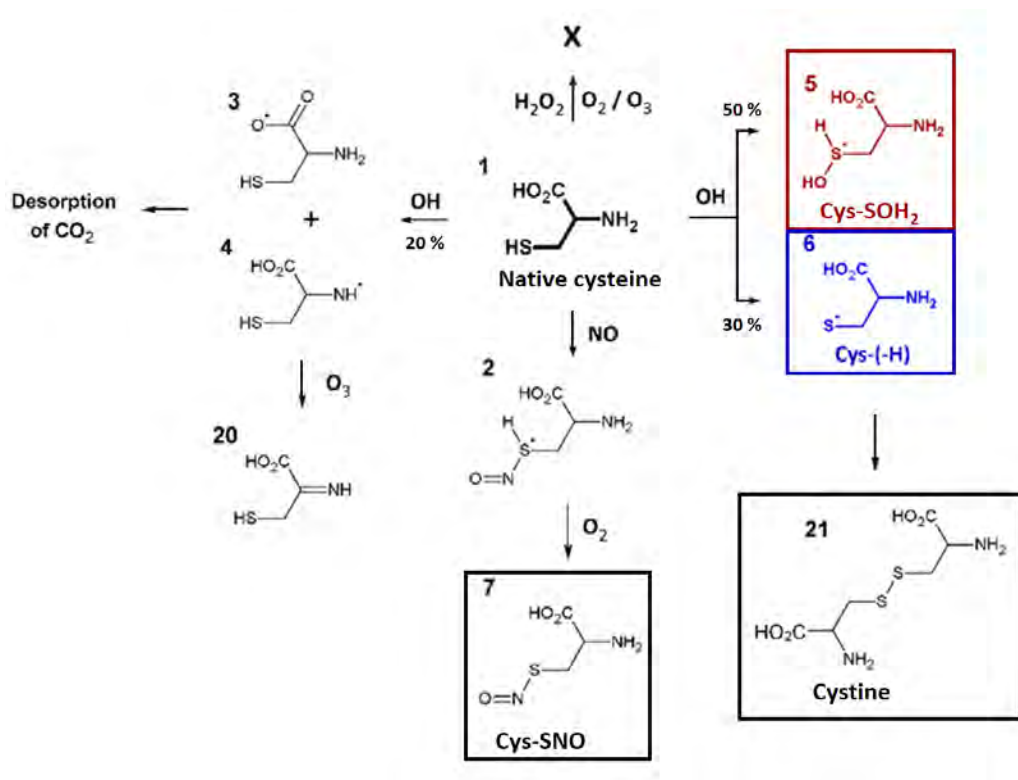


**Figure 5-13. Summary of the predicted reaction paths encountered during the oxidation of native cysteine.** Stable oxidation products are indicated by a solid black box. As the interaction of cysteine with OH radicals resulted in multiple reaction products, branching ratios are depicted on the figure (based on the total amount of reactions observed).

only rough indications.

Reactions with OH on the cysteine backbone were also encountered leading to the formation of products (3) and (4). The latter reactions were usually followed by an interaction with O<sub>2</sub> and O<sub>3</sub> leading to the desorption of CO<sub>2</sub> and the formation of an imine group in the molecule.

The observed adduct radicals, as a result of the oxidation of the thiol group are, in turn, able to react further with various reactive species. This propagation was investigated and created a network of reaction pathways depending on the introduced reactive species. In the case of adduct radical (2), formed after the addition of an NO radical, the oxidation was terminated through a H-abstraction reaction leading to the formation of S-nitroso cysteine, Cys-SNO (product (7)). The follow-up reactions of Cys-SOH<sub>2</sub> (5) and Cys-(-H) (6) are illustrated in separate

schemes in Figure 5-14. The calculations indicated that both adduct radicals were able to react with OH radicals, O<sub>2</sub> and O<sub>3</sub> molecules. When interacting with O<sub>3</sub>, the formation of adduct radical (9) was observed for both Cys-SOH<sub>2</sub> (5) and Cys-( $\cdot$ H) (6), which, in turn, formed sulfinic acid (product (10)) in the presence of O<sub>2</sub>. Furthermore, when O<sub>2</sub>, or OH, interacted with both Cys-SOH<sub>2</sub> (5) and Cys-( $\cdot$ H) (6) an addition or H-abstraction reaction is encountered leading to the formation of sulfenic acid

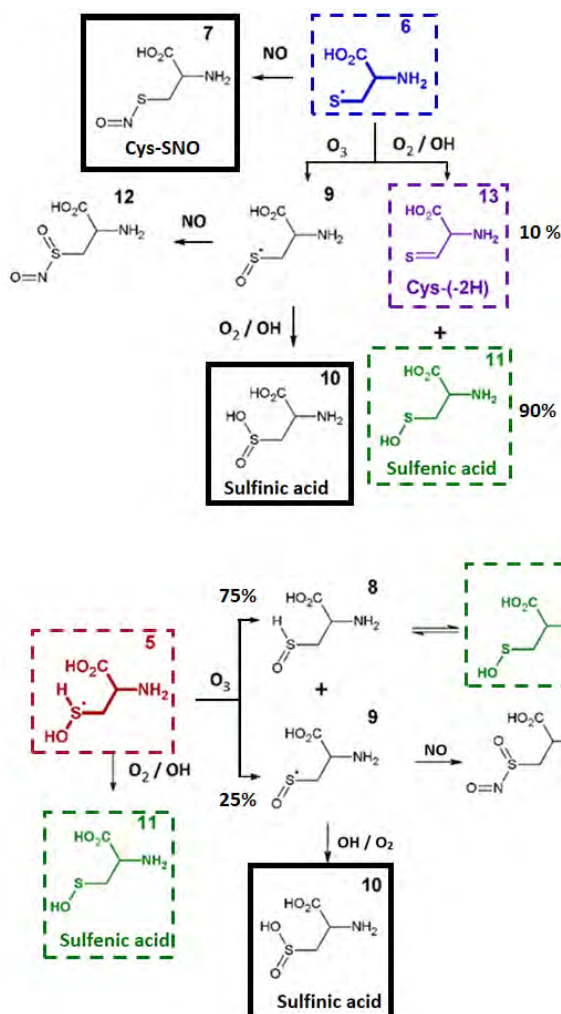


**Figure 5-14.** Summary of the predicted reaction paths encountered during the further oxidation of Cys-( $\cdot$ H) (6, top) and Cys-SOH<sub>2</sub> (5, bottom). Important oxidation products are indicated using a solid black box. Important intermediates are marked with dashed colored boxes. Branching ratios (compared to the total amount of observed reactions) are depicted in cases when multiple reactions products are observed during the simulations.

(Cys- SOH or product (11)), or the formation of a S=C double bond as illustrated in product (13), with 90 and 10% of the total number of reactions observed, respectively. The formation of sulfenic acid was also encountered after the reaction of product (5) with O<sub>3</sub>. Here, next to product (9), leading to the formation of sulfenic acid,

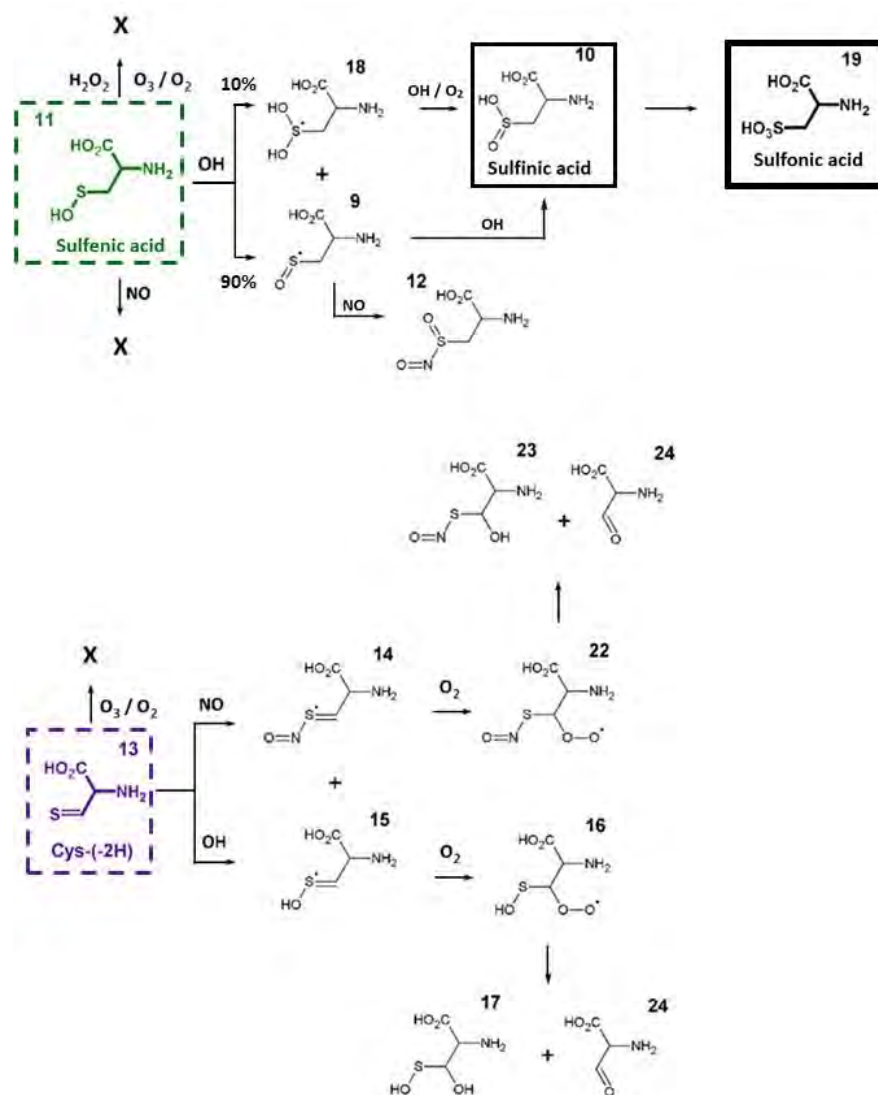


**Figure 5-15.** Summary of the predicted reaction paths encountered during the oxidation of sulphenic acid (top) and Cys-(-2H) (bottom). Stable oxidation products (sulphinic and sulphonic acid) are indicated using a solid black box. Branching ratios (compared to the total amount of observed reactions) are depicted in cases when multiple reactions products are observed during the simulations.

product (8) was formed which is a tautomer of Cys-SOH (11)<sup>46</sup> (in 25 and 75% of the total number of reactions observed, respectively). As product (11) is greatly favored over its tautomer in solution, the former could be expected in solution after reaction of product (5) with O<sub>3</sub>. Furthermore, the addition of NO onto product (6) was encountered, which yielded Cys-SNO (product (7)), similar to the interaction with native cysteine (*cf.* Figure 5-13).

Next to the interactions of product (6) with reactive species, we also investigated the formation of disulfide bonds. For this we simulated the interaction of product (6) with either native cysteine or with another Cys-(-H) adduct radical (product (6)). The simulations indicated that cystine will be formed almost immediately when two Cys-(-H) adduct radicals interact with each other in solution, while an additional H-abstraction is required during the interaction between product (6) and native cysteine.

In the final step of the computational investigation, we considered both sulfenic and sulfinic acid, as well as product (13), for further oxidation. In the case of sulfenic acid, the initiation of oxidation was only observed when interacting with OH radicals, which resulted in either a H-abstraction reaction, leading to the formation of product (9) and therefore to the formation of sulfinic acid in aerobic conditions (*cf.* Figure 5-14), or an OH addition reaction leading to the adduct radical (18). Similar to product (9), adduct radical (18) is able to react with O<sub>2</sub> resulting in the formation of sulfinic acid. Following this scheme again (from sulfenic acid to sulfinic acid), the formation of sulfonic acid (product (19)) can be expected. Finally, Cys-(-2H) (product (13)) was found to react with both OH and NO radicals leading to an addition reaction. Here, the calculations indicated that both products (14) and (15) form peroxides (ROO●) in aerobic conditions. From literature on the oxidation of biomolecules, we know that ROO● are able to react further towards the formation of alcohol and carboxyl groups on the structure<sup>12</sup>. These last steps were not simulated, as this would require more complex systems as well as longer timescales, both beyond the limitations of the used computational method (DFTB). However, using this knowledge, we expect the formation of products (17), (23) and (24) from the observed peroxides. Note that product (24) is the result of the desorption of the oxidized thiol group.

## 5-2.4 Experimental part

### 5-2.4a *Experimental setup*

Two plasma sources were used in this investigation: the COST Reference Microplasma Jet (COST-jet) and the kINPen11. The COST jet was capacitively coupled and driven by an AC voltage at 13.56 MHz. It was operated using pure argon and helium as feed gas, both at 1 standard liter per minute (slm). Various gas admixtures were used: Ar/O<sub>2</sub> (0.004% O<sub>2</sub>), Ar/N<sub>2</sub> (0.01% N<sub>2</sub>), He/O<sub>2</sub> (0.5% O<sub>2</sub>), He/N<sub>2</sub> (0.5% N<sub>2</sub>), or He/air (0.1% O<sub>2</sub> and 0.4% N<sub>2</sub>). All gases were of 5.0 purity. The dissipated power during treatment was held at 590 mW for argon and 330 mW for helium. The kINPen consists of a powered pin electrode (1 MHz, 2-6 kV and pulsed at 2.5 kHz) surrounded by a dielectric tube which served as the outer electrode. A flow rate of 3 slm of pure argon was used with a dissipated power of around 500 mW. Here, again, various gas admixtures were used: O<sub>2</sub> (1%, Ar/O<sub>2</sub>), N<sub>2</sub> (1%, Ar/N<sub>2</sub>) or O<sub>2</sub> and N<sub>2</sub> (0.25% and 0.75%, Ar/air). Both sources were mounted vertically above the treated samples with a distance of 4 and 10 mm for the COST jet and kINPen, respectively.

Cysteine was purchased from Sigma Aldrich and was dissolved in distilled water to a final concentration of 100 µg/ml. Samples of 3 ml were treated for 3 and 10 min for all working conditions.

For the FTIR measurements 20 µl of each sample was desiccated on silicon wafers and 32 FTIR spectra were recorded between 750 and 4000 cm<sup>-1</sup> with a resolution of 4 cm<sup>-1</sup>. The samples were measured using an FTIR micro spectrometer (Spotlight 200, Perkin Elmer) in triplicates. Afterwards, the spectra were normalized, and the areas-under-curve were calculated for the chosen signal bands.

High-resolution MS data were collected using a TripleTOF5600 system and Analyst TF 1.51 software (both Sciex). The treated samples were diluted with 40% methanol containing 0.05% ammonia, and directly infused (10 µl/min) into the systems turbo ion source using negative electrospray ionization. Between 50 and 400 m/z were recorded and peaks were fragmented using CID. Data analysis was performed using Analyst TF 1.51, and PeakView 1.1 (both Sciex), and Mass++ 2.7.6 (Shimadzu).

### 5-2.4b Results and discussion

Fourier Transform Infrared spectroscopy (FTIR) and Mass Spectrometry (MS) were used to elucidate the expected oxidation products after plasma treatment. The experimental part of this investigation was performed by both Dr. J.-W. Lackmann from the Ruhr-Universität Bochum and Dr. K. Wende from the Leibniz Institute for Plasma Science and Technology. The FTIR spectra after the treatment using different plasma sources and gas admixtures are presented in Figure 5-16 for the He COST-jet and Figure 5-17 for the Ar jets (both COST and kINPen11). Compared to the control (indicated in black in both figures), it becomes clear that plasma treatment results in an overall decrease in the S-H bonds and an increase in the O-H and S=O bonds, and to a lesser extent in the C=O bonds. These results point towards the oxidation of the thiol group of cysteine. This is in excellent agreement with the computational results as the reactions observed in the simulations are focused on the sulfur of cysteine. Interesting is the fact that the signals corresponding to the N-O bending mode only increased when admixtures were used, which contain a trace of nitrogen (*i.e.*, He/N<sub>2</sub>, Ar/N<sub>2</sub>, He/air and Ar/air). This indicates that reactive nitrogen species are most likely responsible for the increase in NO containing groups on the modified cysteines after plasma treatment.

From Figure 5-16 and Figure 5-17, it is clear that different treatment conditions (*i.e.*, plasma source and gas admixtures) greatly affect the chemical modifications on cysteine. While similar trends are observed, suggesting that similar reaction products are formed, the ratio of these products, compared to each other, is expected to be different when using different treatment conditions. To further investigate the expected oxidation products, MS spectra were recorded of the treated cysteine solutions. The results are depicted in Figure 5-18 using mirror plots. These mirror plots are used to compare different treatment conditions with each other. Panel A of Figure 5-18 contains the control sample where only a signal for native cysteine (120.0119 m/z) and the homo-dimer cystine (239.0160 m/z) was observed. This changes significantly after plasma treatment, where a multitude of signals, originating from chemically modified cysteine, arise in a time-dependent manner. Some of these signals only appear under specific conditions, allowing for a differentiation of treatment conditions. From Figure 5-18 it becomes clear that the

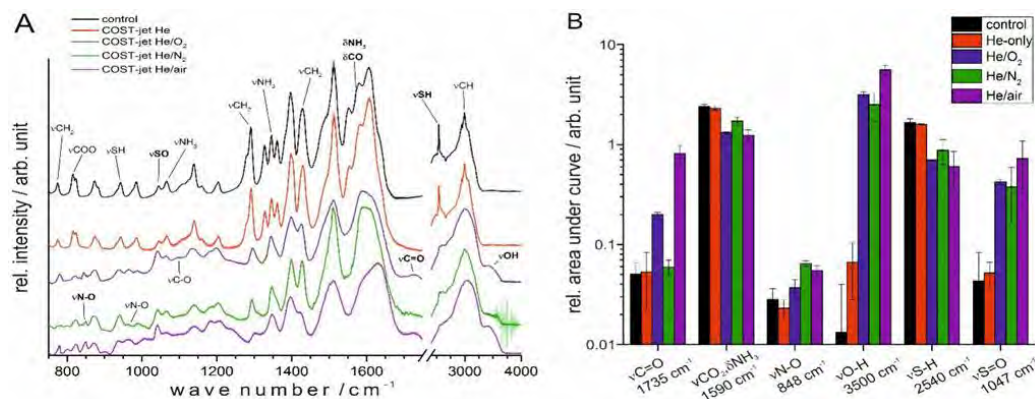


**Figure 5-16. FTIR spectroscopy (A) and peak quantification (B) of He-based plasmas using the COST-Jet.** The spectra were recorded after 10 min of treatment. Bold annotations were used for quantification. “Control” refers to samples treated only with gas flow without admixtures. The graphs are stacked for better visibility. Published in<sup>3</sup>.

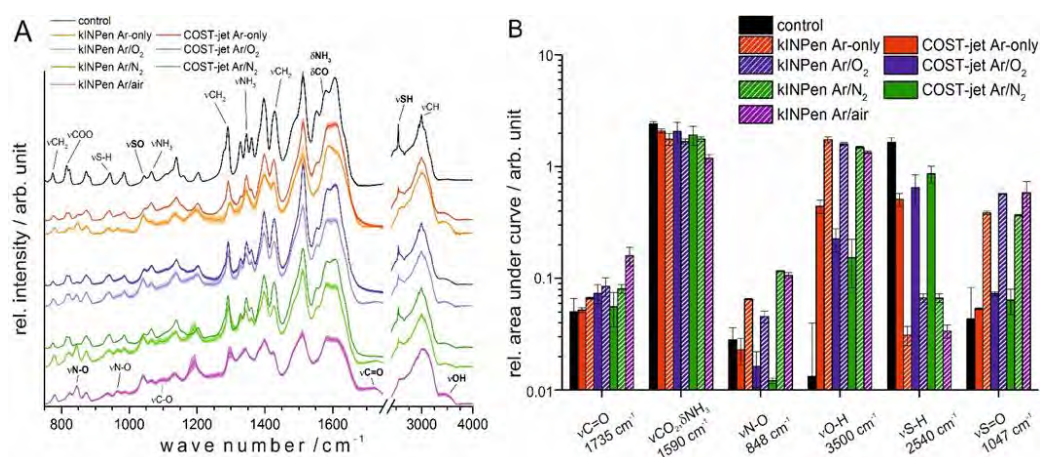


**Figure 5-17. FTIR spectroscopy (A) and peak quantification (B) of Ar-based plasmas using both sources.** The spectra were recorded after 10 min of treatment. Bold annotations were used for quantification. “Control” refers to samples only treated with gas flow without admixtures. The graphs are stacked for better visibility. Published in<sup>3</sup>.

thiol moiety forms the target of oxidation. Among the dominant signals are sulfinic (Cys-SO<sub>2</sub>H; 152.00 m/z), sulfonic acid (Cys-SO<sub>3</sub>H; 168.00 m/z) and cystine. One can clearly see that plasma treatment results in a significant decrease of the cysteine signal towards the formation of cystine, sulfinic and sulfonic acid. From the mentioned oxidation products, sulfonic acid forms the most dominant oxidation product suggesting that sulfinic acid acts as a precursor for sulfonic acid, as also suggested by the performed simulations. Experimental analysis suggested that

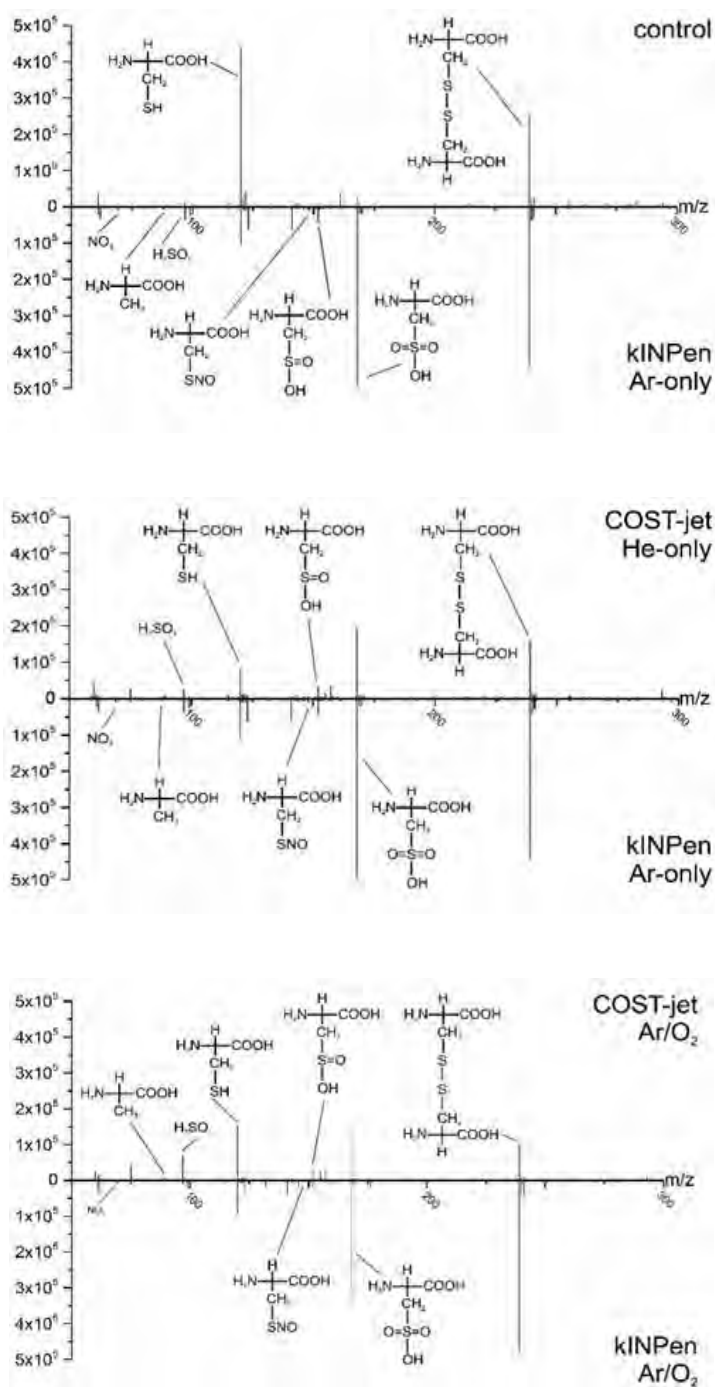


**Figure 5-18.** Mass spectrometry mirror plots of plasma-treated cysteine: survey mass spectra of cysteine solutions, treated for 10min with COST-jet or kINPen using various working gas compositions (He, Ar or Ar with 0.004%  $O_2$ ). "Control" was treated with Ar-only gas using the kINPen for 10 min. Published in<sup>3</sup>.



cystine can further be oxidized towards cystine-S-sulfoxides given the presence of masses larger than cystine (*e.g.*, 271.0058  $m/z$  and 302.9463  $m/z$ ). However, the exact chemical structure could not be identified. Cys-SNO was only found when  $N_2$  was present in the admixture, *i.e.*, air and  $N_2$  plasmas. This corresponds well to the most pronounced oxidation products observed during the simulations (*cf.* Figure 5-13, Figure 5-14 and Figure 5-15).

*A more detailed description of the experimental results can be found in<sup>3</sup>.*

## 5-3 Glutathione

### 5-3.1 Introduction

As is clear from **chapters 3, 4 and 5**, plasma treatment can lead to various chemical modifications on various biological components. However, in addition to these modifications (leading to, among others, DNA damage and cell membrane damage), the redox system of the treated cells can be affected as well. Among these cellular redox mechanisms is the system formed by glutathione (GSH), glutathione disulfide (GSSG) and various enzymes related to the conversion and recycling of GSSG to GSH. GSH acts as an important antioxidant inside cells<sup>47,48</sup>. GSH is easily oxidized to form GSSG, detoxifying  $\text{H}_2\text{O}_2$  and oxygen-based radicals. Afterwards, GSSG is converted back to GSH by glutathione reductase<sup>48</sup>. This recycling mechanism results in an efficient detoxification of intracellular reactive species, which might otherwise cause uncontrolled and undesired chemical modifications at other biomolecules, as observed in **chapters 3, 4 and 5**.

However, next to the conversion of GSH to GSSG, it has been reported that the twice or thrice-fold oxidation of GSH results in the formation of sulfinic and sulfonic acids on the cysteine of GSH, similar to the results presented in **section 5-2**<sup>3,21</sup>, therefore blocking the formation of GSSG. Moreover, it is stated that both  $\text{GSO}_2\text{H}$  (glutathione sulfinic acid) and  $\text{GSO}_3\text{H}$  (glutathione sulfonic acid) form irreversible oxidation products of GSH<sup>49</sup>. In the context of plasma treatment, several studies have demonstrated that plasma has the ability of decreasing the intracellular GSH levels within seconds<sup>6,50,51</sup>. Ishaq *et al.* observed a reduction of intracellular GSH levels by 80% in melanoma cells after a 30 second treatment with a helium plasma jet<sup>50</sup>. Furthermore, Zhao and colleagues reported a strong decrease in free GSH in hepatoma cells when using a helium-oxygen jet system<sup>51</sup>. In addition, Ke *et al.* showed the increase in disulfide bonds, after treatment with a pin-to-plate system in argon atmosphere, indicating an enhanced conversion of GSH to GSSG<sup>47</sup>.

Much like in **section 5-2**, a dual approach is used to investigate the chemical modifications of plasma treatment on GSH and GSSG in order to elucidate the mechanisms of glutathione oxidation induced by plasma treatment. For this investigation, a DBD, already in use for clinical applications, was investigated. The

results presented here will mainly focus on the computational part of this study and are based on the data reported in<sup>2</sup>. For more information on the experimental part of this work, please consult<sup>2</sup>.

### 5-3.2 Computational setup

The chemical modifications of GSH and GSSG, as a result of the interactions with various reactive species (*i.e.*, OH, O<sub>2</sub>, O<sub>3</sub>, H<sub>2</sub>O<sub>2</sub> and NO) were investigated using reactive MD simulations. In this work, MD simulations were performed using the density-functional based tight-binding (DFTB) method. The interactions with O in solution were not investigated for the reasons explained in **section 5-1.1**.

Prior to the MD impact simulations, the GSH or GSSG molecule was introduced in a 25 x 25 x 25 Å<sup>3</sup> cubic simulation box filled with equilibrated water molecules ensuring a density of approximately 1 g/ml around the biomolecule at all times. An example is presented in Figure 5-19. In order to eliminate any stresses, which are a result of introducing the biochemical structure in the solution, the system was further equilibrated at room temperature for 10 ps using a canonical

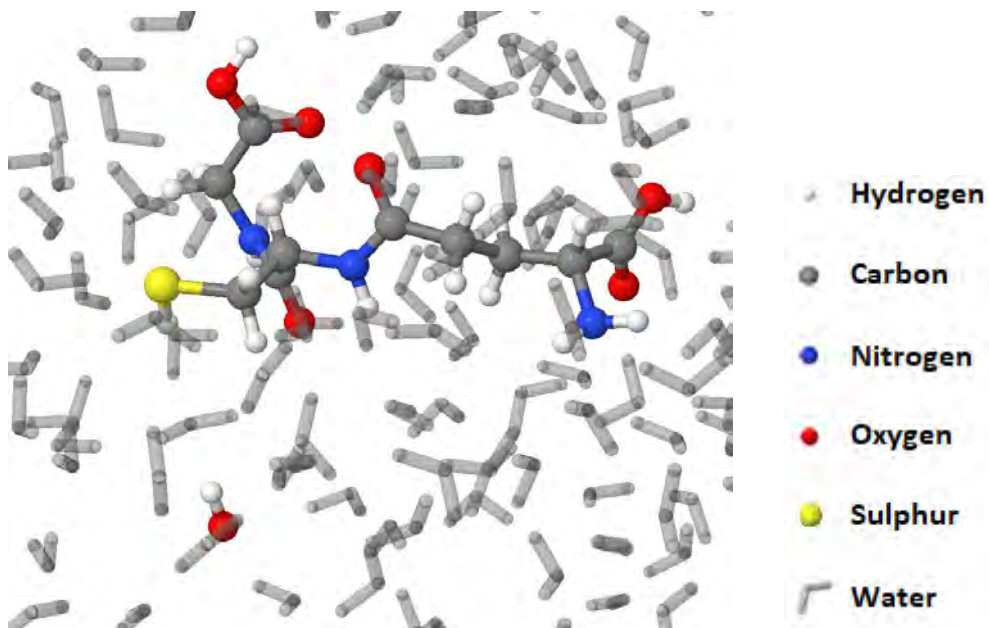


**Figure 5-19. Snapshot of glutathione in solution serving as input for the performed MD calculations.** In addition to the introduction of glutathione in the water box, a single water molecule was replaced by an OH radical.

ensemble (NVT, where the temperature and volume are kept constant). A single reactive species was introduced per simulation by replacing a water molecule with the corresponding reactive species. All impact simulations were performed at room temperature for 10 ps using a Berendsen thermostat with a coupling constant of 100 fs and using periodic boundary conditions. It should be noted that, due to the large number of atoms in the simulated system (*i.e.*, up to 800 as a result of the number of water molecules), only a few ps could be simulated within a reasonable amount of calculation time (*i.e.*, a few weeks). Finally, all simulations were performed using a time step for integration of 0.25 fs. Each interaction has been simulated independently for 25 times. It is important to note that the effect of pH and charges has not been considered during the simulations given the very small dimensions and the limited number of water molecules in the simulated systems.

### 5-3.3 Simulation of GSH reacting with RONS

DFTB simulations were performed to obtain insight in the molecular-scale processes in order to shed light on the observed changes in the chemical structure of both GSH and GSSG. The results are depicted in Figure 5-20 and Figure 5-21 (for GSH and GSSG, respectively). From both figures, it becomes clear that oxidation processes are initiated by OH radicals on cysteine. Indeed, other reactive species, such as  $\text{H}_2\text{O}_2$  or NO, only showed weak interactions with the introduced biomolecule within the 10 ps simulated. It should be noted that reactions with other reactive species are not excluded and might still occur after significantly longer timescales.

As the chemical modifications are mainly situated on the thiol of GSH, similar reactions as depicted in Figure 5-13 are observed. Indeed, interactions between GSH and OH resulted in the abstraction of the thiol H-atom, leading to the formation of a water molecule and a glutathione radical ( $\text{GS}\bullet$ ), located on the cysteine (depicted in red in Figure 5-20). Once the  $\text{GS}\bullet$  is formed, reactions with multiple other species can occur. Introducing NO to the resulting radical system led to an addition reaction on the S-atom toward the formation of S-nitroso glutathione (GSNO). Furthermore, when a second OH radical is introduced to the system, either an addition, similar as in the case of NO, or a second H-abstraction, from the C-atom adjacent to the sulfur, can occur. This results in either GSOH or a  $\text{S}=\text{C}$  double bond, respectively. Moreover, disulfide bond formation has been observed as well during the simulations when the

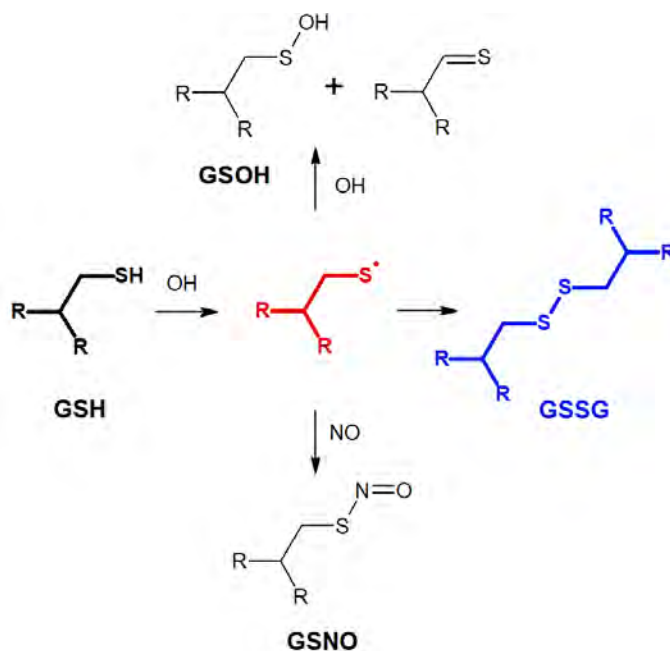


**Figure 5-20. Summary of the reactions between GSH and various reactive species as observed during the reactive MD simulations.** The initial GSH structure is indicated using a bold black structure. The resulting GS•, after H-abstraction by OH, is indicated in red. Published in<sup>2</sup>.

GS• radical (as a result of the H-abstraction of GSH) comes in contact with a GSH molecule, leading to the formation of GSSG (depicted in blue in Figure 5-20). These results are consistent with the observations made during the native cysteine simulations (*cf.* Figure 5-13 and Figure 5-14). It is important to note that, while the full GSH molecule has been simulated in solution, chemical modifications were only encountered on the cysteine moieties of this biomolecule, with in particular the thiol group.

In **section 5-2**, it has been suggested that cystine is able to be modified by plasma-generated reactive species due to the presence of reaction products with a higher mass than cystine. Moreover, GSSG plays an important role in the glutathione redox system of cells. Because of this, it is interesting to also investigate the interactions between GSSG and RONS. Unlike GSH, the initiation sites for oxidation of GSSG are the C-atoms of cysteine (see Figure 5-21). Here, OH radicals interact with GSSG through H-abstraction reactions on either of the two C-atoms of cysteine, leading to either product (1) or product (2) of Figure 5-21 (product (1) has

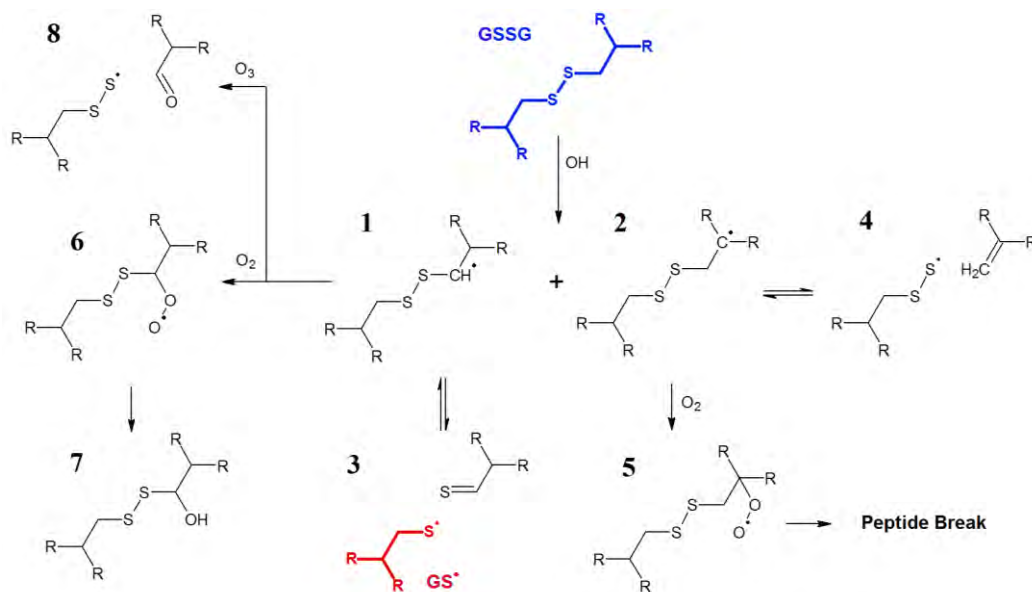


**Figure 5-21. Summary of the reactions between GSSG and various reactive species as observed during the reactive MD simulations.** The initial GSSG structure is indicated in blue. The GS● indicated in red is able to react further as depicted in Figure 5-20. All observed oxidation products are numbered for the sake of clarity. The production of product (7) and the peptide break were not simulated as explained in the text. Published in<sup>2</sup>.

been encountered in 40% of the cases, while product (2) has only been encountered in 20% of the cases). Consequently, an equilibrium is found between the radical and a broken structure, in both cases. Indeed, it has been observed that the disulfide bond breaks after the abstraction of the H-atom found in the side chain of cysteine (*cf.* product (1) and (3)). The disulfide bond break resulted in the formation of a GS● radical (indicated in red in Figure 5-21) which is prone to further oxidation, as observed in the above Figure 5-20. In case the H-abstraction occurs on the C-alpha position (product (2)), the S-C bond, adjacent to the disulfide bond, was often observed to break, leading to an increase in C=C double bonds (product (4)). This bond break was, again, found to be in equilibrium with product (2). Interesting is the fact that both GSSG-radicals (1) and (2) were able to react with molecular oxygen leading to the formation of peroxides (ROO●) as seen in products (5) and (6). From literature on oxidation processes we know that ROO● are able to react further towards the formation of alcohol and carboxyl groups on the structure<sup>12</sup>. These last steps were not simulated as this would require more complex systems, as well as longer

timescales, both beyond the limitations of the used computational method (DFTB). However, using this knowledge we expect the formation of a hydroxyl group adjacent to the disulfide bond (as seen in product (7)) as well as a peptide break after the oxidation of peroxide (5).

Finally,  $O_3$  was observed to be able to react with product (1) only in rare cases (8% of simulations). This led to the oxidation of the C-atom adjacent to the disulfide bond resulting in the formation of an aldehyde and the dissociation of the S-C bond.

## 5-3.4 Experimental part

### 5-3.4a Experimental setup

A DBD setup was used consisting of a cylindrical copper electrode which was covered with aluminum oxide ( $Al_2O_3$ ). The electrode with a diameter of 10 mm was driven by a pulsed power supply at  $-13.5$  kV at 300 Hz. The samples were placed on a grounded aluminum plate and the distance towards the driven electrode was 1 mm. The plasma was operated using ambient air.

GSH and GSSG were purchased from Sigma Aldrich and dissolved in distilled water or sodium phosphate buffer (0.15, pH 7) in such a way that a concentration of 10 mg/ml was obtained. Experiments were performed using 10  $\mu$ L placed on a glass cover slip for 1 to 20 minutes. Control samples were prepared equally without the plasma treatment. The control samples were placed in ambient conditions for 20 minutes.

For the Raman measurements, a Raman microscope WITec alpha 300 RAS (WITec) was used, equipped with a frequency-doubled Nd:YAG laser with a wavelength of 532 nm operating at 17 mW. The laser was focused on the sample using a 100x objective lens (Olympus MPLFLN100X, NA = 0.9) and the radiation was coupled into a microscope by a single mode optical fiber. The scattered light was collected using the same objective lens and measured by a spectrometer unit (UHTS300) consisting of a diffraction grating (600 grooves per mm) and equipped with a back-illuminated electron multiplying charge-coupled device (1600 x 200 pixels, cooled to  $-60$  °C). Every sample was measured 10 times at different positions. Every position was recorded 10 times with an integration time of 2 seconds. All experiments were performed in triplicates.

Electrospray ionization mass spectra were recorded using an Esquire 6000 mass spectrometer (Bruker). Equipped with an ion-trap analyzer, full spectra of GSH and GSSG were recorded in both positive-ion and negative-ion mode to cover as many modified species as possible. Instrumental parameters were optimized for each sample with GSH and GSSG. The capillary voltage was set in a range of  $-22$  to  $25$  V, the spray voltage was between  $3.00$  and  $4.50$  kV, and a capillary temperature of  $180$  °C was employed. The mass scan range was from  $m/z$   $50$  to  $2000$  amu, for  $20$  s scan time. Spectra were acquired using a direct infusion setup with a flow rate of  $5$   $\mu\text{l}/\text{min}$  with a cone voltage of  $20$  kV. To determine occurring in-source fragments, which increase the sample complexity without yielding significant additional information, MS/MS spectra of both GSH and GSSG were acquired using the same conditions with a collision energy ramp between  $2.00$  and  $4.00$  eV. Spectra were deconvoluted and a background of ten times noise ( $500$  counts in positive and  $5$  counts in negative mode) was subtracted before peak annotation. All experiments were performed in duplicates.

### 5-3.4b Results and discussion

Experiments were performed by C. Klinkhammer *et al.* at the Ruhr-Universität Bochum. For this investigation, a combination of Raman spectroscopy and mass-spectroscopy (MS) was performed. The obtained Raman spectra are depicted in Figure 5-22. These results were obtained in buffered solution in order to more closely resemble the performed simulations. Indeed, using distilled water, plasma treatment gradually reduced the pH of the solution (up to a pH value of  $1$  after  $5$  minutes). As the simulations were performed in pure water, the effect of pH cannot be taken into account. Hence, neutral pH was used during the experimental treatment using a buffered solution fixed at pH  $7$ .

From Figure 5-22 a clear decrease of the band at  $2560\text{ cm}^{-1}$  can be observed, which was assigned to the S-H stretching mode. This indicated that the H-atom is easily abstracted within the first minutes. This is consistent with the computational observations indicating that oxidation occurs at the sulfur moiety. The decrease in the S-H band is coupled with an increase in disulfide bonds, indicated by the band at  $508\text{ cm}^{-1}$ . This points towards the formation of GSSG as a result of plasma treatment. However, additional reaction products become visible. This is indicated



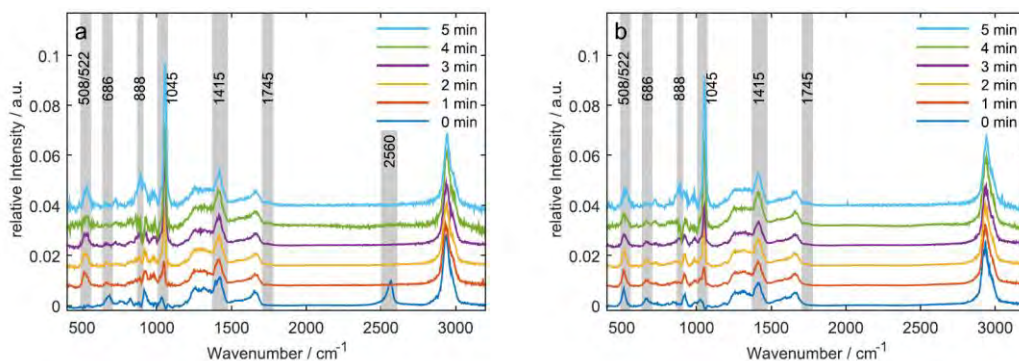


**Figure 5-22. Raman spectra of GSH (a) and GSSG (b) in sodium phosphate buffer after plasma treatment of 0-5 min.** Here, we show the difference spectra obtained by subtraction of pure plasma treated phosphate buffer from background corrected sample spectra each normalized to a phosphate peak at  $400\text{ cm}^{-1}$ . Important peaks are highlighted in grey. Published in<sup>2</sup>.

by the rise in the band at  $1045\text{ cm}^{-1}$ , which is assigned to the S=O stretching mode pointing towards the formation of glutathione sulfonic acids ( $\text{GSO}_3\text{H}$ ). While the formation of GSSG is consistent with the computational observations, the formation of sulfonic acids has not been simulated in this investigation. However, in analogy with the chemical modification of cysteine (*cf.* Figure 5-13, Figure 5-14 and Figure 5-15), multiple simulated reaction products of GSH are precursors of  $\text{GSO}_3\text{H}$ , *e.g.*, GSOH (*cf.* Figure 5-20).

When looking at the Raman spectra of GSSG (Figure 5-22 b), changes in signals can be identified as well. Here, an increase in the band at  $1045\text{ cm}^{-1}$  was observed, which was assigned to the S=O stretching mode due to the oxidation of the sulfur. Interesting is the fact that the S-S stretching mode decreases as a function of time. Coupled with the increase in the S=O band, it can be stated that GSSG acts as an oxidative intermediate when treating GSH. In other words, plasma treatment results in the conversion of GSH to GSSG after which it is chemically modified by the plasma treatment. In the end,  $\text{GSO}_3\text{H}$  and (GSNO) appear to be the end product after plasma treatment of both GSH and GSSG. The latter reaction product is supported by the increase in the band at  $888\text{ cm}^{-1}$ , which was assigned to the S-N=O bending mode. The fact that GSSG breaks up due to interactions with RONS is consistent with the computational observations where  $\text{GS}\bullet$  was observed as a reaction product of GSSG (product (3) in Figure 5-21). Other simulated reaction

products could be identified in the Raman spectra (*e.g.*, product (8) and (4) of Figure 5-21), as a decrease in the C-S stretching mode ( $686\text{ cm}^{-1}$ ) can be observed in Figure 5-22.

The observed chemical modifications are further supported by the MS spectra as presented in Figure 5-23. These mirror plots, first of all, compare the reaction products as a function of time (1 vs 5 min) and compare the relevance of pH-buffered media. It becomes clear from Figure 5-23 a-b that GSH is converted to GSSG (indicated by the decrease and increase of the signals for GSH and GSSG, respectively) and that GSSG acts as an intermediate reaction product in that sense that the signal for GSSG decreases after longer treatment times. GSO<sub>3</sub>H forms the dominant reaction product, which is in agreement with the oxidation of cysteine, as

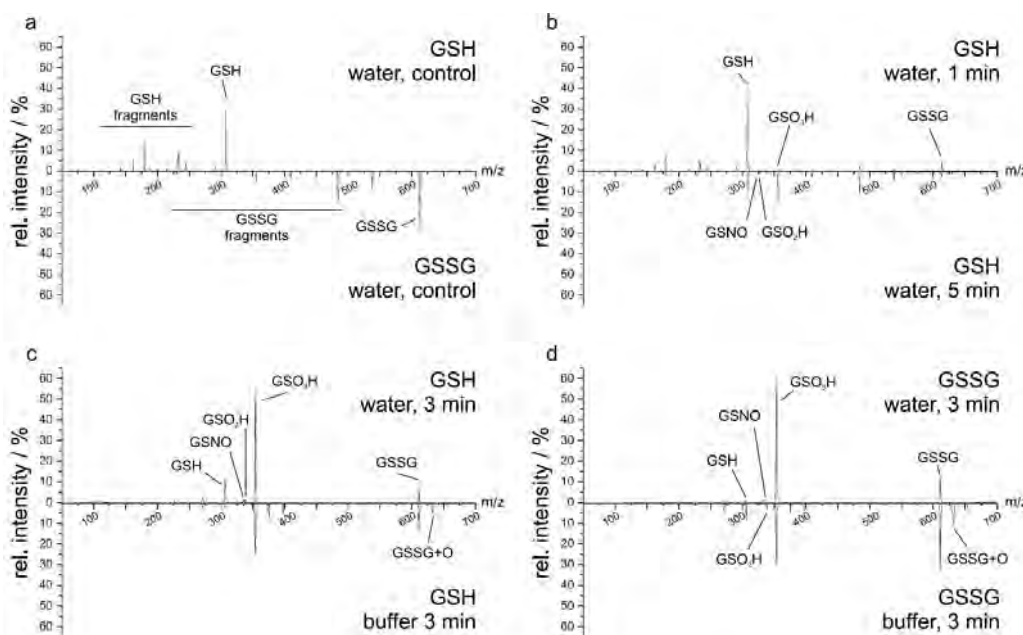


**Figure 5-23. Mirror plots of MS survey scans.** Mirror plots are chosen to show controls (a), the influence of treatment time on GSH in water (b), and to compare the relevance of pH-buffered medium on the resulting chemical modifications at GSH (c) and GSSG (d). (a) and (b) were measured in positive mode, (c) and (d) in negative mode to reduce the buffer influence. The intensities were calculated showing the intensity percentage of a peak relative to the spectrum's total intensity, to alleviate the significant lower counts in negative mode; peaks are annotated with the molecule of corresponding mass; "buffer" indicates the presence of 0.15 M sodium phosphate buffer set to pH 7. GSH and GSSG fragments indicate the presence of in-source fragments of the corresponding molecule. Published in<sup>2</sup>.

discussed in **section 5-2**. This observation further supports the fact that the thiol acts as the dominant target for oxidation by RONS. In addition, GSNO is observed in Figure 5-23, albeit at significantly lower intensities, consistent with the Raman spectra. Finally, while similar reaction products were observed when treating in water or in buffered solution, differences in the relative intensity of the respective signals are observed, indicating that the pH has an effect on the oxidation of GSH and GSSG. However, this could not be simulated using DFTB given the small dimensions.

*A more detailed description of the experimental results can be found in<sup>2</sup>.*

## 5-4 Conclusion

In this chapter, the impact of plasma treatment on proteins and amino acids was investigated. This was performed on four systems: two small peptides (*i.e.*, angiotensin and bradykinin), cysteine and glutathione. The investigations were combined with experimental studies in collaboration with the Biomolecular & Analytical Mass Spectrometry research group at the University of Antwerp (for angiotensin and bradykinin), the Leibniz Institute for Plasma Science and Technology (for cysteine) and the Ruhr-Universität of Bochum (for both cysteine and glutathione). While the experimental studies for the two small peptides were performed to support the computational results, a combined study was performed for the oxidation of cysteine (combining MD simulations with FTIR and MS spectroscopy) and glutathione (combining MD simulations with Raman and MS spectroscopy).

### 5-4.1 Two small peptides

To investigate the impact of plasma treatment on the two small peptides, atomic scale simulations were used to elucidate the interactions between OH radicals with the mentioned peptides (*i.e.*, angiotensin and bradykinin), as well as the further oxidation processes of selected amino acids in these peptides. This was further extended by elucidating the effect of the observed oxidation products on the structural behavior of the peptides, using longer time-scale MD simulations. The model peptides are based on a part of angiotensin (*i.e.*, fragments 1-7) and bradykinin, as they are both small enough to be effectively treated in reactive MD simulations, they contain enough structural variation (*i.e.*, occurrence of various amino acids), and they could easily be purchased for experimental validation.

The computational work was performed in three steps. The first two steps are based on reactive MD simulations, using the DFTB method, while the third step makes use of non-reactive MD simulations. In the first step, we studied the oxidation of both peptides by OH radicals within a timescale of 10 ps. In most cases, this resulted in H-abstraction, but in rare occasions also a direct OH addition reaction was observed. The amino acids that were mainly targeted within both peptides correspond well with experimental data from literature, and the reasons for the

higher reactivity for some amino acids were provided. Indeed, some amino acids were more likely to be oxidized than expected from literature. This can be attributed to the variations in contact surface with the solution and to the chemical environment in which the targeted amino acids are found, indicating the importance of the 3D structure and conformation of the peptide for oxidation, as also reported in literature<sup>22</sup>. This can also explain the high oxidation degree on Pro, found in peptide A, compared to the Pro found in peptide B, or between the two Phe found in peptide B. Moreover, it was observed that peptide B showed a higher number of reactions with the introduced OH radicals compared to peptide A. This observation was confirmed by mass spectra obtained for the native peptides and plasma-treated peptides.

In the second step, the further oxidation upon impact of O<sub>2</sub> and OH on some selected amino acid radicals within each peptide, formed in the first step, was investigated. This step was performed to ensure further oxidation processes to occur on the amino acids of interest, without the need to perform a large number of simulations on every possible oxidized peptide (as the chances are low that the ROS will react with the same amino acid again within the simulated timescale). During the simulations of step two, we observed a rise in carbonyl and hydroxyl groups on the side chains of the amino acids, leading to an increase in the oxygen-content of the peptide. Again, the results were in good agreement with experimental data from literature.

In the final step, we implemented a number of the final oxidation products of the selected amino acids, as obtained from the previous step, in both peptides. After the implementation of the final oxidation products, we investigated the effect of these products on the structural properties of the peptides in aqueous solution over a timescale of 1  $\mu$ s. The PCA results did not show any clear effects on the phase space occupied by the oxidized peptides, compared to their native counterparts. This was supported by IM-MS data for both peptides, recorded by Dr. D. Dewaele *et al.* Comparing the IM-MS spectra of the oxidized peptides with their native counterparts, we observed no clear difference in drift time, suggesting that oxidation has no noticeable effect on the global 3D structure of the peptide, in agreement with the performed PCA analysis. The oxidation of Tyr in peptide A, however, proved to be an

exception, as we encountered a significant decrease in flexibility, but this effect was again reversed when a second oxidation product was introduced in the peptide. Nevertheless, from the average position of the atoms within the structures, we can conclude that the oxidation of even a single amino acid can affect the average 3D conformation, without changing the size of the peptide. In our simulations, this mostly resulted in a higher affinity within the peptide. This can explain the observed protein aggregation when multiple amino acids of different proteins are oxidized, or loss of their native conformation.

## 5-4.2 Cysteine and glutathione

A combined study has been performed using MD simulations (DFTB) with experimental work (FTIR/Raman and MS spectroscopy). In the computational part of this investigation, the interactions between cysteine (on one hand) or GSH/GSSG (on the other hand) and various RONS in water were elucidated. The investigated RONS were OH, O<sub>3</sub>, H<sub>2</sub>O<sub>2</sub> and NO in the presence of O<sub>2</sub>.

Both the experimental and computational results indicated that the thiol moiety is attacked dominantly in both sulfur-containing molecules. Here, the H of the thiol was abstracted after which other species were found to react with the resulting sulfur radical. In both cases (*i.e.*, cysteine and GSH/GSSG) this resulted in the formation of sulfonic acid (-SO<sub>3</sub>H) and S-nitroso groups (-SNO) as end products, while sulfinic acid (-SO<sub>2</sub>H) and the dimers (connected through disulfide bonds forming cystine or GSSG for cysteine and GSH, respectively) were found to be intermediate reaction products. This is of particular interest for glutathione. Indeed, the antioxidative mechanism of GSH results in the conversion of GSH to GSSG. This system is recycled by, among others, glutathione reductase, which converts GSSG back into two GSH which are again able to consume oxidizing species. This leads to an effective detoxification of reactive species in biological tissues. However, our results indicate that plasma treatment can irreversibly modify both GSH and GSSG to form glutathione sulfonic acid (GSO<sub>3</sub>H) and S-nitroso glutathione (GSNO). This therefore, reduces the antioxidative activity of GSH/GSSG in the treated tissues and solutions in a time dependent manner, and can serve as an anti-cancer approach. Indeed, as stated in *section 1-2.3d*, cancer cells rely heavily on the action of their antioxidative systems. GSH/GSSG plays an important role in protecting cancer cells

from oxidative stress, caused by their own RONS. Therefore, reducing the GSH/GSSG levels increases oxidative damages in the treated cancer cells which induces pro-apoptotic signals.

In addition, the effect of the working conditions on the chemical modifications of both cysteine and glutathione has been evaluated in the experimental part of this investigation. It was observed that changing the plasma conditions (different plasma sources and gas admixtures), as well as different liquids (water vs buffered solutions) have a significant impact on the reaction products after treatment. Even though similar reaction products are observed when changing these treatment conditions, the relative concentration of the observed reaction products changes significantly.

### 5-4.3 Concluding remarks

From our results, it is clear that the oxidation of peptides and amino acids is greatly dependent on their chemical environment. From the investigation of the two small peptides angiotensin and bradykinin, on one hand, we observed that even a single oxidation is able to induce changes in the 3D conformation of the peptide. We expect that this will influence the structural properties of the affected protein as a whole, leading to changes in their enzymatic activities, possible accumulation of proteins, as well as the loss of the 3D conformation.

On the other hand, it became clear from the work on cysteine and glutathione that the working conditions during treatment can also greatly affect the expected results, *e.g.*, oxidation products. Using these results, we were able to differentiate between plasma sources, gas admixtures and liquid conditions when a model system is used, *e.g.*, cysteine containing molecules.

Our observations provide additional insight in the expected oxidation mechanisms on proteins and biological tissues and can lead to a better understanding of the interactions between biological targets and plasmas.

## 5-5 References

1. Verlackt, C. C. W. *et al.* Mechanisms of Peptide Oxidation by Hydroxyl Radicals: Insight at the Molecular Scale. *J. Phys. Chem. C* **121**, 5787–5799 (2017).
2. Klinkhammer, C. *et al.* Elucidation of Plasma-induced Chemical Modifications on Glutathione and Glutathione Disulphide. *Sci. Rep.* **7**, 13828 (2017).
3. Lackmann, J.-W. *et al.* Cysteine Modifications: Fingerprinting Modification Patterns to Biologically Characterize Medical Plasmas. *Sci. Rep.* **submitted**, (2018).
4. Topala, I. & Nagatsu, M. Capillary plasma jet: a low volume plasma source for life science applications. *Appl. Phys. Lett.* **106**, 54105 (2015).
5. Lackmann, J.-W. *et al.* Photons and particles emitted from cold atmospheric-pressure plasma inactivate bacteria and biomolecules independently and synergistically. *J. R. Soc. Interface* **10**, 20130591 (2013).
6. Lackmann, J.-W. *et al.* A dielectric barrier discharge terminally inactivates RNase A by oxidizing sulfur-containing amino acids and breaking structural disulfide bonds. *J. Phys. D: Appl. Phys.* **48**, 494003 (2015).
7. Yusupov, M. *et al.* Plasma-Induced Destruction of Bacterial Cell Wall Components: a Reactive Molecular Dynamics Simulation. *J. Phys. Chem. C* **117**, 5993–5998 (2013).
8. Verlackt, C. C. W. *et al.* Atomic-scale insight into the interactions between hydroxyl radicals and DNA in solution using the ReaxFF reactive force field. *New J. Phys.* **17**, 103005 (2015).
9. Yusupov, M. *et al.* Inactivation of the endotoxic biomolecule lipid A by oxygen plasma species: a reactive molecular dynamics study. *Plasma Process. Polym.* **12**, 162–171 (2014).
10. Yusupov, M. *et al.* Reactive Molecular Dynamics Simulations of Oxygen Species in a Liquid Water Layer of Interest for Plasma Medicine. *J. Phys. D: Appl. Phys.* **47**, 25205 (2014).
11. Neta, P., Huie, R. & Ross, A. Rate Constants for Reactions of Peroxyl Radicals in Fluid Solutions. *J. Phys. Chem. Ref. Data* **19**, 413–513 (1990).
12. Stadtman, E. R. Protein oxidation and aging. *Free Radic. Res.* **40**, 1250–1258 (2006).
13. Lula, I. *et al.* Study of angiotensin-(1–7) vasoactive peptide and its  $\beta$ -cyclodextrin inclusion complexes: complete sequence-specific NMR assignments and structural studies. *Peptides* **28**, 2199–2210 (2007).



14. Bonechi, C., Ristori, S., Martini, G., Martini, S. & Rossi, C. Study of bradykinin conformation in the presence of model membrane by nuclear magnetic resonance and molecular modelling. *BBA - Biomembr.* **1788**, 708–716 (2009).
15. de Vleeschouwer, F., Geerlings, P. & de Proft, F. Radical electrophilicities in solvent. *Theor. Chem. Acc.* **131**, 1–13 (2012).
16. Berendsen, H. J. C., Postma, J. P. M., van Gunsteren, W. F., Di Nola, A. & Haak, J. R. Molecular dynamics with coupling to an external bath. *J. Chem. Phys.* **81**, 3684 (1984).
17. Abraham, M. J. *et al.* GROMACS: high performance molecular simulations through multi-level parallelism from laptops to supercomputers. *Softw. X* **1**, 19–25 (2015).
18. Manual, R. GROMACS 5.1.2.
19. Golda, J. *et al.* Concepts and characteristics of the ‘COST Reference Microplasma Jet’. *J. Phys. D. Appl. Phys.* **49**, 84003 (2016).
20. Ellerweg, D., von Keudell, A. & Benedikt, J. Unexpected O and O<sub>3</sub> production in the effluent of He/O<sub>2</sub> microplasma jets emanating into ambient air. *Plasma Sources Sci. Technol.* **21**, 34019 (2012).
21. Takai, E. *et al.* Chemical modification of amino acids by atmospheric-pressure cold plasma in aqueous solution. *J. Phys. D. Appl. Phys.* **47**, 285403 (2014).
22. Espino, J. A. & Jones, L. M. In Cell Footprinting Coupled with Mass Spectrometry for the Structural Analysis of Proteins in Live Cells. *Anal. Chem.* **87**, 7971–7978 (2015).
23. Lins, L., Thomas, A. & Brasseur, R. Analysis of accessible surface of residues in proteins. *Protein Sci.* **12**, 1406–1417 (2003).
24. Berlett, B. S. Protein Oxidation in Aging, Disease, and Oxidative Stress. *J. Biol. Chem.* **272**, 20313–20316 (1997).
25. Fletcher, G. L. & Okada, S. Radiation-Induced Formation of Dihydroxyphenylalanine from Tyrosine and Tyrosine-Containing Peptides in Aqueous Solution. *Radiat. Res.* **15**, 349–354 (1961).
26. Maskos, Z., Rush, J. & Koppenol, W. The hydroxylation of phenylalanine and tyrosine: a comparison with salicylate and tryptophan. *Arch. Biochem. Biophys.* **2**, 521–529 (1992).
27. Roeser, J., Bischoff, R. & Bruins, A. P. Oxidative protein labeling in mass-spectrometry-based proteomics. *Anal. Bioanal. Chem.* **397**, 3441–3455 (2010).

28. Hawkins, C. L. & Davies, M. J. Generation and propagation of radical reactions on proteins. *Biochim. Biophys. Acta - Bioenerg.* **1504**, 196–219 (2001).
29. Uchida, K. Histidine and lysine as targets of oxidative modification Review Article. *Amino Acids* **25**, 249–257 (2003).
30. Kato, Y., Uchida, K. & Kawakishis, S. Oxidative Fragmentation of Collagen and Prolyl Peptide by Cu(II)/H<sub>2</sub>O<sub>2</sub>. *J. Biol. Chem.* **267**, 23646–23651 (1992).
31. Khosravian, N., Kamaraj, B., Neyts, E. C. & Bogaerts, A. Structural modification of P-glycoprotein induced by OH radicals: Insights from atomistic simulations. *Sci. Rep.* **6**, 19466 (2016).
32. Lermyte, F., Martin, E. M., Konijnenberg, A., Lemi re, F. & Sobott, F. Analyzing Biomolecular Interactions by Mass Spectrometry, 81-108 (Wiley-VCH Verlag GmbH & Co. KGaA, 2015)
33. Konijnenberg, A., Butterer, A. & Sobott, F. Native ion mobility-mass spectrometry and related methods in structural biology. *Biochim. Biophys. Acta - Proteins Proteomics* **1834**, 1239–1256 (2013).
34. T rnvall, U. Analytical Methods methods. *Anal. Methods* **2**, 1638 (2010).
35. Kopito, R. R. inclusion bodies and protein aggregation. *Cell Biol.* **10**, 524–530 (2000).
36. Kogelheide, F. *et al.* FTIR spectroscopy of cysteine as a ready-to-use model for plasma-induced chemical modifications. *J. Phys. D: Appl. Phys.* **49**, 4–5 (2015).
37. Bekeschus, S., Schmidt, A. & von Woedtke, T. The Plasma Jet kINPen – a Powerful Tool for Wound Healing Sander. *Clin. Plasma Med.* **4**, 19–28 (2016).
38. Bundscherer, L. *et al.* Impact of non-thermal plasma treatment on MAPK signaling pathways of human immune cell lines. *Immunobiology* **218**, 1248–55 (2013).
39. Fluhr, J. W. *et al.* In vivo skin treatment with tissue-tolerable plasma influences skin physiology and antioxidant profile in human stratum corneum. *Exp. Dermatol.* **21**, 130–4 (2012).
40. Kramer, A. *et al.* Suitability of tissue tolerable plasmas (TTP) for the management of chronic wounds. *Clin. Plasma Med.* **1**, 11–18 (2013).
41. Wende, K. *et al.* Risk assessment of a cold argon plasma jet in respect to its mutagenicity. *Mutat. Res.* **798–799**, 48–54 (2016).

42. Schmidt-Bleker, A., Winter, J., Bösel, A., Reuter, S. & Weltmann, K.-D. On the Plasma Chemistry of a Cold Atmospheric Argon Plasma Jet with Shielding Gas Device. *Plasma Sources Sci. Technol.* **25**, 15005 (2016).
43. Metelmann, H.-R. *et al.* Head and Neck Cancer Treatment and Physical Plasma. *Clin. Plasma Med.* **3**, 17–23 (2015).
44. Metelmann, H.-R. *et al.* Scar Formation of Laser Skin Lesions after Cold Atmospheric Pressure Plasma (CAP) Treatment: a Clinical Long Term Observation. *Clin. Plasma Med.* **1**, 30–35 (2013).
45. Lademann, J. *et al.* Risk assessment of the application of tissue-tolerable plasma on human skin. *Clin. Plasma Med.* **1**, 5–10 (2013).
46. Penn, R. E., Bleck, E. & Revelle, L. K. Methanesulfenic Acid. *J. Am. Chem. Soc.* **100**, 3622–3623 (1978).
47. Ke, Z., Yu, Z. & Huang, Q. Assessment of Damage of Glutathione by Glow Discharge Plasma at the Gas-Solution Interface through Raman Spectroscopy. *Plasma Process. Polym.* **10**, 181–188 (2013).
48. Forman, H. J., Zhang, H. & Rinna, A. Molecular Aspects of Medicine Glutathione: Overview of its protective roles, measurement, and biosynthesis. *Mol. Aspects Med.* **30**, 1–12 (2009).
49. Murray, C. I. & Van Eyk, J. E. Proteomic Tools for Characterizing Cysteine Redox Status. *Circ. Cardiovasc. Genet.* **5**, 591 (2012).
50. Ishaq, M. *et al.* Atmospheric gas plasma-induced ROS production activates TNF-ASK1 pathway for the induction of melanoma cancer cell apoptosis. *Mol. Biol. Cell* **25**, 1523–1531 (2014).
51. Zhao, S. *et al.* Atmospheric Pressure Room Temperature Plasma Jets Facilitate Oxidative and Nitrative Stress and Lead to Endoplasmic Reticulum Stress Dependent Apoptosis in HepG2 Cells. *PLoS One* **8**, e73665 (2013).

## 6 Molecular Dynamics Simulations: Water

The majority of this chapter has been published in Verlack, C. C. W., Neyts, E. C. & Bogaerts, A. *J. Phys. D. Appl. Phys.* **50**, 11LT01 (2017)<sup>1</sup>.



## 6-1 Introduction

The interaction of cold atmospheric pressure plasmas (CAPs) with liquid surfaces has been gaining increasing interest over the past decades for various applications, like water treatment and material synthesis, as well as in *plasma medicine*<sup>2-4</sup>. In recent years, many studies have been conducted to gain insight in the plasma-liquid interaction (see, *e.g.*, <sup>5-10</sup>). Recently, an extensive overview has been presented on plasma-liquid interactions stating the upcoming challenges as well as the unresolved questions<sup>11</sup>. Obviously, more fundamental studies are required, based on both experiments and computer simulations. Computational research, both on the macroscopic scale and the atomic scale, can be very useful to gain better insight in the underlying mechanisms<sup>12-15</sup>. Macroscopic investigations, such as fluid dynamics and chemical kinetics modeling<sup>13-15</sup>, provide a global representation of the experimental mechanisms, which allows easy comparison with experiments, but they require detailed information like reaction rate coefficients as input for the model. This detailed information can be provided by atomic scale simulations, such as molecular dynamics (MD).

Such MD simulations have been performed by Yusupov and coworkers, investigating the behavior of various reactive oxygen species (ROS) in water<sup>12</sup>. It was observed that hydroxyl radicals (OH) and hydrogen peroxide molecules (H<sub>2</sub>O<sub>2</sub>) are able to penetrate the gas-liquid interface, quickly entering the liquid, and that O atoms and OH radicals penetrate the liquid interface through H-abstraction reactions, resulting in the formation of new OH radicals in the bulk liquid. A classical force field was used in the MD simulations to describe the time-dependent behavior of the ROS. Although such simulations describe the investigated system in a reactive and dynamic manner, the force field parametrization defines the accuracy of the results. Recent experimental work<sup>5</sup> showed that transport of O atoms into the liquid is an effective process, leading to an increasing concentration of O in water, which was not observed in the discussed simulations. This led us to believe that the classical force field might not be accurate enough to describe the interactions of the O atoms with water, and that more accurate methods, based on quantum mechanics, might be needed. The latter are, however, computationally more intensive, limiting the time and length scales of the systems to be simulated. It was demonstrated that the

density-functional based tight-binding (DFTB) method is more suitable to describe the behavior of oxygen-based radicals than a classical force field, as the electron distribution of each individual atom is taken into account so that radicals can be characterized (*i.e.*, defining unpaired electrons)<sup>16</sup>. Indeed, using this technique, we were able to successfully describe the interactions between OH radicals and the TM6 part of the membrane protein P-glycoprotein<sup>17</sup>. Furthermore, in **chapter 5**, we were able to investigate the oxidation of cysteine and cysteine-holding molecules using DFTB. This was in excellent agreement with experimental observations.

Therefore, in this work, we apply the DFTB method to examine the interaction of oxygen-based radicals, *i.e.*, OH and O, with water molecules. Here, we use third order DFTB (*i.e.*, DFTB3 complemented with the 3ob-2-1 parameter set), which employs the third series expansion of the mentioned energy equation, resulting in a self-consistent computational method. DFTB3 is able to accurately describe hydrogen binding energies, proton affinities and proton transfers, for systems up to  $10^3$  atoms<sup>16,19</sup>. Thus, it should provide a more realistic description of the interaction of oxygen-based radicals with water than classical force fields, such as ReaxFF (*cf.* **chapters 3 and 4**).

## 6-2 Results and discussion

Figure 6-1 shows a snapshot of the molecular system investigated. A simulation box with dimensions of  $15 \times 15 \times 15 \text{ \AA}^3$ , containing water molecules, ensuring a density of 1 mg/ml around the introduced radicals, was equilibrated at room temperature in the canonical ensemble, employing the Nosé-Hoover thermostat<sup>20</sup>. Subsequently, one or two  $\text{H}_2\text{O}$  molecules were replaced with either OH radicals or O atoms, and the interactions were simulated for 10 ps, using a time step of 0.25 fs. It should be noted that small dimensions are used in this investigation, resulting in relatively high concentrations. However, the aim of our work was to study the interactions between the radicals, dissolved in water, at the moment they take place. Here, the assumption was made that two radicals in experimental conditions will eventually meet each other and interact. Minimal effects of the simulation box on the results are expected as the introduced radicals are embedded in several shells of water molecules, greatly reducing the influence of long range interactions. In DFTB3 the number of unpaired electrons must be specified as an

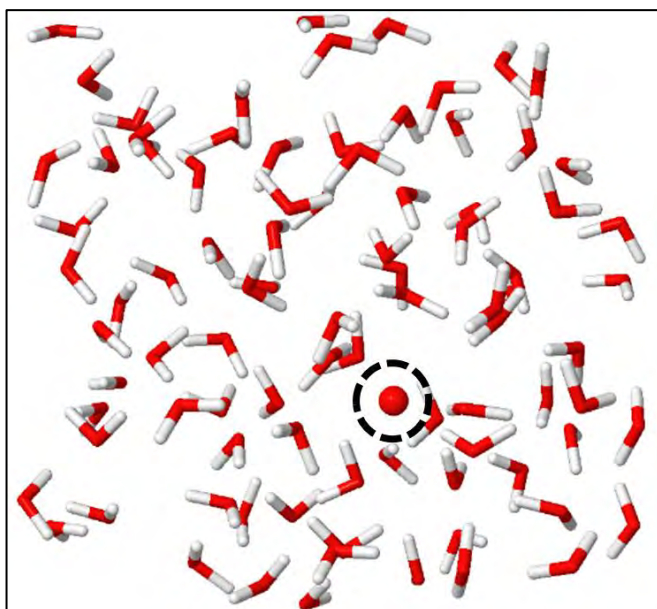


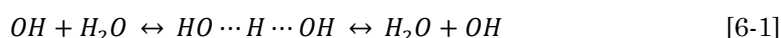
**Figure 6-1. Illustration of the investigated molecular system: a box of  $\text{H}_2\text{O}$  molecules, where one  $\text{H}_2\text{O}$  molecule is replaced by an O atom (black circle). H and O atoms are depicted in white and red, respectively.**



input parameter, which remains constant throughout the whole simulation, *i.e.*, 1 for each OH radical in the system, 0 for singlet O and 2 for triplet O.

## 6-2.1 OH radicals in water

Introducing a single OH radical in the water system resulted in a stable solution, as also previously reported by Yusupov *et al.*<sup>12</sup>. A significant affinity between the OH radical and H atoms of the surrounding water molecules was observed, yielding H-transfer, according to the following equilibrium reaction:



This observation suggests that the transport of OH radicals through the water is not only governed by diffusion, but also through reactions with water molecules, as also reported by Yusupov *et al.*<sup>12</sup>.

However, in the case of two OH radicals in the water system, the situation is more complex. Two different events were encountered during ten identical simulation runs: (i) a H-abstraction between the two radicals, resulting in a single O atom and a water molecule (*cf.* Figure 6-2), or (ii) a side-to-side complex of the two radicals (*cf.* Figure 6-3). Both events were encountered five and two times, respectively. Interestingly, the formation of this side-to-side complex (case (ii)) reduced the interactions with the surrounding water molecules. In other words, no H-transfer, as described above, was observed after the formation of this complex. This is most likely caused by the O $\cdots$ O interaction which decreases the attractive forces towards the H-atoms of the surrounding water molecules. This is further supported by the fact that the observed complex remains intact over the remaining course of the simulation. The reason for the difference in number of observations between the two interactions can be attributed to two phenomena. First, the H-abstraction often occurred during an interaction of the second OH radical with water (as mentioned above). Second, the formation of the side-by-side complex requires a certain orientation of interaction between the two OH radicals and this lowers the probability for the formation of this complex compared to the H-abstraction reaction. However, no statistical conclusion can be drawn given the limited number of interactions simulated.

Both observations are different from the previous classical MD simulations of Yusupov *et al.*, where only one OH radical at a time was simulated, and only the first event was observed (*cf.* reaction 6-1). The current results (*cf.* Figure 6-2 and Figure 6-3) are, however, in line with *ab initio* calculations performed by Codorniu-Hernández *et al.* in 2014<sup>21</sup>, reporting both the production of O atoms, when two OH radicals are found in a head-to-tail formation (Figure 6-2), and the formation of a metastable side-to-side complex, like our observations in Figure 6-3.

Interesting is the fact that the formation of  $\text{H}_2\text{O}_2$  has not been observed during the simulations, as it is prevented by the presence of an energy barrier<sup>21</sup>. As such, longer time scales, beyond the reach of DFTB (which is situated in the picosecond

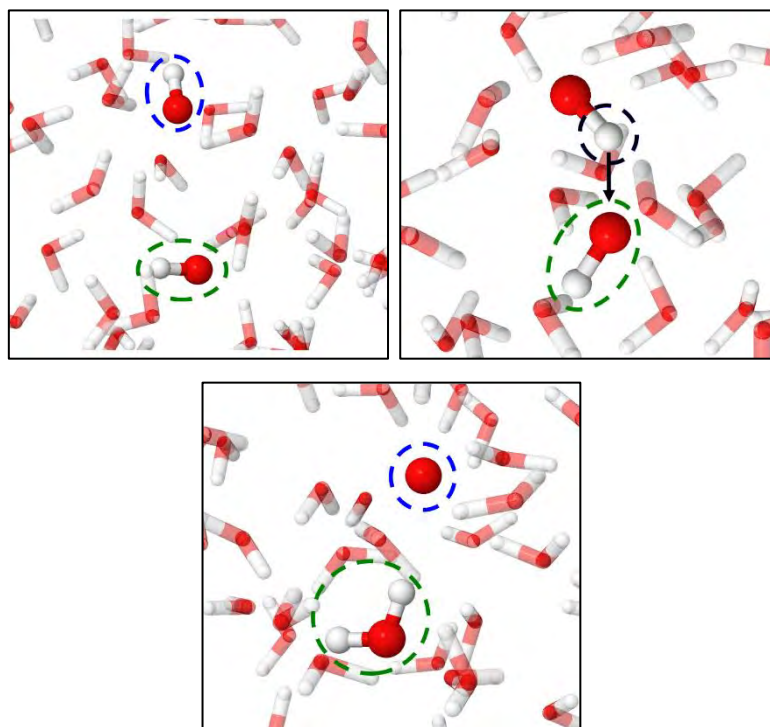


**Figure 6-2.** Snapshots of three consecutive iterations of the DFTB simulations, displaying the H-abstraction between the two introduced OH radicals (indicated by a green and blue dashed circle) (left figure). After the formation of a head-to-tail interaction between the two OH radicals (right figure), a H-abstraction occurs (indicated by the black arrow), resulting in the formation of atomic O and a water molecule (green), stable in the aqueous solution (bottom figure). The chemical species of interest are depicted with solid spheres, while the surrounding water molecules are depicted as semitransparent sticks. O and H are shown in red and white, respectively.

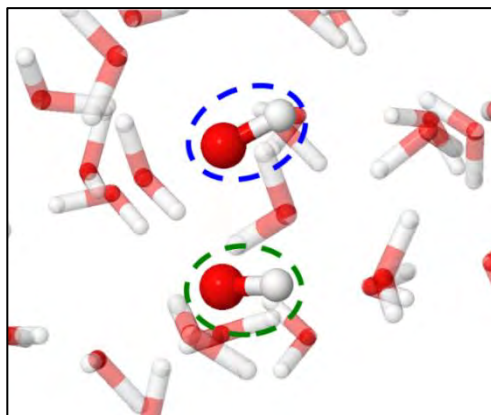


**Figure 6-3. Snapshot of the side-to-side interaction of two OH radicals (indicated using a dashed green and blue circle).** The chemical species of interest are depicted with solid spheres, while the surrounding water molecules are depicted as semitransparent sticks. O and H are shown in red and white, respectively.

range), are required for these reactions to take place. Furthermore, DFTB is unable to accurately describe this energy barrier. However, this has been estimated using *ab initio* calculations performed by Codorniu-Hernández *et al.*<sup>21</sup>.

## 6-2.2 O atoms in water

Because our calculations predict that the OH radicals give rise to O atom formation inside the water, we also investigated the behavior of O atoms in bulk water, for both singlet O (*i.e.*, no unpaired electrons defined for the calculations), and triplet O (*i.e.*, two unpaired electrons defined for the calculations). The results for both systems are depicted in Figure 6-4. In the case of singlet O (*cf.* Figure 6-4 left), the formation of oxywater ( $\text{O}\cdots\text{OH}_2$  complex) was observed in all simulations, even within the first iterations, and the observed complex remained stable in the solution throughout the rest of the simulation. Despite the fact that oxywater is the metastable isomer of hydrogen peroxide (with a free energy of formation of the latter of about -29 kcal/mol<sup>21</sup>), the formation of  $\text{H}_2\text{O}_2$  is not observed during the simulated time scale, suggesting that this transition should have a (small) energy barrier, as also reported in literature<sup>21</sup>.

However, in the case of triplet oxygen, no reaction was observed within the simulated time scale, indicating the stability of this species inside bulk water (*cf.* Figure 6-4 right). This correlates well with the formation of a stable triplet O atom

after the head-to-tail interaction of two OH radicals, as depicted in Figure 6-2. The stability of triplet O in the liquid is supported by the experimental work of Hefny *et al.*<sup>5</sup>, who observed both the oxidation of phenol and the formation of O<sub>2</sub> when O atoms were introduced in the plasma system, and more interestingly, no increase in H<sub>2</sub>O<sub>2</sub> was observed, indicating the absence of OH radicals in the treated solution. These observations thus clearly support the stability of triplet O atoms in water, as predicted by our DFTB simulations. Moreover, as no increase in H<sub>2</sub>O<sub>2</sub> is observed experimentally, we expect that triplet O occurs more than singlet O (as oxywater) in solution, as also suggested by Codorniu-Hernández *et al.*<sup>21</sup>.

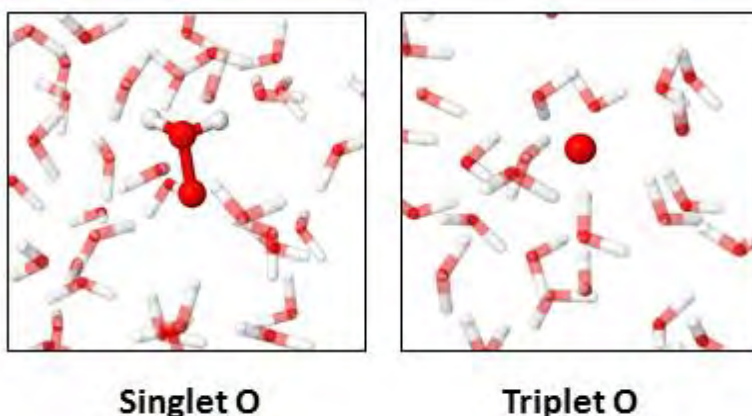


**Figure 6-4. Snapshot of the interactions between an O atom and surrounding water molecules, for singlet O (left) and triplet O (right).** When singlet O is introduced, the formation of oxywater is observed, while triplet O remains stable in solution. The chemical species of interest are depicted using solid spheres, while the surrounding water molecules are depicted as semitransparent sticks. O and H atoms are shown in red and white, respectively.



## 6-3 Conclusion

We used DFTB MD simulations to investigate the behavior of OH radicals and O atoms in bulk water. Our results indicate that the transport of OH radicals in bulk water is not only governed by diffusion, but also through an equilibrium reaction of H-abstraction with water molecules, in line with the work of Yusupov *et al.*<sup>12</sup>. However, when an OH radical encounters another OH radical, some distinct reactions are observed. When both radicals interact through a head-to-tail interaction, a H-abstraction occurs, resulting in the formation of a new water molecule and a triplet O atom, which remains stable in the aqueous solution. However, when both OH radicals form a side-to-side configuration, a cluster, stable in solution, is observed. These observations are supported by *ab initio* calculations<sup>21</sup>. Finally, when investigating the behavior of both singlet and triplet O atoms in bulk water, our calculations reveal that singlet O interacts with water to create oxywater within the first few interactions of the MD simulations, which is expected to form H<sub>2</sub>O<sub>2</sub>, while triplet O remains stable throughout the simulated time scale of 10 picoseconds. The latter is in line with the experimental work of Hefny *et al.*<sup>5</sup>. This observation highlights the importance of atomic O in the chemistry of plasmas in contact with liquids. Indeed, given the high reactivity of atomic O with RONS and biomolecules, we expect that this species will play a crucial role in the processes found in the upper layers of the treated solution and cannot be neglected when investigating the further mechanisms of RONS in water and with biomolecules.



## 6-4 References

1. Verlack, C. C. W., Neyts, E. C. & Bogaerts, A. Atomic scale behavior of oxygen-based radicals in water. *J. Phys. D. Appl. Phys.* **50**, 11LT01 (2017).
2. Foster, J., Sommers, B. S., Gucker, S. N., Blankson, I. M. & Adamovsky, G. Perspectives on the Interaction of Plasmas With Liquid Water for Water Purification. *IEEE Trans. PLASMA Sci.* **40**, 1311–1323 (2012).
3. Kong, M. G. *et al.* Plasma medicine: an introductory review. *New J. Phys.* **11**, 115012 (2009).
4. Mariotti, D., Patel, J. & Vladimir, S. Plasma-Liquid Interactions at Atmospheric Pressure for Nanomaterials Synthesis and Surface Engineering. *Plasma Process. Polym.* **9**, 1074–1085 (2012).
5. Hefny, M. M., Pattyn, C., Lukes, P. & Benedikt, J. Atmospheric Plasma Generates Oxygen Atoms as Oxidizing Species in Aqueous Solutions. *J. Phys. D. Appl. Phys.* **49**, 404002 (2016).
6. Shimizu, T., Iwafuchi, Y., Morfill, G. E. & Sato, T. Formation of thermal flow fields and chemical transport in air and water by atmospheric plasma. *New J. Phys.* **13**, 53025 (2011).
7. Locke, B. R., Sato, M., Sunka, P., Hoffmann, M. R. & Chang, J.-S. Electrohydraulic Discharge and Nonthermal Plasma for Water Treatment. *Ind. Eng. Chem. Res.* **45**, 882–905 (2006).
8. Lukes, P., Dolezalova, E., Sisrova, I. & Clupek, M. Aqueous-Phase Chemistry and Bactericidal Effects from Gaseous Plasmas in Contact with Water. *Plasma Sources Sci. Technol.* **23**, 15019 (2014).
9. Van Rens, J. F. M. *et al.* Induced Liquid Phase Flow by RF Ar Cold Atmospheric Pressure Plasma Jet. *IEEE Trans. PLASMA Sci.* **42**, 2622–2623 (2014).
10. Bruggeman, P. & Leys, C. Non-thermal plasmas in and in contact with liquids. *J. Phys. D. Appl. Phys.* **42**, 1–28 (2009).
11. Bruggeman, P. J. *et al.* Plasma-liquid interactions: a review and roadmap. *Plasma Sources Sci. Technol.* **25**, 53002 (2016).
12. Yusupov, M. *et al.* Reactive Molecular Dynamics Simulations of Oxygen Species in a Liquid Water Layer of Interest for Plasma Medicine. *J. Phys. D. Appl. Phys.* **47**, 25205 (2014).



13. Lindsay, A., Anderson, C., Slikboer, E., Shannon, S. & Graves, D. Momentum, heat, and neutral mass transport in convective atmospheric pressure plasma-liquid systems and implications for aqueous targets. *J. Phys. D. Appl. Phys.* **48**, 424007 (2015).
14. Tian, W. & Kushner, M. J. Atmospheric pressure dielectric barrier discharges interacting with liquid covered tissue. *J. Phys. D. Appl. Phys.* **47**, 165201 (2014).
15. Chen, C. *et al.* A Model of Plasma-Biofilm and Plasma-Tissue Interactions at Ambient Pressure. *Plasma Chem. Plasma Process.* **34**, 403–441 (2014).
16. Gaus, M., Cui, Q. & Elstner, M. DFTB3: Extension of the Self-Consistent-Charge Density-Functional Tight-Binding Method (SCC-DFTB). *J. Chem. Theory Comput.* **7**, 931–948 (2011).
17. Khosravian, N., Kamaraj, B., Neyts, E. C. & Bogaerts, A. Structural modification of P-glycoprotein induced by OH radicals: Insights from atomistic simulations. *Sci. Rep.* **6**, 19466 (2016).
18. Elstner, M. *et al.* Self-consistent-charge density-functional tight-binding method for simulations of complex materials properties. *Phys. Rev. B* **58**, 7260–7268 (1998).
19. Gaus, M., Goez, A. & Elstner, M. Parametrization and benchmark of DFTB3 for organic molecules. *J. Chem. Theory Comput.* **9**, 338–354 (2013).
20. Hoover, W. G. Canonical dynamics: equilibrium phase-space distributions. *Phys. Rev. B* **31**, 1695–1697 (1985).
21. Codorniu-Hernández, E., Hall, K. W., Ziemianowicz, D., Carpendale, S. & Kusalik, P. G. Aqueous production of oxygen atoms from hydroxyl radicals. *Phys. Chem. Chem. Phys.* **16**, 26094 (2014).

## 7 Fluid Dynamics Simulations: Plasma-Liquid Interactions

The majority of this chapter is being published in Verlackt, C. C. W., Van Boxem, W., Bogaerts, A. *Phys. Chem. Chem. Phys.* **in press** (2018)<sup>1</sup>.



## 7-1 Introduction

As already explained in **section 1-2.2**, a multitude of CAP sources, specifically to be used in biomedical applications, have been developed in the past decennia by various research groups worldwide<sup>2-6</sup>. Among these sources are dielectric barrier discharges (DBDs) and so-called floating-electrode DBDs, atmospheric pressure plasma jets (APPJs), including microscale APPJs, and the so-called plasma needle. As a result, a wide variety of setups, parameters and conditions are available for biomedical applications.

Recently, a novel approach for biomedical plasma treatment has been introduced and became subject of increasing investigation<sup>7-9</sup>: the use of Plasma Treated Liquids (PTLs). Using PTLs, biological substrates are treated with a liquid that has been in contact with a plasma source prior to the biomedical application as explained in *section 1-2.2d*. In this way, the plasma-generated species are induced in a liquid. This liquid is then used to transport these (usually more long-lived) plasma-induced chemicals to the biological substrate. This enables a more homogeneous treatment of the tissue and the ability to store the plasma activity<sup>9</sup>. In this way, plasma treatment can be assured even at moments or institutes where no plasma source is available. Furthermore, the substrate only comes in contact with liquid-soluble and long-lived reactive oxygen and nitrogen species (RONS) such as  $\text{H}_2\text{O}_2$ ,  $\text{HNO}_2$  and  $\text{HNO}_3$ , eliminating the effects of the plasma-generated radicals and UV radiation. Finally, PTL can be injected inside the tissue, whereas direct CAP treatment transports RONS in the first few layers only<sup>10,11</sup> due to the often high reactivity and the short half-live of most plasma species<sup>12</sup>. More information can be found in *section 1-2.2d*.

Although the confidence for the applicability and added value of PTLs in plasma medicine is clearly increasing<sup>13-18</sup>, insight in the fundamental mechanisms of the generation of reactive species and in the activity of PTLs is still lagging<sup>19</sup>. While experiments can provide useful information, computational approaches can also be of great value, and are ideally suited to provide answers to the open questions. Babaeva and Kushner<sup>20</sup> computationally investigated the interaction between DBD plasma filaments and dry wounds<sup>20</sup>. This was expanded by introducing a liquid layer in a 0D chemical kinetics model<sup>21</sup> (used to calculate complex chemistry as a function

of time, without taking into account spatial dimensions) to investigate the interaction and penetration of the electric fields on liquid covered wounds. Chen *et al.*<sup>22</sup> used a similar model to evaluate the plasma-liquid chemistry for a He/O<sub>2</sub> DBD using a set of 21 plasma species and 267 reactions, in the framework of treating biofilms and biological tissues<sup>22</sup>. In addition, Suda *et al.*<sup>23</sup> presented a 0D chemical kinetics model for a He/N<sub>2</sub> DBD, investigating the effect of the gap on the surface voltage as well as the accumulation of plasma species in a liquid layer<sup>23</sup>. They used a model containing 10 species and 20 reactions. Another important computational study on the interactions of DBD with a liquid layer was performed by Tian and Kushner<sup>24</sup>. They presented a 2D fluid model for the accumulation of reactive species in the liquid. The obtained knowledge was extended by Lietz and Kushner<sup>25</sup>, who used a chemical kinetics model to gain more detailed insight in the plasma-liquid chemistry when treating liquid covered tissue with a DBD. Finally, Liu and coworkers<sup>26,27</sup> provided interesting insight in the propagation of reactive species in the liquid phase and investigated the effect of the gap on the simulated plasma chemistry<sup>26,27</sup>. For this purpose, they used an extensive model containing 53 RONS and 624 reactions to calculate the chemistry both in the gas and liquid phase.

The above studies all focus on the interaction of DBD plasma with a liquid and were often performed using chemical kinetics models, which do not provide spatial insight. Only a few papers report on modeling the interactions between a plasma jet and a liquid surface. Norberg *et al.*<sup>28</sup> investigated the impact of the operating voltage on the generation and accumulation of reactive species in a liquid layer using a 2D fluid model for a He plasma jet<sup>28</sup>. This study provided insight in the difference between direct (touching) and indirect (non-touching) treatment of a liquid layer using a plasma jet. In 2016, the authors expanded their model with the focus to elucidate the delivery of electric field from an APPJ to liquid-covered tissue and again evaluated the effect of the voltage on the calculated system<sup>29</sup>. Finally, essential understanding in the accumulation of species in the liquid layer was obtained by Lindsay and Graves<sup>30</sup>. They investigated the transport of a limited number of biologically relevant reactive species produced by a He plasma jet to liquid water, using a 2D model containing 13 species and 23 reactions.

In this chapter, we present a 2D axisymmetric fluid dynamics model to

investigate both the accumulation and reactivity of biologically relevant reactive species in a buffered aqueous solution during the treatment with an Ar plasma jet, based on the kINPen design, flowing in (humid) ambient air (78.09% N<sub>2</sub>, 20.95% O<sub>2</sub> and 0.96% H<sub>2</sub>O). This plasma jet is widely used in experiments<sup>31–36</sup>, and even in clinical studies<sup>37–39</sup>, but its interaction with a liquid has not been described in a two-dimensional model system before. We focus especially on the biologically relevant reactive species. In total, 20 gaseous and 22 aqueous species are included, as well as 57 and 42 reactions in the gas and liquid phase, respectively<sup>36,40</sup>. Using an Ar plasma jet with a flow rate of 3 slm, we expect high gas velocities<sup>41</sup>, which will have a tremendous impact on convection, and therefore on the plasma chemistry in both the gas and the liquid. Therefore, we focus especially on these effects, providing information on the accumulation and reactivity of the reactive species in the liquid phase during treatment.



## 7-2 Methodology

### 7-2.1 General processes described in the model

A two-dimensional axisymmetric fluid dynamics model was developed in COMSOL Multiphysics™ version 5.0. This model combines three physical modules: (i) transport of momentum, governed by the time-independent Navier-Stokes equations, (ii) transport of heat, controlled by the principle of conservation of energy, and (iii) transport of mass, which is affected by diffusion and convection.

For the transport of momentum, the Navier-Stokes equations (*cf.* equations 7-1 and 7-2) are used:

$$\rho \nabla \cdot \vec{u} = 0 \quad [7-1]$$

$$\rho(\vec{u} \cdot \nabla \vec{u}) = \nabla \left[ -pI + \mu(\nabla \vec{u} + (\nabla \vec{u})^T) - \frac{2}{3}\mu(\nabla \cdot \vec{u})I \right] \quad [7-2]$$

These two expressions represent the conservation of mass and momentum, respectively.  $\rho$  is the overall mass density,  $\vec{u}$  the fluid velocity,  $\mu$  the dynamic viscosity,  $p$  the static pressure, and  $I$  represents a unity matrix. Both  $\rho$  and  $\mu$  are determined by the properties of the material (*i.e.*, air and water in our case).

The equation for heat transport is based on the principle of conservation of energy (*cf.* equation 7-3):

$$\rho C_p \left( \frac{\delta T}{\delta t} + \vec{u} \cdot \nabla T \right) = \nabla \cdot (k \nabla T) + Q \quad [7-3]$$

$C_p$  is the heat capacity at constant pressure and  $k$  represents the thermal conductivity.  $Q$  stands for additional heat sources introduced to the system, such as the heat of evaporation (see later). The left side of the equation considers the changes in temperature as a function of time and due to convection. The first term on the right side represents the conductive heat flux.

The equation for mass transport used in this model is equation 7-4:

$$\frac{\delta c_i}{\delta t} + \nabla \cdot (-D_i \nabla c_i) + \vec{u} \cdot \nabla c_i = R_i \quad [7-4]$$



$c_i$  and  $D_i$  represent the concentration and diffusion coefficient of each species  $i$ .  $R_i$  is the sum of all production and loss terms in the simulation, as described by chemical reactions. The left side of the equation represents changes in concentration as a function of time and due to diffusion (governed by  $D_i$ ) and convection (*cf.* velocity  $\vec{u}$ ).

Using this model, four major processes are described: (i) transport of species in the gas and liquid phase, by both diffusion and convection, (ii) gas and liquid phase chemistry, (iii) transport of species over the gas-liquid interface and (iv) transport of heat, affecting both the chemistry and the transport of species. Combining all these processes in a fully coupled simulation, able to describe time-scales up to minutes as used in experimental treatments, results in a computationally highly demanding model. For this reason, we do not simulate the active discharge of the plasma itself, and we only consider the afterglow of the plasma. Indeed, when simulating a discharge, very fast processes have to be taken into account (like electron impact reactions), which hinders the calculation of the model for the envisioned time-scales (*i.e.*, minutes). However, in order to obtain reliable results, we use results from 0D plasma chemical kinetics models<sup>36,40</sup>, which describe the plasma discharge for a plasma jet in great detail, as input for our model.

The presence of a plasma discharge or an electric field in the effluent might affect the flux of reactive species in the plasma effluent. However, we expect that this will have no significant impact on the results for three reasons. First, the discharge could in principle result in heating of the gas, influencing the momentum of the gas molecules. This could be coupled back to the inlet flow. Although we only simulate the effluent, we consider the increase in temperature as a result of the plasma discharge, for the calculation of both the gas flow and the gas chemistry (see below). However, this effect turns out to be minor. Second, the plasma species are influenced by the discharge and electric fields, but the majority of the flow consists of neutral gas species, which will not be affected by the plasma. Finally, the electric field could have an impact on the momentum of certain plasma species, which could enhance the flux of species in the effluent. However, this only holds true for devices with a significant electric field in the effluent.

## 7-2.2 Simulated system

The geometry used in this investigation is illustrated in Figure 7-1, and represents the kINPen plasma jet. This plasma source consists of two electrodes, *i.e.*, a central pin electrode, with diameter of 1 mm, surrounded by a grounded electrode with inner diameter of 1.6 mm. The dimensions of the simulated liquid vessel are 7 cm x 3.5 cm, leading to a volume of approximately 135 mL. We assume that the liquid vessel is not filled to the very top during experimental treatment. As such, a wall with a height of 0.5 cm is introduced at the end of the liquid interface, mimicking the

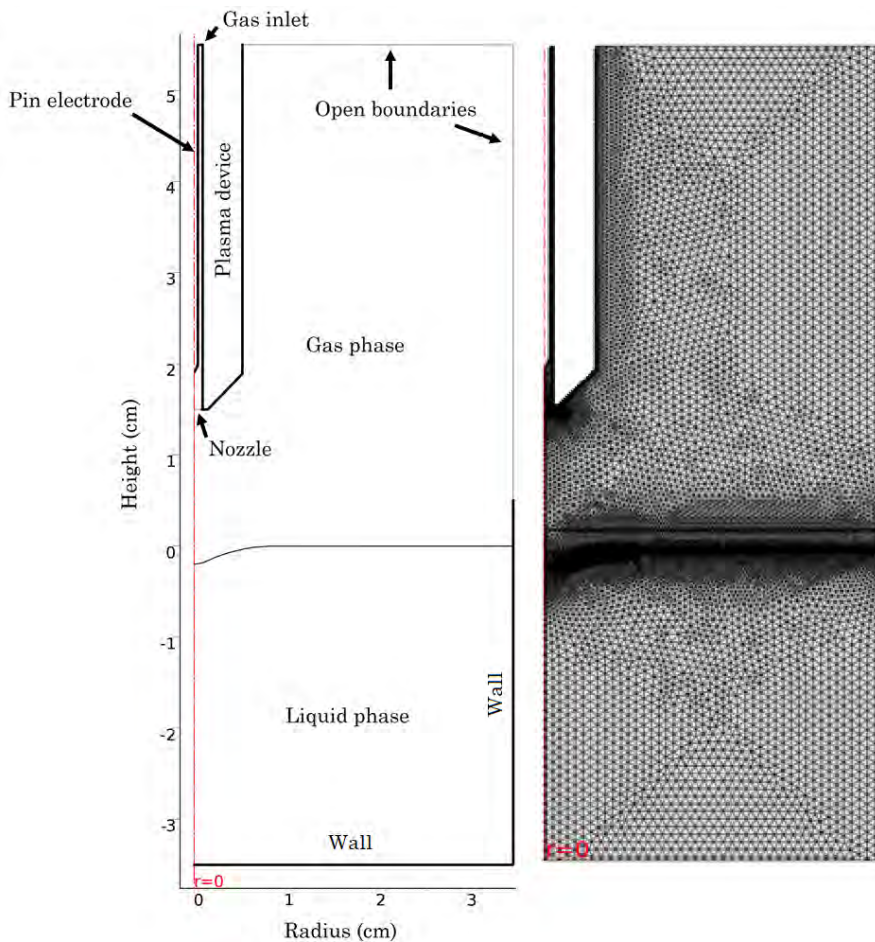


**Figure 7-1. Schematic representation of the geometry used during the fluid calculations and an example of the mesh for such geometry.** The geometry is represented by an axisymmetric 2D model (at  $r=0$ ) going through the center of the plasma jet.

**Table 7-1. Dimensions and working conditions used in the model.**

<b>Inner diameter of plasma jet</b>	1.6 mm
<b>Diameter of pin electrode</b>	1 mm
<b>Dimensions of water vessel</b>	7 cm diameter; 3.5 cm height
<b>Volume liquid</b>	135 mL
<b>Flow rate at inlet of plasma jet device</b>	3 slm
<b>Gap between nozzle of plasma jet device and liquid surface</b>	15 mm

top border of the liquid container. During the simulations, treatment in open air is assumed, which is implemented using open boundaries in the gas phase.

A treatment gap of 15 mm was chosen, because experimental results with the kINPen-IND (*i.e.*, the type of kINPen investigated here) showed an active discharge at the liquid surface for smaller treatment gaps<sup>42</sup>, which significantly affects the liquid chemistry. As the plasma discharge itself is not simulated here, a larger treatment gap (*i.e.*, 15 mm) is used. The general parameters of the geometry are listed in Table 7-1. We consider a 2D axisymmetric model, and the symmetry axis is situated at the center of the plasma jet. As such, the full geometry can be obtained by rotating the 2D image of Figure 7-1 around the red dashed line at  $r = 0$ .

Because of the high velocity of the plasma jet (*i.e.*, maximum velocity of 72.8 m/s at a gas flow rate of 3 slm; see **section 7-3**), a depression in the surface is often observed experimentally<sup>43,44</sup>. The depth and width of this depression are highly dependent on the treatment conditions and the plasma jet used. Due to lack of detailed information, we set the depression in our model to 2 mm deep and 9 mm wide.

We consider a buffered solution at  $\text{pH} = 7.3$ . To achieve this, the concentration of  $\text{H}^+$  and  $\text{OH}^-$  are kept fixed, and are determined by the applied pH value. We assure that charge neutrality of the liquid is preserved, in spite of the fact that more negative ions are present, due to the pH used and the liquid chemistry (*cf.* **section 7-3**). Indeed, we assume that positive counter ions, which are responsible for the preservation of charge balance (*e.g.*,  $\text{K}^+$  or  $\text{Na}^+$ ), do not take part in chemical reactions with the reactive species. Therefore, they are not included in the liquid chemistry in this model.

### **7-2.3 Mesh**

In order to perform the calculations, the geometry is divided in a large number of smaller areal elements, collectively forming a grid –or mesh– on the geometry. In this way, the geometry is represented by a finite number of areal elements on which the calculations, for the properties of the system, are performed. Naturally, increasing the number of mesh elements increases the resolution and smoothness of the calculated results but also leads to a significant increase in calculation time. For the calculations performed in this thesis, a triangular mesh is used. Here, the geometry is divided in a number of triangles with different sizes and shapes, depending on the position. Indeed, using triangles enhances the flexibility of defining larger and smaller elements, leading to coarser (low density of mesh elements) or finer (high density of mesh elements) mesh regions in the geometry. In this way, properties can be calculated with higher spatial resolution, compared to the rest of the geometry, without significantly increasing the calculation time. On one hand, as the plasma chemistry and the transfer of species over the gas/liquid interface is crucial in the investigations, smaller mesh elements are used to describe these areas. On the other hand, as the bulk liquid is expected to contain mainly long-lived plasma species, larger mesh elements are typically used. An example of such a mesh is depicted on the right side of Figure 7-1, containing a total of 20,307 elements.

### **7-2.4 Fluid flow**

We use the time-independent Navier-Stokes equations in our model (*cf.* equations 7-1 and 7-2). These equations are solved until steady-state is reached, after which the steady-state velocity profile is used as input for the time-dependent calculation of the convection-diffusion equations for heat and mass transport. This approach is justified as the feed gas of the plasma device is typically already flowing prior to the discharge. In this model, a flow rate of 3 slm (standard liters per minute) is used. As the hydraulic diameter of the nozzle is 1.6 mm, this yields a gas flow velocity of 72.8 m/s, and thus a Reynolds number of *ca.* 3500 is obtained, resulting in a turbulent gas flow. Therefore, the flow in the gas phase is calculated using the Reynolds-averaged Navier-Stokes equations (RANS) in air at 1 atm. For this purpose, the k- $\epsilon$  turbulence model, as built in COMSOL Multiphysics, is utilized. This is a

widely used and well-established model for the description of a turbulent fluid flow. More details can be found in<sup>45</sup>. The maximum velocity of the liquid in our model, as a result of the shear stress of the gas flowing over the liquid interface, is typically much lower than that of the gas, *i.e.*, 10.4 m/s. Therefore, a laminar behavior is expected and introduced in the water phase.

## 7-2.5 Transport of heat

The initial temperature of both the gas and liquid phase is set to 293 K. However, as a plasma jet is typically characterized by a higher gas temperature, the temperature of the inflowing gas and the walls inside the plasma jet device is set to 327 K, corresponding to the gas temperature reported in<sup>36,46</sup>. Indeed, as the active discharge is not simulated, the temperature corresponding to this discharge is implemented with the inflowing gas. To assure that the gas at the nozzle has a temperature of 327 K, the walls inside the plasma device are kept at this temperature as well. All the other walls in the model are considered to be isolating, except for the gas-liquid interface, where a continuous heat flow is assured.

## 7-2.6 Chemistry and transport of species

The gas phase and liquid phase species considered in our model are listed in Table 7-2. They are known to be either biologically relevant or act as precursors for biologically relevant reactive oxygen and nitrogen species (RONS). Furthermore, they are based on the results obtained from the 0D model of Van Gaens and Bogaerts<sup>40</sup>. In that model, 85 different gas phase species and 1928 different chemical reactions were included, which is not feasible in this 2D fluid model, certainly when describing plasma treatment times of several minutes. Therefore, we include here only the most important RONS and corresponding reactions, as reported in<sup>40</sup>. This results in 20 gas phase species and 22 liquid phase species (see Table 7-2). Both sets of species include molecules (long-lived species) as well as radicals and excited species (short-lived species). As ions do not play a significant role in the chemistry of the plasma effluent, as calculated by the 0D simulations, they are not considered in the gas phase in our model (*cf.* Table 7-2). Furthermore,  $O_2(a) (^1\Delta_g)$  is included as excited species in the gas phase, as it contributes significantly to the production of reactive species in the effluent<sup>40,41</sup>. However, given the limited knowledge on the liquid

chemistry, it could not be included in the liquid phase. Note that only RONS are introduced in the solution. As already stated in *section 1-2.2d*, other species, such as metals, chlorine ions and biomolecules, will also have an impact on the generation and accumulation of reactive species. For instance, transition metal ions are expected to form complexes with the generated radicals, affecting their life-time in solution. Furthermore, chlorine ions are expected to react with reactive oxygen species, forming, *e.g.*, HOCl. However, due to the lack of knowledge on the respective reactions, this chemistry is not included in the model presented in this chapter and will be investigated in an upcoming PhD research.

The gas phase species are introduced via the inlet at the very top of the plasma jet device (*cf.* Figure 7-1), with concentrations that will be specified below. The open boundaries of the model in the gas phase mimic the ambient air (78.09% N<sub>2</sub>, 20.95% O<sub>2</sub> and 0.96% H<sub>2</sub>O) with a pressure of 1 atm. In this way, fresh air is introduced in the model when an inward flow is present, due to differences in pressure and concentration of the ambient air species. The walls of the liquid (*cf.* Figure 7-1) are treated with the non-slip condition, reducing the lateral velocity at the walls to 0 m.s<sup>-1</sup>.

The discharge (and the plasma chemistry) inside the plasma jet device is not considered in this model, because this would lead to excessive calculation times when using the model for actual plasma treatment times of several minutes, as explained in *section 7-2.1*. Therefore, the concentrations of the important species flowing

**Table 7-2. Gas phase and liquid phase species included in the model**

	Gas phase species	Liquid phase species
<b>Molecules and atoms</b>	H <sub>2</sub> , O <sub>2</sub> , O <sub>3</sub> , H <sub>2</sub> O, H <sub>2</sub> O <sub>2</sub> , N <sub>2</sub> , ONOOH, HNO <sub>2</sub> , HNO <sub>3</sub> , N <sub>2</sub> O <sub>5</sub> , Ar	H <sub>2</sub> , O <sub>2</sub> , O <sub>3</sub> , H <sub>2</sub> O, H <sub>2</sub> O <sub>2</sub> , N <sub>2</sub> , ONOOH, HNO <sub>2</sub> , N <sub>2</sub> O <sub>5</sub>
<b>Radicals</b>	O, OH, HO <sub>2</sub> , N, NO, NO <sub>2</sub> , NO <sub>3</sub> , H	O, OH, HO <sub>2</sub> , NO, NO <sub>2</sub> , NO <sub>3</sub> , H
<b>Excited species</b>	O <sub>2</sub> (a) ( <sup>1</sup> Δ <sub>g</sub> )	
<b>Ions</b>		H <sup>+</sup> , O <sub>2</sub> <sup>-</sup> , OH <sup>-</sup> , NO <sub>2</sub> <sup>-</sup> , NO <sub>3</sub> <sup>-</sup> , ONOO <sup>-</sup>

**Table 7-3. Gaseous species number densities in  $\text{cm}^{-3}$  at the inlet of the plasma jet device.** They serve as input data for the calculation of the gas phase and have been adopted from<sup>41</sup> for an Ar kINPen plasma jet. Species that are not included in this table are assumed to have a zero inlet concentration.

Species	Inlet concentration	Species	Inlet concentration
OH	$2 \times 10^{14}$	H	$1 \times 10^{15}$
H <sub>2</sub> O <sub>2</sub>	$1 \times 10^{13}$	N	$6 \times 10^{13}$
HO <sub>2</sub>	$3 \times 10^{13}$	NO	$7 \times 10^{13}$
O	$1 \times 10^{15}$	NO <sub>2</sub>	$1 \times 10^{12}$
O <sub>3</sub>	$7 \times 10^{11}$	HNO <sub>2</sub>	$2 \times 10^{12}$
<sup>1</sup> O <sub>2</sub>	$2 \times 10^{14}$	HNO <sub>3</sub>	$2 \times 10^{10}$
H <sub>2</sub>	$4 \times 10^{11}$		

out of the jet device are required as input in this model. They are adopted from Wende *et al.*<sup>41</sup> for the Ar plasma jet studied in this work (kINPen). However, in practice, the gas phase species are introduced in our model through the inlet of the plasma jet device, as mentioned above. The concentrations of these species are kept constant throughout the device, until they reach the nozzle, where the species interact with the ambient air and start to react with the air molecules. The inlet concentrations of the various species are listed in Table 7-3.

As the liquid phase is kept at a pH of 7.3, HNO<sub>3</sub>, as a strong acid, is deprotonated as soon as it enters the liquid. Hence, it only occurs in our liquid model in its deprotonated form, NO<sub>3</sub><sup>-</sup> (*cf.* Table 7-2). For the weak acids (*i.e.*, HNO<sub>2</sub>, HO<sub>2</sub> and ONOOH), equilibrium processes are introduced based on their pK<sub>a</sub> values (being 3.4, 4.88 and 6.8, respectively), so that the balance between the protonated and deprotonated form is maintained in the liquid, as governed by the pH value.

Besides the 20 gas phase species and 22 liquid phase species, a set of 57 gas phase and 42 liquid phase reactions is considered. The set of reactions in the gas phase is a combination of the most important reactions reported by Van Gaens and Bogaerts, and by Schmidt-Bleker *et al.*<sup>36,40</sup> for an Ar plasma jet flowing in humid air. However, these models were only for the gas phase (active discharge plasma and afterglow). Given the limited data available in literature on liquid reactions and reaction rate coefficients for this system, only a small liquid phase reaction set can be used. We adopted the reaction set as used by<sup>47</sup>, but we extended it using the NIST database for kinetics in solution<sup>48</sup>. A full list of the reactions included in the model

**Table 7-4. Diffusion constants used in the gas phase ( $D_{i,gas}$ ) and liquid phase ( $D_{i,liquid}$ ) and Henry constants ( $H_i$ ) used in the model for the various species  $i$ , as well as the references where these data are adopted from. Species that do not have a value for  $D_{i,gas}$  or  $D_{i,liquid}$  are not considered in the gas or liquid phase, respectively.**

Species	$D_{i,gas}$ $10^{-5} m^2.s^{-1}$	Ref.	$D_{i,liquid}$ $10^{-9} m^2.s^{-1}$	Ref.	$H_i$ $mol.L^{-1}.atm^{-1}$	Ref.
Ar	12.2	52				
O <sub>2</sub>	2.1	52	2.3	30	$1.3 \times 10^{-3}$	53
N <sub>2</sub>	2.1	52	2.6	54	$6.5 \times 10^{-4}$	53
H <sub>2</sub>	12.2	52	1	30	$7.8 \times 10^{-4}$	
H <sub>2</sub> O	2.3	52	2.299	55		
OH	4	52	2.8	30	$3.03 \times 10^1$	53
H <sub>2</sub> O <sub>2</sub>	2	52	1.7	30	$7.9 \times 10^4$	53
HO <sub>2</sub>	2	52	1.7	same as H <sub>2</sub> O <sub>2</sub>	$5.56 \times 10^3$	53
O	3.2	52	2.8	same as OH	$1.3 \times 10^{-3}$	same as O <sub>2</sub>
O <sub>3</sub>	1.5	52	1.76	56	$1.22 \times 10^{-2}$	53
<sup>18</sup> O <sub>2</sub>	2.1	52				
H	12.2	52	1	30	$7.8 \times 10^{-4}$	same as H <sub>2</sub>
N	2.9	52				
NO	2	52	2.2	30	$1.9 \times 10^{-3}$	53
NO <sub>2</sub>	1.7	52	1.85	30	$1.93 \times 10^{-2}$	53
NO <sub>3</sub>	0.9	52	2.5	same as HNO <sub>3</sub>	3.28	53
HNO <sub>2</sub>	2.1	52	2.5	30	$4.9 \times 10^{-1}$	53
HNO <sub>3</sub>	2.1	52	2.5	30	$1.7 \times 10^6$	53
N <sub>2</sub> O <sub>5</sub>	1	52	1	57	2.1	53
ONOOH	1.78	52	2.5	30	$4.8 \times 10^6$	30
H <sup>+</sup>			7	30		
OH <sup>-</sup>			5.29	30		
O <sub>2</sub> <sup>-</sup>			2.3	estimated		
NO <sub>2</sub> <sup>-</sup>			1.7	30		
NO <sub>3</sub> <sup>-</sup>			1.7	30		
ONOO <sup>-</sup>			1.7	same as NO <sub>3</sub> <sup>-</sup>		

for both the gas and liquid phase, along with their reaction rate coefficients, can be found in Table 7-A in the **Appendix-7** at the end of the chapter.

Besides the chemical reactions between the species, the concentration profiles of the various species are also determined by diffusion and convection. Convection is governed by the gas or liquid velocity profile, as calculated by the Navier-Stokes equations (*cf.* reactions 7-1 and 7-2), while diffusion is dependent on the diffusion coefficients of the species in both the gas and liquid phase. These values are listed in Table 7-4.



### 7-2.7 Boundary conditions at the interface

The three modules considered in this model (*i.e.*, transport of momentum, heat and mass; *cf.* **section 7-2.1**) are calculated separately for both the gas and liquid phase. However, they are coupled to each other through the gas-liquid interface in four ways: (i) Although no inlet or initial velocity is defined in the liquid, the liquid flow is coupled with the gas flow through a drag force implemented at the gas-liquid interface. This results in a shear stress in the liquid from the gas flowing over the interface. In practice, this means that a moving wall is introduced in the model for the liquid at the interface, which has the lateral velocity of the gas at the other side of the interface,  $u_g$ . Furthermore, the gas velocity at the interface is reduced compared to the bulk gas flow, due to the presence of the interface, which is, again, treated as a moving wall with a lateral velocity of the liquid,  $u_l$ . In this way, the gas flow and liquid flow are coupled in the model through the interface. (ii) In addition, transport of heat is considered to be continuous over the interface and governed by the properties of the respective phase (*i.e.*, the thermal conductivity, heat capacity and specific heat ratio of both air and water). (iii) Transport of species over the interface is controlled by Henry's law. This means that the concentrations of both the gas phase and liquid phase species are set to be in equilibrium with each other at the interface.

$$c_{i,liquid} = c_{i,gas} * H_i * RT \quad [7-5]$$

Where  $H_i$  is the Henry's constant of species  $i$ ,  $R$  the gas constant and  $T$  the temperature. The Henry's constants used in this model for the various species, as well as the diffusion constants of these species in the gas phase and liquid phase, are listed in Table 7-4. In this model, the assumption is made that only neutral species are able to enter the gas phase from the liquid, while ions will remain in the liquid phase. (iv) Finally, the evaporation of water is implemented at the interface, as well as the heat of evaporation. The evaporation of water is included via the water vapor pressure at the interface in the gas phase as follows<sup>49</sup>:

$$\log_{10} p_{vap} = 8.07131 - \frac{1730.63}{233.426 + T} \quad [7-6]$$

$p_{vap}$  represents the vapor pressure of water and  $T$  the temperature. The constants in the equation are known as Antoine's coefficients, which are material specific, and are the Antoine's coefficients for liquid water<sup>49</sup>. This is coupled to the heat of water evaporation, which can affect the temperature of the liquid. This is included in the following way<sup>50</sup>:

$$Q = J_{z,H_2O} \cdot H_{vap} \quad [7-7]$$

Where  $J_{z,H_2O}$  is the molar flux of H<sub>2</sub>O at the interface as a result of evaporation, and  $H_{vap}$  represents the latent heat of evaporation for water (set to be 2260 kJ/kg<sup>51</sup>).

## 7-3 Results and discussion

### 7-3.1 Flow behavior of gas and liquid phase

As explained in **section 7-2.4**, the first step in the investigation was to simulate both the gas and liquid flow, until steady-state was reached. Subsequently, the gas and liquid flow velocities were introduced as input in the time-dependent model. Figure 7-2 illustrates the steady-state gas and liquid flow behavior, for an inlet gas flow rate of 3 slm Ar in the geometry. The color map in Figure 7-2 illustrates the velocity magnitudes in both gas and liquid phase, while the velocity directions are depicted with arrows. This inlet gas flow rate of 3 slm yields an average gas velocity of 26.1 m/s in the afterglow (*cf.* Figure 7-2). This is in agreement with calculated values reported in literature, for the same plasma jet diameter of 1.6 mm<sup>54,64</sup>. The gas that exits the nozzle was found to reach the interface (height of 0 cm) and subsequently flowed along the interface outwards, inducing shear stress on the liquid. Because of this, the upper liquid layer (thickness of 200 μm) started to flow in the same direction as the gas flow, with maximum velocity of 10.4 m/s. This liquid flow resulted in the formation of a reverse vortex near the border of the liquid vessel. A close-up of this reverse vortex is presented at the right side in Figure 7-2. Furthermore, when reaching the border of the liquid vessel (at radius = 3.5 cm), the velocity in the liquid greatly reduced within the reverse vortex (to a maximum value of 0.54 m/s).

Due to the presence of this reverse vortex, the liquid (at a depth of 200  $\mu\text{m}$  and lower) started flowing back towards the center (radius = 0 cm), in the opposite direction compared to the liquid flow at the interface. When reaching the center of the vessel, the flow was subsequently guided towards the bulk of the liquid (*cf.* Figure 7-2). This resulted in an interesting flow pattern in the liquid, which, at first sight, seems to contradict some experimentally observed flow patterns<sup>43,44</sup>. However, the depth at which the liquid flowed in the opposite direction greatly depended on the velocity of the gas that flows along the interface, and thus on the gas flow rate.

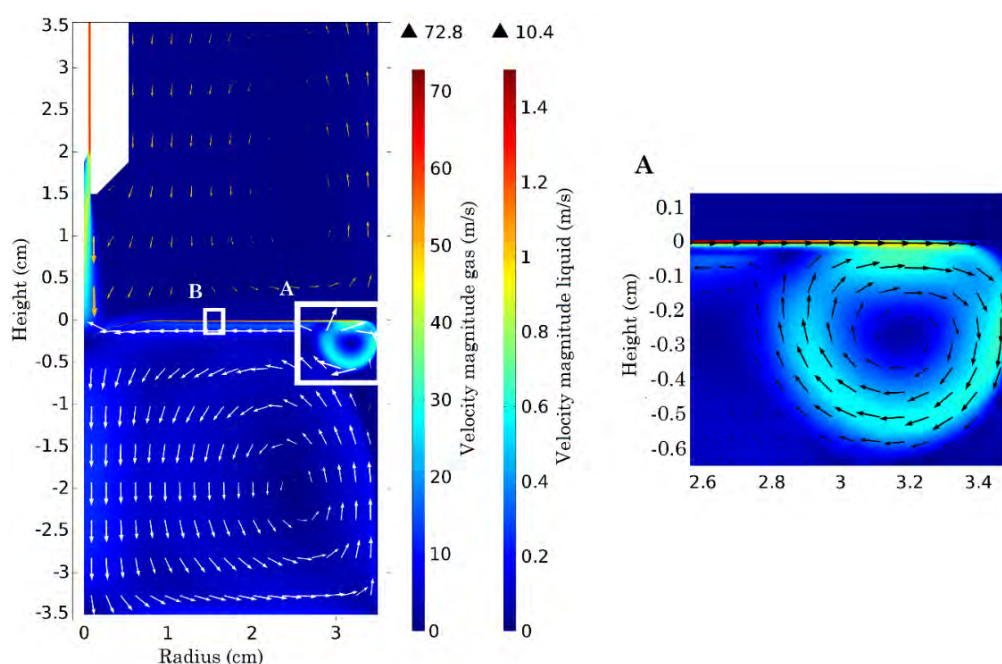


**Figure 7-2. 2D plot of the velocity magnitude (depicted in rainbow color scale) in both gas and liquid phase, at an inlet gas flow rate of 3 slm.** The direction of the flow is indicated by yellow and white arrows for the gas and liquid phase, respectively. The arrows are logarithmically scaled based on the velocity magnitude, for the sake of clarity. The symmetry axis is located at radius = 0 cm. Given the vast difference between the liquid velocity at the interface and bulk, the color scale is shifted to lower values for the sake of clarity. The values above the color scale indicate the highest velocity in both gas and liquid phase (in m/s). A zoom of the 2D plot in the white box indicated with letter 'A' is presented on the right side of the figure. It shows a close-up of the reverse vortex in the liquid, located at the interface, using the same color scale as in the main figure. The arrows indicating the direction of the flow are depicted in black in the right figure. The white box indicated with letter 'B' represents the close-up used in Figure 7-3.

At 3 slm, this opposite flow in the liquid phase occurred at a depth of *ca.* 200  $\mu\text{m}$ , while it was roughly at 300  $\mu\text{m}$  for 2 slm and 400  $\mu\text{m}$  for 1 slm. This is illustrated in Figure 7-3 for these three different flow rates. Note that the color codes of the gas flow and liquid flow are the same in this figure, to indicate that the liquid velocity at the interface is equal to that of the gas flow. The observations reported by Hefny, *et al.*<sup>44</sup> are obtained at helium flow rates of 1.4 slm and a gap of 4 mm, giving rise to significantly lower gas velocities at the liquid interface, and this affects the flow pattern inside the liquid, as is clear from Figure 7-3.

To illustrate this in more detail, we calculated the liquid flow pattern for an inlet Ar flow rate of 0.1 slm, yielding an average gas velocity of 0.7 m/s in the afterglow, and the result is presented in Figure 7-4. For 0.1 slm Ar flow rate, an almost identical liquid flow pattern was observed as presented in the experimental paper of Hefny, *et al.*<sup>44</sup>. Indeed, the reverse flow reached depths of around 1 cm, leading to an opposite flow pattern in the liquid bulk compared to the flow pattern in the case of 1, 2 and 3 slm of Ar (*cf.* Figure 7-2 and Figure 7-3). Thus, it is clear that a higher gas velocity forces the observed reverse vortex towards the interface and to the border of the liquid vessel.

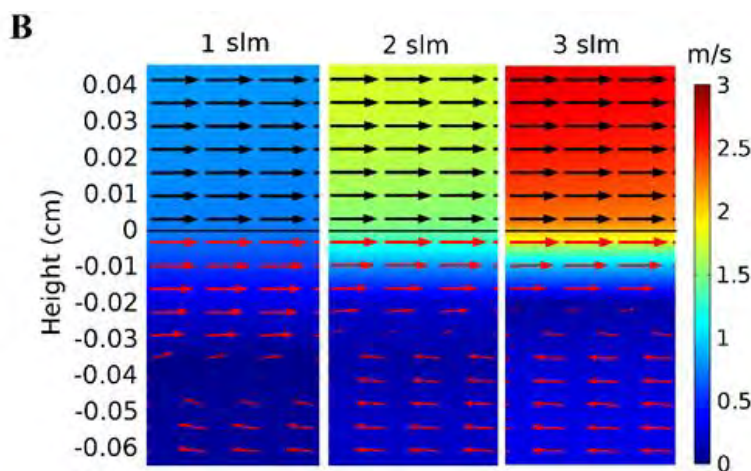


**Figure 7-3.** Close-up of the interface (in the white box indicated by letter ‘B’ in Figure 7-2) at three different inlet gas flow rates, *i.e.*, 1, 2 and 3 slm. The same liquid color code is used for both the gas and liquid phase, to clearly indicate that the maximum liquid velocity is found in the top layers of the liquid, and is equal to the velocity of the gas at the interface. The arrows indicate the direction of the flow in the gas phase (black) and liquid phase (red). The gas-liquid interface (at a height of 0 cm) is indicated by a black line.

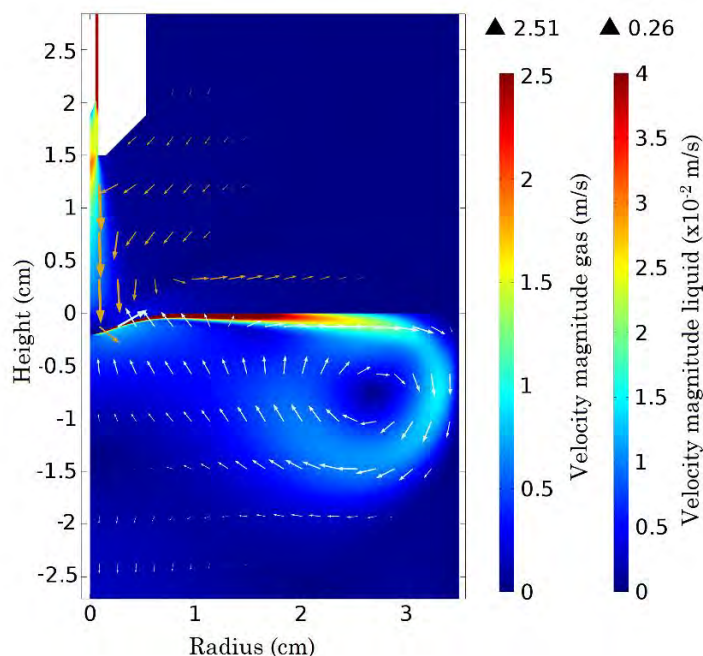


**Figure 7-4.** 2D plot of the velocity magnitude (depicted in rainbow color scale) in both gas and liquid phase, at an inlet gas flow rate of 0.1 slm. The direction of the flow is indicated by yellow and white arrows for the gas and liquid phase, respectively. The arrows are logarithmically scaled based on the velocity magnitude, for the sake of clarity. The symmetry axis is located at radius = 0 cm. The values above the color scale indicate the highest velocity in both gas and liquid phase (in m/s).

### 7-3.2 Temperature profile in gas and liquid phase

Using the steady-state velocity profiles presented above, the transport of heat and mass was calculated as a function of time, yielding the temperature and species concentration profiles. The temperature profiles in both the gas and the liquid, after 1 minute of plasma treatment, are presented in Figure 7-5. As soon as the inlet gas (initially at 327 K) reached the interface, it flowed along the liquid surface outwards, as was illustrated in Figure 7-2. The temperature of the gas quickly decreases once it came in contact with the liquid, reaching the liquid temperature. At the same time, the liquid temperature, which was initially 293 K, slightly decreased as a function of time, to an average of 291 K after 1 minute. Furthermore, the temperature of the liquid and gas at the interface was identical, reaching a minimum value of 289 K at the border of the liquid vessel and the reverse vortex (at radius = 3.5 cm in Figure 7-5).

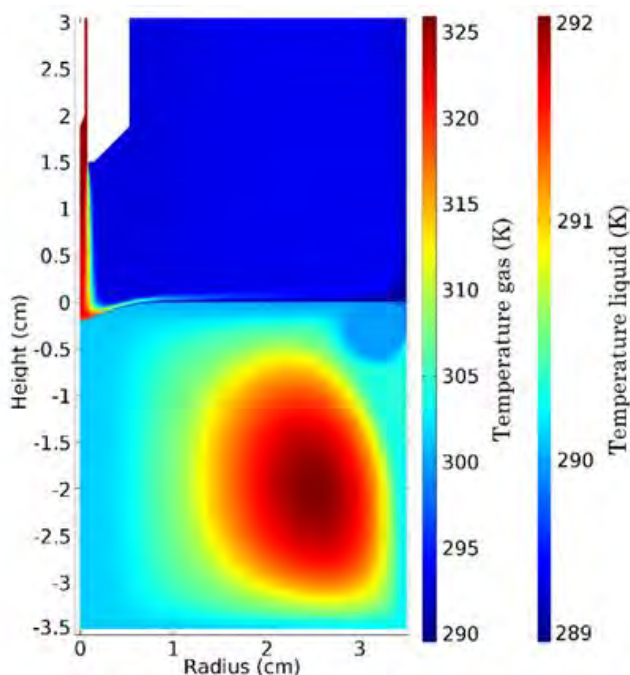


**Figure 7-5.** 2D plot of the temperature in both the gas and liquid phase after 1 minute of plasma treatment, presented in rainbow scale.

The drop in liquid temperature (to 289 K) was a result of the evaporation of water due to convection and is consistent with the model predictions by Lindsay and Graves<sup>30</sup>. When the water vapor above the interface is blown away by the plasma jet, liquid water evaporates in order to maintain the equilibrium in vapor pressure. This evaporation process consumes heat, leading to some cooling of the liquid, as observed in Figure 7-5. The slight drop in liquid temperature might be, at first sight, counterintuitive, as the initial temperature of the gas was higher than that of the liquid, so one might expect a heating effect. To verify that the drop in liquid temperature by evaporation was more important than the eventual rise due to the higher gas temperature, a calculation was performed where the evaporation was disabled. The results are presented in Figure 7-6.

It is clear from this figure that the liquid temperature increased slightly (*i.e.*, less than 1 K after 1 min), indicating that the cooling effect of evaporation of the liquid was indeed stronger than the heating effect by the warm gas effluent. Furthermore, note that the calculations were performed using a liquid volume of 135 mL, with an interface of 38.5 cm<sup>2</sup>. Thus, the area of evaporation ( $\approx 38.5$  cm<sup>2</sup>) is more

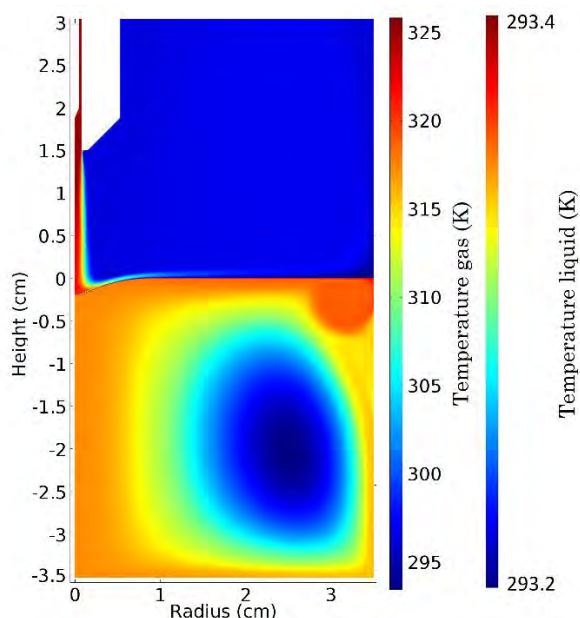


**Figure 7-6. 2D plot of the temperature in both the gas and liquid phase presented in rainbow scale when heat of evaporation is disabled.**

than 100 times larger than the area where the warm effluent reaches the liquid ( $\approx 0.28 \text{ cm}^2$ ), and thus, cooling of the liquid can indeed be expected.

### 7-3.3 Species concentrations in the gas phase

Figure 7-7 shows the species number densities in the afterglow as a function of distance from the nozzle of the plasma jet device. The interface is located at 17 mm (15 mm gap + 2 mm depression). At the top of Figure 7-7, a timescale axis is included, which was obtained from the distance in combination with the local gas velocity of the effluent. This time-information is useful when interpreting the gas chemistry. A clear increase in densities of the long-lived species, *i.e.*,  $\text{O}_3$ ,  $\text{HNO}_2$ ,  $\text{HNO}_3$ ,  $\text{H}_2\text{O}_2$  and  $\text{H}_2$  was observed, while the densities of the radicals, *i.e.*,  $\text{OH}$ ,  $\text{O}$ ,  $\text{N}$ ,  $\text{H}$  and  $\text{HO}_2$ , showed a steady decrease, indicating that they are consumed for the formation of the more long-lived species.  $\text{NO}$  appears to be an exception, as its density remained relatively constant, and it reached the gas-liquid interface with a density of around  $5 \times 10^{13} \text{ cm}^{-3}$ . The latter also explains the increase in  $\text{NO}_2$  density, because the production of  $\text{NO}_2$  mainly relied on the presence of  $\text{NO}$  in the effluent (through the reactions between  $\text{NO}$  and  $\text{O}$ ,  $\text{HO}_2$  or  $\text{NO}_3$ , see Table 7-A). The trends



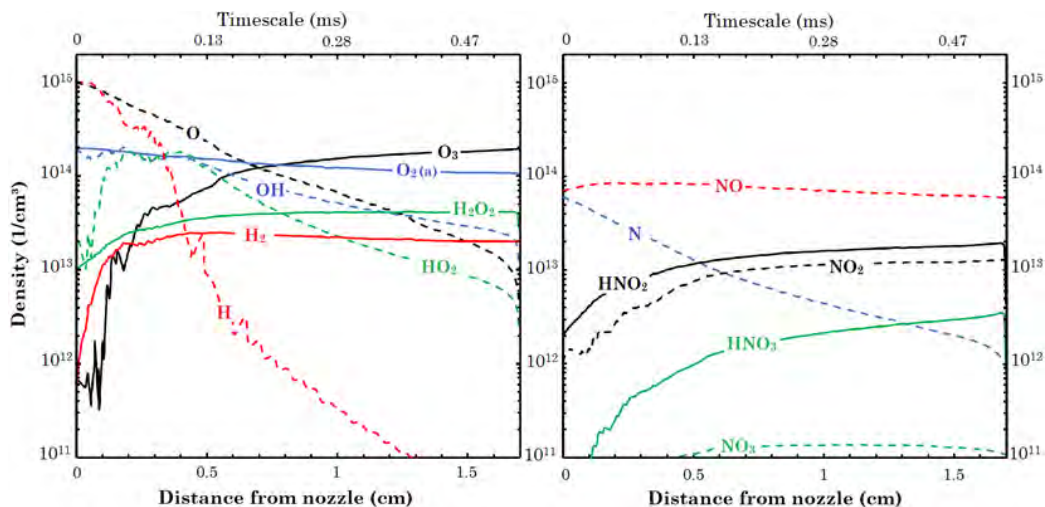


**Figure 7-7. Number densities of the biologically relevant reactive oxygen and nitrogen species (RONS) in the gas phase, after 1 min of plasma treatment.** The species containing O and/or H are plotted in the left panel, while the species containing also N are plotted in the right panel. Radicals are indicated with dotted lines, while molecules are depicted using solid lines. The gas-liquid interface is located at 17 mm distance from the nozzle (gap + 2 mm depression). The densities of species with a high Henry's constant, such as  $\text{H}_2\text{O}_2$  and OH, show a sudden drop at the interface due to the fast transfer to the liquid phase. The timescale indicated at the top axis is calculated from the distance and the local gas velocity.

in NO and  $\text{NO}_2$  densities are in good agreement with the results of other plasma models<sup>36,41,58</sup>, indicating that NO is more stable than the other short-lived species and plays an active role in the production of  $\text{NO}_2$ . Indeed, the reaction rates for NO (both production and loss) were typically lower than the reaction rates for OH, O, N and  $\text{HO}_2$ . Thus, more time was needed for NO to be consumed, leading to a relative high density of NO in the effluent (*cf.* Figure 7-7). Although the comparison between 0D chemical kinetics models and fluid dynamics-kinetics models is difficult due to different assumptions and approximations, the observed trends in Figure 7-7 are in good agreement with the density profiles as calculated by 0D simulations using similar input parameters<sup>41</sup>. This validates the reduced chemistry and confirms that the most important gas phase chemistry is included in our model.

Some species presented in Figure 7-7 (*i.e.*,  $\text{O}_3$ ,  $\text{HO}_2$ , OH and H) exhibit a non-smooth density profile. This is especially pronounced in the first 0.5 cm of the afterglow. There are two reasons for this behavior. First of all, it can be explained by the turbulent gas flow pattern found under the nozzle. Hence, the diffusion of



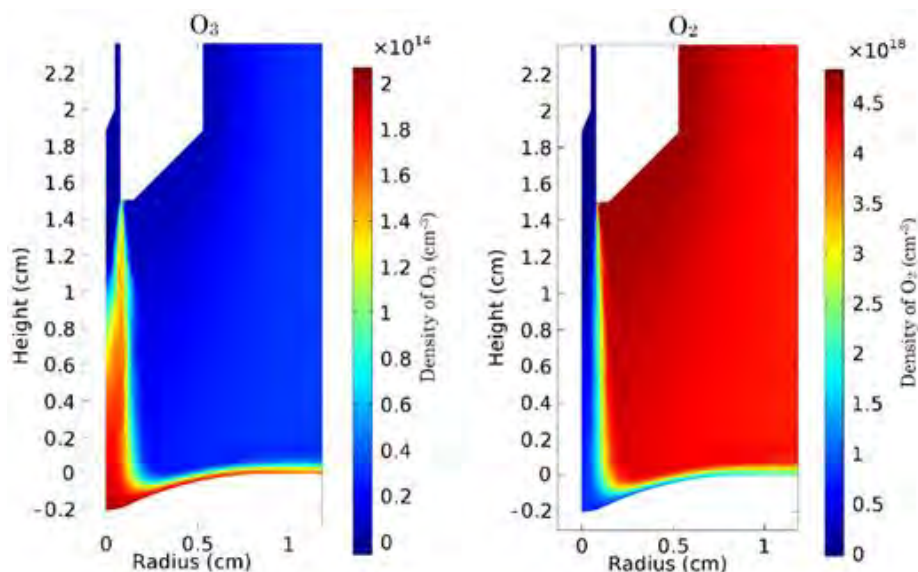


**Figure 7-8.** 2D plot of the number densities of O<sub>3</sub> (left) and O<sub>2</sub> (right) in the gas phase, after 1 min of plasma treatment and at a gas flow rate of 3 slm. The axis of symmetry is located at radius = 0 cm. The O<sub>3</sub> density increases sharply near the nozzle, where the concentration of O<sub>2</sub> is very high. As the gas flow is turbulent in this region, this will affect the density profile of O<sub>3</sub> when O atoms react with the ambient O<sub>2</sub> gas molecules (*cf.* reaction 2 of Table 7-A). See also Figure 7-7.

ambient air components (*i.e.*, O<sub>2</sub>, N<sub>2</sub> and H<sub>2</sub>O) becomes more turbulent, and the species for which the production heavily relied on the concentration of the ambient air components, will show a non-smooth density profile as a function of distance. For instance, the production of O<sub>3</sub> in the afterglow, close to the nozzle, is controlled by reaction 2 of Table 7-A, leading to an increase in O<sub>3</sub> density at the side of the nozzle, where the density of O<sub>2</sub> is high. This is shown in Figure 7-8. However, the gas flow turbulence at the side of the nozzle is more pronounced as well, explaining the non-smooth profile for the O<sub>3</sub> density. A similar explanation can be given for the HO<sub>2</sub> density, which is mostly produced by reaction 40 of Table 7-A close to the nozzle.



In addition, the non-smooth density profile close to the nozzle can also be explained by the sharp boundary condition in our model, as chemical reactions only start when the species leave the nozzle. As the concentration of radicals, such as H

and OH, was high at the nozzle (*cf.* Table 7-3), these species start to react immediately, which can have a great impact on their densities in the first millimeters after the nozzle.

### 7-3.4 Transport of species in the liquid phase

At the gas-liquid interface (distance = 1.7 cm in Figure 7-7), a sharp drop in the density of various species can be observed, *i.e.*, more specifically, those with a high Henry's constant, *i.e.*,  $\text{H}_2\text{O}_2$ , OH, O,  $\text{HO}_2$ ,  $\text{HNO}_2$ ,  $\text{HNO}_3$  and  $\text{NO}_3$  (*cf.* Table 7-4). Furthermore, the densities of species with a low Henry's constant will remain constant above the gas-liquid interface. This behavior is shown in Figure 7-9 for the 2D density profiles of  $\text{H}_2\text{O}_2$  and  $\text{O}_3$ , which are characterized by a high and low Henry's constant, respectively.

Once the gas species are in the liquid, they will be transported by both diffusion and convection. Due to the rather high velocity of the liquid at the interface (*cf.* Figure 7-2), convection contributed most to the transport of species in the liquid. This is also clear from Figure 7-9, where the flow pattern in the liquid (*cf.* Figure 7-2) is clearly visible in the density profiles of the dissolved species. The importance of

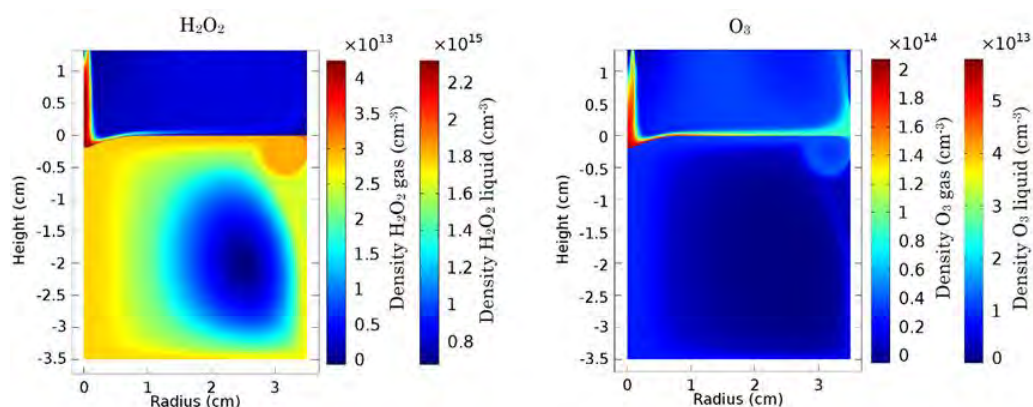


**Figure 7-9.** 2D plot of the number densities of  $\text{H}_2\text{O}_2$  (left) and  $\text{O}_3$  (right) in the gas phase just above the interface, as well as in the liquid, after 1 min of plasma treatment and at a flow rate of 3 slm. The axis of symmetry is located at radius = 0 cm.  $\text{H}_2\text{O}_2$  has a Henry's constant of  $7.9 \times 10^4$  leading to an accumulation in the liquid phase and a depletion in the gas phase (*cf.* Figure 7-7).  $\text{O}_3$  has a Henry's constant of  $1.22 \times 10^{-2}$  and will therefore accumulate in the gas phase just above the interface, leading to a much lower concentration in the liquid phase.

convection for the transport and accumulation of species in the bulk liquid was also demonstrated by Lindsay and Graves<sup>30</sup>, who reported a steady increase in the concentration of reactive species in the liquid, when convection was turned on.

Following the liquid flow, the dissolved species initially remained at the gas-liquid interface, and accumulated in the observed reverse vortex. Afterwards, they were found to flow back along the top layers of the liquid, following the liquid flow, after which they were introduced in the bulk liquid (as seen in Figure 7-9 left).

### 7-3.5 Species concentrations in the liquid phase

The 1D spatial density profiles of the biologically relevant reactive species in the liquid are presented in Figure 7-10, *i.e.*, at a depth of 100  $\mu\text{m}$  along the interface

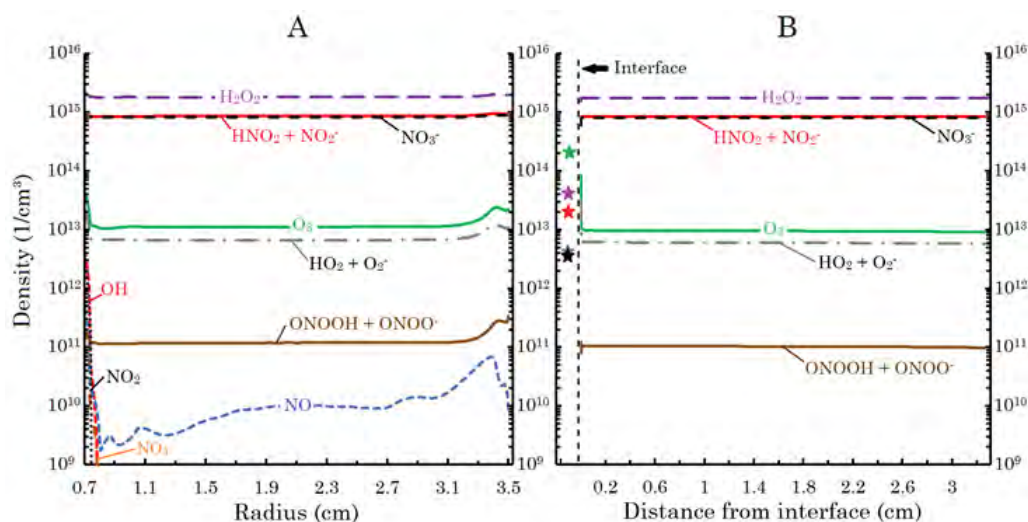


**Figure 7-10. Number densities of the biologically relevant reactive oxygen and nitrogen species (RONS) in the liquid, after 1 min of plasma treatment and at a flow rate of 3 slm.** (A) Densities at a depth of 100  $\mu\text{m}$  below the gas-liquid interfaces as a function of radial distance. The densities of OH,  $\text{NO}_2$  and  $\text{NO}_3$  decrease dramatically when introduced in the liquid. They are only present right below the interface, and only for about 1 mm in the radial direction. They do not exist in deeper layers, and are therefore not present in (B). (B) Densities along the symmetry axis ( $r = 0$  cm) as a function of depth. The densities of the corresponding gas phase species above the interface are indicated by an asterisk, showing that the density of  $\text{O}_3$  is much higher in the gas phase compared to the liquid phase (due to a low Henry's constant) while the opposite is true for  $\text{H}_2\text{O}_2$ ,  $\text{HNO}_2$  and  $\text{HNO}_3$  (due to a high Henry's constant). The densities of gaseous  $\text{HO}_2$  and  $\text{HNO}_3$  are almost identical, so their asterisks overlap.

(Figure 7-10-A) and as a function of depth at the symmetry axis (Figure 7-10-B). Note that the plot in Figure 7-10-A only starts at  $r = 0.7$  cm, due to the presence of the depression in the liquid.

The fast consumption of short-lived species, *i.e.*, OH, NO<sub>2</sub> and NO<sub>3</sub>, in the liquid is obvious from Figure 7-10-A. Indeed, their densities dropped with multiple orders of magnitude within 1 mm along the interface, and they were completely consumed in the lower liquid layers for the production of long-lived species (explaining why their densities are not plotted in Figure 7-10-B). This clearly demonstrates their importance in the liquid chemistry at the liquid depression (where the effluent interacts with the interface) and the first layers in the solution. In addition, the densities of the other species, *i.e.*, H<sub>2</sub>O<sub>2</sub>, HNO<sub>2</sub>/NO<sub>2</sub><sup>-</sup>, NO<sub>3</sub><sup>-</sup>, HO<sub>2</sub>/O<sub>2</sub><sup>-</sup>, O<sub>3</sub> and ONOOH/ONOO<sup>-</sup>, remained relatively constant as a function of distance, both in the horizontal and vertical direction. As the liquid needed roughly 0.2 seconds to reach 3.5 cm along the symmetry axis (*cf.* Figure 7-10-B), it can be concluded that the chemistry required longer timescales to significantly affect the concentration of the long-lived species.

In Figure 7-10-B, the gas densities of the species that reach the bulk liquid are shown by an asterisk in the same color (taken at 1.65 cm below the nozzle, *i.e.*, before the sudden depletion, as presented in Figure 7-7). Note that only the densities of the long-lived species are presented in this figure. The action of Henry's law is very clear, because species with high Henry's constant, *i.e.*, H<sub>2</sub>O<sub>2</sub>, HNO<sub>2</sub> and HNO<sub>3</sub>, were found at significantly higher densities in the liquid phase compared to their densities in the gas phase, while the opposite was true for O<sub>3</sub>, which has a low Henry's constant. Moreover, the accumulation of the dissolved species at the reverse vortex is visible from Figure 7-10-A, showing an increase in the densities for all the reactive species at radial distance of 3.4 – 3.5 cm. As mentioned, this was caused by the sudden decrease in liquid velocity and the recirculation inside this vortex, leading to an accumulation of the species.

Note that NO clearly accumulated in the reverse vortex, with densities almost comparable with some long-lived species, while it was immediately consumed in the bulk liquid. Indeed, NO is not found in Figure 7-10-B. The same is true for NO<sub>3</sub>, which was also accumulated in the reverse vortex, reaching a maximum density of

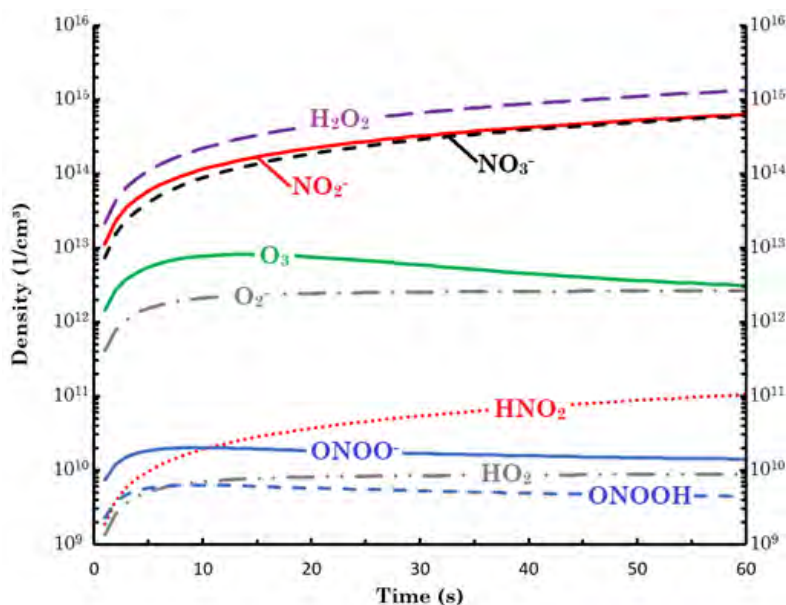
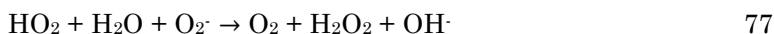


**Figure 7-11. Number densities of the reactive species that accumulate in the liquid, as a function of time.** The number densities are averaged over the entire liquid volume (135 mL). The pH of the liquid was set at 7.3. As  $\text{HNO}_2$ ,  $\text{HO}_2$  and  $\text{ONOOH}$  are weak acids, both the neutral molecule and their conjugated base are presented in the figure.

$7.5 \times 10^8 \text{ cm}^{-3}$  at a radial position around 3.36 cm (not shown in Figure 7-10, because of the too low density).

From Figure 7-10-B, it can be deduced that only  $\text{H}_2\text{O}_2$ ,  $\text{HNO}_2/\text{NO}_2^-$ ,  $\text{NO}_3^-$ ,  $\text{O}_3$ ,  $\text{HO}_2/\text{O}_2^-$  and  $\text{ONOOH}/\text{ONOO}^-$  were able to enter the bulk liquid and accumulate in the solution. To obtain more insight in the accumulation of these species, their number density, averaged over the entire liquid volume (135 mL) as a function of time, are plotted in Figure 7-11. It should be stressed that these accumulations were only calculated during plasma treatment and not after. After 1 minute of plasma treatment,  $\text{H}_2\text{O}_2$  had the highest density ( $1.3 \times 10^{15} \text{ cm}^{-3}$ ) in the solution, followed by  $\text{NO}_2^-$  and  $\text{NO}_3^-$  ( $6.3 \times 10^{14}$  and  $6.0 \times 10^{14} \text{ cm}^{-3}$ , respectively). The densities of these species increased monotonically as a function of time during plasma treatment, consistent with results obtained from experimental studies<sup>59,60</sup>. This increase, however, was not observed for the other species, which were found in much lower numbers. The concentration of  $\text{O}_2^-$  increased sharply in the first 10 seconds, and subsequently reached a constant value of around  $2.6 \times 10^{12} \text{ cm}^{-3}$ . As  $\text{HO}_2$  and  $\text{O}_2^-$  were connected through a  $\text{pK}_a$  value of 4.88, the same was true for  $\text{HO}_2$ , albeit at a

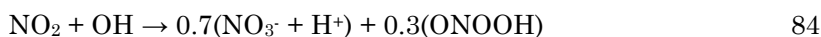
significantly lower concentration. This was caused by the increasing importance of loss reactions 77 and 92 (see Table 7-A), which eventually became equal to the accumulation of  $\text{HO}_2/\text{O}_2^-$  (via solvation and production reactions), leading to a steady-state as observed in Figure 7-11.



The concentration of  $\text{O}_3$  also increased steeply, reaching a maximum value of  $8.1 \times 10^{13} \text{ cm}^{-3}$  after 14 seconds, but it declined steadily afterwards. This was the result of an important loss reaction (reaction 70 in Table 7-A), which is affected by the increasing concentration of  $\text{NO}_2^-$ , consistent with the work of Lukès *et al.*<sup>59</sup>.



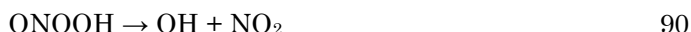
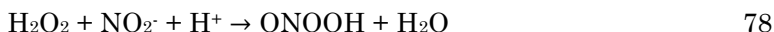
A similar trend was also found for  $\text{ONOOH}/\text{ONOO}^-$ , but the reason is less trivial. Within the solution, the production of  $\text{ONOOH}/\text{ONOO}^-$  was mainly controlled by reactions 83 and 84 of Table 7-A, and thus it depended on the concentration of short-lived species like  $\text{OH}$ ,  $\text{HO}_2$  and  $\text{NO}$ .



Therefore, the production of  $\text{ONOOH}/\text{ONOO}^-$  mainly took place just beneath the gas-liquid interface, where these species had a reasonable density. However, the concentrations of other long-lived species, such as  $\text{H}_2\text{O}_2$  and  $\text{NO}_2^-$ , just beneath the interface also increased, due to recirculation in the liquid (*cf.* Figure 7-2). Because of this, the short-lived species, necessary to produce  $\text{ONOOH}/\text{ONOO}^-$ , were consumed by reactions with these long-lived species, thus decreasing the production rates of  $\text{ONOOH}/\text{ONOO}^-$ . Combined with the fact that  $\text{ONOOH}/\text{ONOO}^-$  decomposed again in water into short-lived species, such as  $\text{OH}$ ,  $\text{NO}$ ,  $\text{O}_2^-$  and  $\text{NO}_2$  (reactions 89-91 in Table 7-A), explains the drop in the concentration of  $\text{ONOOH}/\text{ONOO}^-$  as a function of time. In the bulk liquid, the production of  $\text{ONOOH}/\text{ONOO}^-$  was governed by the reaction between  $\text{H}_2\text{O}_2$  and  $\text{NO}_2^-$  (reaction 78 in Table 7-A). However, this process is much

slower compared to the reactions with short-lived species as observed in the interface, and therefore only had a small contribution to the production of ONOOH/ONOO $\cdot$  during plasma treatment.

Thus, from Figure 7-11, it can be expected that only H<sub>2</sub>O<sub>2</sub>, HNO<sub>2</sub>/NO<sub>2</sub> $\cdot$  and NO<sub>3</sub> $\cdot$  will remain in the solution after treatment, while O<sub>3</sub>, HO<sub>2</sub>/O<sub>2</sub> $\cdot$  and ONOOH/ONOO $\cdot$  will be consumed, due to faster loss than production rates.



### 7-3.6 Overview of the liquid chemistry

Finally, the most important chemistry in the liquid phase was investigated, with special attention to the differences between the bulk liquid and the initial layers just beneath the gas-liquid interface around the depression in the liquid (called here “liquid interface” for the sake of clarity). An overview is presented in Figure 7-12. It starts from the gas phase species that (i) interact with the liquid interface (*cf.* Figure 7-7), and (ii) play a role in the liquid chemistry (*cf.* Figure 7-10). The focus was especially directed to the species with the highest densities in Figure 7-11, *i.e.*, H<sub>2</sub>O<sub>2</sub>, HNO<sub>2</sub>/NO<sub>2</sub> $\cdot$ , NO<sub>3</sub> $\cdot$ , O<sub>3</sub>, HO<sub>2</sub>/O<sub>2</sub> $\cdot$  and ONOOH/ONOO $\cdot$ . The species are written in boxes of which the thickness is a measure for the species relative density in that specific phase (bold being the highest density, such as O<sub>3</sub> in the gas phase, and dashed being the lowest, such as NO<sub>3</sub> in the gas phase). In this figure, reactions with ambient gas molecules (N<sub>2</sub>, O<sub>2</sub> and H<sub>2</sub>O) are included, but these species are not depicted for the sake of clarity.

As shown in Figure 7-7, O<sub>3</sub> reached the gas-liquid interface with the highest density of all RONS, followed by NO, H<sub>2</sub>O<sub>2</sub>, and HNO<sub>2</sub>. This is indicated by the thickness of the boxes of these species in the gas phase in Figure 7-12. Note that H<sub>2</sub> also reached the gas-liquid interface with relatively high density (*cf.* Figure 7-7), but as it was not involved in reactions that provide a significant contribution to the liquid phase species, it is not included in Figure 7-12. The same applies for O<sub>2</sub>(a), which is not included in the liquid phase chemistry, because of lack of data (as explained in



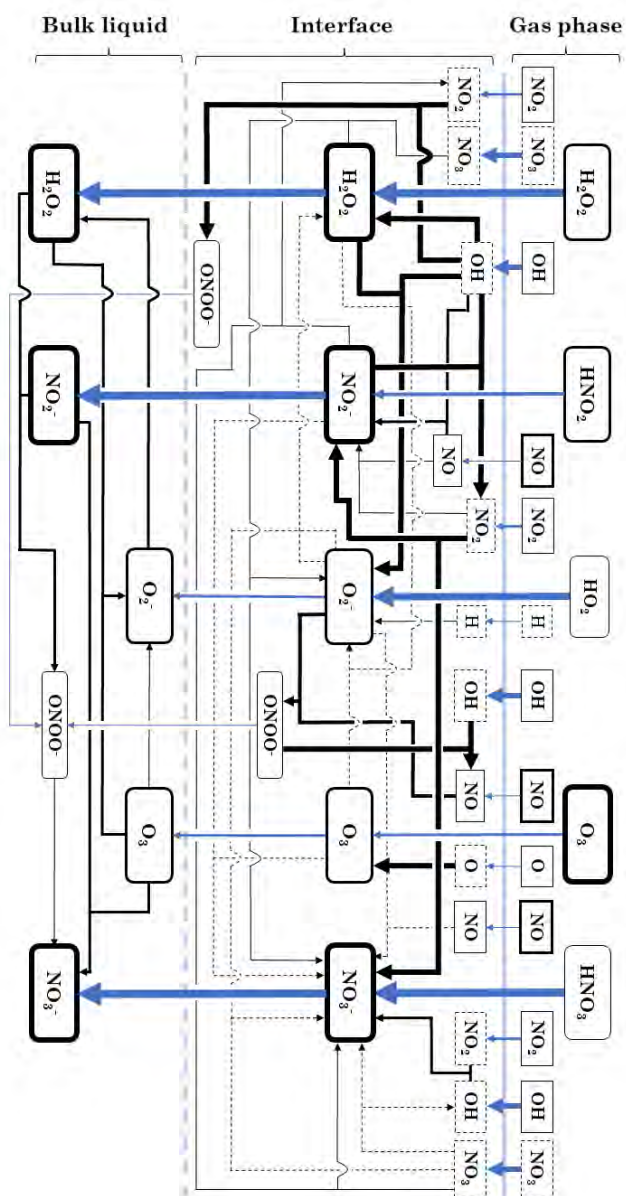


**Figure 7-12. Reaction diagram of the observed liquid chemistry.** The diagram mainly focuses on the reactive species found in the bulk liquid. Three parts are considered: gas phase, liquid interface (representing the small region near the depression in the liquid, where the radicals are still present, cf. Figure 7-A) and bulk liquid. The species are written in boxes of which the thickness indicates the relative density of the species in that phase (gas, liquid interface or bulk liquid). Diffusion from one phase to another is indicated with vertical blue arrow lines, where the thickness represents the fraction of that species that reaches the destination. Chemical reactions are indicated with black arrow lines, and in the liquid interface the thickness is again a measure for the relative contribution of this reaction towards the products. In the bulk liquid, a constant line thickness is used, as the species are typically only produced here via 1 or 2 reactions. Reactions with ambient air molecules ( $\text{O}_2$ ,  $\text{N}_2$  or  $\text{H}_2\text{O}$ ) are included in the figure, but these species are not depicted for the sake of clarity. The equilibrium between  $\text{HNO}_2/\text{NO}_2$ ,  $\text{HO}_2/\text{O}_2$  and  $\text{ONO}_2/\text{ONO}$  is included in the reaction set (see Table 7-A) and these species are considered together, but for the sake of clarity, the species are only indicated here by their deprotonated form, which has the highest density.



**section 7-2.6).** The transfer of species from one phase to the other is represented by vertical blue arrow lines in Figure 7-12, and the thickness of the arrow line is a measure for the fraction of that species that reaches its destination. For instance,  $\text{H}_2\text{O}_2$  and  $\text{HNO}_2$  could easily enter the liquid due to its high Henry's constant, so the blue arrow line is thick compared to that of  $\text{O}_3$ , which has a low Henry's constant. Indeed, despite the high density of  $\text{O}_3$  and  $\text{NO}$  above the liquid interface (*cf.* Figure 7-7), only a small fraction was able to enter the liquid due to their low Henry's constant, leading to liquid densities that did not exceed the order of  $10^{13} \text{ cm}^{-3}$  in contrast to the density of, *e.g.*,  $\text{H}_2\text{O}_2$  which reached  $1.3 \times 10^{15} \text{ cm}^{-3}$  (*cf.* Figure 7-11).

In Figure 7-12, chemical reactions are depicted by black arrow lines. In the liquid interface, the thickness indicates the relative importance of that reaction for the reaction products, while in the bulk liquid, a constant line thickness is used, as typically only one or two reactions contribute to the production of reactive species.

It is clear from Figure 7-12 that the production of  $\text{H}_2\text{O}_2$ ,  $\text{HNO}_2/\text{NO}_2^-$  and  $\text{NO}_3^-$  was driven by  $\text{OH}$ ,  $\text{NO}$  and  $\text{NO}_2$  in the liquid interface, besides, of course, solvation of the gas phase species. The most important reactions were reactions 71, 81 and 85 of Table 7-A, consuming a large part of  $\text{OH}$ ,  $\text{NO}$  and  $\text{NO}_2$  for the production of  $\text{H}_2\text{O}_2$ ,  $\text{HNO}_2$  and even  $\text{NO}_3^-$ . These three reactions together contributed up to 99% of the total production of  $\text{H}_2\text{O}_2$ ,  $\text{HNO}_2/\text{NO}_2^-$  and  $\text{NO}_3^-$  at the depression (interface) in the liquid, besides solvation of the gas species.



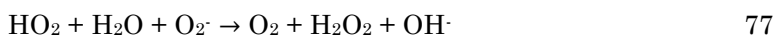
In addition,  $\text{OH}$  was not only responsible for the production of  $\text{H}_2\text{O}_2$  and  $\text{HNO}_2/\text{NO}_2^-$ , but it also contributed to the partial decomposition of  $\text{H}_2\text{O}_2$  in the liquid interface, forming  $\text{HO}_2$  (reaction 75 in Table 7-A), as well as to partial decomposition of  $\text{NO}_2^-$ , forming  $\text{NO}_2$  and  $\text{OH}^-$  (reaction 76 in Table 7-A).



The rising  $\text{NO}_2$  concentration by reaction 76, in turn, resulted in a rise in the

production of  $\text{NO}_2^-$  and  $\text{NO}_3^-$  through reaction 85. The above five reactions, *i.e.*, 71, 75, 76, 81 and 85, constitute the most important processes found in the liquid interface, eventually generating  $\text{H}_2\text{O}_2$ ,  $\text{HNO}_2/\text{NO}_2^-$ ,  $\text{NO}_3^-$  and  $\text{HO}_2/\text{O}_2^-$ .

This picture changed significantly in the bulk liquid, where  $\text{H}_2\text{O}_2$  was generated by the self-decomposition of  $\text{HO}_2/\text{O}_2^-$  (reaction 77 in Table 7-A), while  $\text{NO}_3^-$  was mostly produced by the reaction between  $\text{O}_3$  and  $\text{HNO}_2/\text{NO}_2^-$  (reaction 70 in Table 7-A). Unlike  $\text{H}_2\text{O}_2$  and  $\text{NO}_3^-$ , the other species, *i.e.*,  $\text{HNO}_2/\text{NO}_2^-$ ,  $\text{HO}_2/\text{O}_2^-$  and  $\text{O}_3$  accumulated in the bulk solely through diffusion and convection from the liquid interface, and were not formed through chemical reactions (due to the absence of the required short-lived species). However,  $\text{HO}_2/\text{O}_2^-$ ,  $\text{O}_3$  and  $\text{HNO}_2/\text{NO}_2^-$  were involved in both reactions 77 and 70, which formed the main loss processes for these species in the bulk liquid.



$\text{O}_3$  in the liquid mostly originated from the reaction between  $\text{O}$  and  $\text{O}_2$ , as transfer from the gas phase was limited by a low Henry's constant. In turn,  $\text{O}_3$  was mainly involved in reaction 70 towards the formation of  $\text{NO}_3^-$  (*cf.* Figure 7-12), both in the liquid interface and in the bulk liquid, as already stated above. Although this reaction was the major loss process for  $\text{O}_3$ , it contributed very little to the total production of  $\text{NO}_3^-$  in the liquid interface, where reaction 85 was much more important. Furthermore, despite being among the most pronounced reactions in the bulk liquid, the rate of reaction 70 was still very low, which explains the relatively slow changes in the density of  $\text{O}_3$  in the bulk as a function of time (*cf.* Figure 7-11).

Next to  $\text{H}_2\text{O}_2$ ,  $\text{NO}_2^-$ ,  $\text{O}_3$  and  $\text{NO}_3^-$ , also  $\text{O}_2^-$  was observed in the bulk, albeit at significantly lower concentrations (*cf.* Figure 7-11). Like  $\text{H}_2\text{O}_2$ , the accumulation of  $\text{O}_2^-$  in the liquid resulted from the combination of solvation (as  $\text{HO}_2$  also has a high Henry's constant) and the presence of  $\text{OH}$  in the liquid interface, which was able to react with  $\text{H}_2\text{O}_2$ , forming  $\text{HO}_2$  through reaction 75 (see above). Furthermore,  $\text{OH}$  was also able to react with  $\text{HO}_2/\text{O}_2^-$ , forming  $\text{O}_2$  via reactions 73 and 74 (Table 7-A). Both reactions 73 and 74 are found to be the main loss processes for  $\text{HO}_2/\text{O}_2^-$  in the liquid

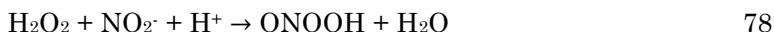
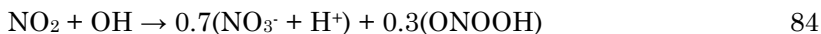
interface (not depicted in Figure 7-12).



Despite the presence of several production reactions for solvated  $\text{O}_2^-$ , its density in the liquid remained low (not exceeding  $10^{13} \text{ cm}^{-3}$ , *cf.* Figure 7-11), due to the presence of NO in the liquid interface (*cf.* Figure 7-10-A), leading to the formation of ONOOH/ONOO $\cdot$  (reaction 83 in Table 7-A). In the bulk, however, the self-decomposition of  $\text{O}_2^-/\text{HO}_2$  becomes the most important loss process, forming  $\text{H}_2\text{O}_2$  through reaction 77 (see above), and to a lesser extent by reaction 92 (due to the lower concentration of  $\text{HO}_2$  in a solution with pH 7.3).



Finally, ONOOH/ONOO $\cdot$  was mainly formed in the liquid interface from OH and  $\text{NO}_2$ , through reaction 84. However, given the fast solvation of ONOOH from the gas phase to the liquid phase (*cf.* high Henry's constant), it can be expected that ONOOH generated in the gas phase also contributed to its liquid density, but due to a lack of sufficient data in literature, the gas phase chemistry of ONOOH could not be included in this model. The liquid chemistry changes in the bulk, where reaction 78 formed the main production source for ONOOH/ONOO $\cdot$ , albeit at a much slower rate. However, the latter increases with increasing acidity<sup>59</sup>.



ONOOH also decomposed into  $\text{NO}_3^-$  (reaction 89). Because of this, combined with reactions 90-91, the concentration of ONOOH remained very low in the liquid (not exceeding  $2 \times 10^{10} \text{ cm}^{-3}$ ), and was found to decrease as a function of time, as explained above (*cf.* Figure 7-11). This is consistent with experimental observations at neutral pH, where ONOOH/ONOO $\cdot$  is stated to be unstable in solution, forming, among others,  $\text{NO}_3^-$ <sup>61,62</sup>.

Thus, OH, NO and  $\text{NO}_2$  were formed in the bulk liquid, and quickly reacted

with other species found in the solution to generate long-lived species like  $\text{H}_2\text{O}_2$ ,  $\text{HNO}_2/\text{NO}_2^-$  and  $\text{NO}_3^-$ , and decompose  $\text{O}_3$  in the investigated solution. Moreover, the generation of these short-lived species ( $\text{OH}$ ,  $\text{NO}$  and  $\text{NO}_2$ ) is expected to have contributed to the oxidation of biomolecules found in the treated solution<sup>59,63</sup>.



In summary, this model predicted that the long-lived species (*i.e.*,  $\text{H}_2\text{O}_2$ ,  $\text{HNO}_2/\text{NO}_2^-$ ,  $\text{ONOOH}/\text{ONOO}^\cdot$ ,  $\text{O}_3$  and  $\text{NO}_3^-$ ) were mainly generated in the liquid interface, through either solvation from the gas phase, as well as reactions governed by  $\text{OH}$ ,  $\text{NO}$  and  $\text{NO}_2$  originating from the gas phase. Furthermore, these long-lived reactive species accumulated in the bulk liquid a result of diffusion and convection from the liquid interface. Chemical reactions in the bulk liquid were found at significantly lower rates, and they favored the production of both  $\text{H}_2\text{O}_2$  and  $\text{NO}_3^-$ . While  $\text{H}_2\text{O}_2$  was solely produced by the self-decomposition of  $\text{HO}_2/\text{O}_2^\cdot$  in the bulk liquid (in addition to the transport from the liquid interface), the calculations revealed that the production of  $\text{NO}_3^-$  was favored in the presence of  $\text{HNO}_2/\text{NO}_2^-$  through the interplay between either  $\text{H}_2\text{O}_2$  and  $\text{HNO}_2/\text{NO}_2^-$  (with  $\text{ONOOH}/\text{ONOO}^\cdot$  as intermediate) or  $\text{O}_3$  and  $\text{HNO}_2/\text{NO}_2^-$ .

The results presented in this chapter of course depend on the simulated working conditions, such as the treatment gap, flow rate and pH of the treated liquid. Decreasing the flow rate and/or increasing the gap leads to a significant increase in the time needed for the plasma species to come in contact with the liquid interface, which has an impact on the simulated chemistry. As a result, the short-lived gas species (*i.e.*,  $\text{O}$ ,  $\text{N}$ ,  $\text{OH}$ ,  $\text{HO}_2$  and  $\text{NO}_3$ ) will have more time to be consumed towards the formation of the long-lived gas species (*i.e.*,  $\text{H}_2\text{O}_2$ ,  $\text{O}_3$ ,  $\text{HNO}_2$  and  $\text{HNO}_3$ ). This will lead to a decrease in the density of the short-lived gas species and an increase in the density of the long-lived gas species, at the liquid interface, with decreasing flow rate and/or increasing gap. This, in turn, will greatly influence the observed liquid chemistry at the liquid interface (*cf.* Figure 7-12). Indeed, a lower density of short-lived liquid species at the interface will result in lower reaction rates for the

formation of the long-lived liquid species. The decrease in formation of long-lived liquid species at the liquid interface will, however, be compensated by the higher density of long-lived gas species that come in contact with the liquid interface, as mentioned above. Simultaneously, a lower gas velocity also influences the number of species that is introduced in the system per unit of time. Combined, the number of reactive species inside the liquid will decrease with decreasing flow rate.

Furthermore, as the concentration of  $H^+$  and  $OH^-$  has a significant impact on the simulated chemistry, due to equilibrium of weak acids, pH dependent reactions and reactions with either  $H^+$  or  $OH^-$ , the pH of the solution will play a crucial role in the results observed in this work. On one hand, as  $H_2O_2$  and  $HNO_2/NO_2^-$  are known to form  $ONOOH/ONOO^-$  at decreasing pH values<sup>59</sup>, we expect a slow decrease of these reactive species, eventually forming  $NO_3^-$  (through  $ONOOH/ONOO^-$  as intermediate)<sup>59</sup> and decreasing the activity of the produced PTL as a function of time, as was indeed observed in experiments<sup>59</sup>. On the other hand, a decrease in the ozone density in solution with increasing pH can be expected. This is, first of all, caused by the increasing importance of the peroxone chemistry at high pH values (reaction 93 of Table 7-A). Additionally, we expect that reactions with  $OH^-$  and  $NO_2^-$  will become more important with increasing pH (reactions 69 and 70 of Table 7-A), leading to the further consumption of ozone in solution.

In the future, this model will be extended in order to investigate the effect of different working conditions (flow rate, gap, liquid volume and pH) on the liquid chemistry and on the accumulation of reactive species in more detail. In addition, the behavior after plasma treatment (*i.e.*, no inlet velocity and plasma species densities) will be investigated, for the evolution of the species in the produced PTL at longer timescales, and to investigate the stability of the PTL after plasma treatment.

## 7-4 Conclusion

A 2D axisymmetric fluid dynamics model was developed to investigate the plasma jet-liquid interactions for an Ar plasma jet (kINPen), focusing in particular on the accumulation and chemical reactions of plasma-generated reactive species in a buffered aqueous solution, as well as transport from the gas phase. Twenty gas phase species and 22 liquid phase species are included, which react in 57 gas phase reactions and 42 liquid phase reactions. Furthermore, transport of the plasma species from the gas phase to the liquid, governed by Henry's law, as well as water evaporation, is taken into account. These results indicated that the flow pattern in the liquid depended on the velocity of the effluent, which was determined by the gap and the gas flow rate. Due to the high gas phase velocity, the generation of a reverse vortex in the liquid was observed, which relocates towards the gas-liquid interface with increasing velocity. This resulted in a complex flow pattern at the liquid interface, which affects the chemistry in the liquid. Indeed, due to the liquid flow pattern, short-lived reactive species remained close to the interface and did not reach the bulk liquid. The observed liquid flow pattern also resulted in the accumulation of long-lived reactive species, *i.e.*,  $\text{H}_2\text{O}_2$ ,  $\text{HNO}_2/\text{NO}_2^-$ ,  $\text{NO}_3^-$ ,  $\text{O}_3$ ,  $\text{HO}_2/\text{O}_2^-$  and  $\text{ONOOH}/\text{ONOO}^-$ , as well as  $\text{NO}$  and  $\text{NO}_3$ , in the reverse vortex situated at the border of the liquid vessel.

As the short-lived reactive species were consumed at the interface, generating long-lived reactive species, they were not encountered in the bulk liquid. Indeed, the results showed that only  $\text{H}_2\text{O}_2$ ,  $\text{HNO}_2/\text{NO}_2^-$ ,  $\text{NO}_3^-$ ,  $\text{O}_3$ ,  $\text{HO}_2/\text{O}_2^-$  and  $\text{ONOOH}/\text{ONOO}^-$  were present in the bulk liquid during plasma treatment. Furthermore, from these results it can be expected that only  $\text{H}_2\text{O}_2$ ,  $\text{HNO}_2/\text{NO}_2^-$  and  $\text{NO}_3^-$  will remain in the liquid after plasma treatment, consistent with experimental observations<sup>59,60</sup>. The other species found in the bulk liquid, *i.e.*,  $\text{O}_3$ ,  $\text{HO}_2/\text{O}_2^-$  and  $\text{ONOOH}/\text{ONOO}^-$ , were consumed in the liquid chemistry. Indeed,  $\text{O}_3$  was consumed by the reaction with  $\text{HNO}_2/\text{NO}_2^-$ , while  $\text{HO}_2/\text{O}_2^-$  and  $\text{ONOOH}/\text{ONOO}^-$  decomposed to form either  $\text{H}_2\text{O}_2$  or both  $\text{HNO}_2/\text{NO}_2^-$  and  $\text{NO}_3^-$ , respectively.

Finally, it should be noted that the simulations presented here were performed only while the plasma jet was turned on. This means that a continuous flow of new species was introduced during the simulations. Because of this, our simulations can

provide no conclusion yet on the stability of the simulated PTLs after plasma treatment. The latter should be investigated in more detail, as indeed, switching off the plasma will have an impact on the liquid flow, and therefore on the further accumulation of species. Hence, in the near future the PTL behavior after plasma treatment (*i.e.*, no inlet velocity and plasma species densities) should be considered, to investigate the evolution of the species in the produced PTL, and more in general, the stability of the PTL, after plasma treatment.

This study provides valuable insight in the interaction of a plasma jet with liquid water, for the generation of plasma treated liquids, as well as for plasma medicine more in general.

## 7-5 Appendix-7

**Table 7-A. Reaction list with all gas phase and liquid phase reactions included in the model, as well as the rate coefficients (or the data to calculate the rate coefficients) and the references where these data were adopted from.** The rate coefficients for the gas phase reactions are given in the Arrhenius form:  $k = A \times (T_g/300)^B \times \exp(-C/T_g)$ , with units of  $s^{-1}$ ,  $cm^3s^{-1}$  and  $cm^6s^{-1}$  for first, second and third order reactions. The unit of A is the same as for k, B is dimensionless, and the unit of C and  $T_g$  is K. The unit for the liquid phase rate coefficients is  $s^{-1}$ ,  $m^3mol^{-1}s^{-1}$  and  $m^6mol^{-2}s^{-1}$  for first, second and third order reactions, respectively.

No.	Reaction	Reaction rate coefficient			Ref.
	Gas phase reactions	A	B	C	
1	$O + OH \rightarrow H + O_2$	$1.81 \times 10^{-11}$	-0.31	-177	58
2	$O + O_2 + M \rightarrow O_3 + M$	$6.40 \times 10^{-35}$	0	-663	58
3	$O + NO_2 \rightarrow NO + O_2$	$6.50 \times 10^{-12}$	0	-120	58
4	$O + O_3 \rightarrow O_2 + O_2$	$8.00 \times 10^{-12}$	0	2060	58
5	$O + O_3 \rightarrow {}^1O_2 + O_2$	$1.00 \times 10^{-11}$	0	2300	58
6	$O + O + M \rightarrow {}^1O_2 + M$	$6.93 \times 10^{-35}$	-0.63	0	36
7	$O + HO_2 \rightarrow OH + O_2$	$2.71 \times 10^{-11}$	0	-224	58
8	$O + NO + M \rightarrow NO_2 + M$	$1.00 \times 10^{-31}$	-1.6	0	58
9	$O + NO_3 \rightarrow NO_2 + O_2$	$1.70 \times 10^{-11}$	0	0	58
10	$O + O + M \rightarrow O_2 + M$	$5.21 \times 10^{-35}$	0	-900	58
11	$O + N + M \rightarrow NO + M$	$1.02 \times 10^{-32}$	-0.5	0	58
12	$O + HNO_3 \rightarrow OH + NO_3$	$3.00 \times 10^{-17}$	0	0	58
13	$O + NO_2 + M \rightarrow NO_3 + M$	$9.00 \times 10^{-32}$	-2	0	58
14	$O + H_2O_2 \rightarrow HO_2 + OH$	$1.79 \times 10^{-13}$	2.92	1394	58
15	$O + H_2O_2 \rightarrow H_2O + O_2$	$1.45 \times 10^{-15}$	0	0	58
16	$O + HNO_2 \rightarrow OH + NO_2$	$2.00 \times 10^{-11}$	0	3000	58
17	$O_2 + NO_3 \rightarrow NO_2 + O_3$	$1.00 \times 10^{-17}$	0	0	58
18	$O_2 + {}^1O_2 \rightarrow O_3 + O$	$3.00 \times 10^{-21}$	0	0	36
19	${}^1O_2 + M \rightarrow O_2 + M$	$3.00 \times 10^{-18}$	0	200	58
20	${}^1O_2 + HO_2 \rightarrow OH + O_2 + O$	$1.66 \times 10^{-11}$	0	0	58



21	${}^1\text{O}_2 + \text{O}_3 \rightarrow \text{O}_2 + \text{O}_2 + \text{O}$	$1.00 \times 10^{-14}$	0	0	58
22	$\text{O}_3 + \text{NO} \rightarrow \text{NO}_2 + \text{O}_2$	$4.30 \times 10^{-12}$	0	1560	58
23	$\text{O}_3 + \text{NO}_2 \rightarrow \text{NO}_3 + \text{O}_2$	$1.40 \times 10^{-13}$	0	2470	58
24	$\text{O}_3 + \text{OH} \rightarrow \text{HO}_2 + \text{O}_2$	$1.69 \times 10^{-12}$	0	941	58
25	$\text{O}_3 + \text{HNO}_2 \rightarrow \text{HNO}_3 + \text{O}_2$	$5.00 \times 10^{-19}$	0	0	36
26	$\text{O}_3 + \text{O}_3 \rightarrow {}^1\text{O}_2 + \text{O}_2 + \text{O}_2$	$1.00 \times 10^{-11}$	0	2300	58
27	$\text{O}_3 + \text{H} \rightarrow \text{OH} + \text{O}_2$	$2.71 \times 10^{-11}$	0.75	0	58
28	$\text{OH} + \text{NO}_2 + \text{M} \rightarrow \text{HNO}_3 + \text{M}$	$4.60 \times 10^{-29}$	-5.49	1180	58
29	$\text{OH} + \text{NO} + \text{M} \rightarrow \text{HNO}_2 + \text{M}$	$7.40 \times 10^{-31}$	-2.4	0	58
30	$\text{OH} + \text{H}_2\text{O}_2 \rightarrow \text{H}_2\text{O} + \text{HO}_2$	$4.53 \times 10^{-12}$	0	288.9	58
31	$\text{OH} + \text{OH} \rightarrow \text{H}_2\text{O} + \text{O}$	$5.49 \times 10^{-14}$	2.42	-970	58
32	$\text{OH} + \text{HO}_2 \rightarrow \text{H}_2\text{O} + \text{O}_2$	$4.80 \times 10^{-11}$	0	-250	58
33	$\text{OH} + \text{HNO}_2 \rightarrow \text{H}_2\text{O} + \text{NO}_2$	$2.70 \times 10^{-12}$	0	-260	58
34	$\text{OH} + \text{OH} + \text{M} \rightarrow \text{H}_2\text{O}_2 + \text{M}$	$8.00 \times 10^{-31}$	-0.8	0	58
35	$\text{OH} + \text{HNO}_3 \rightarrow \text{H}_2\text{O} + \text{NO}_3$	$1.50 \times 10^{-13}$	0	0	58
36	$\text{HO}_2 + \text{NO} + \text{M} \rightarrow \text{HNO}_3 + \text{M}$	$5.60 \times 10^{-33}$	0	0	58
37	$\text{HO}_2 + \text{NO} \rightarrow \text{NO}_2 + \text{OH}$	$3.60 \times 10^{-12}$	0	-270	36
38	$\text{HO}_2 + \text{HO}_2 + \text{M} \rightarrow \text{H}_2\text{O}_2 + \text{O}_2 + \text{M}$	$1.70 \times 10^{-33}$	0	-999.5	36
39	$\text{HO}_2 + \text{N} \rightarrow \text{NO} + \text{OH}$	$2.20 \times 10^{-11}$	0	0	58
40	$\text{H} + \text{O}_2 + \text{M} \rightarrow \text{HO}_2 + \text{M}$	$6.09 \times 10^{-32}$	-0.8	0	58
41	$\text{H} + \text{OH} + \text{M} \rightarrow \text{H}_2\text{O} + \text{M}$	$8.00 \times 10^{-31}$	-2.6	0	58
42	$\text{H} + \text{HO}_2 \rightarrow \text{H}_2 + \text{O}_2$	$2.06 \times 10^{-11}$	0.84	277	58
43	$\text{H} + \text{H}_2\text{O}_2 \rightarrow \text{H}_2\text{O} + \text{OH}$	$4.00 \times 10^{-11}$	0	2000	58
44	$\text{H} + \text{HNO}_2 \rightarrow \text{H}_2 + \text{NO}_2$	$2.00 \times 10^{-11}$	0	3700	58
45	$\text{H} + \text{NO}_3 \rightarrow \text{NO}_2 + \text{OH}$	$5.80 \times 10^{-10}$	0	750	58
46	$\text{H} + \text{HO}_2 \rightarrow \text{OH} + \text{OH}$	$1.66 \times 10^{-10}$	0	413	58
47	$\text{H} + \text{NO}_2 \rightarrow \text{OH} + \text{NO}$	$4.00 \times 10^{-10}$	0	340	58
48	$\text{H}_2 + \text{OH} \rightarrow \text{H}_2\text{O} + \text{H}$	$9.54 \times 10^{-13}$	2	1490	58
49	$\text{N} + \text{O}_2 \rightarrow \text{NO} + \text{O}$	$3.30 \times 10^{-12}$	-1	3150	58

<b>50</b>	$\text{N} + \text{NO} \rightarrow \text{N}_2 + \text{O}$	$8.20 \times 10^{-11}$	0	-410	58
<b>51</b>	$\text{N} + \text{NO}_3 \rightarrow \text{NO}_2 + \text{NO}$	$3.00 \times 10^{-12}$	0	0	58
<b>52</b>	$\text{N} + \text{OH} \rightarrow \text{H} + \text{NO}$	$4.70 \times 10^{-11}$	0	0	58
<b>53</b>	$\text{N} + \text{N} + \text{M} \rightarrow \text{N}_2 + \text{M}$	$1.38 \times 10^{-34}$	0	0	58
<b>54</b>	$\text{N} + \text{NO}_2 \rightarrow \text{NO} + \text{NO}$	$1.33 \times 10^{-12}$	0	-220	58
<b>55</b>	$\text{NO}_3 + \text{NO} \rightarrow \text{NO}_2 + \text{NO}_2$	$1.80 \times 10^{-11}$	0	-110	58
<b>56</b>	$\text{NO}_3 + \text{NO}_2 + \text{M} \rightarrow \text{N}_2\text{O}_5 + \text{M}$	$2.80 \times 10^{-30}$	-3.5	0	58
<b>57</b>	$\text{N}_2\text{O}_5 + \text{M} \rightarrow \text{NO}_2 + \text{NO}_3 + \text{M}$	$1.33 \times 10^{-3}$	-3.5	11000	58
<b>Liquid phase reactions</b>		<b>k</b>	<b>Ref.</b>		
<b>58</b>	$\text{H} + \text{H}_2\text{O} \rightarrow \text{H}_2 + \text{OH}$	$1.00 \times 10^{-2}$	24		
<b>59</b>	$\text{H} + \text{H} \rightarrow \text{H}_2$	$7.50 \times 10^6$	24		
<b>60</b>	$\text{H} + \text{OH} \rightarrow \text{H}_2\text{O}$	$7.00 \times 10^6$	24		
<b>61</b>	$\text{H} + \text{H}_2\text{O}_2 \rightarrow \text{OH} + \text{H}_2\text{O}$	$9.00 \times 10^4$	24		
<b>62</b>	$\text{H} + \text{O}_2 \rightarrow \text{HO}_2$	$2.10 \times 10^7$	24		
<b>63</b>	$\text{H} + \text{HO}_2 \rightarrow \text{H}_2\text{O}_2$	$1.00 \times 10^7$	24		
<b>64</b>	$\text{H} + \text{NO}_2 \rightarrow \text{OH} + \text{NO}$	$1.20 \times 10^6$	24		
<b>65</b>	$\text{H} + \text{NO}_2 \rightarrow \text{HNO}_2$	$1.00 \times 10^7$	24		
<b>66</b>	$\text{O} + \text{H}_2\text{O} \rightarrow \text{OH} + \text{OH}$	$1.30 \times 10^1$	24		
<b>67</b>	$\text{O} + \text{O}_2 \rightarrow \text{O}_3$	$3.00 \times 10^6$	24		
<b>68</b>	$\text{O}_2 + \text{NO} \rightarrow 0.7(\text{NO}_3) + 0.3(\text{ONOO})$	$1.20 \times 10^7$	24		
<b>69</b>	$\text{O}_3 + \text{O}_3 + \text{OH} \rightarrow \text{O}_2 + \text{O}_2 + \text{HO} + \text{O}_2$	$2.10 \times 10^{-1}$	48		
<b>70</b>	$\text{O}_3 + \text{NO}_2 \rightarrow \text{O}_2 + \text{NO}_3$	$3.30 \times 10^2$	48		
<b>71</b>	$\text{OH} + \text{OH} \rightarrow \text{H}_2\text{O}_2$	$1.00 \times 10^7$	24		
<b>72</b>	$\text{OH} + \text{H}_2 \rightarrow \text{H} + \text{H}_2\text{O}$	$4.20 \times 10^4$	24		
<b>73</b>	$\text{OH} + \text{HO}_2 \rightarrow \text{H}_2\text{O} + \text{O}_2$	$6.00 \times 10^6$	24		
<b>74</b>	$\text{OH} + \text{O}_2 \rightarrow \text{OH} + \text{O}_2$	$8.00 \times 10^6$	24		
<b>75</b>	$\text{OH} + \text{H}_2\text{O}_2 \rightarrow \text{H}_2\text{O} + \text{HO}_2$	$2.70 \times 10^4$	24		
<b>76</b>	$\text{OH} + \text{NO}_2 \rightarrow \text{OH} + \text{NO}_2$	$1.00 \times 10^7$	24		
<b>77</b>	$\text{HO}_2 + \text{H}_2\text{O} + \text{O}_2 \rightarrow \text{O}_2 + \text{H}_2\text{O}_2 + \text{OH}$	$9.68 \times 10^1$	48		

78	$\text{H}_2\text{O}_2 + \text{NO}_2^- + \text{H}^+ \rightarrow \text{ONOOH} + \text{H}_2\text{O}$	$1.1 \times 10^{-3}$	59
79	$\text{NO} + \text{NO} + \text{O}_2 \rightarrow \text{NO}_2 + \text{NO}_2$	2.30	24
80	$\text{NO} + \text{NO}_2 + \text{H}_2\text{O} \rightarrow \text{HNO}_2 + \text{HNO}_2$	$2.00 \times 10^2$	24
81	$\text{NO} + \text{OH} \rightarrow \text{HNO}_2$	$2.00 \times 10^7$	24
82	$\text{NO} + \text{O}_2^- \rightarrow \text{NO}_3^-$	$8.00 \times 10^6$	24
83	$\text{NO} + \text{O}_2^- \rightarrow \text{ONOO}^-$	$3.20 \times 10^6$	24
84	$\text{NO}_2 + \text{OH} \rightarrow 0.7(\text{NO}_3^- + \text{H}^+) + 0.3(\text{ONOOH})$	$5.30 \times 10^6$	24
85	$\text{NO}_2 + \text{NO}_2 + \text{H}_2\text{O} \rightarrow \text{HNO}_2 + \text{H}^+ + \text{NO}_3^-$	$1.50 \times 10^2$	24
86	$\text{NO}_3 + \text{OH}^- \rightarrow \text{OH} + \text{NO}_3^-$	$8.00 \times 10^4$	48
87	$\text{N}_2\text{O}_5 + \text{H}_2\text{O} \rightarrow \text{NO}_3^- + \text{NO}_3^- + \text{H}^+ + \text{H}^+$	$1.20 \times 10^{-3}$	24
88	$\text{HNO}_2 + \text{HNO}_2 \rightarrow \text{NO} + \text{NO}_2 + \text{H}_2\text{O}$	$1.34 \times 10^1$	30
89	$\text{ONOOH} \rightarrow \text{NO}_3^- + \text{H}^+$	1.20	64
90	$\text{ONOOH} \rightarrow \text{OH} + \text{NO}_2$	$3 \times 10^{-1}$	64
91	$\text{ONOO}^- \rightarrow \text{NO} + \text{O}_2^-$	$2 \times 10^{-2}$	64
92	$\text{HO}_2 + \text{HO}_2 \rightarrow \text{O}_2 + \text{H}_2\text{O}_2$	$8.3 \times 10^2$	48
93	$\text{H}_2\text{O}_2 + \text{O}_3 + \text{OH}^- \rightarrow \text{OH} + \text{HO}_2 + \text{O}_2 + \text{OH}^-$	$5.5 \times 10^{3-Z}$ $Z = 11.6\text{-pH}$	65
94	$\text{OH} + \text{ONOO}^- \rightarrow \text{OH}^- + \text{O}_2 + \text{NO}$	$4.8 \times 10^6$	26
95	$\text{NO}_3 + \text{H}_2\text{O}_2 \rightarrow \text{NO}_3^- + \text{HO}_2 + \text{H}^+$	$1.00 \times 10^3$	26
96	$\text{NO}_3 + \text{O}_2^- \rightarrow \text{NO}_3^- + \text{O}_2$	$1.00 \times 10^6$	26
97	$\text{NO}_3 + \text{NO}_2^- \rightarrow \text{NO}_3^- + \text{NO}_2$	$1.2 \times 10^6$	26
98	$\text{O}_3 + \text{OH} \rightarrow \text{O}_2 + \text{HO}_2$	$1.00 \times 10^5$	48
98	$\text{H}_2\text{O} \rightarrow \text{H}^+ + \text{OH}^-$	$7 \times 10^{-2}$	30
99	$\text{H}^+ + \text{OH}^- \rightarrow \text{H}_2\text{O}$	$7 \times 10^6$	30
100	$\text{HNO}_2 \leftrightarrow \text{H}^+ + \text{NO}_2^-$	$\text{pKa} = 3.4$	
101	$\text{ONOOH} \leftrightarrow \text{H}^+ + \text{ONOO}^-$	$\text{pKa} = 6.8$	
102	$\text{HO}_2 \leftrightarrow \text{H}^+ + \text{O}_2^-$	$\text{pKa} = 4.88$	

## 7-6 References

1. Verlackt, C. C. W., Van Boxem, W. & Bogaerts, A. Transport and Accumulation of Plasma Generated Species in Aqueous Solution. *Phys. Chem. Chem. Phys.* **in press**, (2018).
2. Lu, X., Naidis, G. V., Laroussi, M., Reuter, S., Graves, D. B. & Ostrikov, K. Reactive species in non-equilibrium atmospheric-pressure plasmas: generation, transport, and biological effects, *Phys. Rep.*, **630**, 1-84 (2016)
3. Golda, J. *et al.* Concepts and characteristics of the ‘COST Reference Microplasma Jet’. *J. Phys. D. Appl. Phys.* **49**, 84003 (2016).
4. Weltmann, K. *et al.* Plasma Processes and Plasma Sources in Medicine. *Contrib. to Plasma Phys.* **654**, 644–654 (2012).
5. Winter, J., Brandenburg, R. & Weltmann, K. Atmospheric pressure plasma jets: an overview of devices and new directions. *Plasma Sources Sci. Technol.* **24**, 64001 (2015).
6. Ehlbeck, J. *et al.* Low temperature atmospheric pressure plasma sources for microbial decontamination. *J. Phys. D. Appl. Phys.* **44**, 13002 (2011).
7. Sato, T., Yokoyama, M. & Johkura, K. A key inactivation factor of HeLa cell. *J. Phys. D. Appl. Phys.* **44**, 372001 (2011).
8. Vandamme, M. *et al.* ROS implication in a new antitumor strategy based on non-thermal plasma. *Int. J. Cancer* **130**, 2185–94 (2012).
9. Adachi, T., Tanaka, H., Nonomura, S., Hara, H. & Kondo, S. Plasma-activated medium induces A549 cell injury via a spiral apoptotic cascade involving the mitochondrial-nuclear network. *Free Radic. Biol. Med.* **79**, 28–44 (2015).
10. Partecke, L. I. *et al.* Tissue tolerable plasma (TTP) induces apoptosis in pancreatic cancer cells in vitro and in vivo. *BMC Cancer* **12**, 473–483 (2012).
11. Duan, J., Lu, X. & He, G. On the penetration depth of reactive oxygen and nitrogen species generated by a plasma jet through real biological tissue. *Phys. Plasmas* **24**, 73506 (2017).
12. Pacher, P., Beckman, J. S. & Liaudet, L. Central Control of Breathing in Mammals: Neuronal Circuitry, Membrane Properties, and Neurotransmitters. *Physiol. Rev.* **87**, 315–424 (2007).
13. Ye, F. *et al.* Plasma-activated medium suppresses choroidal neovascularization in mice: a new therapeutic concept for age-related macular degeneration. *Sci. Rep.* **5**, 1–7 (2014).

14. Mohades, S., Laroussi, M. & Maruthamuthu, V. Moderate plasma activated media suppresses proliferation and migration of MDCK epithelial cells. *J. Phys. D. Appl. Phys.* **50**, 185205 (2017).
15. Tanaka, H. *et al.* Plasma-Activated Medium Selectively Kills Glioblastoma Brain Tumor Cells by Down-Regulating a Survival Signaling Molecule, AKT Kinase. *Plasma Med.* **1**, 265–277 (2011).
16. Takeda, S. *et al.* Intraperitoneal Administration of Plasma-Activated Medium: Proposal of a Novel Treatment Option for Peritoneal Metastasis From Gastric Cancer. *Ann. Surg. Oncol.* **24**, 1188–1194 (2017).
17. Traylor, M. J. *et al.* Long-term antibacterial efficacy of air plasma-activated water. *J. Phys. D. Appl. Phys.* **44**, 472001 (2011).
18. Ma, R. *et al.* Non-thermal plasma-activated water inactivation of food-borne pathogen on fresh produce. *J. Hazard. Mater.* **300**, 643–651 (2015).
19. Bruggeman, P. J. *et al.* Plasma-liquid interactions: a review and roadmap. *Plasma Sources Sci. Technol.* **25**, 53002 (2016).
20. Babaeva, N. Y. & Kushner, M. J. Reactive Fluxes Delivered by Dielectric Barrier Discharge Filaments to Slightly Wounded Skin. *J. Phys. D. Appl. Phys.* **46**, 25401 (2013).
21. Babaeva, N. Y., Tian, W. & Kushner, M. J. The Interaction Between Plasma Filaments in Dielectric Barrier Discharges and Liquid Covered Wounds: Electric Fields Delivered to Model Platelets and Cells. *J. Phys. D. Appl. Phys.* **47**, 235201 (2014).
22. Chen, C. *et al.* A Model of Plasma-Biofilm and Plasma-Tissue Interactions at Ambient Pressure. *Plasma Chem. Plasma Process.* **34**, 403–441 (2014).
23. Suda, Y. *et al.* Computational study of temporal behavior of incident species impinging on a water surface in dielectric barrier discharge for the understanding of plasma-liquid interface. *Jpn. J. Appl. Phys.* **54**, 01AF03 (2015).
24. Tian, W. & Kushner, M. J. Atmospheric pressure dielectric barrier discharges interacting with liquid covered tissue. *J. Phys. D. Appl. Phys.* **47**, 165201 (2014).
25. Lietz, A. M. & Kushner, M. J. Air plasma treatment of liquid covered tissue: long timescale chemistry. *J. Phys. D. Appl. Phys.* **49**, 425204 (2016).
26. Liu, Z. C. *et al.* Physicochemical Processes in the Indirect Interaction Between Surface Air Plasma and Deionized Water. *J. Phys. D. Appl. Phys.* **48**, 495201 (2015).

27. Liu, D. X. *et al.* Aqueous reactive species induced by a surface air discharge: Heterogeneous mass transfer and liquid chemistry pathways. *Sci. Rep.* **6**, 1–11 (2016).
28. Norberg, S. A., Tian, W., Johnsen, E. & Kushner, M. J. Atmospheric pressure plasma jets interacting with liquid covered tissue: touching and not-touching the liquid. *J. Phys. D. Appl. Phys.* **47**, 475203 (2014).
29. Norberg, S. A., Johnsen, E. & Kushner, M. J. Helium atmospheric pressure plasma jets interacting with wet cells: delivery of electric fields. *J. Phys. D. Appl. Phys.* **49**, 185201 (2016).
30. Lindsay, A., Anderson, C., Slikboer, E., Shannon, S. & Graves, D. Momentum, heat, and neutral mass transport in convective atmospheric pressure plasma-liquid systems and implications for aqueous targets. *J. Phys. D. Appl. Phys.* **48**, 424007 (2015).
31. Bekeschus, S., Schmidt, A. & von Woedtke, T. The Plasma Jet kINPen – A Powerful Tool for Wound Healing. *Clin. Plasma Med.* **4**, 19–28 (2016).
32. Bundscherer, L. *et al.* Impact of non-thermal plasma treatment on MAPK signaling pathways of human immune cell lines. *Immunobiology* **218**, 1248–55 (2013).
33. Fluhr, J. W. *et al.* In vivo skin treatment with tissue-tolerable plasma influences skin physiology and antioxidant profile in human stratum corneum. *Exp. Dermatol.* **21**, 130–4 (2012).
34. Kramer, A. *et al.* Suitability of tissue tolerable plasmas (TTP) for the management of chronic wounds. *Clin. Plasma Med.* **1**, 11–18 (2013).
35. Wende, K. *et al.* Risk assessment of a cold argon plasma jet in respect to its mutagenicity. *Mutat. Res.* **798–799**, 48–54 (2016).
36. Schmidt-Bleker, A., Winter, J., Bösel, A., Reuter, S. & Weltmann, K.-D. On the Plasma Chemistry of a Cold Atmospheric Argon Plasma Jet with Shielding Gas Device. *Plasma Sources Sci. Technol.* **25**, 15005 (2016).
37. Metelmann, H.-R. *et al.* Head and Neck Cancer Treatment and Physical Plasma. *Clin. Plasma Med.* **3**, 17–23 (2015).
38. Metelmann, H.-R. *et al.* Scar Formation of Laser Skin Lesions after Cold Atmospheric Pressure Plasma (CAP) Treatment: a Clinical Long Term Observation. *Clin. Plasma Med.* **1**, 30–35 (2013).
39. Lademann, J. *et al.* Risk assessment of the application of tissue-tolerable plasma on human skin. *Clin. Plasma Med.* **1**, 5–10 (2013).
40. Van Gaens, W. & Bogaerts, A. Reaction Pathways of Biomedically Active Species in an Ar Plasma Jet. *Plasma Sources Sci. Technol.* **23**, 1–27 (2014).

41. Wende, K. *et al.* Identification of the Biologically Active Liquid Chemistry Induced by a Nonthermal Atmospheric Pressure Plasma Jet. *Biointerphases* **10**, 29518 (2015).
42. Van Boxem, W. *et al.* Anti-Cancer Capacity of Plasma-Treated Pbs: Effect of Chemical Composition on Cancer Cell Cytotoxicity. *Sci. Rep.* **7**, 16478 (2017).
43. Van Rens, J. F. M. *et al.* Induced Liquid Phase Flow by RF Ar Cold Atmospheric Pressure Plasma Jet. *IEEE Trans. PLASMA Sci.* **42**, 2622–2623 (2014).
44. Hefny, M. M., Pattyn, C., Lukes, P. & Benedikt, J. Atmospheric Plasma Generates Oxygen Atoms as Oxidizing Species in Aqueous Solutions. *J. Phys. D. Appl. Phys.* **49**, 404002 (2016).
45. Wilcox, D. C. *Turbulence Modelling for CFD*. (DCW Industries, Inc., 1993).
46. Van Gaens, W. *et al.* Numerical Analysis of the Effect of Nitrogen and Oxygen Admixtures on the Chemistry of an Argon Plasma Jet Operating at Atmospheric Pressure. *New J. Phys.* **17**, 33003 (2015).
47. Tian, W., Lietz, A. M. & Kushner, M. J. The Consequences of Air Flow on the Distribution of Aqueous Species During Dielectric Barrier Discharge Treatment of Thin Water Layers. *Plasma Sources Sci. Technol.* **25**, 55020 (2016).
48. NIST Solution Kinetics Database. at <<http://kinetics.nist.gov/solution/>>
49. Antoine, M. C. Tensions des Vapeur: Nouvelle Relation Entre les Tensions et les Températures. *Comptes Rendus des Séances l'Académie des Science* **107**, 836–837 (1888).
50. Bird, R. B., Stewart, W. E. & Lightfoot, E. N. *Transport Phenomena*. (John Wiley & Sons, 2007).
51. Datt, P. in *Encyclopedia of Snow, Ice and Glaciers*, 703 (Springer Netherlands, 2011).
52. Sakiyama, Y., Graves, D. B., Chang, H.-W., Shimizu, T. & Morfill, G. E. Plasma Chemistry Model of Surface Microdischarge in Humid Air and Dynamics of Reactive Neutral Species. *J. Phys. D. Appl. Phys.* **45**, 425201 (2012).
53. Sander, R. Compilation of Henry's Law Constants for Inorganic and Organic Species of Potential Importance in Environmental Chemistry. (Max-Planck Institute of Chemistry, 1999).
54. Wise, D. L. & Houghton, G. Diffusion coefficients of neon, krypton, xenon, carbon monoxide and nitric oxide in water at 10–60°C. *Chem. Eng. Sci.* **23**, 1211–1216 (1968).

55. Holz, M., Heil, S. & Sacco, A. Temperature-Dependent Self-Diffusion Coefficients of Water and Six Selected Molecular Liquids for Calibration in Accurate <sup>1</sup>H NMR PFG Measurements. *Phys. Chem. Chem. Phys.* **2**, 4740–4742 (2000).
56. Johnson, P. N. & Davis, R. A. Diffusivity of Ozone in Water. *J. Chem. Eng. Data* **41**, 1485–1487 (1996).
57. Stewart, D. J., Griffiths, P. T. & Cox, R. A. Reactive Uptake Coefficients for Heterogeneous Reaction of N<sub>2</sub>O<sub>5</sub> with Submicron Aerosols of NaCl and Natural Sea Salt. *Atmos. Chem. Phys.* **4**, 1381–1388 (2004).
58. Van Gaens, W. & Bogaerts, A. Kinetic Modelling for an Atmospheric Pressure Argon Plasma Jet in Humid Air. *J. Phys. D: Appl. Phys.* **46**, 275201 (2013).
59. Lukes, P., Dolezalova, E., Sisrova, I. & Clupek, M. Aqueous-Phase Chemistry and Bactericidal Effects from Gaseous Plasmas in Contact with Water. *Plasma Sources Sci. Technol.* **23**, 15019 (2014).
60. Girard, P. *et al.* Synergistic Effect of H<sub>2</sub>O<sub>2</sub> and NO<sub>2</sub> in Cell Death Induced by Cold Atmospheric He Plasma. *Sci. Rep.* **6**, 29098 (2016).
61. Girard, F. *et al.* Formation of Reactive Nitrogen Species including Peroxynitrite in Physiological Buffer exposed to Cold Atmospheric Plasma. *RSC Adv.* **6**, 78457–78467 (2016).
62. Pfeiffer, S. *et al.* Metabolic Fate of Peroxynitrite in Aqueous Solution. *J. Biol. Chem.* **272**, 3465–3470 (1997).
63. Graves, D. B. Oxy-nitroso shielding burst model of cold atmospheric plasma therapeutics. *Clin. Plasma Med.* **2**, 38–49 (2014).
64. Loegager, T. & Sehested, K. Formation and Decay of Peroxynitric Acid: a Pulse Radiolysis Study. *J. Phys. Chem.* **97**, 10047–10052 (1993).
65. Staehelin, J. & Hoigné, J. Decomposition of Ozone in Water: Rate of Initiation by Hydroxide Ions and Hydrogen Peroxide. *Environ. Sci. Technol.* **16**, 676–681 (1982).





## **Conclusion and outlook**



Plasma medicine aims to use cold atmospheric pressure plasmas (CAPs) for biomedical applications, either by assisting the treatment (*e.g.*, combining CAPs with surgery or chemotherapy for the treatment of cancer) or by serving as an alternative to existing therapies (*e.g.*, using CAPs to heal chronic wounds). CAPs are ideally suited to be used during medical treatment, as these devices are able to generate biologically relevant species (*i.e.*, reactive oxygen and nitrogen species, or RONS) at atmospheric conditions (*i.e.*, room temperature and pressure and in air). Furthermore, they can be created using a wide range of different setups and working conditions, highlighting the flexibility of CAPs as they are able to be adjusted for the application at hand. These applications are mainly focused on decontamination, wound healing and cancer treatment.

As plasmas produce a chemical cocktail of various species (*i.e.*, molecules, atoms, radicals, excited and charged species), photons and electromagnetic waves, changing the setup and working conditions also has a great impact on the plasma-generated components. Therefore, the flexibility of plasmas also greatly increases the complexity of the treatment from a chemical, physical but also medical point of view. Moreover, not only a wide variety of working conditions and setups are available, also a vast range of different biological tissues must be taken into account, making *plasma medicine* an interdisciplinary and very complex field.

We can define roughly three types of research questions in plasma medicine:

1. Which components, and how many, are generated or created by the plasma device?
2. How do these plasma-generated components interact with the treated substrates/tissues?
3. What is the impact of the plasma-substrate interactions on the biology of the treated substrate?

The research performed in this thesis aims to provide answers to the second type of questions, by investigating the interactions between plasma generated reactive species (*i.e.*, RONS) and various substrates (*i.e.*, biomolecules and liquid water).

RONS act on the treated cells in various ways. By interacting or reacting with different cellular components, a multitude of cellular activities are affected (*i.e.*,

initiated, inhibited or altered). This triggers a series of response activities in the cell itself and within its microenvironment. Because of this, knowledge on the initial interactions between the plasma-generated components and the treated tissue is of the utmost importance. With this knowledge, the immediate effects on the affected cell activities can be investigated. Only then can we understand the biological impact of plasma treatment.

This thesis provides insight in these initial interactions, *i.e.*, the role that RONS play in affecting cellular components, and therefore cellular activities. The performed work can be divided in two parts:

- (i) elucidating the actual interactions between RONS and biomolecules (*i.e.*, sugar, DNA and proteins).
- (ii) obtaining insight in the transport of RONS in aqueous solutions.

For part (i), atomic scale simulations were used to investigate the reactivity of biological systems upon interaction with RONS. This was performed with classical MD simulations for sugars in vacuum, solution and as a dried droplet (*cf.* **chapter 3**), and for DNA in solution (*cf.* **chapter 4**). The protein systems were investigated in solution using a quantum mechanical method (*cf.* **chapter 5**). A method of higher accuracy was chosen here, due to the increased complexity of the systems. In all cases, oxidation reactions were observed, which were initiated by short-lived reactive species (*i.e.*, hydroxyl radicals or nitric oxide). In the presence of other reactive species (*e.g.*, hydrogen peroxide or ozone) and molecular oxygen, a vast range of oxidation products were often observed after the initial H-abstraction. This is interesting as oxidation can either alter the activity of the affected biomolecule (*e.g.*, inactivation of glycoproteins) or result in irreversible damage to the system (*e.g.*, DNA modifications).

In **chapter 3**, only mild oxidation of D-glucose was observed, leading to a rise in C=O double bonds and slight decrease in ether bonds, which results in the opening of the D-glucose ring. As sugars are found in various cellular systems (*e.g.*, DNA or membrane-bound proteins), the observed oxidation can alter the activity of the affected systems.

In **chapter 4**, it was concluded that DNA oxidation can result in severe

damage to the genetic code it holds, and therefore to the whole cellular system. The oxidation of nucleobases can lead to the inability of proteins to recognize the genetic code, leading to incorrect responses. This is, in part, prevented by repair mechanisms, which act when DNA oxidation is detected, aiming to reverse the occurring damage. Although the cell is able to reverse DNA damage, some oxidation products are, however, falsely recognized (possibly leading to DNA mutations) or are irreversible. In this chapter, the precursors for FapydG, FapydA and 8-oxo-purines were predicted by the simulations upon oxidation of DNA, which are markers for DNA damage and are known to induce DNA mutations, inflicting changes in the cellular activity. Furthermore, DNA strand breaks were observed as well, which become irreversible when two strand breaks occur on both DNA strands, leading to double strand breaks and therefore the cleavage of the DNA molecule. These observations highlight the damaging nature of reactive species when they come in contact with DNA, and it has the ability to affect the cell as a whole. Indeed, when the oxidative damage occurs on vital parts of the DNA, apoptosis will be induced when repair mechanisms fail to recognize and/or reverse this damage.

In **chapter 5**, the oxidation of proteins and peptides was investigated. Four different systems were considered: two peptides, cysteine and the cysteine-containing antioxidant glutathione (GSH). From the oxidation of the peptides and GSH, insight was obtained on the most expected sites of attack. These targets corresponded well with experimental observations from literature. However, a few amino acids acted differently than expected. This might be attributed to environmental factors: *i.e.*, contact surface and polarity of neighboring amino acids. On one hand, this is interesting as this means that different proteins will act differently to the introduced oxidative species. On the other hand, this also enhances the complexity of plasma-cell interactions, because the interaction with proteins cannot be easily predicted. An example is the oxidation of thiols found on cysteine. Oxidation is initiated by a H-abstraction on the sulfur atom, resulting in a sulfur radical. This facilitates the formation of disulfide bonds within the biomolecule or between two separate molecules (*cf.* GSH/GSSG). However, overoxidation was found to chemically modify these disulfide bonds, breaking them and yielding the formation of irreversible oxidation products, like sulfonic acids. As environmental factors have an impact on

the degree of oxidation (*e.g.*, position of cysteine in the protein and the 3D conformation), they will affect the severity of the chemical modifications of cysteine and consequent disulfide bonds. This makes predicting the impact of RONS on such proteins difficult.

In the second part of this thesis (ii), DFTB-MD, as well as 2D fluid dynamics simulations were used to investigate the interactions and accumulation of biologically relevant reactive species in solution during the treatment with a plasma jet (*cf.* **chapters 6 and 7**). Combined, it was observed that plasma species can successfully enter the treated liquid, but the short-lived species are readily consumed, forming more long-lived reactive species (*i.e.*, hydrogen peroxide, nitric and nitrous acid). This is of great importance because this suggests that liquid covered cells will most likely only come in contact with these long-lived species which, in turn, will direct the initial interactions with the cell, inflicting stress. The induced stress will activate various response mechanisms, which can increase the production of reactive species (inter- or intracellular). The increase in oxidative species will lead to oxidative damage as discussed above (*cf.* **chapter 3, 4 and 5**).

The picture drawn in this thesis focusses on the initial interactions with the cells or other biological substrates during plasma treatment, which forms only a part of the research done and needed in the field of plasma medicine (*cf.* research question type 2). These interactions will trigger and direct other effects, which will have an impact on the observed biology (*cf.* research question type 3). Furthermore, the initial interactions are strongly dependent on the used working conditions (*cf.* research question type 1). Therefore, understanding the impact on the working conditions is vital in order to better understand and control the initial interactions with the treated biological substrate. This, in turn, will provide the means to understand the impact of the treatment on the biology in the treated cells and deeper inside the treated tissue, in order to control the biological effects during the plasma treatment of wounds and cancer, alone and in combination with other treatments.

Because of this, I believe that, first of all, efforts should be made to elucidate the impact of various working conditions on the generation and transport of reactive species to the substrate. This can be done based on the results and the model as presented in **chapter 7**. Using fluid dynamics simulations, the influence of the

treated liquid on the formation and behavior of reactive species can be investigated. I expect that the pH and the presence of other species, *e.g.*, chlorine (as presented in buffered saline solutions), metals or biomolecules (such as amino acids and sugars, present in liquid cell media), will influence the liquid phase chemistry and, as a result, the accumulation of reactive species in the liquid. As buffered saline solutions and cell media are typically used as plasma treated liquids, rather than pure water, it would be interesting to extend the fluid dynamics model in this respect. Moreover, this knowledge can be further used when considering the direct treatment of liquid-covered tissue. A question interesting to focus on is: 'What is the impact of a biological substrate, at the bottom of the liquid, on the chemistry in the liquid and which species will mainly interact/react with this substrate?' Together, this will provide great insight, necessary when investigating the initial interactions between plasma-generated species and biological systems. In addition, the communication between plasma-generated species and cells is still largely unknown. In this context, it would be interesting to obtain molecular scale knowledge on how RONS affect the activity of various cellular components. The focus should go to the cell-membrane and membrane-bound systems. Interesting targets are membrane-bound proteins like CD44, NRF2 and TRPM2, as well as catalase. This knowledge can be coupled back to the working conditions to obtain better control and to be able to anticipate the biological response to the plasma treatment.





## **Academic curriculum vitae**



## List of publications related to this thesis

1. **Verlackt, C. C. W.**, Van Boxem, W. & Bogaerts, A. Transport and Accumulation of Plasma Generated Species in Aqueous Solution. *Phys. Chem. Chem. Phys.* **in press** (2018).
2. Gorbanev, Y., **Verlackt, C. C. W.**, Tinck, S., Tuenter, E., Foubert, K., Cos, P. & Bogaerts, A. Combining experimental and modelling approach to study the sources of reactive species induced in water by the COST RF plasma jet. *Phys. Chem. Chem. Phys.* **20**, 2797-2808 (2018)
3. Lackmann, J.-W., Wende, K., **Verlackt, C. C. W.**, Golda, J., Volzke, J., Kogelheide, F., Held, J., Bekeschus, S., Bogaerts, A., Schulz-von der Gathen, V. & Stapelmann, K. Cysteine Modifications: Fingerprinting Modification Patterns to Biologically Characterize Medical Plasmas. *Sci. Rep.* **submitted**.
4. Klinkhammer, C., **Verlackt, C.**, Smilowicz, D., Kogelheide, F., Bogaerts, A., Metzler-Nolte, N., Stapelmann, K., Havenith, M. & Lackmann, J.-W. Elucidation of Plasma-induced Chemical Modifications on Glutathione and Glutathione Disulphide. *Sci. Rep.* **7**, 13828 (2017).
5. **Verlackt, C. C. W.**, Van Boxem, W., Dewaele, D., Sobott, F., Benedikt, J., Neyts, E. C. & Bogaerts, A. Mechanisms of Peptide Oxidation by Hydroxyl Radicals: Insight at the Molecular Scale. *J. Phys. Chem. C* **121**, 5787–5799 (2017).
6. **Verlackt, C. C. W.**, Neyts, E. C. & Bogaerts, A. Atomic scale behavior of oxygen-based radicals in water. *J. Phys. D. Appl. Phys.* **50**, 11LT01 (2017).
7. **Verlackt, C. C. W.**, Neyts, E. C., Jacob, T., Fantauzzi, D., Golkaram, M., Shin, Y.-K., van Duin, A. C. T. & Bogaerts, A. Atomic-scale insight into the interactions between hydroxyl radicals and DNA in solution using the ReaxFF reactive force field. *New J. Phys.* **17**, 103005 (2015).



## List of publications not included in this thesis

1. Van der Paal, J., Neyts, E. C., **Verlackt, C.** & Bogaerts, A. Effect of lipid peroxidation on membrane permeability of cancer and normal cells subjected to oxidative stress. *Chem. Sci.* **7**, 489 (2016).
2. Bogaerts, A., Khosravian, N., Van der Paal, J., **Verlackt, C. C. W.**, Yusupov, M., Kamaraj, B. & Neyts, E. C. Multi-level molecular modelling for plasma medicine. *J. Phys. D: Appl. Phys.* **49**, 54002 (2016).
3. Park, J. H., Kumar, N., Park, D. H., Yusupov, M., Neyts, E. C., **Verlackt, C. C. W.**, Bogaerts, A., Kang, M. H., Uhm, H. S., Choi, E. H. & Attri, P. A comparative study for the inactivation of multidrug resistance bacteria using dielectric barrier discharge and nano-second pulsed plasma. *Sci. Rep.* **5**, 13849 (2015).
4. Van der Paal, J., **Verlackt, C. C.**, Yusupov, M., Neyts, E. C. & Bogaerts, A. Structural modification of the skin barrier by OH radicals: a reactive molecular dynamics study for plasma medicine. *J. Phys. D: Appl. Phys.* **48**, 155202 (2015).
5. Cambre, S., Campo, J., Beirnaert, C., **Verlackt, C.**, Cool, P. & Wenseleers, W. Asymmetric dyes align inside carbon nanotubes to yield a large nonlinear optical response. *Nat. Nanotechnol.* **10**, 248 (2015).
6. Yusupov, M., Neyts, E. C., **Verlackt, C. C.**, Khalilov, U., van Duin, A. C. T. & Bogaerts, A. Inactivation of the endotoxic biomolecule lipid A by oxygen plasma species: a reactive molecular dynamics study. *Plasma Process. Polym.* **12**, 162–171 (2014).
7. Bogaerts, A., Yusupov, M., Van der Paal, J., **Verlackt, C. C. W.** & Neyts, E. C. Reactive Molecular Dynamics Simulations for a Better Insight in Plasma Medicine. *Plasma Process. Polym.* **11**, 1156–1168 (2014).
8. Neyts, E. C., Yusupov, M., **Verlackt, C. C.** & Bogaerts, A. Computer simulations of plasma–biomolecule and plasma–tissue interactions for a better insight in plasma medicine. *J. Phys. D: Appl. Phys.* **47**, 293001 (2014).



## Conference contributions

1. Verlackt, C. C. W., Van Boxem, W., Neyts, E. & Bogaerts, A. Exploring the nature of plasma-liquid interactions, *23<sup>rd</sup> International Symposium for Plasma Chemistry*, 30 July - 04 August (2017) Montreal, Canada  
*Oral Presentation.*
2. Verlackt, C. C. W., Neyts, E. C. & Bogaerts, A. Evaluating the behavior of plasma generated reactive species in contact with water, both at macroscopic and molecular scale, *International Conference on Plasmas with Liquids*, 5-9 March (2017) Prague, Czech Republic  
*Poster Presentation.*
3. Verlackt, C. C. W., Yusupov, M., Neyts, E. & Bogaerts, A. Atomic scale insight in peptide oxidation: molecular dynamics, *Plasma and bio workshop*, 2 February (2017), Bochum, Germany  
*Invited Oral Presentation.*
4. Verlackt, C. C. W., Lackmann, J.-W. & Bogaerts, A. Insight in the plasma induced oxidation of peptides at the molecular scale, *6<sup>th</sup> International Conference on Plasma Medicine*, 4-9 September (2016) Bratislava, Slovakia  
*Poster Presentation.*
5. Verlackt, C. C. W., Van der Paal, J., Verheyen, C., Khosravian, N., Kamaraj, B., Neyts, E. C. & Bogaerts, A. Multi-level molecular modeling for plasma medicine, *ITN-ARGENT*, 4-5 May (2016) Frankfurt, Germany  
*Invited Oral Presentation.*
6. Verlackt, C. C. W., Van Boxem, W., Neyts, E. C. & Bogaerts, A. Investigating the interactions between reactive oxygen species and biomolecules by means of reactive atomic-scale simulations, *BIOPLASMAS & PLASMAS WITH LIQUIDS – Joint Conference of COST ACTIONS TD1208&MP1101*, 13-17 September (2015) Bertinoro, Italy  
*Poster Presentation.*
7. Verlackt, C. C. W., Van der Paal, J., Yusupov, M., Khosravian, N., Kamaraj, B., Neyts, E. C. & Bogaerts, A. A Multi-scale Modeling Approach for Molecular Level Insight in Plasma Medicine, *iPlasmaNano-VI*, 25-29 August (2015) Beijing, China  
*Invited Oral Presentation.*



8. Verlackt, C. C. W., Van der Paal, J., Yusupov, M., Neyts, E. C. & Bogaerts A. Multi-level molecular modeling for plasma medicine, *22<sup>nd</sup> International Symposium on Plasma Chemistry*, 5-10 July (2015) Antwerp, Belgium  
*Oral Presentation.*
9. Verlackt, C. C. W., Neyts, E. C. & Bogaerts A. Atomic Scale Simulations of the Oxidative Stress Caused by Hydroxyl Radicals on DNA, *2<sup>nd</sup> International Workshop on Plasma for Cancer Treatment*, 16-17 March (2015) Nagoya, Japan  
*Poster Presentation.*
10. Verlackt, C. C. W., Yusupov, M., Neyts, E C. & Bogaerts, A. Atomic scale simulations of plasma interactions with the bacterial membrane and biofilm, *5<sup>th</sup> International Conference on Plasma Medicine*, 17-24 May (2015) Nara, Japan  
*Oral Presentation.*